Universidad de Granada

Dinámica **Ambiental**
UNIVERSIDAD DE GRANADA

Instituto Interuniversitario de Investigación del Sistema Tierra en Andalucía (IISTA)

Programa de Doctorado de Dinámica de Flujos Biogeoquímicos y sus Aplicaciones

Universidad de Granada

Morpho-hydrodynamics of a highly altered tidally-dominated bay

Doctoral Thesis

Author: Carmen Zarzuelo Romero

Advisors: Miguel Ortega Sánchez & Manuel Díez Minguito

November 2015

Editor: Universidad de Granada. Tesis Doctorales
Autor: Carmen Zarzuelo Romero
ISBN: 978-84-9163-318-1
URI: http://hdl.handle.net/10481/55547

Agradecimientos

Gracias a cada una de las personas que de una forma u otra han formado parte de todos estos años de duro trabajo, que culminan y se materializan en esta tesis.

En primer lugar, quiero agradecer a mis directores de Tesis, Miguel Ortega y Manuel Díez, por vuestra eterna paciencia. Sin vuestra guía, apoyo y conocimientos nunca hubiese podido llegar hasta aquí.

Quiero darle las gracias a Miguel Losada por haberme permitido formar parte de este gran grupo y haberme brindado todas las herramientas posibles para poder seguir avanzando en el camino. Gracias a toda la gente del Grupo de Dinámica de Flujos Ambientales que me han acogido durante estos años prestándome toda ayuda solicitada, en especial a mis compañeros: Andrea, Marta, Porro, Antonio, Pedros... que me han hecho la vida ceamera más fácil y llevadera.

My gratitude also to professors Andrea D'Alpaos and Luca Carniello for their hospitality, dedication and interest during my stay at the University of Padua.

Agradezco a la Junta de Andalucía por haber financiado mi formación predoctoral mediante la concesión de una beca FPDI. También agradezco al Puerto de Cádiz por todas las facilidades que me han dado en la realización de las campañas de campo.

A mis hombrazotes y cayeta, por todas las risas, charlas, cenas... pero sobre todo por haberme demostrado la palabra amistad. A mis amigas de toda la vida, por seguir estando cerca aún viviendo cada una en un lado diferente.

A mis pies y mis manos, mi madre y hermana por no haberme dejado caer, por esa sonrísa cuando se me torcía el morro. Por haber lidiado la etapa más dura con una entereza digna de envidiar, y porque os quiero con locura. A mis tíos, primos y abuelos, por haberos ilusionado desde la cosa más insignificante haciéndome sentir que era lo más importante.

En especial a ti José, por ser mi mejor compañero en este viaje. Por haberme aguantado, soportado y sufrido durante estos años llenos de curvas. Gracias por no querer cambiarme y hacerme sentir la persona más afortunada; y por supuesto a tu familia por hacerme sentir como en casa.

Y por último con permiso de todos, esta tesis va dedicada a mi maestro porque a él le debo sin duda la mayor parte de lo que soy hoy. A ti papa, por haberme inculcado la investigación y el significado de las palabras: lucha y superación. Por haberme enseñado

infinidad de valores, pero sobre todo el no rendirse jamás. Este trabajo lo iniciamos juntos, y aunque físicamente no puedas ver el resultado final, sé que donde estés estarás orgulloso de lo conseguido.

Para Antonio

Abstract

The morphology of many tidal inlets and estuaries is characterized by a complex pattern of channels and sandy shoals, both in space and time. This dynamic behaviour is caused by the interaction between water motion and sediment transport. Observations in many study areas clearly indicate that morphological behaviour is sensitive to changes in external conditions caused e.g. by sea level rise and/or human activities (Van der Spek, 1997; Schuttelaars and de Swart, 2000).

In this Thesis, hydrodynamic and human activities influences on morphology are addressed in the Bay of Cádiz, an estuary located in the south–west of Spain. The Bay of Cádiz is a highly altered embayment in which socio-economical develpments and ecological interests conflict. Shipping requires the stability of the navigation channel, maintained with periodical dredgings. Further modifications on the morphology of this area are marshes occupation and the construction of a new bridge to favor the road connectivity between the city of Cádiz and mainland. These usually confronts with the natural status of the ecosystem and the activities derived from it. This work studies both through observations and numerical simulations the impact of some of these modifications on the morpho-hydrodynamics of the Bay of Cádiz.

The Bay of Cádiz is a semidiurnal, mesotidal, and low-inflow estuary located in the SW of the Iberian Peninsula, facing towards the Gulf of Cádiz (Atlantic Ocean). The Bay of Cádiz is dynamically comprised of three areas with a total extension of 140 km^2: a deeper outer area connected to the open sea; a shallower inner area, which harbors most of the remaining marshes; and a central sector, the Puntales Channel, that connects the inner and outer areas, characterized by irregular boundaries due to urban developments and port infrastructures. This current overall morphology is the result of the natural evolution induced by past geological events, climatic agents, biological factors and human activities.

Recently, since 2012, the morphology of the Bay of Cádiz has changed again as a result of human activities. “La Pepa” Bridge was completed in 09/24/2015. It is one of the longest (5 km) and highest (69 m over mean sea level) bridges of Europe, and crosses the Puntales Channel connecting the city of Cádiz with the Peninsula. A new container terminal (which increase 22.5% the port surface) is under construction at the Port of Cádiz; when it is done, $3.6 \cdot 10^6 m^3$ of sediment will be dredged to shift and deepen the current navigation channel. The impacts of these interventions on the water and sediment exchange in the whole estuarine area are assessed in this Thesis.

The methodology followed to reach this objective is twofold. Firstly, a comprehensive

field survey was carried out with a total of 10 instruments deployed at 7 stations from December 22, 2011 to April 18, 2012. Measurements of sea level, currents, water quality, and wind were used to evaluate water circulation and sediment transport within the bay and, in particular, the water exchange between the inner and outer basins on intratidal and subtidal/morphodynamics time scales. Secondly, the field observations and its analysis are supported and complemented by the results of two numerical models implemented, calibrated and validated within the Bay of Cádiz and inner shelf. Modeling scenarios are devised to assess the consequences of current and future interventions within the Bay, namely, the construction of the new port terminal, the deepening of the navigation channel, and the construction of the new bridge. The models are (1) the DELFT3D model, which simulates hydrodynamic flow and sediment transport in three dimensions, suitable for simulating the overall circulation of the Bay (Lin et al., 1998, 2002), and (2) the model developed by Carniello et al. (2005), which combines wind waves with tidal fluxes in a tidal basin. The Carniello model is more convenient in shallower, intertidal areas, and irregular basins (e.g. tidal creeks).

Results indicate that, at intra-tidal time scale, the estuary is tidally driven and dynamically short. The water levels and currents are in quadrature. The amount of dissipated tidal energy destabilizes the water column, resulting in a weakly stratified system. This effect is more significant at the constriction, where, the change of the bottom slope apparently induces cyclonic rotation in the semidiurnal tidal ellipse. At the subtidal scale, barotropic subtidal flows were evaluated and analyzed. The circulation patterns of the inner (seasonally hypersaline) and outer portions operate almost independently. The observed residual water volume exchange between the inner and outer basins does not exceed $2 \cdot 10^7\,\mathrm{m}^3$. The residual exchange is largely wind-driven. For winds over 8 m/s, the cross-correlation between the wind and residual volumes attains values $\sim$0.70, whereas lower cross-correlations are found for weaker winds.

The capability of the bay to exchange water and transport sediment between the inner and outer bay deteriorates after the deepening of the navigation channel and the construction of the new port terminal and the new bridge. This may have an impact on the ecological status of the bay. The influence of the dredging and the new terminal are concentrated at the entrance to the central sector of the bay and close to the channel. The dredging would increase siltation in the shallower areas close to the new channel, which subsequently reduce the amount of sediment input into the basins. The bridge mostly affect the Puntales Channel and the inner bay. Due to the presence of the new bridge, the difference of tidal elevation between the inside and outside water levels may increase. The hydrodynamic changes and their effect on sediment erosion, deposition and transport may cause far-field geomorphological changes away from the dredge location, including the potential erosion of intertidal areas. The most changes in the erosion/deposition patterns are found in the area with strong bottom frictions and tidal asymmetries. At the scales analyzed in this work, tidal currents, the spring-neap cycles cause suspended sediment concentration to vary in time and space. Wind forcing is also found to be important. It is capable of entrain and transport sand and mud from the inner area, specially northward winds.

The hydro- and morphodynamic changes show that the effects of future interventions

are far from damped out, and it will take many decades before a new equilibrium will be reached.

Resumen

Las bahías son áreas caracterizada por un gran dinamismo debido principalmente al intercambio de agua y sedimentos entre los ambientes terrestre y marino. Este intercambio permite el desarrollo de entornos únicos, con una alta productividad ecológica y de gran importancia para otros ecosistemas marinos. Se encuentran, además, entre los ecosistemas costeros más afectados por las actividades del hombre, ya que en ellas conviven espacios naturales de alto valor ambiental con actividades industriales de elevado impacto económico y social. En particular, las relacionadas con la actividad portuaria tienen un peso relevante, desarrollándose además a su alrededor grandes núcleos urbanos.

El caso particular de la Bahía de Cádiz (suroeste español) despierta un especial interés por las numerosas intervenciones y alteraciones que han tenido lugar desde mediados del siglo pasado, así como por su particular morfología y situación geográfica. La bahía es un espacio marítimo singular con una extensión total de 140 km^2 y que se divide en tres partes: una zona exterior más profunda conectada con el mar, una zona interior menos profunda, y el sector central, conocido como Canal de Puntales, que conecta las zonas exterior e interior. Los registros históricos indican que los primeros asentamientos humanos se formaron hace más de 3.000 años, debido a la ubicación geo-estratégica de la zona. La morfología actual es el resultado de la evolución natural inducida por sucesos pasados geológicos, agentes climáticos, factores biológicos y actividades humanas.

Debido al auge económico y demográfico de la zona, se han desarrollado diversas actividades antropogénicas que han alterado la configuración y el comportamiento tanto de la bahía como de su sistema costero; entre ellas destacan la construcción del Puerto de Cádiz, la del Puerto de la Zona Franca y la del Puente Carranza. Este crecimiento y desarrollo de la zona continua actualmente con nuevas intervenciones que se encuentran en desarrollo: la ampliación del Puerto de Cádiz y la construcción de un nuevo puente. Todas estas construcciones perturban el comportamiento natural de la bahía y constituyen la principal motivación de esta tesis doctoral: (1) caracterizar la dinámica de la Bahía y (2) analizar cómo estas intervenciones futuras pueden afectar a su hidrodinámica y morfodinámica.

Desde 2012 se están llevando las dos intervenciones de gran relevancia anteriormente citadas: (1) el puente de "La Pepa", uno de los más largos (5 km) y altos (69 m) de Europa, y que atraviesa el Canal de Puntales conectando la ciudad de Cádiz con la península, que fue terminado en septiembre de 2015; (2) una nueva terminal de contenedores en el Puerto de Cádiz que incrementará en un 22,5 % su superficie de atraque; cuando finalice será necesario, además, realizar un dragado de $3,6 \cdot 10^6\,m^3$ para adaptar y profundizar el canal de navegación actual. Sin embargo, los impactos esperados de estas intervenciones

sobre los intercambios de agua y sedimentos en toda la bahía no han sido evaluados a escala morfodinámica/submareal en detalle.

Pese a la importancia de la Bahía en el contexto regional y nacional, hasta el momento no se han llevado a cabo medidas intensivas de larga duración (meses) insitu que permitan caracterizar la hidrodinámica de la bahía y conocer así en detalle su comportamiento. Asimismo, la influencia de las diferentes intervenciones desarrolladas durante los últimos décadas tampoco han sido estudiadas. Los principales trabajos previos se han centrado en analizar las constantes mareales y la influencia de la estacionalidad en la variabilidad mareal. Así pues, esta tesis se enmarca en un estudio integral que mediante datos de campo y la implementación, calibración y validación de modelos numéricos, permita alcanzar los objetivos que se plantean.

Para alcanzar dichos objetivos, en primer lugar se ha realizado un estudio exhaustivo de la zona que permitió conocer los puntos que suscitan mayor interés; con esa información se diseñó una primera campaña de campo intensiva para medir presiones, corrientes, viento, conductividad, temperatura y sólidos en suspensión; dicha campaña tuvo lugar entre Diciembre del 2011 y Abril del 2012, y en la ella se instalaron un total 7 estaciones de medida.

Posteriormente, para caracterizar la dinámica global en toda la bahía, se han implementado dos modelos numéricos morfodinámicos: el DELFT3D y el desarrollado por Carniello en 2005 (Universidad de Padova). Se acudió a este segundo modelo por las discrepancias obtenidas en zonas poco profundas e intermareales. El modelo Delft3D, forzado con marea, oleaje y viento, fue calibrado y validado con los niveles de agua ($R \sim 0,99$), las corrientes instantáneas ($R \sim 0,88$) y residuales ($R \sim 0,8$) medidas durante la campaña de campo. El segundo modelo implementado combina viento con los flujos mareales; se obtuvieron excelentes comparaciones durante un período de 40 días con los niveles de agua ($R \sim 0,99$), las corrientes instantáneas ($R \sim 0,88$) y residuales ($R \sim 0,8$), y el prisma de marea ($R \sim 0,73$). A este modelo se le acopló el módulo de transporte de sedimentos, y se obtuvieron buenas correlaciones entre los datos observados y los modelados ($R \sim 0,66$).

A partir tanto de los datos medidos como de los resultados proporcionados por los modelos, se ha caracterizado y analizado en primer lugar la dinámica de la Bahía. Su comportamiento es semejante a un estuario corto, estando los niveles de marea y corrientes en cuadratura. A escala submareal, los patrones de circulación del interior (hipersalinos) y exterior (térmicas) operan casi independientemente. La transformación de la onda de marea, el flujo de energía, la energía disipada, y los flujos submareales barotrópicos fueron evaluados y analizados a partir de las elevaciones y corrientes obtenidas a partir de los modelos numéricos. La cantidad de energía disipada desestabiliza la columna de agua, siendo un sistema débilmente estratificado. Este efecto es más significativo en la constricción, en donde el cambio de la pendiente del fondo aparentemente induce a la rotación ciclónica de la elipse de marea semidiurna. El intercambio de volumen de agua residual observado entre la cuenca interna y externa no excede de $2 \cdot 10^7\,\mathrm{m}^3$. El viento es el agente que más afecta al intercambio residual y al transporte de sedimentos entre los sacos. Para vientos mayores de 8 m/s, las correlaciónes entre los vientos y volúmenes residuales alcanzan valores de $\sim$ 0,70, mientras que las correlaciones son inferiores para

vientos menores. También se ha observado que existe una correlación directa del viento con la concentración y el movimiento de sedimentos, en particular cuando el viento procede del sur. Los mayores cambios en los patrones de erosión/sedimentación se han encontrado en las áreas con mayor fricción de fondo y asimetría de marea.

Usando los modelos numéricos implementados, se han podido simular diferentes escenarios correspondiente con las futuras intervenciones. Se han representado 4 escenarios: el escenario 1 (Sc_1) corresponde con la situación actual, en el escenario 2 (Sc_2) se ha representado la amplicación de la terminal del Puerto de Cádiz y el nuevo canal de navegación, el escenario 3 (Sc_3) corresponde con el diseño del nuevo puente, y uniendo todas las intervenciones se ha diseñado el escenario 4 (Sc_4) que corresponderá con la situación futura definitiva.

Estas intervenciones tienen un gran impacto en la dinámica de la bahía. Los resultados indican que habrá un deterioro en el intercambio de agua y sedimentos entre la bahía interior y exterior, lo que afectará al entorno ecológico de la misma. Por ejemplo, los efectos morfodinámicos debidos al dragado y la nueva terminal (Sc_2) se concentran en la entrada de la sección central y en los alrededores del canal de navegación. El transporte de sedimentos varía con las corrientes de marea. El dragado aumenta la marea y por tanto la corriente, provocando un mayor transporte de sedimentos que tenderá a depositarse en zonas menos profundas cercanas al canal. Por otro lado, el sector central y el saco interno se verán afectados por la construcción del puente (Sc_3). Debido a ello, el prisma de marea entre el saco interno y externo se verá incrementado. Los cambios hidrodinámicos y su efecto sobre la erosión de sedimentos, la deposición y el transporte pueden causar cambios geomorfológicos secundarios a largo plazo, incluyendo la posible erosión de las zonas intermareales.

Los cambios hidrodinámicos y morfodinámicos muestran que los efectos de las futuras intervenciones están lejos de ser amortiguados, y pasarán decádas hasta que se alcance un nuevo equilibrio. Los resultados derivados de esta tesis doctoral muestran la importancia de caracterizar a fondo la dinámica y prever el impacto que las intervenciones humanas tendrán en bahías de geometría compleja dominadas por procesos mareales.

Contents

List of Figures

List of Tables

Chapter 1
Introduction

1.1 Motivation and Background

Bays are large bodies of water connected to the open ocean or sea and usually formed by two portions, the outer and inner basins, which are usually fed by the small rivers, streams and tidal creeks. The shallow-water systems are mainly dominated by tidal asymmetries, which are generated by nonlinear processes of interaction. These effects promote a net flow of sediment in the direction of such asymmetries (Aubrey and Speer, 1985; Aldridge, 1997). Bays are becoming more important in modern society, due to their strategic locations and unique natural environments. Many estuaries worldwide have been modified in the past decades, in order to reclaim land and to allow even larger ship access to inland waterways. While it is highly profitable, environmental problems may also come if proper management decisiones are not taken. The channel deepening and straightening as well as reclamation of the intertidal area have been some of the most popular interventions. The tidal amplification, the changes of the erosion/deposition patterns, the increasing estuarine circulation, and the increasing tidal asymmetry are some poorly known examples of the effects caused by anthropogenic influences. The coastal zones constitute ecosystems which are generally subjected to antrophic pressure, being bays and shallow environment with low water renewal the most susceptible to be impacted.

The water exchange between estuaries and adjacent seas has been extensively studied in the few past decades due to its socio-economic and environmental significance and its effect on shelf and estuarine ecosystems. The hydraulic exchange between basins, that are frequently separated by morphological features such as constrictions, dictates the water properties and the short-to-long-term transport of dissolved and suspended matter. Barotropic forcing in these areas is mainly induced by tides; the establishment of which is due to remote winds; the seasonal cycle of temperature; among others. Baroclinic flows are typically induced by density gradients and other horizontal inhomogeneties and local winds (Valle-Levinson, 2010; Lv et al., 2014). The dominance of these processes depends on the temporal scale that is being considered. Short-period semidiurnal or diurnal tidal motions are often the most energetic forces acting on estuaries. Nevertheless, long-period subtidal motions are important because they control the long-term transport (Wong and Moses-Hall, 1998; Valle-Levinson and Blanco, 2004a).

Bays frequently have an inlet where human settlements have historically been of great importance, mainly during the most recent decades. These man-made alterations mod-

ify the tidal exchange in coastal embayments, disrupting the pathway of the tidal waters entering the estuaries and the tidal range and flushing characteristics of these systems. As a consequence, these human interventions change the sediment transport patterns in many bays and estuaries around the world. These effects are evident at remarkable sites such as the Ems estuary (Van Maren et al., 2015b), China's Bohai Bay (Lu et al., 2009) and the San Francisco Bay (Knowles and Cayan, 2004; Barnard et al., 2013), among others.

Water circulation, solute transport, and morphology could be highly modified by human-induced pressures. Many estuarine systems are degraded after the development of port infrastructure and navigation channels (Wang et al., 2014), land reclamation, and cross-bay bridge construction (Li et al., 2014; Van Maren et al., 2015a; Del Río et al., 2015). One example of a heavily altered bay is the Bay of Cádiz (SW Spain); historical records indicate that the first human settlements in this bay were formed more than 3.000 y.a. The last marshes in this environment coincide with urban development and port infrastructure. Since the last century, had changed dramatically as a result of human activities, like the constructions of the Ports and Bridges. Since 2012, a new container terminal is under construction at the Port of Cádiz, and the navigation channel under the new bridge will be deepened (Zarzuelo et al., 2015a).

Among the different anthropogenic activities at these environments, navigation and dredging, urban occupation, and marsh reclamation for accommodating new infrastructures have stronger influences on the hydro- and morphodynamics (Knowles and Cayan, 2004; Lu et al., 2009; Barnard et al., 2013; Van Maren et al., 2015b). They also add complexity to the understanding of the main physical drivers of water circulation (Valle-Levinson and Blanco, 2004b; Carniello et al., 2005; Zhong and Li, 2006; Valle-Levinson, 2008; D'Alpaos et al., 2010) and mixing (Waiters et al., 1985; Hole, 2004; Burchard and Hofmeister, 2008; Venier et al., 2014). Despite the advances achieved during recent years, the assessment and prediction of present and future impacts on the hydrodynamics of bays are still challenging tasks for both managers and scientists (Li et al., 2014).

Although many previous pioneering studies were based on in situ measurements or historical data, such as the harmonic analysis of tides and tidal currents at the San Francisco Bay (Gartner, 1986), the complexity of these environments and the physical processes involved demand integral approaches. During recent decades, advanced 2D and 3D numerical models have been developed in combination with field data for calibration and testing. These models are being used at these environments to improve our prediction capabilities at various spatial and temporal scales. Some of these models are Delft3D (Lesser et al., 2004), COHERENS (Shi J. and X., 2010) HEM-3D (Hong and Shen, 2012), MIKE (Schoen et al., 2014) and MOHID (Liu et al., 2004; Vaz et al., 2009). Furthermore, several authors have developed their own models, combining a two-dimensional finite elements model (Umgiesser and Bergamasco, 1993) with the finite difference SWAN wave propagation model run in stationary mode (i.e., Carniello et al. (2005); Zhong and Li (2006); Carniello et al. (2011, 2012)). In addition to these models, other three-dimensional hydrodynamic models are used to simulate barotropic tidal circulation (Walstra et al., 2000; Hong and Shen, 2012). These models have been applied to study a wide range of sites and phenomena. Olabarrieta et al. (2011) and Elias and Hansen (2012) analyzed wave-current interactions and sediment transport, respectively, by applying the numeri-

cal model Delft3D, whereas Bart Chadwick and Largier (1999) studied the circulation and tidal exchange at the bay-ocean boundary. Scully (2010) showed the potentiality of these models for processes such as chemical controls, biological constituents and salt and heat balance, whereas Serrano et al. (2013) concluded that the tidal propagation between two inlets was dominated by pressure gradients and friction, describing a quasi-standing tidal wave in currents and amplitudes.

To characterize in detail the dynamics of short and irregular embayments, the Bay of Cádiz (southwestern Spain) system will be described as an example of a highly altered embayment. Although there have been a number of previous studies on the complex dynamics of the site, these studies were focused on other aspects such as the seasonal variability of the tidal constituents, the influence of the tidal circulation on pollutant transport and marine sediment evolution during centuries (Álvarez et al., 1999; Álvarez et al., 2003; Periáñez et al., 2013), tidal behaviour in Sancti-Petri creeks (Vidal, 2002) or on wave-tide interactions (Kagan et al., 2001, 2005) and the feedback between flow and suspended sediment (Álvarez et al., 1999; Periáñez et al., 2013).

1.2 Objectives

1.2.1 Main objectives

The main objectives of this Thesis are (1) to understand the current behaviour, evolution and physical processes underlying the dynamics of the Bay of Cádiz, and (2) to assess the consequences of the ongoing and planned human interventions on the morpho-hydrodynamics of the bay.

1.2.2 Specific objectives

To achieve the main objective, the following specific objectives are defined:

1. To characterize the Bay of Cádiz for a better understanding of the impact that the tidal flats and the complex geometry has on this type of sites.

2. To record in situ measurements of the main hydrodynamic variables: water levels, currents, waves, temperature, salinity and turbidity.

3. To implement hydrodynamic numerical models at both the intratidal and subtidal time scales. The models should solve the Navier-Stokes equations under the shallow water and Boussinesq assumptions and include all the relevant forcing factors: tides, winds, river discharges and wave conditions.

4. To analyze the current hydrodynamic behaviour along the bay and assess the governing physical processes and dominant physical mechanisms.

5. To assess the current morphodynamic evolution along the bay and to analyze the sediment transport patterns.

6. To apply the model to different scenarios to evaluate the potential changes in the dynamics due to the ongoing and planned human interventions.

1.3 Outline of the Thesis

Besides the motivation (Chapter 1) and conclusions (Chapter 8), this Thesis is organized in 6 main chapters. Each of them responds to one of the specific objetives outlined before.

In order to understand the dynamics of the bay, we need to identify the behaviour underlying this system. The bay has changed considerably over time, partly due to natural causes and partly as a result of man-induced interventions. Chapter 2 is focused on the description of the field site and its long-term evolution. Furthermore, the long field survey that has been carried out is explained in detail in the last part of the chapter.

In Chapter 3, the two numerical models applied in this thesis are presented and described: governing equations, computational grid, boundary conditions, calibration and testing methodology. The models are used to compute the circulation in the Bay of Cádiz induced by the main forcing agents. Chapter 4 describes the calibration and testing of the models, which are implemented using the field measurements.

Chapters 5 and 6 concern detailed analysis of the present behaviour of the bay. The former summarizes the short-period tidal transformation in the Bay of Cádiz, focusing on elevations and currents, as well as tidal energy flux and dissipation. Furthermore, the results of subtidal flows between the inner and outer basins are evaluated and linked to the forcing. This Chapter is under review in *Ocean Engineering*, journal indexed in the Journal Citation Reports with an impact factor of 1.353. The later deals with the assessment of the sediment dynamics on the bay in terms of residual sediment transport, and the analysis of the dominant flow and sediment transport patterns, processes and mechanisms for the present state.

In Chapter 7 we analyze the intra- and sub-tidal circulations driven by different forcings for the different geometrical configurations of the bay. For this purpose, four scenarios were defined. Scenario 2 represents the new terminal of the Cádiz port and the new navigation channel, whereas scenario 3 corresponds to the new bridge. Finally, scenario 4 includes all the interventions (final configuration of the bay); the results are subsequently compared and analyzed. Part of this Chapter has been published in *Estuarine, Coastal and Shelf Science*, journal indexed in the Journal Citation Reports with an impact factor of 2.057.

Finally, Chapter 8 summarizes the results and the main conclusions, and provides recommendations for further research.

1.4 Publications derived from this Thesis

Refereed Journal Papers

- **Zarzuelo C**, Díez-Minguito M, López-Ruiz A, Ortega-Sánchez M and Losada M (2015). Hydrodynamics response to planned human interventions in a highly altered embayment: The example of the Bay of Cádiz (Spain). *Estuarine, Coastal and Shelf Science*, 167, 75–85. DOI: 10.1016/j.ecss.2015.07.010.

- **Zarzuelo C**, Díez-Minguito M and Ortega-Sánchez M (2015). Observations of tidal and subtidal barotropic flows in a constricted bay. *Ocean Engeeniering (Under review)*

- **Zarzuelo C**, D'Alpaos A, Carniello L, Díez-Minguito M and Ortega-Sánchez M (2015). Sand-mud transport in a tidally-dominated and exchanges with a tidal creek. *Journal Geophysical Research (in preparation)*.

International Peer-Reviewed Conferences

- **Zarzuelo C.**, Díez-Minguito M., D'Alpaos A., Carniello L., Rosal-Salido J. and Ortega-Sánchez M. (2016). Morphodynamic response to human activities in the Bay of Cádiz (2012-2015). In: 35th International Conference on Coastal Engineering (ICCE).

- **Zarzuelo C.**, D'Alpaos A., Carniello L., Finotello A., Díez-Minguito M. and Ortega-Sánchez M. (2015). Modeling sediment transport induced by tidal currents and wind waves in the Bay of Cádiz. XXIV Congress on Differential Equations and Applications/XIV Congress on Applied Mathematics. Cádiz, Spain.

- Rosal-Salido J., **Zarzuelo C.**, Díez-Minguito M., Ortega-Sánchez M. and Losada M. (2015). Residual circulation in the Bay of Cádiz (SW Spain): Field analysis and numerical modeling. ASLO Aquatic Sciences Meeting, Granada, Spain.

- **Zarzuelo C.**, Díez-Minguito M., Ortega-Sánchez M., López-Ruiz A. and Losada M.(2014). Morpho-hydrodynamics and response to planned human interventions in a highly altered embayment: the example of the Bay of Cádiz (Spain). ECSA 54 Conference – Coastal systems under change: tuning assessments and managements tools, Sesimbra (Portugal).

Spanish Conferences

- Rosal-Salido J., **Zarzuelo C**, Díez-Minguito M., Ortega-Sánchez M. and Losada M. (2015). Circulación residual en la Bahía de Cádiz: Análisis de campo y modelado numérico. XIII Jornadas Españolas de Ingeniería de Costas y Puertos. Avilés, Spain. *(In Spanish)*.

- **Zarzuelo C**, Ortega-Sánchez M, Díez-Minguito M, Rodríguez A and Losada MA (2013). Caracterización hidrodinámica de la Bahía de Cádiz mediante medidas de campo. XII Jornadas Españolas de Ingeniería de Costas y Puertos. Cartagena, Spain. *(In Spanish)*.

Chapter 2
Study Site

This Chapter describes the field site and the field survey that was carried out. After a review of the historical evolution and the present configuration of the Bay of Cádiz, the characterization of the main forcing agents is given. Finally, the field survey is detailed, which was designed using the previous information. This description can be found in Zarzuelo et al. (2015b).

2.1 Field Site

2.1.1 Introduction

The Bay of Cádiz is located in the northern sector of the Gulf of Cádiz (SW Spain), between the Guadalquivir River mouth and Trafalgar Cape (Figure 2.1). Three main zones can be distinguished considering the textural characteristics of the marine deposits and the sedimentary environments: an inner sector (C-Figure 2.1) relatively sheltered from wave action, where muds and clays prevail in the sea bottom; an outer sector (A-Figure 2.1) between 15 and 20 m depth, more exposed to waves, with predominance of sands and silts; and a transition zone to the continental shelf, between 20 m and 30 m depth, where muddy sediments are dominant although sands are also present. In the outer sector, the sedimentary facies distribution show alternating strips or bands of sands, muddy sands, sandy muds and muds. Contacts between bands are parallel or normal to the coastline and to isobaths, reproducing the general coastal physiography and the distribution of rocky shoals.

The hydrodynamic regime is controlled by the North Atlantic Surface Water Flow (NASW), which sweeps the continental margin towards the SE, and by surge and tidal currents. The surge has a seasonal character, but the westerly component prevails. Two main environmental sectors can be distinguished: the Outer bay to the North (A-Figure 2.1), which is affected by waves, currents and storms, especially of a westerly nature. Its bottom is predominantly sandy, but silt and clay are also present. The Inner bay (C-Figure 2.1) to the SSE, is a wide lagoon surrounded by an extensive muddy tidal flat and a dense tidal channel net. The main coastal current flows towards the SE, as a consequence of the coastline configuration, facing Westerly and SW winter storms. Although Westerly winds prevail, Easterly winds are also important, generating currents towards the N and NW (Gutiérrez-Mas et al., 2004).

As a result of climatic forcings (Gutiérrez-Mas, 2011) and strong human alterations,

the geological and sedimentary processes (Gutiérrez-Mas et al., 2003) and biological factors (Ligero et al., 2002) have been changing during the last decades.

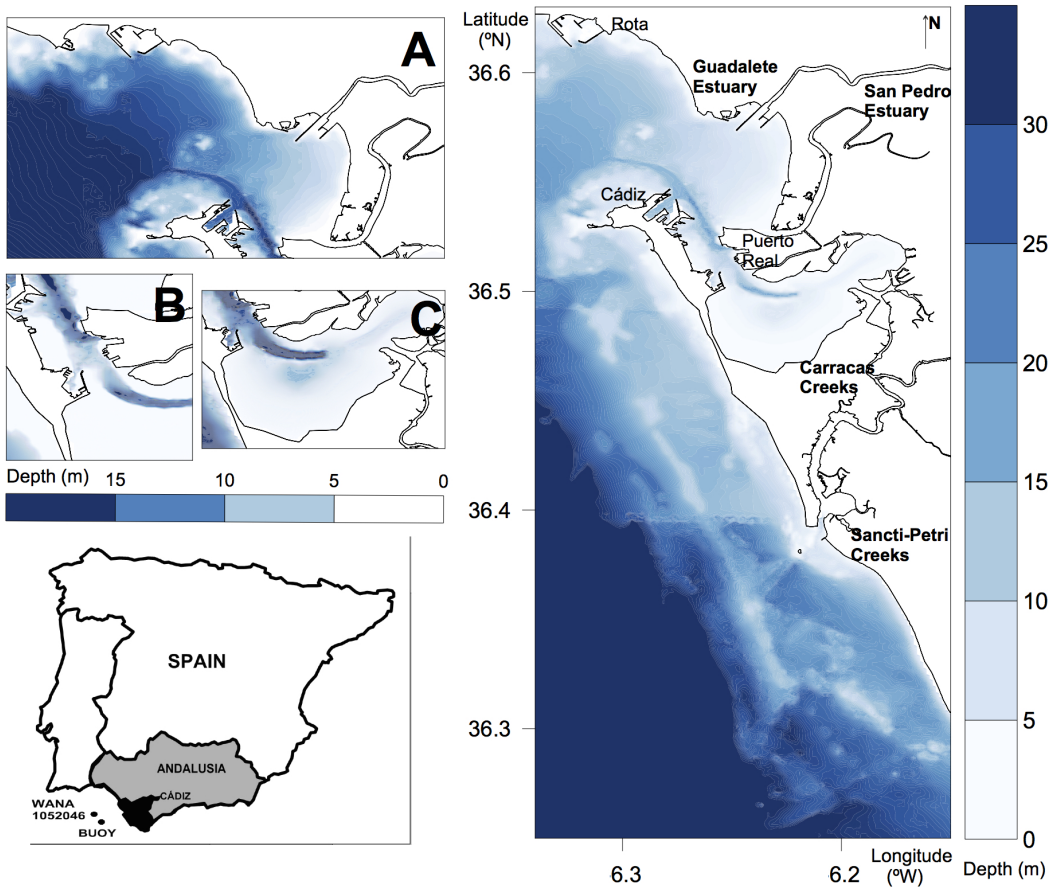

Figure 2.1: Location of the Bay of Cádiz. The outer, central, and inner areas of the Bay are denoted by A, B, and C, respectively. The inset shows location of the Buoy of the Gulf of Cádiz and WANNA 1052046.

2.1.2 Morphology

2.1.2.1 Historical evolution of the area

A full understanding of the marine sedimentation in the transitional zone between the coast and the continental shelf needs to take into account the different factors that control the nature and distribution of the deposits: 1) sea level fluctuations, 2) sediment source areas, 3) hydrodynamic regime acting on the zone and 4) physiography and structure of the geological substratum, often related to the recent tectonic activity. The first factor affects wide regions, whereas the others act more locally.

In the Gulf of Cádiz (SW Spain) the Holocene marine sedimentation was mainly related to the last transgressive maximum and the later sea-level stabilisation (Maldonado and Nelson, 1999). Several Holocene phases of coastal progradation have been distinguished and dated in the coastal spit-bars. The inner continental shelf deposits usually

form prograding wedges, especially near the main river mouths (Hernández-Molina et al., 2000). In the early Holocene the Bay of Cádiz , as we know it, was not yet formed. Sea level was many meters below the actual level ($2.5-3$ m). However the melting of ice caps and glaciers, and increasing temperatures since the last glacial period, resulted in a rapid increase of the sea level, which was estimated around 0.4 mm/century. This increase caused a subsidence of the land surface and specially, the inner bay suffered a strong deposition, turning the mouth river into estuaries or marshes.

During Miocene-Pliocene, the tectonic movement gave rise to a depression (Gutiérrez-Mas et al., 2003; Gutiérrez-Mas, 2011). The depression caused a large delta, whose sediments are preserved now. Between Pliocene and Quaternary, there was a tectonic movement which generated faults with vertical and lateral movements. These faults divided the Bay in a set of blocks with relative motions between them. During episodes of increase of the sea level, the coastal reliefs were changed until forming different entities, which can be seen nowadays (i.e. Cádiz and San Fernando cities, or rocky headlands like El Puerto de Santa Maria or Puerto Real). In medieval times, there was a descent of the sea, so the coastline was displaced several tens of kilometers seaward compared to the current one. Low and sandy cords appeared in the flooding areas, which originated the separation between bay and sea across marshes and rivers (Gutiérrez-Mas et al., 2003).

The surroundings of the Bay are constituted by low hills where post-Orogenic Neogene and Quaternary sands, clays and marls outcrop. The bay was generated as a tectonic depression during a distensive tectonic phase in the Late Miocene-Pliocene. The depression was occupied by a deltaic system that gave rise to a characteristic stratigraphic sequence, containing a Plio-Quaternary shelly conglomerate. This unit developed during the Middle and Late Pliocen until the Pleistocen and represents the rocky substratum and the acoustic basement in the Bay of Cádiz marine zone. An unconformity separates this unit from a more recent thin deposit constituted by fluvial red sands and quartzite pebbles (Zazo, 1999).

Recent Quaternary marine siliciclastic sediments overlay all these units. They are constituted of sands, silts and clays, and were presumably deposited in Late Pleistocene and Holocene times (Zazo, 1999). During the Late Quaternary, postglacial eustatic sea level fluctuations and tectonic movements controlled the spatial distribution of coastal environments. In the inner Bay and Guadalete mouth the Flandrian transgression favoured the aggradational accumulation of estuarine deposits.

In the next episode of sea level descents, the flows of the rivers provided sediments which were mixed with the sediments bay. However, with the sea level rise, the coastal plain were flooded and they caused the coastline and the mouth rivers retreats. Furthermore, alluvial environments were transformed in coastal and marine environments, giving rise to a number of beaches and marine deposits in the bay. The latest changes favored to the silting of Bay of Cádiz due to the amount of sediment transported by the rivers, the litoral drift and tidal sedimentation. Nowadays, marshes and rivers are beginning to dry by human behaviour.

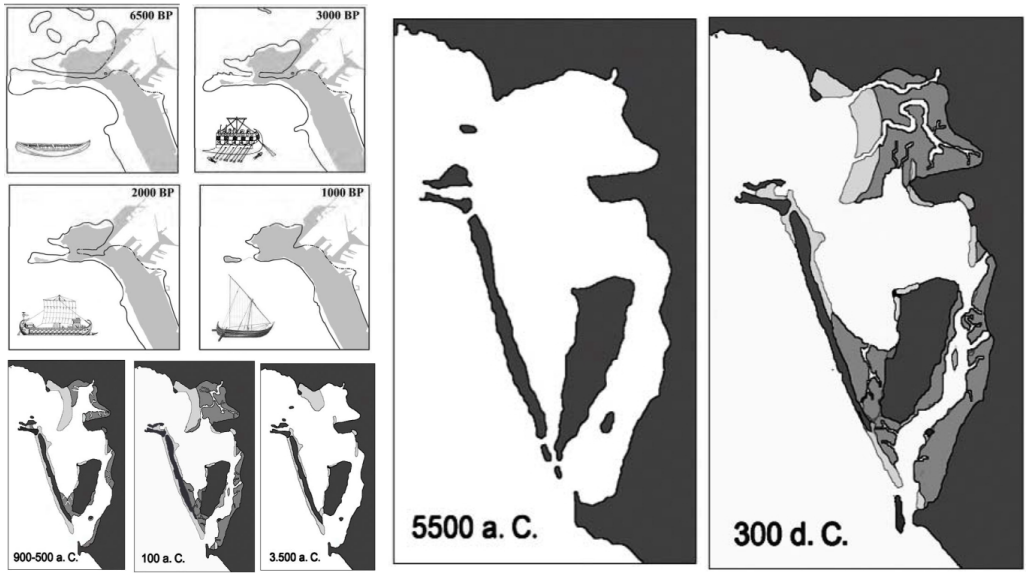

Figure 2.2: Evolution of the Bay of Cádiz, adapted from Arteaga et al. (2008). Upper left panels: Urban Geoarchaeology Project Cádiz. Reconstruction of ancient coastlines around the current town of Cádiz, in different historical periods, namely in prehistoric times Final Neolithic (6500 BP.); the Phoenician Gadir (3000 BP.); Roman Gades (2000 BP.); and finally, in times of Yazirat Qadir (1000 BP). As gray background are shown the shape of the current Cádiz peninsula.

During the following sea level highstand, from 6500 yr BP to the present, progradational estuarine and marine sediments have overlaid all the previous units. Until 900 BP, the tidal basins had been reduced, shifting the bay coastline through seaward. The decreasing of sea-level and the availability of sediments (supplied by rivers and the erosion of capes and former coastal deposits) resulted in decreasing shoreline transgression rates. The tidal basins were filled in with sediments, and the tidal inlets began to close. Hence, an extension of the marshes and coastal environments are carried out from 100 BP (see Figure 2.1 and Figure 2.2).

The melting of the ice after the last glacial period causes a dramatic rise in sea level over 100 meters. After the peak, the coastline is quite stable and begins silting the Bay of Cádiz. Around 300 AD the southern part of the bay (San Fernando) was transformed into an open coast with lagoons and tidal flats, while the northern part of the bay (Puerto de Santa María) consisted of several estuaries (Guadalete and San Pedro), see Figure 2.1 and Figure 2.2. The western part of the bay (Puerto Real) was still dry land, due to a stiff and erosion-resistant deposit. In the XVIII century, the Bay clogging causes the emergence of many low. Littoral drift currents delimit the sandy arrow Valdelagrana north and Sancti-Petri cutting and south, gradually closing the inlet.

Despite the increase in sea levels, the characteristic features of the Bay of Cádiz , the barrier islands, separated by inlets and connecting basins have remained intact or with minimum changes (although the size increased due to westward expansion). Since 1950 many constructions were developed that altered the initial configuration of the bay and impacted in the dynamic.

At present the Bay is about 30 km long and 15 km wide, and consists of two wide embayments separated by a rocky headland at Puerto Real. The coastal zone presents wide

tidal flats isolated from the open sea by sandy beach ridges and littoral spits. The coastline is oriented NNW–SSE, with some E–W sections that give the coast a stepped outline, strongly controlled by tectonic features (Gutiérrez-Mas and Gracia, 1994). The continental shelf has an average width of 40 km, and the slope drops away sharply from a depth of about 150–200 m. The physiography of the seabed shows a close concordance with the shoreline, the isobaths generally running parallel to the coast. Submarine pre-Holocene materials include Plio-Quaternary, Late Miocene and Mesozoic units. The main sedimentary sources to the continental shelf and littoral zones are the Guadiana and Guadalquivir rivers, and sediments supplied by them are transported to the Bay of Cádiz by a Westto-East longshore current. In the Bay of Cádiz the Guadalete River is still a major supplier of sediments.

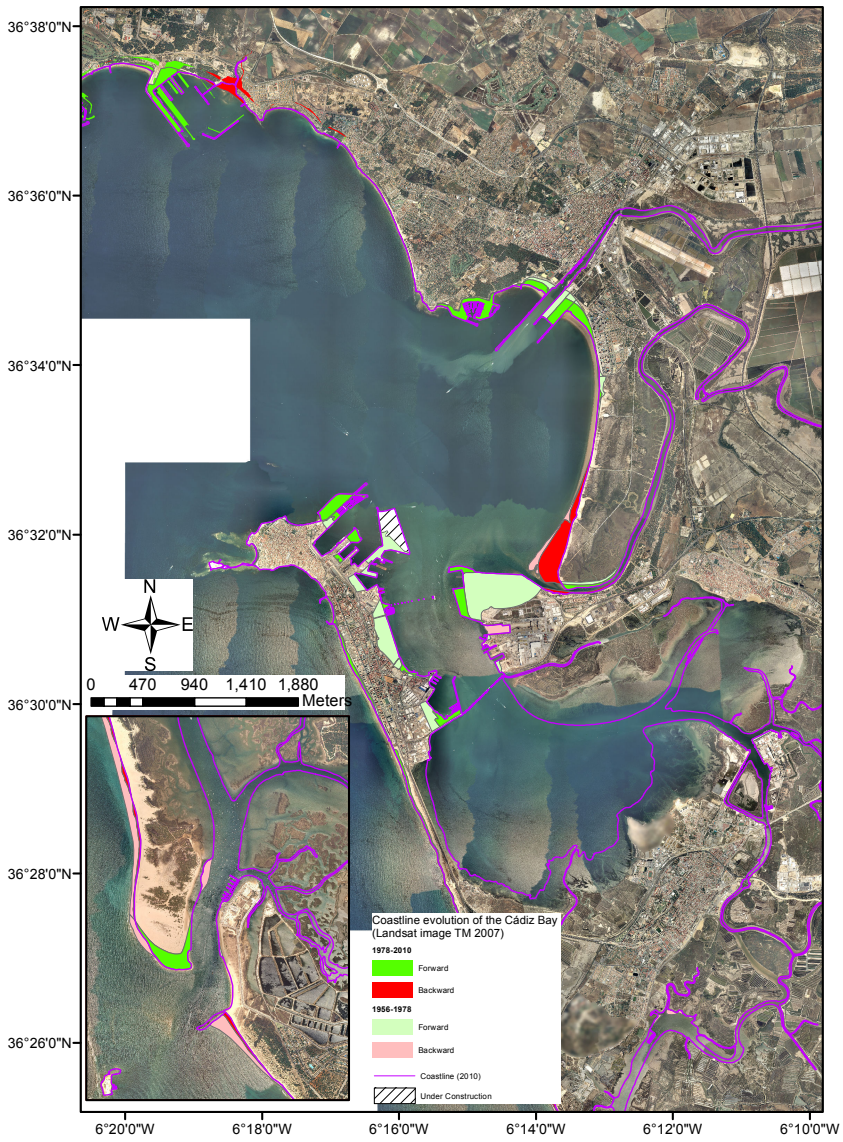

Figure 2.3: Coastline Evolution of the Bay of Cádiz .

2.1.2.2 The Bay of Cádiz

The Bay of Cádiz can be divided into two basins (inner and outer bays) that are connected through a constriction: The Puntales channel (Zarzuelo et al., 2015a). Three well-defined areas can thus be identified: a deeper outer area connected with the open sea (labeled as A in Figure 2.1), a shallower inner one (C-Figure 2.1), and the Puntales channel (B-Figure 2.1). The Natural Park of the Bay encompasses a 10,522 ha flat landscape of sandy beaches, marshes, salt pans, freshwater lakes and tidal inlets, as well as the two natural areas of Isla del Trocadero and the Sancti–Petri and Carraca creeks (Figure 2.1).

The outer bay (A-Figure 2.1), which is affected by waves, tidal currents, and freshwater discharges during the wet seasons, extends 70 km^2 with an average depth of 15 m and a mean slope of 1.5 ‰. Sandy bottoms (90 %) and rocky shores and cliffs (10 %) characterize this area (Sánchez-Lamadrid et al., 2002). The San Pedro and Guadalete rivers flow into this area (Figure 2.1), and their discharges are mainly controlled by upstream dams.

The Puntales channel (B-Figure 2.1) constricts the water exchange, and harbors most of the Port of Cádiz infrastructures. The channel is 3.8 km long and 1.3 km wide, and its principal axis is oriented 33° anti-clockwise from the North. Depths in the main channel range from 11 to 15 m with maximum values of 18 m below mean low water. Mean slope in B attains a value of 9 ‰. The larger slopes (15%) in the Bay are reached at the southern end of the strait.

The inner Bay (area C in Figure 2.1) shows a maximum depth of 8 m and mean slopes of 2 ‰, which allow for extensive muddy intertidal flats. Nowadays, area C extends 50 km^2, although substantial extensions of marshes have been lost due to human activities. Bottoms are predominantly muddy (97%). A dense tidal channel network flow into this part, being Sancti–Petri and Carracas creeks the main tidal channels. The northern part is connected to the inner part of the Bay of Cadiz at La Carraca, and the southern part is connected to the Atlantic Ocean at Sancti–Petri. It has many secondary channels that feed a very complex system of small channels with large areas of marshes. Their mean depths varies from 9 m at the seaward boundary to 3 m at the inner bay boundary.

The creeks are located at the south of the bay connected with the inner bay. Sancti-Petri and Carraca creeks are very shallow domains subjected to the bay's tidal dynamics and forms part of the coastal marsh system of the Cádiz Bay Natural Park. Sancti-Petri creek has an extension of 170 ha, and comprises intertidal flats around the fringes, expanses of subtidal flats (to 2 m deep) and deeper channels (6-8 m) that discharges to the Atlantic Ocean. This reach of the tidal creek is roughly funnel shaped and is surrounded by intertidal flats, where the maximum depth is 5 m. The water column is typically well-mixed. The highest values of concentration of suspended particulate are found Sancti-Petri tidal creek (13 mg/L). The sediments in the creeks are predominantly muds, since this area is protected from winds and waves.

2.1.3 Characterization of Forcing Agents

As in others semi-enclosed coastal bodies of water, the main forcings are tides, wind, waves and river inputs. Tides in the Gulf of Cádiz are semidiurnal and mesotidal. The

main tidal constituent is the M2 (12.42 h). The tidal range in the adjacent coastal waters varies from ~ 1 m during neap tides to ~ 4 m during spring tides. The tidal character inside the Bay is co-oscillating, induced by the Kelvin-type wave which propagates northwards in the North Atlantic. Tides penetrate into the lagoon mainly from the outer area (A) and propagate into the inner bay (C) through the Puntales channel (B). The inner bay is also connected intermitently to the open sea through the Carracas and Sancti-Petri creeks (Figure 2.1), although the tidal prism is significantly smaller in this case and the connection channels dry out at approximately mid-tide stage during spring tides.

Offshore wind and wave conditions (see central panel in Figure 2.1) are continuously monitored at the buoy 2342 (6,96° W, 36.48° N) managed by Puertos del Estado (Ministry of Public Works). The data recorded are significant spectral wave height (H_s), spectral peak period (T_p), mean wave direction (θ), wind speed (V_v) and wind direction (θ_v), reported every hour since 1996. This information will be used to characterize the average and extreme maritime climate and also as offshore boundary conditions during the field survey.

Westerly and easterly winds are predominant in the study area. They are characterized by maximum velocities of, respectively, 22.4 m/s and 20.8 m/s, with average values of approximately 8.3 m/s and 10.1 m/s. Due to the coastline orientation (approx. NNW-SSE), westerly winds yield both sea and swell waves. Easterly winds have no significant fetch thus producing only sea waves. Waves predominantly propagate from W (historically, they represent 32.7 % of the total amount of waves) and WNW (27.7 %). Mild to low wave energy conditions (those that verify $1.5\,\text{m} < H_s$) are dominant (63 %); moderate-energy sea states ($1.5\,\text{m} \leq H_s < 3\,\text{m}$) and storm conditions ($H_s \geq 3\,\text{m}$) are less frequent (32.7 % and 4.3 %, respectively). Wave periods vary typically between 5 and 15 s (~ 87 %), with predominant average values of 8 s for sea conditions and 13 s for swell conditions.

Precipitations are mainly concentrated in autumn and winter (~ 600 mm/month), decreasing in spring and with a pronounced drop in the summer. The maximum (minimum) evaporation occurs in summer (winter), namely, $\sim$ 170mm/month $\approx 9.1\,\text{m}^3/\text{s}$ ($\sim$ 50mm/month $\approx 2.7\,\text{m}^3/\text{s}$) (Ferrón et al., 2007; De la Paz et al., 2008). The freshwater inputs into the Bay come predominantly from Guadalete and San Pedro rivers (Figure 2.1). The temporal evolution of the freshwater discharges is mainly conditioned by the regulation of the drainage basins. Net discharges are normally lower than $8\,\text{m}^3/\text{s}$ and rarely exceeding than $20\,\text{m}^3/\text{s}$ after some strong events during winter.

The Bay of Cádiz is a temperate environment, with mild winters (average temperatures in December and January of $\sim 10°$ C) and hot summers ($\sim 26°$ C in July and August) lacking of extreme values. The maximum salinity is observed during summer months (De la Paz et al., 2008), due to the enhanced evaporation. Mean salinity values in the inner bay range from 32 psu (practical salinity units) in autumn and winter months (wet season) to ca. 42 in summer (dry season). The water temperature from the bay shows a seasonal trend with high values in August (24-26 °C) and low values in December (12 °C) (Rueda and Salas, 2003). The hydrological balance indicates that the Bay of Cádiz may seasonally be under a low-inflow state in which the density gradient is reversed and the Bay behaves as a inverse estuary (Largier et al., 1996).

2.2 Field Survey

2.2.1 Introduction

To understand the hydrodynamic and morphological patterns around the Bay of Cádiz, a field survey to measure velocities, water levels, waves, water quality and suspended sediment was carried out. The locations of the measuring stations can be seen in Figure 2.4. The timing of the field survey was chosen based on an analysis of historical environmental conditions: winter months from December to February produce storms, high off-shore wave heights, increased input from Guadalete and San Pedro estuary, and elevated water levels.

2.2.2 Field measurements

Instruments were deployed on 4 concrete anchors (Figure 2.5) and 3 bottom mounts placed on the seabed at the locations indicated in Figure 2.4. The instruments were deployed twice, and were retrieved once in between for de–fouling, battery replacement and gathering the data. A total of 10 instruments were deployed at 7 measuring stations (I1-I4, T1-T3; Figure 2.4) from December 22, 2011 to April 18, 2012. The locations of stations I1-I5 were selected considering the future location of the new bridge “La Pepa" ($36.52°N, 6.27°W$), which crosses the constriction, and the new port terminal ($36.54°N, 6.27°W$), to evaluate their possible impacts on the water exchange between the inner and outer basins. Station I1 was close to the future location of the terminal, whereas stations I2 and I3 were located all along the central constriction. Station I5 was placed near the Puntales channel inside the inner bay. The distance between I1 and I4 is 5.5 km, which was paced inside the inner bay. I2 is located in the middle of the Puntales channel, to analyze the exchange between A and C. Finally, station T1 was located at the San Pedro river mouth, whereas stations T2 and T3 were on Carracas and Sancti-Petri creeks, respectively.

Station T1 was located at the San Pedro river mouth, whereas stations T2 and T3 were placed on Carracas and Sancti-Petri creeks, respectively. At station I1, an Acoustic Doppler Current Profiler (ADCP) of 2 MHz and Conductivity and Temperature probes (CT) were deployed (table 2.1). At I2, an ADCP of 1MHz, a CT and an optical backscatter sensor (hereinafter OBS) were deployed. I3 and I4 accommodated an ADCP of 2MHz. Stations T1, T2 and T3 had tidal gauges. Table 2.1 also summarizes the sampling periods for each instrument. The devices were programmed to measure 1024 samples of the water surface elevation, pressure and orbital velocities hourly. For the remaining time within the hour, water current profiles are obtained with a sampling time of 15 minutes and an average interval of 120 s. CT data were 4 samples every hour. Wind data were provided at buoy 2342 (6.96° W, 36.48° N) at Puertos del Estado (Spanish Ministry of Public Works).

In addition to the field measurement campaign, a wide array of other data are available for calibration and validation of numerical models of Bay of Cádiz . Wind and wave conditions are continuously monitored at the buoy 2342 (inset in Figure 2.1) (6.96° W, 36.48° N) managed by Puertos del Estado (Spanish Ministry of Public Works). The data

Location	Instrument	Depth	Sampling periods
I1	CT	10 m	12/22/11 - 04/18/12
	ADCP		12/22/11 - 03/15/12
I2	CT	13 m	12/22/11 - 04/18/12
	ADCP, OBS		
I3	ADCP	8 m	12/22/11 - 04/18/12
I4		6 m	
T1	Tidal gauge	2.5 m	02/10/12 - 05/22/12
T2		3 m	
T3		3 m	

Table 2.1: Locations, depths, and sampling periods for ADCPs, OBSs and CTs.

recorded since 1996 are significant spectral wave height, spectral peak period (T_p), mean wave direction (θ), wind speed (V_w) and wind direction (θ_w), reported every hour. This information will be used to characterize the average and extreme maritime climate and also as offshore boundary conditions during the field survey.

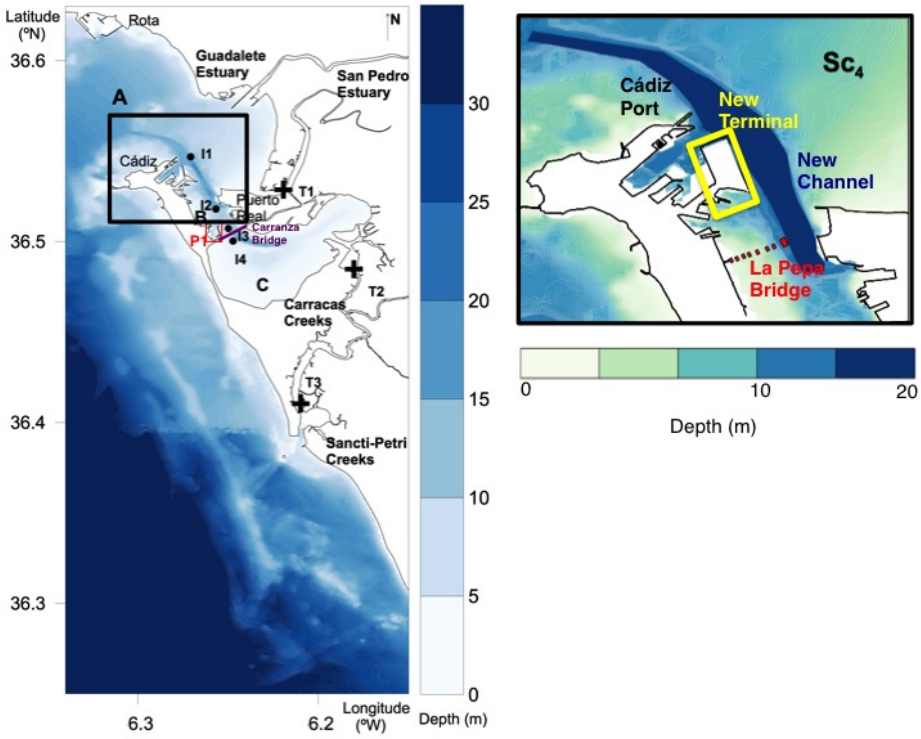

Figure 2.4: The Bay of Cádiz. Shaded areas are the outer (marked as A), central (B), and inner (C) bays. Labels I1-I4 correspond to current meters, and labels T1-T3 to tidal gauges. Label P1 corresponds to the Zona Franca Port. The inset shows the locations of the future interventions: Red color the new bridge, yellow color the new terminal and blue color the new navigation channel.

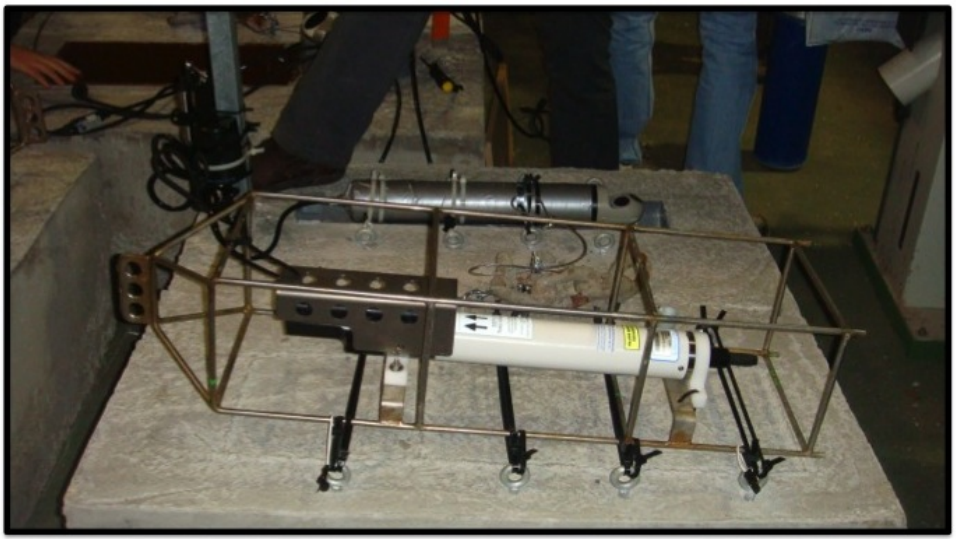

Figure 2.5: Picture of the instruments (table 2.1) installed during the field campaign at I1.

Chapter 3
Numerical Model (I): Description

This chapter describes the two numerical models that are applied in this thesis. The first model (DELFT3D) consists of a number of integrated modules which together allow the simulation of hydro and morphodynamics. It is quite demanding in terms of computational time. Furthermore, the usage of the model in very irregular domains is quite imprecise. As a consequence, the second model implemented combines wind waves with tidal fluxes in highly irregular bathymetry, characterized by deep channels emergent salt marshes, and extensive tidal flats (Carniello et al., 2005, 2012).

3.1 Numerical Model I – DELFT3D

The DELFT3D package, developed by WL|Delft Hydraulics in close cooperation with Delft University of Technology, is a model system that consists of a number of integrated modules which together allow the simulation of hydrodynamic flow (under the shallow water assumption), computation of the transport of water-borne constituents (e.g., salinity and heat), short wave generation and propagation, sediment transport and morphological changes, and the modeling of ecological processes and water quality parameters (Lesser et al., 2004). The DELFT3D modeling framework is divided in two modules: Hydrodynamic (FLOW) and Wave module (WAVE).

3.1.1 Hydrodynamic module

3.1.1.1 Governing equations

FLOW module performs the hydrodynamic computations and simultaneous calculation of the transport of salinity and heat. The advantages of this online approach are the following: (1) three-dimensional hydrodynamic processes and the adaptation of non-equilibrium sediment concentration profiles are automatically accounted for in the suspended sediment calculations; (2) the density effects of sediment in suspension (which may cause density currents and/or turbulence damping) are automatically included in the hydrodynamic calculations; (3) changes in bathymetry can be immediately fed back to the hydrodynamic calculations; and (4)sediment transport and morphological simulations are simple to perform and do not require a large data file to communicate results between the hydrodynamic, sediment transport, and bottom updating modules (Lesser et al., 2004).

The DELFT3D-FLOW module solves the unsteady shallow-water equations in two (depth-averaged) or three dimensions. The system of equations consists of the horizontal momentum equations, the continuity equation, the transport equation, and a turbulence closure model. The vertical momentum equation is reduced to the hydrostatic pressure relation as vertical accelerations are assumed to be small compared to gravitational acceleration and are not taken into account (Lesser et al., 2004). The user may choose coordinate system to solve the hydrodynamic equations: we use cartesian rectangular. For the sake of clarity, the equations are presented in their Cartesian rectangular form only.

3.1.1.1.1 Vertical σ-coordinates system. The vertical σ-coordinate is scaled as ($-1 \geq \sigma \leq 0$)

$$\sigma = \frac{z - \zeta}{h} \tag{3.1}$$

where z is the vertical cartesian coordinate (m); ζ is the water surface elevation above reference datum (m) and h is the water depth (m). In a σ-coordinate system, the layer interfaces are chosen following planes of constant σ (Figure 3.1).

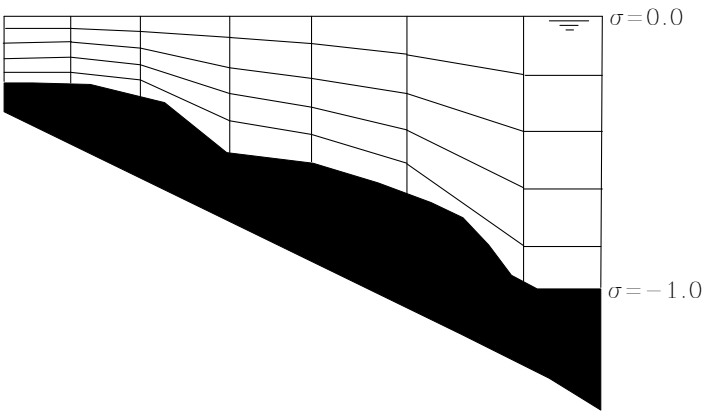

Figure 3.1: An example of a vertical grid consisting of five equal thickness σ-layers.

3.1.1.1.2 Generalized Lagrangian Mean (GLM) reference frame. In simulations including waves, the hydrodynamic equations are written and solved in a GLM reference frame (Andrews and McIntyre, 1978; Groeneweg, 1998, 1999). The relationship between the GLM velocity and the Eulerian velocity is given by

$$U = u + u_s \tag{3.2}$$

$$V = v + v_s \tag{3.3}$$

where U and V velocity components, u and v are Eulerian velocity components, and u_s and v_s are the Stokes' drift components. For details and verification results, we refer to Walstra et al. (2000).

3.1.1.1.3 Hydrostatic pressure assumption. Under the so-called "shallow water assumption", the vertical momentum equation reduces to the hydrostatic pressure equation. Under this assumption, vertical acceleration due to buoyancy effects or sudden variations in the bottom topography is not taken into account. The resulting expression is

$$\frac{\partial P}{\partial \sigma} = -\rho g h \tag{3.4}$$

where P is the pressure (Pa); g is the gravity (m/s^2) and ρ is the local fluid density (kg/m^3).

3.1.1.1.4 Horizontal momentum equations. The horizontal momentum equation are

$$\frac{\partial U}{\partial t} + U\frac{\partial U}{\partial x} + V\frac{\partial U}{\partial y} + \frac{w}{h}\frac{\partial U}{\partial \sigma} - fV = -\frac{1}{\rho_0}P_x + F_x + M_x + \frac{1}{h^2}\frac{\partial}{\partial \sigma}\left(\nu_v \frac{\partial u}{\partial \sigma}\right)$$

$$\frac{\partial V}{\partial t} + U\frac{\partial V}{\partial x} + V\frac{\partial V}{\partial y} + \frac{w}{h}\frac{\partial V}{\partial \sigma} - fU = -\frac{1}{\rho_0}P_y + F_y + M_y + \frac{1}{h^2}\frac{\partial}{\partial \sigma}\left(\nu_v \frac{\partial v}{\partial \sigma}\right) \tag{3.5}$$

in which the horizontal pressure terms, P_x and P_y, are given by (Boussinesq approximations)

$$\frac{1}{\rho_0}P_x = g\frac{\partial \zeta}{\partial x} + g\frac{h}{\rho_0}\int_\sigma^0 \left(\frac{\partial \rho}{\partial x} + \frac{\partial \sigma'}{\partial x}\frac{\partial \rho}{\partial \sigma'}\right) d\sigma'$$

$$\frac{1}{\rho_0}P_y = g\frac{\partial \zeta}{\partial y} + g\frac{h}{\rho_0}\int_\sigma^0 \left(\frac{\partial \rho}{\partial y} + \frac{\partial \sigma'}{\partial y}\frac{\partial \rho}{\partial \sigma'}\right) d\sigma' \tag{3.6}$$

where w is the vertical velocity component in sigma coordinate system (s^{-1}); ν_v and ν_H are the Kinematic velocity in vertical and horizontal direction, respectively (m^2/s); ρ_0 is the reference density of water (kg/m^3); f is the Coriolis coefficient (inertial frequency) (s^{-1}); M_x and M_y represent the contributions due to external sources or sinks of momentum (external forces by hydraulic structures, discharge or withdrawal of water, wave stresses, etc).

The horizontal Reynold's stresses, F_x and F_y, are determined using the eddy viscosity concept (e.g., Rodi (1984)). For large-scale simulations (when shear stresses along closed boundaries may be neglected) the forces F_x and F_y reduce to the simplified formulations

$$F_x = \nu_H\left(\frac{\partial^2 U}{\partial x^2} + \frac{\partial^2 U}{\partial y^2}\right) \tag{3.7}$$

$$F_y = \nu_H\left(\frac{\partial^2 V}{\partial x^2} + \frac{\partial^2 V}{\partial y^2}\right) \tag{3.8}$$

in which the gradients are taken along σ-planes.

3.1.1.1.5 Continuity equation. The depth-averaged continuity equation is given by

$$\frac{\partial \zeta}{\partial t} + \frac{\partial \left[h\overline{U}\right]}{\partial x} + \frac{\partial \left[h\overline{V}\right]}{\partial y} = S \tag{3.9}$$

in which S represents the contributions per unit area due to the discharge or withdrawal of water, evaporation, and precipitation; and $\overline{U}$ and $\overline{V}$ are the depth-averaged GLM velocity components (m/s).

The vertical velocity, ω, in the σ-coordinate system, is computed from the continuity equation

$$\frac{\partial w}{\partial \sigma} = -\frac{\partial \zeta}{\partial t} - \frac{\partial [hU]}{\partial x} - \frac{\partial [hV]}{\partial y} \tag{3.10}$$

by integrating in the vertical from the bed to a level σ. At the surface, the effects of precipitation and evaporation are taken into account. The vertical velocity, ω, is defined at the iso-σ-surfaces. ω is the vertical velocity relative to the moving σ-plane and may be interpreted as the velocity associated with up- or down-welling motions. The vertical velocities in the Cartesian coordinate system can be expressed int he horizontal velocities, water depths, water levels, and vertical coordinate velocities according to

$$w = \omega + U\left(\sigma\frac{\partial h}{\partial x} + \frac{\partial \zeta}{\partial x}\right) + V\left(\sigma\frac{\partial h}{\partial y} + \frac{\partial \zeta}{\partial y}\right) + \left(\sigma\frac{\partial h}{\partial t} + \frac{\partial \zeta}{\partial t}\right) \tag{3.11}$$

3.1.1.1.6 Transport equation. The advection-diffusion equation reads

$$\frac{\partial [hc]}{\partial t} + \frac{\partial [hUc]}{\partial x} + \frac{\partial [hVc]}{\partial y} + \frac{\partial [wc]}{\partial \sigma}$$

$$= h\left[\frac{\partial}{\partial x}\left(D_H\frac{\partial c}{\partial x}\right) + \frac{\partial}{\partial}\left(D_H\frac{\partial c}{\partial y}\right)\right] + \frac{1}{h}\frac{\partial}{\partial \sigma}\left[D_V\frac{\partial c}{\partial \sigma}\right] + hS \tag{3.12}$$

in which S represents source and sink terms per unit area.

To solve these equations, the horizontal and vertical velocity (ν_H and ν_V) and diffusivity (D_H and D_V) need to be prescribed. In FLOW, the horizontal viscosity and diffusivity are assumed to be a superposition of three parts: (1) molecular viscosity, (2) "3D turbulence", and (3) "2D turbulence".

For use in the transport equation, the vertical eddy diffusivity is scaled from the vertical eddy viscosity according to

$$D_V = \frac{\nu V}{\sigma_c} \tag{3.13}$$

in which σ_c is the Prandtl-Schmidt number given by

$$\sigma_c = \sigma_{c0} F_\sigma(Ri) \tag{3.14}$$

where σ_{c0} is purely a function of the substance being transported. In the case of the algebraic turbulence model, $F_\sigma(Ri)$ is a damping function that depends on the amount of density stratification present via the gradient Richardson's number (Simonin et al., 1989). The damping function, $F_\sigma(Ri)$, is set equal to 1.0 if the $k-\epsilon$ turbulence model is used, as the buoyancy term in the $k-\epsilon$ model automatically accounts for turbulence-damping effects caused by vertical density gradients.

3.1.1.1.7 Turbulence closure models. Several turbulence closure models are implemented in FLOW. All model are based on the so-called "eddy viscosity" concept (Kolmogorov, 1942; Prandtl, 1945). The eddy viscosity in the models has the following form:

$$\nu_V = c_\mu' L\sqrt{k} \tag{3.15}$$

in which c_μ' is a constant determined by calibration, L is the mixing length, and k is the turbulent kinetic energy.

The used turbulence closure model is the $k-\epsilon$ turbulence closure model in which both the turbulent energy k and the dissipation ϵ are produced by production terms representing shear stresses at the bed, surface, and in the flow. The "concentrations" of k and ϵ in every grid cell are then calculated by transport equations.

3.1.1.2 Boundary conditions

3.1.1.2.1 Bed and free surface boundary conditions. In the σ-coordinate system, the bed and the free surface correspond with σ-lines. Therefore, the vertical velocities at these boundaries are simply

$$\omega(-1) = 0 \tag{3.16}$$

and (3.17)

$$\omega(0) = 0 \tag{3.18}$$

Friction is applied at the bed as follows:

$$\frac{\nu_V}{h}\frac{\partial u}{\partial \sigma}|_{\sigma=-1} = \frac{\tau_{bx}}{\rho} \tag{3.19}$$

$$\frac{\nu_V}{h}\frac{\partial v}{\partial \sigma}|_{\sigma=-1} = \frac{\tau_{by}}{\rho} \tag{3.20}$$

where τ_{bx} and τ_{by} are bed shear stress components that include the effects of wave-current interaction.

3.1.1.2.2 Lateral boundary conditions. Along closed boundaries the velocity component perpendicular to the closed boundary is set to zero (free-slip condition). In this Thesis, the boundary conditions is water level Verboom and Slob (1984).

3.1.1.3 Solution procedure

FLOW is based on finite differences. To discretize the 3D shallow water equations in space the model are is covered by a rectangular, curvilinear, or spherical grid. It is assumed that the grid is orthogonal and well structured. The variables are arranged in a pattern called the Arakawa C-grid (a staggered grid). In this arrangement, the water level points (pressure points) are defined in the center of a (continuity) cell; the velocity components are perpendicular to the grid cell faces where they are situated (Figure 3.2).

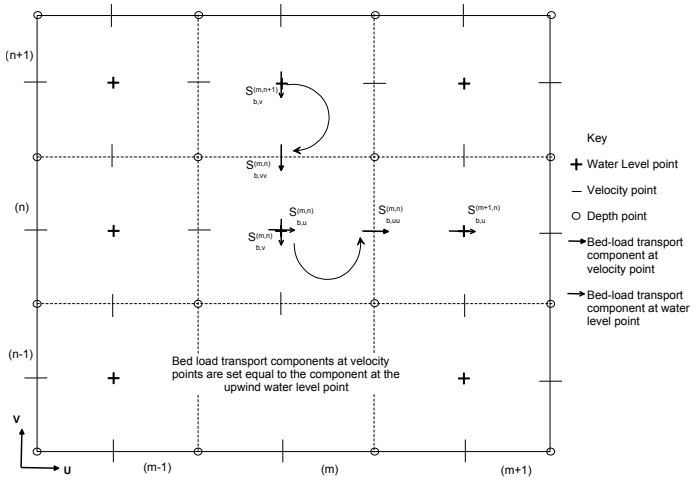

Figure 3.2: The DELFT3D staggered grid showing the upwind method of setting bedload sediment transport components at velocity points.Water- level points are located in the center of the sediment control volumes.

3.1.2 Wave module

3.1.2.1 General

Wave effects can also be included in a FLOW simulation by running the separate WAVE module. The WAVE module must be accessed before running the FLOW module. This will result in a communication file being stored that contains the results of the wave simulation (RMS wave height, peak spectral period, wave direction, mass fluxes, etc.) on the same computational grid is used by the FLOW module. The FLOW module can then read the wave results and include them in flow calculations. Wave simulations may be performed using the second-generation wave model HISWA (Holthuijsen et al., 1989) or the third-generation SWAN model (Holthuijsen et al., 1993).

3.1.2.2 Wave effects

In coastal seas, wave action may influence morphology for a number of reasons. The following processes are presently available in FLOW.

- Wave forcing due to breaking (by radiation stress gradients) is modeled as a shear stress at the water surface (Svendsen, 1985; Stive and Wind, 1986). This radiation stress gradient is modeled using the simplified expression of Dingemans et al. (1987), where contributions other than those related to the dissipation of wave energy are neglected.

- The effect of the enhanced bed shear stress on the flow simulation is accounted for by following the parameterizations of Soulsby et al. (1993).

- The wave-induced mass flux is included and is adjusted for the vertically nonuniform Stokes drift (Walstra et al., 2000).

- The additional turbulence production due to dissipation in the bottom wave boundary layer and due to wave whitecapping and breaking at the surface is included as extra production terms in the $k-\epsilon$ turbulence closure model (Walstra et al., 2000).

- Streaming (a wave-induced current in the bottom boundary layer directed in the direction of wave propagation) is modeled as additional shear stress acting across the thickness of the bottom wave boundary layer (Walstra et al., 2000).

Processes 2, 3 and 4 have only recently been included in FLOW and are essential if the (wave-averaged) effect of waves on the flow is to be correctly represented in 3D simulations. This is especially important for the accurate modeling of sediment transport in a nearshore coastal zone.

3.1.2.3 Wave model

The spectral wave model SWAN was applied in stationary, third-generation mode to propagate waves from the continental shelf to the coastline. SWAN simulates the evolution of wave action density using the action balance equation (Holthuijsen et al., 1993; Booij et al., 1999; Ris et al., 1999). The model takes into account propagation in geographical space, depth- and current-induced refraction, shifting of the intrinsic radian frequency due to variation in mean current and depth, as well as the generation and dissipation of waves by wind and breaking respectively (Elias and Hansen, 2012).

3.2 Numerical model II – WWTM + STA-BEM

The implemented morphodynamic model is made up of a wind-wave tidal model (hereinafter WWTM) (Carniello et al., 2011) and a sediment transport and bed evolution module (hereinafter STA-BEM) (Carniello et al., 2012).

3.2.1 Hydrodynamic model

3.2.1.1 Tidal model

The hydrodynamic model solves the two-dimensional shallow water equations modified to deal with flooding and drying processes in very irregular domains. On the basis of the idea that refined subgrid modeling of bathymetric data could lead to a physically consistent, and "universal" (i.e., not dependent on the numerical technique) solution of the wetting and drying problem, a new set of two dimensional shallow water equations was developed (D'Alpaos and Defina, 1995; Defina, 2000).

The presence of bottom irregularities, which strongly affect the dynamics and the continuity in very shallow flows, is considered in the model from a statistical point of view. Assuming the hydrostatic approximation, the three dimensional Reynolds equations are suitably averaged over a representative elementary area (REA) and then integrated over the depth. The resulting subgrid model for ground irregularities proves to be very effective in the simulation of tide propagation in shallow lagoons.

The averaged equations are

$$\frac{\partial q_x}{\partial t}+\frac{\partial}{\partial x}\left(\frac{q_x^2}{Y}\right)+\frac{\partial}{\partial y}\left(\frac{q_x q_y}{Y}\right)-\left(\frac{\partial R_{xx}}{\partial x}+\frac{\partial R_{xy}}{\partial y}\right)+\frac{\tau_{bx}}{\rho}-\frac{\tau_{wx}}{\rho}+gY\frac{\partial h}{\partial x}=0 \tag{3.21}$$

$$\frac{\partial q_x}{\partial t}+\frac{\partial}{\partial x}\left(\frac{q_x q_y}{Y}\right)+\frac{\partial}{\partial y}\left(\frac{q_y^2}{Y}\right)-\left(\frac{\partial R_{xy}}{\partial x}+\frac{\partial R_{yy}}{\partial y}\right)+\frac{\tau_{by}}{\rho}-\frac{\tau_{wy}}{\rho}+gY\frac{\partial h}{\partial y}=0 \tag{3.22}$$

$$\eta\frac{\partial h}{\partial t}+\frac{\partial q_x}{\partial x}+\frac{\partial q_y}{\partial y}=0 \tag{3.23}$$

where t denotes time, q_x,q_y are the flow rates per unit width in the x, y (planform) directions respectively, R_{ij} are the Reynolds stresses (i, j denoting either the x or y coordinates), $\tau_{b,curr}=(\tau_{bx},\tau_{by})$ is the stress at the bottom produced by the tidal current, $\tau_w=(\tau_{wx},\tau_{wy})$ is the wind shear stress at the free surface, ρ is fluid density, h is the free surface elevation, g is gravity. Y is the equivalent water depth, defined as the volume of water per unit area actually ponding the bottom, η is the local fraction of wetted domain which can be interpreted as an h-dependent storativity coefficient (similar to the one used in groundwater hydraulics), accounting for the actual area that can be wetted or dried during the tidal cycle.

In the model, the surface elevation h is assumed to vary linearly between element nodes (i.e., p1 discretization) while the depth integrated velocity components q_x, q_y are assumed constant within each element (i.e., p0 discretization). At each time step, the hydrodynamic model yields nodal water levels which are used by the wind wave model to assess wave group celerity and bottom influence on wave propagation. Moreover, depth integrated velocity and water depth computed with the hydrodynamic model are used to evaluate the bottom shear stress produced by the combined action of tidal currents and wind waves.

3.2.2 The wind-wave tidal model (WWTM)

The wind wave model is based on the conservation of the wave action N, which is defines as the ratio of wave energy E to the relative wave frequency σ. The WWTM uses the parameterized approximation of the wave action conservation equation whose complete formulation reads (Hasselmann, 1973)

$$\frac{\partial N}{\partial t}+\frac{\partial}{\partial x}c_{gx}N+\frac{\partial}{\partial y}c_{gy}N+\frac{\partial}{\partial \sigma}c_{\sigma}N+\frac{\partial}{\partial \theta}c_{\theta}N=\frac{S}{\sigma} \tag{3.24}$$

Here the wave action density, N, is defined as the ratio of wave energy, E, to the relative wave frequency, σ, and it is a function of space (x,y), time (t), frequency (σ) and direction (θ), i.e. $N=N(x,y,t,\sigma,\theta)$. The first term on the left hand side of Equation 3.24 is the local rate of change of wave action density in time; the second and third terms propagate the wave action density in space (c_{gx} and c_{gy} are the x and y components of the wave group celerity); the fourth and fifth terms propagate the wave action density in the space of wave frequency (σ) and direction (θ), respectively. The term S on the right hand side of Equation 3.24 describes all the external sources contributing to wave energy (see (Carniello et al., 2011) for further details).

Some terms of equation 3.24 can be neglected by making some justifiable assumptions. The simplified approach is particularly suitable for long-term morphological studies, in which the simulated period is very long. The monochromatic wave assumption allows us to neglect the fourth term in equation 3.24. Moreover, according to linear wave theory, we consider the wave period T, and thus the wave frequency $\sigma=2\pi/T$, constant during propagation. This simplification, combined with the monochromatic assumption, makes it possible to use the dispersion equation relating the wave number k ($k=2\pi/\lambda$, λ being the wavelength) to the water depth Y:

$$\sigma=\sqrt{g\,k\tanh(k\,Y)} \tag{3.25}$$

Moreover, the model assumes that the direction of wave propagation instantaneously readjusts to match the wind direction.

Lin et al. (2002) show that wind and wave data collected in the Chesapeake Bay indicate that the mean wave direction closely follows the wind direction. With the above assumption model neglects the refraction.

According to the above discussion the fifth term of the wave action conservation equation 3.24 can be neglected, thus obtaining

$$\frac{\partial N}{\partial t}+\frac{\partial}{\partial x}c_{gx}N+\frac{\partial}{\partial y}c_{gy}N=\frac{S}{\sigma} \tag{3.26}$$

where the group celerity c_g is given, according to the linear wave theory, as

$$c_g=\frac{1}{2}c\left(1+\frac{2kY}{\sinh(kY)}\right) \tag{3.27}$$

where c is the phase celerity ($c=\sigma/k$).

The term S on the right hand side of equation 3.26 describes all the external physical phenomena contributing to wave energy. They can be either positive e.g., wind energy input, or negative e.g., bottom friction, white capping, and depth-induced breaking. The implementation of each source term in the model is described in the following paragraphs.

3.2.3 The sediment transport and bed evolution model (STA-BEM)

When modeling sediment transport and bed evolution in tidal estuaries and lagoons, it is crucial to consider both cohesive and non-cohesive sediments and the behavior of mixtures as a function of the clay content. It is then important to distinguish cohesive from non-cohesive sediment and to schematize the bed composition; we decided to use two size classes of sediments: non-cohesive sand and cohesive mud, which is the sum of clay and silt. The transition between the non-cohesive and cohesive behavior of a mixture is mainly determined by the clay content. However, since the clay-to-silt ratio is approximately constant for a specific estuary or tidal basin (Van Ledden, 2003; Van Ledden et al., 2004), we use a threshold mud fraction, p_{mc}, to discriminate between non-cohesive and cohesive behavior.

The sediment transport model is based on the solution of the advection diffusion equation

$$\frac{\partial C_i Y}{\partial t} + \nabla \mathbf{q} C_i - \nabla(\mathbf{D} Y \nabla C_i) = E_i - D_i; i = s, m \tag{3.28}$$

where C is the depth averaged sediment concentration, $\mathbf{q}$=(q_x, q_y) the flow rate per unit width, Y the equivalent water depth (i.e. the volume of water per unit area as defined by (Defina, 2000)), $\mathbf{D}$ the two-dimensional diffusion tensor, E and D the entrainment and deposition rates, and the subscript i ($i = s, m$) the sand and mud fraction respectively. Equation 3.28 is simplified by assuming that diffusion can be neglected compared to advection (e.g. (Pritchard and Hogg, 2003), see also (Carniello et al., 2012) for further details).

In the model, the deposition rate of sand is computed as

$$D_s = -w_s r_0 C_S \tag{3.29}$$

where w_s is the sand settling velocity and r_0 is the ratio of near-bed to depth averaged concentration which is here assumed constant ($r_0 = 1.4$) as suggested by Parker et al. (1987).

Deposition of pure cohesive mud is given by the Krone's formula:

$$D_m = -w_m C_m \tag{3.30}$$

$$\max\{0; 1 - \tau_b/\tau_d\} \tag{3.31}$$

Here w_m is the mud settling velocity, τ_b the bottom shear stress, and τ_d the critical shear stress for deposition. The settling velocities w_s and w_m are computed using the

Van Rijn (1984) formulation for solitary particles in clear and still water thus neglecting the flocculation process which affects settling velocity when grain diameter is greater than $20\mu m$ (Mehta, 1989).

Experimental investigations with sand-mud mixtures indicate that the erosion rate of a mixture cannot be described by existing formulas for pure sand and pure mud since the rate strongly depends on the degree os cohesion of the mixture (Williamson and Ockenden, 1993; Torfs, 1995; Garcia, 2008).

For the case of non-cohesive mixture ($p_m < p_{mc}$) the Van Rijn (1984) formula describes reasonably well the sand erosion rate while visual observations suggest that the mud fraction is easily washed out when the bed behaves non-cohesively (Murray, 1977). Van Ledden (2003); Van Ledden et al. (2004) proposed an erosion formula for non-cohesive mud as a function of the bed load transport rate and the saltation length of sand particles. For cohesive sediment mixture ($p_m > p_{mc,cr}$) both sand and mud entrainment can be evaluated using Partheniades' erosion formula (Williamson and Ockenden, 1993; Torfs, 1995).

Based on the above, the erosion rates for non-cohesive ($p_m < p_{mc}$) and cohesive ($p_m > p_{mc}$) mixtures are written as:

$$E_s = \begin{cases} (1-p_m)\, w_s \left(\dfrac{D_{50}/Y}{D_*^{0.3}} \right) & p_m \le p_{mc} \\ (1-p_m)\, M_c T & p_m \ge p_{mc} \end{cases} \tag{3.32}$$

$$E_m = \begin{cases} \dfrac{p_m}{1-p_m} M_{nc} T & p_m \le p_{mc} \\ p_m M_c T & p_m \ge p_{mc} \end{cases} \tag{3.33}$$

Here D_* is the dimensionless grain size ($D_* = D_{50}\left[(1-s)\, g/\nu^2\right]^{1/3}$, where s is the specific density and ν the kinematic viscosity) and M_c and M_{nc} are respectively the specific entrainment for cohesive and non-cohesive mixtures given as (Van Rijn, 1993; Van Kesteren et al., 1997; Van Ledden, 2003)

$$M_{nc} = \alpha \frac{\sqrt{(1-s)\, g D_{50}}}{D_*^{0.9}} \tag{3.34}$$

$$M_c = \left(\frac{M_{nc}}{M_m} \cdot \frac{1}{1-p_{mc}} \right)^{\dfrac{1-p_m}{1-p_{mc}}} \cdot M_m \tag{3.35}$$

where M_m is the specific entrainment for pure mud, and T is the transport parameter, which describes a sharp transition between $T = 0$ and $T = \tau_b/\tau_c - 1$.

$$T = -1 + \left(1 + \left(\frac{\tau_b}{\tau_c} \right)^{\varepsilon} \right)^{1/\varepsilon} \tag{3.36}$$

where ε is a non-dimensional calibration parameter.

In the model the bed shear stress (τ_b) is computed using the empirical formulation suggested by (Soulsby et al., 1993) which accounts for the non-linear interaction between the wave and current boundary layers, whereas, following Van Ledden (2003); Van Ledden et al. (2004) the critical shear stress (τ_c) is assumed to vary monotonically between pure sand (τ_{cs}) and pure mud (τ_{cm}) depending on the mud content:

$$\tau_c = \begin{cases} (1+p_m)\,\tau_{cs} & p_m \le p_{mc} \\ \dfrac{\tau_{cs}\,(1+p_{mc}) - \tau_{cm}}{1-p_{mc}}\,(1-p_m) + \tau_{cm} & p_m \ge p_{mc} \end{cases} \tag{3.37}$$

It is worth noting that equation 3.32 and 3.33 give the potential entrainment of sand and mud since they are limited by the local and temporal availability of each size-class of the mixture.

Given an initial bed configuration, the bed evolution module computes the bed evolution both in term of bottom elevation and bed composition as a consequence of different sand/mud deposition and erosion rates whereas bed porosity n of the mixture is assumed to be constant ($n = 0.4$) in time and space independent of the mud content.

The change in bed level is a direct consequence of the erosion and deposition fluxes of sand and mud: at each time step the variation in bed elevation (dz_b/dt) is evaluated as

$$(1-n)\frac{dz_b}{dt} = (D_s + D_m) - (E_s + E_m) \tag{3.38}$$

The model uses a well-mixed active layer just below the bed surface (Hirano, 1971, 1972; Armanini and Di Silvio, 1988; Armanini, 1995). The active layer thickness Δz_b can increase by local deposition but cannot decrease by erosion below a threshold value Δz_{b0}: if this tends to occur, the layer thickness is re-established incorporating part of the sub-layer into the active layer. The sub-layer characteristics are constant and set equal to the initial bed composition. the model updates the bed composition by evaluating the variation of the mud content (p_m) as a consequence of sand and mud fluxes between the active layer, the above-water column and, if necessary, the sub-layer.

Chapter 4
Numerical Model (II): Implementation

In this chapter the models that have been described in detail in Chapter 3 are implemented, calibrated and tested using the field measurements detailed in Chapter 2: water levels, currents (both at tidal and residual scales), wave height and suspended sediment concentration. The results show good agreement with observations and with other previous works. The majority of the results in this chapter were published in Zarzuelo et al. (2015a).

4.1 Initial Data: Bathymetry and Topography

The simulations presented herein are carried out within a computational domain suitably set up to predict the tidally induced circulation in shallow basins such as the Bay of Cádiz. To run the model, a mesh was constructed on the basis of accurate bathymetry and topography data. The offshore bathymetry data were provided by the Instituto Hidrográfico de la Marina (Spanish Ministry of Defence), while the detailed multi-beam bathymetry of the bay was provided by the Port Authority of Cádiz. The topography was obtained from the Digital Elevation Model of the Regional Government (Junta de Andalucía) at a resolution of $10 \times 10\,\mathrm{m}^2$. In areas in which multiple data sets overlapped, preference was given to the highest resolution multi-beam data (Hansen et al., 2013).

4.2 Model Setup I – DELFT3D

4.2.1 Flow module: Calibration and Testing

The module is suitable for predicting the tidally induced circulation in shallow seas such as the Bay of Cádiz. To run the model, a Cartesian grid covering the entire bay was defined with a total of 545×245 cells (Figure 4.1) and ten σ-layers in the vertical direction. The mean size of each cell is approximately $200 \times 200\,\mathrm{m}^2$. However, in areas where more detail is required, $60 \times 60\,\mathrm{m}^2$ cells are defined. These values are of the same order of those used in previous works (Liu et al., 2004).

We calibrated and tested the flow module following a widely used methodology (i.e., Lesser et al. (2004); Olabarrieta et al. (2011); Elias and Hansen (2012); Hansen et al. (2013). A four-step approach (Elias and Hansen, 2012) is followed to ensure accurate results. First, a tidal forcing is imposed at the seaward boundary using the amplitudes and phases of

the twelve dominant components provided by the Oregon State Tidal Prediction Software (OTPS) (Egbert and Erofeeca, 2002). Second, the system is forced with a uniform wind obtained from Buoy 2342 (Figure 2.1). Third, the model is run and calibrated using the wind drag and Chezy coefficients. Finally, the model's performance is tested by comparing the results with the observed tidal currents and elevations at stations I1 and I2 (Figure 4.2).

The module was calibrated and tested using the field data described in subsection 2.2 for three different variables: water level (η) and instantaneous (u, v) and residual currents ($|\overline{U}|$). We obtained excellent agreements for these three variables, equal to or even better than those obtained in previous similar studies (Vaz et al., 2009; Carballo, 2009; Carniello et al., 2012; Elias and Hansen, 2012; Safak et al., 2015; Van Maren et al., 2015b). Moreover, residual currents have been calibrated and tested despite its difficulty and not being a usual task performed in similar studies.

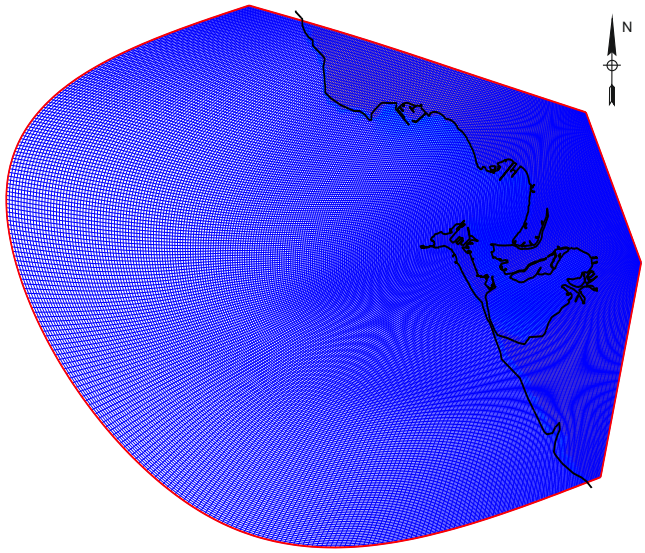

Figure 4.1: Representation of the mesh used for the flow module of the numerical model Delft3D.

The time period January 17 to 30, 2012 was selected to calibrate the instantaneous and residual tidal flows. According to the observations, the wind velocities and wave heights during this period were low enough to dismiss their influence. Similar to other studies (Lesser et al., 2004; Iglesias and Carballo, 2009; Elias and Hansen, 2012), the flow module was very sensitive to the wind drag coefficient and the bed roughness. Hence, these were the primary calibration parameters. The best fit was obtained for the Chezy roughness coefficients $(80, 60)\,\mathrm{m}^{1/2}/\mathrm{s}$ and a wind drag coefficient of 0.005. These parameters are uniform in the mesh, like in other previous works (e.g., Iglesias et al. (2012)). There are some perturbations in the initial period due to the smoothing time (defined as 90 minutes). Using these parameters, an excellent agreement between the observed and simulated water levels was achieved (correlation coefficient R = 0.99). The R and skill values (see Appendix A) for the tidal currents are lower, but the agreement is also good ($R = 0.89$, $S = 0.75$) (Figure 4.2, circle dots). Although the fit for the residual currents is more demanding, an excellent agreement is also obtained with $R = 0.8$ values.

	η_{I1}	η_{I2}	u_{I1}	u_{I2}	v_{I1}	v_{I2}	$\lvert\overline{\mathbf{U}}_{I1}\rvert$	$\lvert\overline{\mathbf{U}}_{I2}\rvert$
RMSE	0.14 (m)	0.15 (m)	0.16 (m/s)	0.13 (m/s)	0.16 (m/s)	0.19 (m/s)	0.04 (m/s)	0.05 (m/s)
R	0.99	0.99	0.93	0.88	0.93	0.90	0.79	0.78
S	0.99	0.99	0.73	0.73	0.89	0.83	0.79	0.77

Table 4.1: Root mean square errors (*RMSE*), correlation coefficients (*R*) and skill coefficients (*S*), for the elevations, velocities and residual currents at I1 and I2. The overline represents the semidiurnal average.

As a final step, the calibrated Flow module was tested in the period January 29 to February 10, 2012 (Figure 4.2, square dots). The results of the model were again compared with the observed water levels and currents at I1 and I2. The high skill parameter values (Wilmott, 1981), which are lower for the east currents, indicate that the model is able to accurately reproduce the tidal dynamics of the study area. Considering that the Bay of Cádiz is relatively small, the density and length of the measurements and the results of the calibration guarantee the accuracy of the model to reproduce the overall hydrodynamics of the bay. The calibration/testing results have been compared with extensive field studies to verify the accuracy of the hydrodynamics, demonstrating its potential for application to any altered field site.

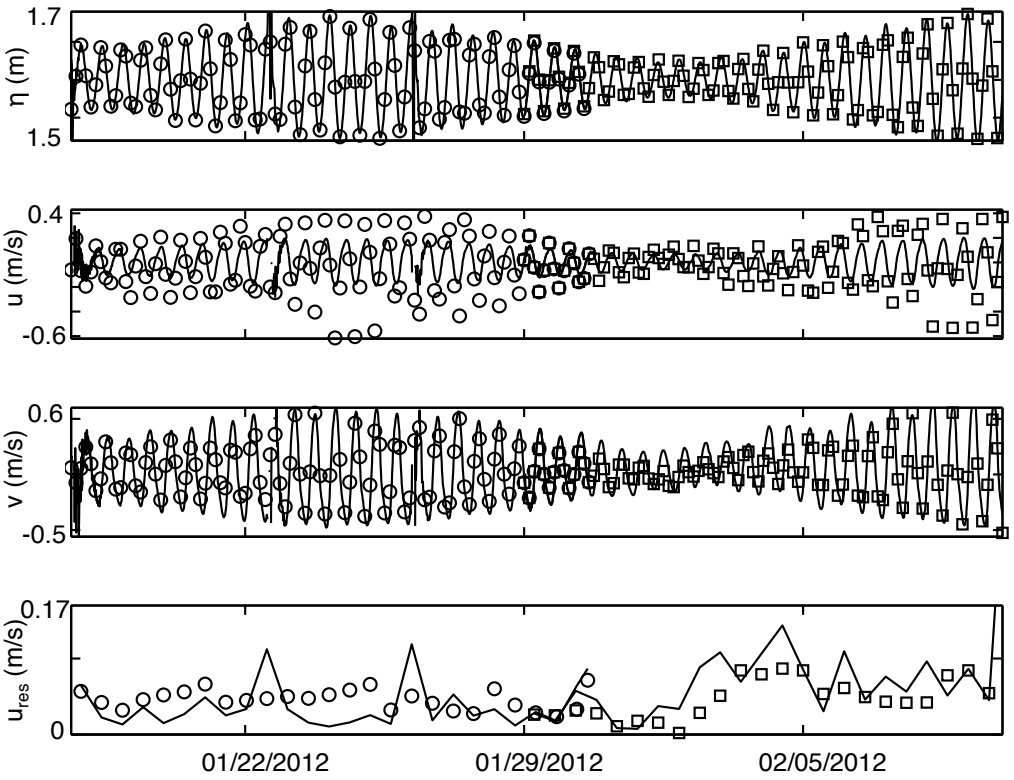

Figure 4.2: Calibration (circles) and testing (squares) for station I1. Dots (line) correspond to the observed (modeled) data. The water level is shown in the first panel; the East and North velocities are shown in the second and third panel, respectively. The residual current magnitude is shown in the fourth panel.

Figures 4.3 and 4.4 show observed and simulated values of the east and north velocity component, respectively, in the surface, mid-depth and bottom layer at I1. The agreement is very good in the three layers, although being slightly lower at the bottom. In the

surface layer some velocity peaks are underestimated; however, the underlying non-tidal current is correctly reproduced. On the whole there is good agreement between simulated and observed values, as is indicated by the correlation and skill coefficients, and the mean square errors (Tables 4.1 and 4.2).

	$u_{surface}$	$u_{mid-depth}$	u_{bottom}	$v_{surface}$	$v_{mid-depth}$	v_{bottom}
$RMSE$	0.091 (m/s)	0.094 (m/s)	0.096 (m/s)	0.094 (m/s)	0.098 (m/s)	0.106 (m/s)
R	0.91	0.90	0.89	0.93	0.92	0.92
S	0.91	0.90	0.89	0.93	0.91	0.89

Table 4.2: Root mean square errors ($RMSE$), correlation coefficients (R) and skill coefficients (S), for east and north velocity component in the surface, mid-depth and bottom layer at I1.

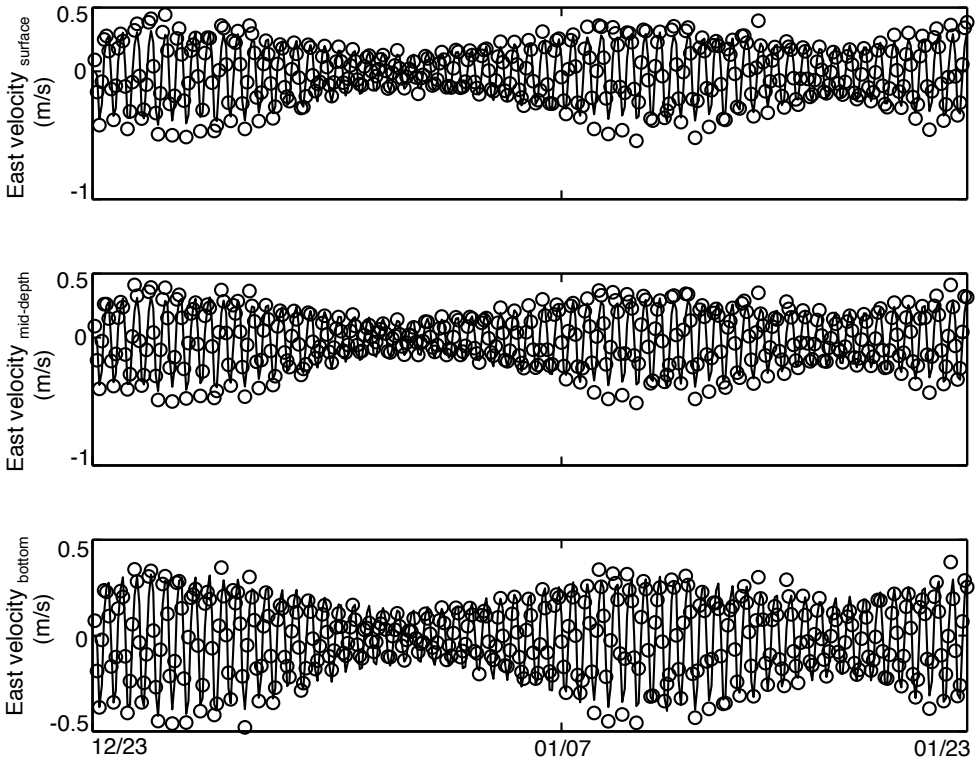

Figure 4.3: Observed (line) and simulated (circles) east velocity component in the surface, mid-depth and bottom layer at I1. Positive and negative values indicate inward and outward Flow module, respectively. Calibration (circles) and testing (squares) for station I1.

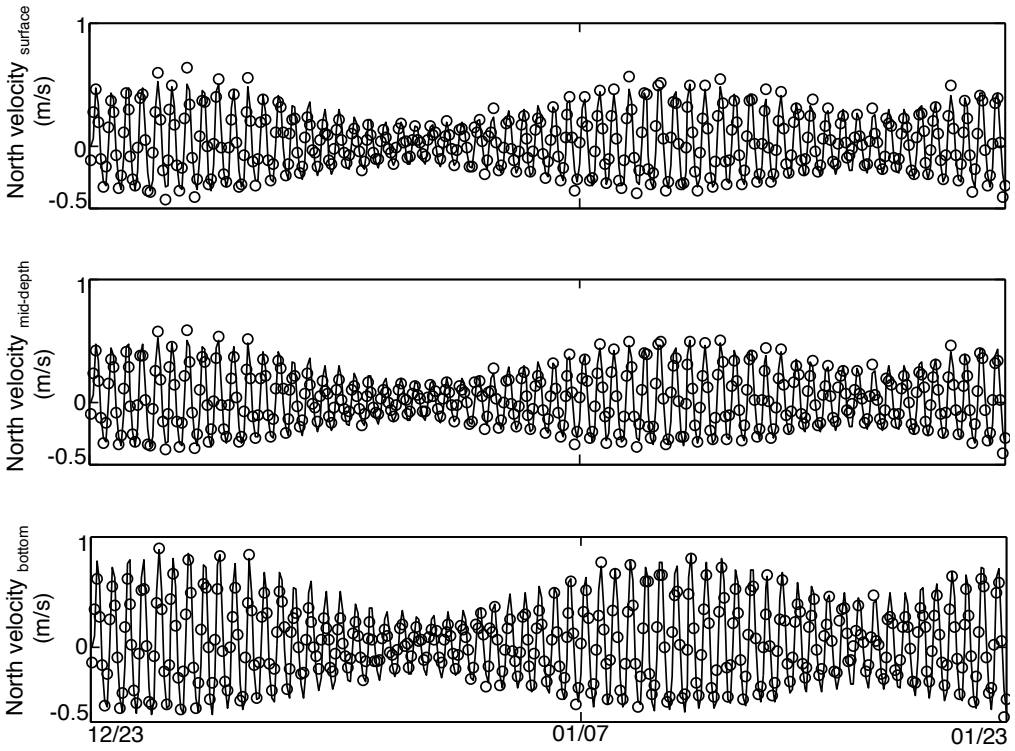

Figure 4.4: Observed (line) and simulated (circles) north velocity component in the surface, mid-depth and bottom layer at I1. Positive and negative values indicate inward and outward Flow module, respectively. Calibration (circles) and testing (squares) for station I1.

4.2.2 Wave module: Calibration and Testing

Two grids of progressively increasing resolution were created to accurately resolve the wave propagation, growth and decay in the nearshore (545×245 cells, $200 \times 200\,m^2$, 245×245 cells, $150 \times 50\,m^2$; Figure 4.5). The wave propagation grid coincides with the flow module grid. The largest wave domain that extends off the shelf is rotated such that the northwest-west corner is near the Gulf of Cádiz buoy (Figure 4.1). Sensitivity testing revealed that this domain is large enough to capture the complex wave refraction and sheltering patterns around the Pt. Cadiz headland.

For module calibration, we compare the wave heights computed from I1 measurements with model results. Given the magnitude and spatial extent of strong tidally-driven currents, inclusion of wave-current interactions is critical for accurate wave modeling. The hydrodynamic and wave were therefore run in so-called quasi-nonstationary mode. This involves a two-way coupling of a nonstationary hydrodynamic calculation in combination with regular stationary wave simulations. Every 15 minutes during the hydrodynamic simulation Wave module is activated and performs a stationary simulation, using the measured wave spectra, and computed water levels, currents and bed levels passed from the flow module. The results of the wave simulations are stored on the computational grid (flow) and included in the flow calculations through additional forcing terms near surface and bed shear stresses streaming and increased turbulence (Fredsoe, 1985; Dingemands et al., 1987; Walstra et al., 2000; Elias and Hansen, 2012).

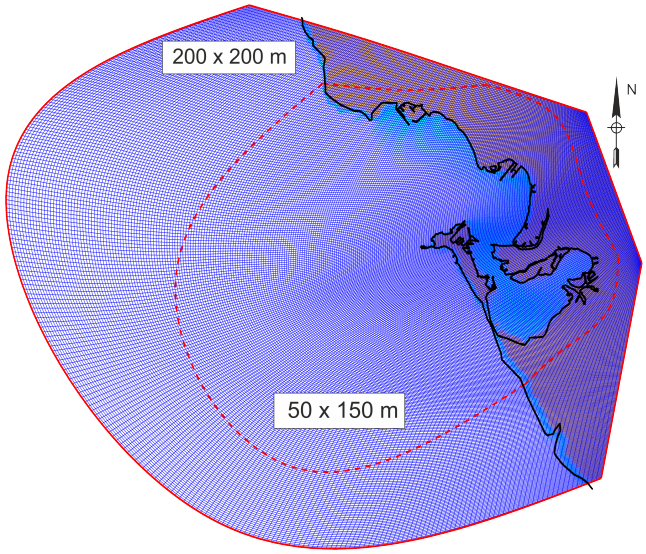

Figure 4.5: Representation of the mesh used for the combined flow and wave modules of the Delft3D numerical model.

The best agreement between modeled and observed wave parameters was found using the following settings: (1) the default Collins bottom friction value for swell propagation of 0.002 m^2/s^3(Hasselmann, 1973; Van Vledder et al., 2010), (2) dissipation by white-capping using the van der Westhuysen formulation (Van der Westhuysen et al., 2007). Wave heights within the surf zone were found to be sensitive to the specific method of dissipation implemented in the Wave module: the best agreement was obtained by applying the recently implemented bi-phase breaker model of Van der Westhuysen (2010) with the default coefficients; (3) non-linear triad interaction using the Lumped Triad Approximation (LTA, $\alpha = 0.1, \beta = 9$) following Eldeberky and Battjes (1996) was de-activated because of increased run times and poor performance at sites that feature narrow banded swell (Elias and Hansen, 2012).

Thirty-seven frequency bins between 0.03 and 1 Hz were used along with 72 directional bins in full circle. Convergence criteria were 98% of cells and maximum 50 iterations, to obtain full convergence for all Wave modules cases. During the selected time frame coherent measurements for I1 over a wide range of representative forcing conditions were presents. Skill values between the measured and modeled Wave heights ranged between 0.5 and 0.8 (Figures 4.6).

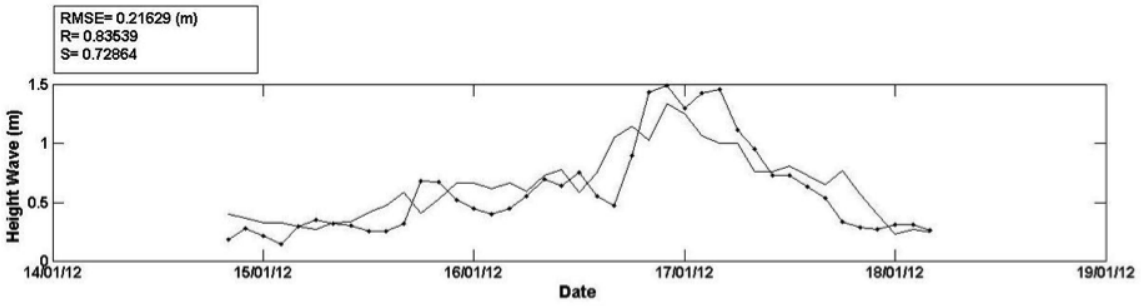

Figure 4.6: Observed (continuous line) and simulated (dot line) wave heights at I1.

4.3 Model Setup II (WWTM+STA-BEM)

4.3.1 WWTM+STA-BEM: Calibration and Testing

The mesh consists of about 31367 nodes and more than 62105 triangular elements (Figure 4.8). The smallest element size is about 10 m which forces us to use a time step of 2 s.

The WWTM module is calibrated and tested following the four-step outlined previously in section 4.2.1. In the third step we used the Strickler bed roughness coefficients to run and calibrate the model at stations I1 and I3. Finally, the model performance is tested by comparing the results with the observed tidal currents and elevations at stations I1, I3, I4, I5, T1, T2 and T3.

The sediment transport model was calibrated and tested against turbidity measurements collected at I3. The WWTM+STA-BEM model parameters used in the simulations (Table 4.3) were determined through a calibration procedure through which parameter α and the specific entrainment rate for mud (M_m) were adjusted to give the best fit to the data while the critical shear stresses for sand (τ_{crS}) and mud (τ_{crM}), the critical shear stress for deposition (τ_{DEP}), and the mean grain size (D_{50S}, D_{50M}) were assumed. The initial active layer thickness was set to $\triangle z_{b0} = 0.02$ m (a sensitivity analysis was performed conclusing that this parameter does not significantly influence the solution).

Parameter	Description	Value
D_{50S}	Mean grain diameter for pure Sand	$200\mu_m$
D_{50M}	Mean grain diameter for pure Mud	$20\mu_m$
τ_{crM}	Critical shear stress for pure Sand	0.5 Pa
τ_{crS}	Critical shear stress for pure Mud	0.8 Pa
τ_{DEP}	Critical shear stress for pure deposition	1.0 Pa
M_m	Specific entrainment parameter for pure mud	$2 \cdot 10^{-2}$ gm/s
α	Entrainment parameter for non–cohesive mixture (eq 3.34)	$1 \cdot 10^{-5}$
$\triangle z_{b0}$	Initial active layer thickness	0.02 m

Table 4.3: Parameters used in the sediment transport model.

Figure 4.7 shows the geologic map of the Bay of Cádiz. The bed is composed by mud (≤ 0.063 mm), fine-sand (0.25 mm) and coarse-sand (0.60 mm). The present simulations incorporate the same initial bed sediment composition. The area is also characterized by a pattern of very shallow channels and shoals including a large area of tidal flats. Sediment is transported as a suspended load, due to both diffusive and advective processes. In this type of short embayments, the diffusive transport mechanisms are dominant. We used this distribution to reconstruct the bed composition in term of mean grain size used in the model.

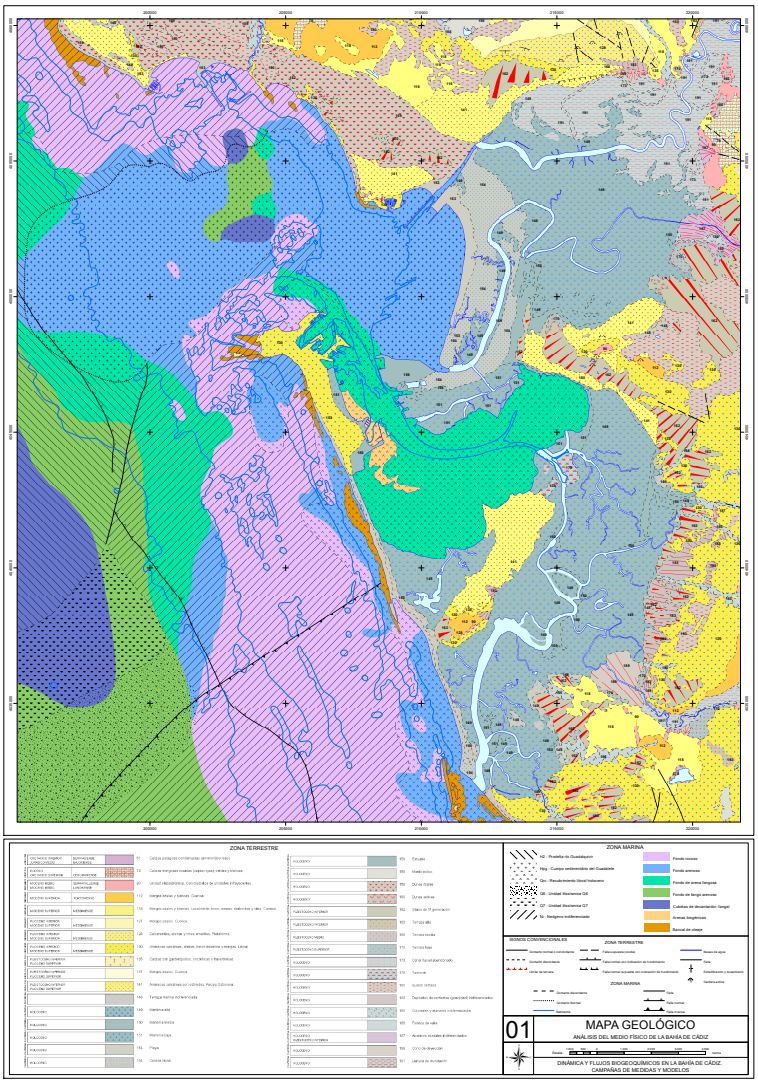

Figure 4.7: Geologic map of the Bay of Cádiz.

The dates from January 17 to 26, 2012, were selected to calibrate the model. The Flow module was very sensitive to the Strickler bed roughness, which was therefore considered as the primary calibration parameter. Ten different classes are used to define the Strickler coefficients, whose values range from 10 to 35 $m^{1/3}/s^{-1}$.

Using these parameters, excellent agreement between the observed and simulated water levels was achieved (correlation coefficient $R = 0.99$). The regression coefficient R and skill values (Olabarrieta et al., 2011) for the tidal currents are lower, but the agreement is also good ($R = 0.94, S = 0.9$) (Table 4.4).

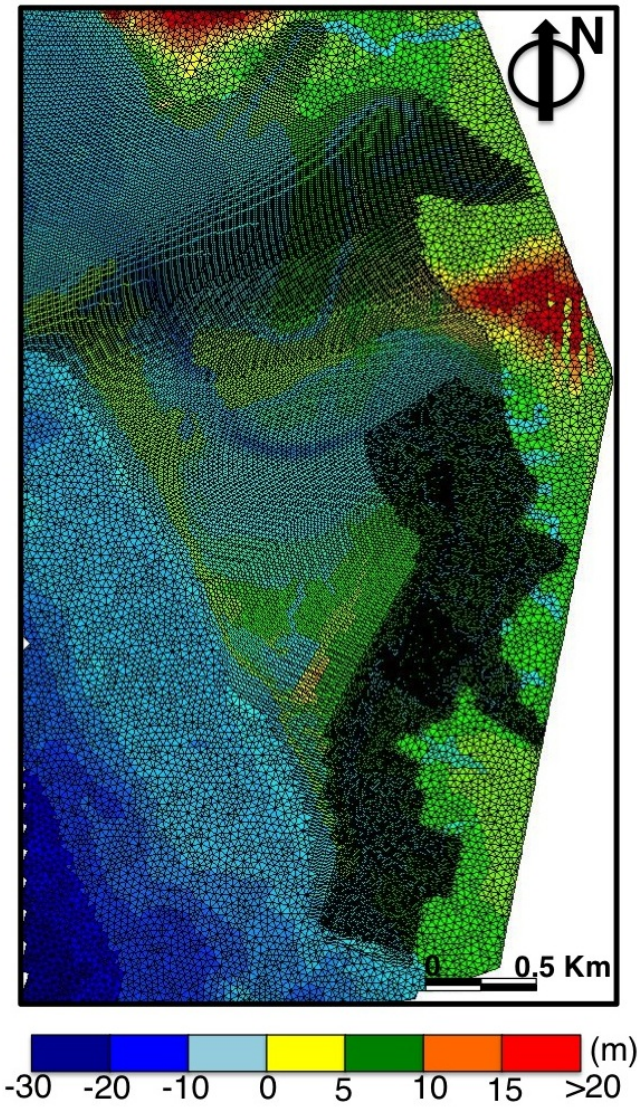

Figure 4.8: Representation of the first mesh corresponding with the numerical model WWTM+STA-BEM.

	Water Level(m)			East Velocity(m/s)			North Velocity(m/s)		
	RMSE	*R*	*S*	*RMSE*	*R*	*S*	*RMSE*	*R*	*S*
I_1	0.070	0.99	0.99	0.083	0.94	0.83	0.059	0.96	0.91
I_2	0.075	0.99	0.99	0.062	0.95	0.91	0.062	0.95	0.91

Table 4.4: Root mean square errors (*RMSE*), correlation coefficients (*R*) and skill coefficients (*S*), for the calibration period of the elevations and velocities at I1 and I2.

	Water Level (m)			East Velocity (m/s)			North Velocity (m/s)		
	RMSE	*R*	*S*	*RMSE*	*R*	*S*	*RMSE*	*R*	*S*
I_1	0.080	0.99	0.99	0.099	0.87	0.83	0.110	0.96	0.91
I_2	0.070	0.99	0.99	0.087	0.91	0.91	0.160	0.94	0.93
I_3	0.100	0.99	0.99	0.260	0.69	0.67	0.330	0.77	0.51
I_4	0.120	0.99	0.99	0.090	0.79	0.71	0.100	0.93	0.85
T_1	0.820	0.82	0.67	**X**	**X**	**X**	**X**	**X**	**X**
T_2	0.560	0.87	0.80	**X**	**X**	**X**	**X**	**X**	**X**
T_3	0.220	0.97	0.97	**X**	**X**	**X**	**X**	**X**	**X**

Table 4.5: Root mean square errors (*RMSE*), correlation coefficients (*R*) and skill coefficients (*S*), for the testing period of the elevations and velocities at I1, I2, I3, I4, T1, T2 and T3.

The testing period spans from February 02 to March 14, 2012 (Figures 4.9; circle dots). The results of the model are again compared with the observed water levels and currents at I1, I2, I3, I4, T1, T2 and T3. The high values of the skill parameter (Table 4.5), lower for the east currents, indicate that the model is able to accurately reproduce the tidal dynamics of the Bay of Cádiz.

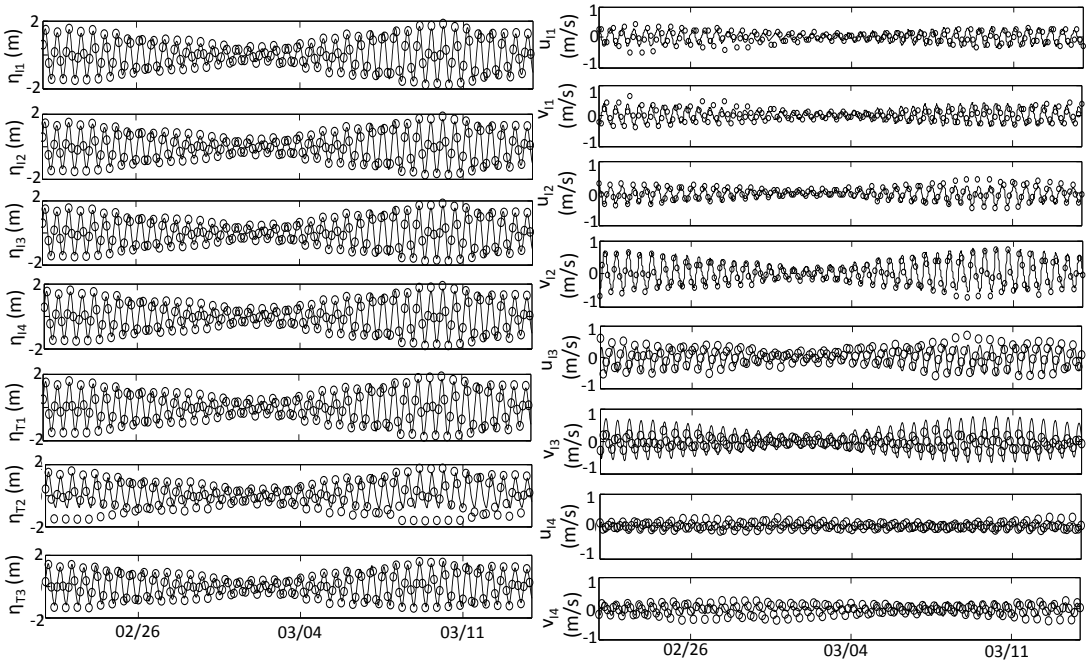

Figure 4.9: Calibration (circles) for stations I1, I2, I3, I4, T1, T2 and T3. Dots (line) correspond to the observed (modeled) data. The water level is shown in the left panels; the East and North velocities are shown in the right panels.

Although the fit for the residual currents (Figure 4.10-first panel) is more demanding, according to the classification proposed by Van Rijn et al. (2003), a good agreement is also obtained with $R \approx 0.8$ values Table 4.6. Furthermore, the tidal prism also been calibrated (Figure 4.10-second panel) with a good agreement ($R \approx 0.73$, table 4.6). Finally, the suspended sediment concentration (Figure 4.10-third panel) was analyzed at station I3 and compared with the model results. The correlation is lower than the others variables, however considering previous study (Carniello et al., 2012) the agreement is good ($R \sim 0.65$, Table 4.6). Considering that the Cádiz Bay is relatively small, the density and length of the measurements and the results of the calibration allow us to accurately reproduce the overall hydrodynamics of the bay by means of the numerical models. The calibration/testing results have been compared with extensive field studies (i.e. Elias and Hansen (2012); Safak et al. (2015); Van Maren et al. (2015b)) to verify the accuracy of the hydrodynamics, demonstrating its potential for application to any altered field site.

	Residual Current(m/s)			Tidal Prism(m^3)			Sediment Suspension Concentration(mg/l)		
	RMSE	*R*	*S*	*RMSE*	*R*	*S*	*RMSE*	*R*	*S*
I_2	0.04	0.79	0.8	1.01	0.74	0.73	24.1	0.66	0.65

Table 4.6: Root mean square errors (*RMSE*), correlation coefficients (*R*) and skill coefficients (*S*), for the calibration period of the residual currents, the tidal prism and the suspended sediment concentration at I3.

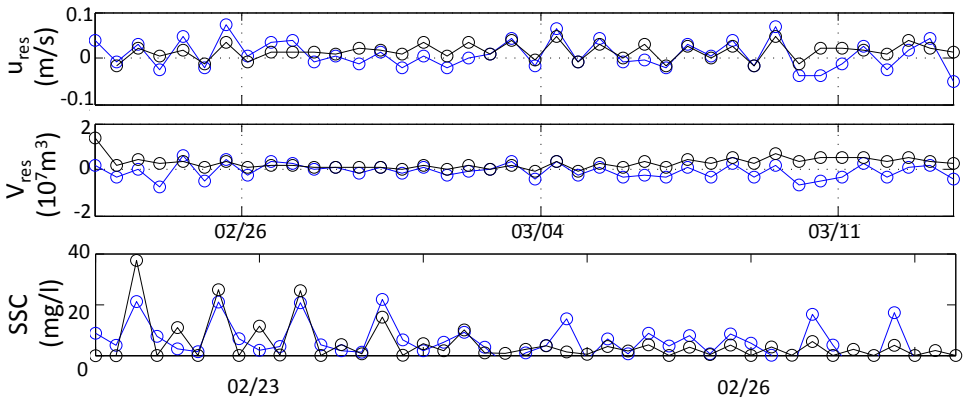

Figure 4.10: Comparison of measured (black line) and computed (blue lines) for station I2. The residual current magnitude is shown in the first panel; the tidal prisms is shown in the second panel; the suspended sediment concentration is shown in the third panel.

Chapter 5
Hydrodynamics of the tidally-dominated bay

This Chapter focuses on the characterization of the hydrodynamics of the current configuration of the Bay of Cádiz. The tidal wave transformation, the incoming and dissipated tidal energy and the barotropic subtidal flows are evaluated and analyzed, with the aim of examining the tidal and residual water exchange along the Bay. Carniello et al. (2005) model is used to simulate the hydrodynamic behaviour in the creeks, whereas DELFT3D is used for the rest of the bay. Most of these results are presented in Zarzuelo et al. (2015a,b).

5.1 Pre-processing: data analysis

While analyzing the field data described in section 2.2, many erroneous and/or unusual data were detected. Thus, a procedure was established to assure consistency. Firstly, we filter the raw data to eliminate anomalies. The pressure time series acquired by the water instruments were post-processed to obtain the instantaneous free surface elevations. Using a numerical and statistical nonlinear approach for an irregular wave through the Nielsen formulation (Nielsen, 1986), allow to correlate pressure and surface level (Figure 5.1). Tide propagation and transformation along Cádiz Bay were analyzed by means of a harmonic analysis of both water levels and velocities (Pawlowicz et al., 2002). This analysis was performed for the one-month period when all of the instruments were simultaneously measured (February 16 to March 14). A one-week gap in the elevation time series was reconstructed using the same technique. East-North velocities were projected along the Puntales channel axis. Hereafter, coordinates (x, y) represent the cross and along channel axis, respectively. The residual currents, tidal prism and exchange volumes were calculated by averaging the flow over one M2 tidal cycle (Jonge, 1992). The Fourier Series Coefficients of the dynamic pressure and velocities treated at a depth z are used to calculate the energy spectrum each one and with them to use statistic analyze, and so to obtain each one of cited variables above.

With the goal to facilitate linking observations with processes, the (local) measurements are placed in a wider context with the use of horizontal velocity and elevations fields obtained from the Delft3D numerical model (Chapter 4).

5.2 Tide propagation

The tidal character inside the bay is co-oscillating, and is induced by a Kelvin-type wave, which propagates northward along the North Atlantic eastern margin. Tides penetrate into the bay mainly from the outer area (A) and propagate into the inner bay (C) through the Puntales channel (B). The inner bay is also connected intermittently to the open sea through the Carracas and Sancti-Petri creeks, although the tidal prism is significantly smaller in this case and the connection channels dry out at approximately the mid-tide stage during spring tides. The geometry of the bay transforms and distorts the tide as it propagates into shallower waters.

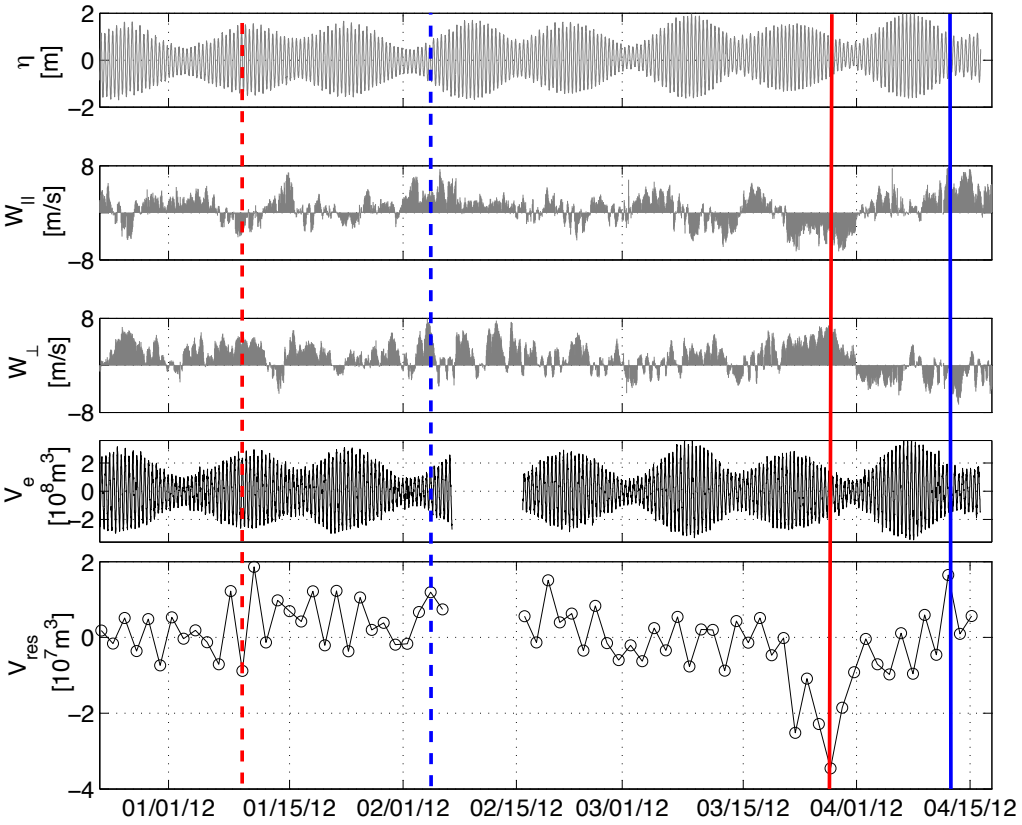

Figure 5.1: From top to bottom: the elevation recorded during the field survey at I1 is shown in the first panel; panels 2 and 3 depict the along- and across-channel wind velocity measured off the coast at buoy 2342; Panel 4 shows the water volume exchange at section I3. Panel 5 depicts the residual water volume exchanged through the cross-section at I3. The blue and red dots (lines) correspond with the cases of correlation between wind and residual water volume. Events are identified as 1a (1b) and 2a (2b) respectively.

5.2.1 Tidal Elevations

Figure 5.7 shows the tidal range $\Delta\eta_k$ (normalized to the value at I1, $\Delta\eta_{I1}$) at stations $k = \{I3, I4, I5, T1, T2\}$. Station I3 exhibits values close to unity, which indicates that the tidal range does not vary substantially between I1 and I3. As the tide propagates inside the bay, the channel convergence yields a relative increase of the tidal ranges (I4). The tidal range at I5 decreases due to inverse shoaling. No significant spring-neap variations are

observed in $\Delta\eta_k/\Delta\eta_{I1}$ at $k = \{I3, I4, I5\}$, indicating a linear relation between the tidal amplitudes at these stations. The ratios are lower than unity in the stations located in tidal creeks (T1 and T2) due to the enhanced tidal damping generated by friction (Blanton et al., 2002). Apparently a marked spring-neap variation is observed in T1 and T2. Values larger than unity are observed during neap tides, whereas negative values appear during spring tides (e.g., a reduction of 14% in the tidal range is found at T1). This is due to the dependence of friction on the amplitude of the tidal flow. Differences of the relative tidal range between T1 and T2 arise from the effects of the channel convergence.

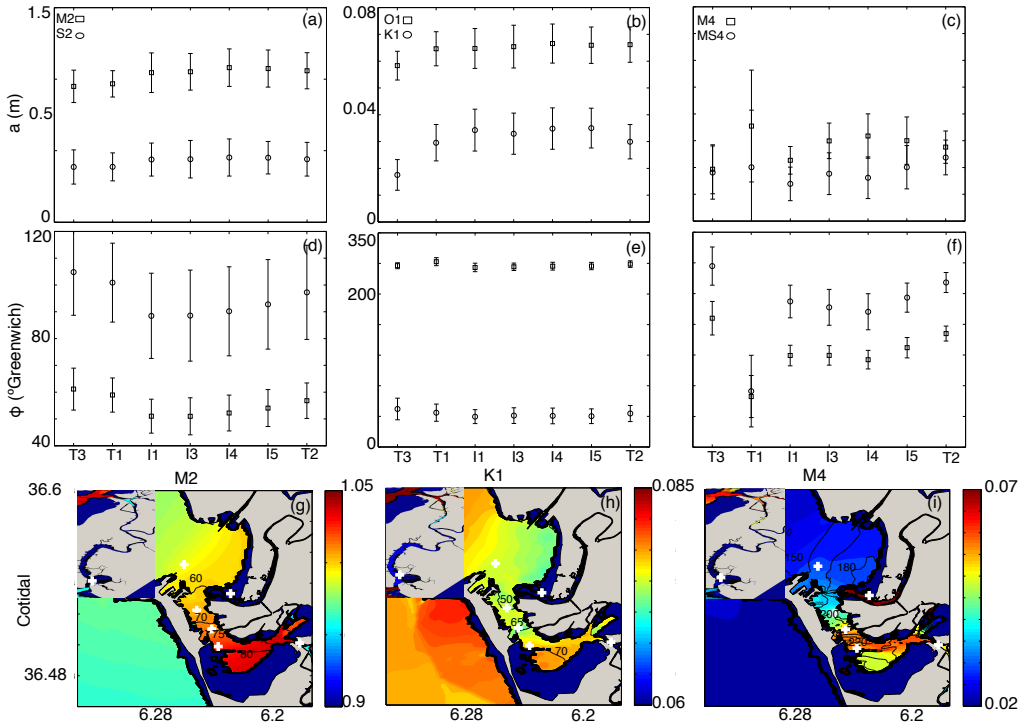

Figure 5.2: Spatial variation of the amplitudes (a) (first row) and phases (ϕ) (second row) of each indicated tidal component obtained from the harmonic analysis. The error bars in amplitudes and phases represent the 95% confidence interval. The amplitude and phase fields of the tidal elevation obtained from the Delft3D model are shown in the third row. White crosses indicate the instrument locations. The first, second and third columns show semidiurnal, diurnal and quarter-diurnal tidal information, respectively.

The spatial variability of the amplitude and phase of each tidal constituent provide additional insight of the transformation processes (Figure 5.2). The first and second rows of Figure 5.2 correspond to the observed data. The third row shows the Delft3D results. As expected, the semi-diurnal species are the most energetic in the embayment (Figure 5.2, a). Under normal conditions, the embayment is tidally dominated and presumably weakly stratified, because the net freshwater inflow during an M2 cycle is much lower compared to the tidal prism (small Estuary Number), even at the Puntales channel constriction. The amplitude of the semi-diurnal M2 constituent does not show remarkable variations: within the error bars, a slight increase inwards of 2 cm is visible in the M2 component from station I1 to I4, i.e., along the Puntales channel. The along-channel differences are even less pronounced for the S2 component. Similarly to the tidal range, the amplitude at station I5 exhibits, within the error bars, a slight decrease with respect to

those observed along the Puntales channel. The tidal phases (Figure 5.2,-d) grow almost linearly between I2 and I5 (more clearly for semi- and quarter-diurnal tides). Wave celerity ($c \approx 9.7\,\mathrm{m/s}$) is lower than for the shallow water, frictionless case ($c_0 = \sqrt{gh} \sim 10\,\mathrm{m/s}$). Stations T1 and T3, located at secondary tidal channels, recorded lower amplitudes and higher phases than those inside the bay. This is due to the greater friction (lower wave speed) that the tide suffers as it propagates through areas in which the intertidal flats are significant. The behaviour of the diurnal constituents (Figure 5.2,-b), which constitute the second most energetic group, is similar to that found for the semidiurnal ones. The larger wavelengths yield an even lower spatial variation in phase (Figure 5.2,-e).

Part of the wave energy associated with the semi-diurnal constituents is transferred to the quarter-diurnal M4 and MS4 overtides due to non-linear effects (Figure 5.2, c and d). These constituents significantly contribute to the tidal asymmetry, which in turn affects the sediment transport. Overall, the M4 and MS4 amplitudes are mainly generated where the tide shoals. The amplitude ratio $a_{\mathrm{M4}}/a_{\mathrm{M2}}$ ranges from 0.021 to 0.034, exhibiting its greatest value near the San Pedro estuary mouth at T1 (0.034). These values are similar to the ratios obtained for many other estuaries, or specific stretches of estuaries (Friedrichs and Aubrey, 1988; Blanton et al., 2002; Díez-Minguito et al., 2012). Higher ratios are expected in tidal creeks and tidal flats. The relative phase difference $2\phi_{\mathrm{M2}} - \phi_{\mathrm{M4}}$ (Aubrey and Speer, 1985) is not greater than 180° in all of the stations, which suggests that the tide has flood-dominant characteristics.

The co-amplitude and co-phase charts obtained with the Delft3D model are consistent with the local measurements (Figure 5.2, third row). The M2 amplitude experiences a slight increase as it propagates inwards (Figure 5.2,-g). The tidal phases grow from the outer to the inner bay from 50° to 90°, which represents 1.38 hours. The amplitude of the diurnal constituent K1, however, attains its minimum value in the outer bay and Puntales channel (Figure 5.2, h). The propagation time in this case, 20°, is lower than for the M2 component. This is consistent with a larger wave-length. Contrary to the semidiurnal and diurnal constituents, the maximum amplitude and phase for the constituent M4 component (Figure 5.2,-i) is attained near I5, where shoaling occurs and the friction is greater. The magnitudes are approximately 0.065 m and 240°, respectively.

Maps showing the tide amplitude and current amplitude for the main constituents, M2 (upper) and M4 (down), are presented in Figures 5.3 and 5.4. These maps are in agreement with those presented in (Álvarez et al., 1999; Periáñez et al., 2013). These data are from an harmonic analysis. The observations give amplitudes about 1 mm higher than the model in the deep and shallow stations, respectively. Considering the confidence intervals, the maximum (relative) difference between both sets of parameters varies from 2% in both of them (here they are not represented). The phases compare even better, returning a complete coincidence within the confidence intervals.

Upper left and right panels in figure 5.3 shows the amplitude and phase of M2. The tide amplitude descends by a few cm (80 %) from the bay connection with the creeks ($0.75\,m$) towards the connection ($0.3\,cm$) between Sancti-Petri and Carraca, this behaviour is confirmed by previous studies (Vidal, 2002). However, the maximum values of the amplitude is reached at the mouth of Sancti-Petri creek ($0.9\,m$), from there the amplitude descend to surroundings. The average phase in the deep area (mouths of the creeks),

less influenced by bottom friction and therefore more representative of tidal circulation, is close to 270° where the external tide behaves like a standing wave. On the contrary, the maximum phase are observed in the area lees deep. Phase lag of M2 along the main channel is about 2:27 h from the mouth to 5 km inland.

Upper left and right panels in figure 5.4 shows the amplitude and phase of M4. M4 is caused by the asymmetric distortion of the tide curve typically seen in shallow water, has generally ben totally attributed to the classical shallow-water terms, but it will be seen that in fact there is also a frictional contribution. M4 increase from an amplitude of 0.02 m at the bay and Atlantic Ocean to 0.16 m, where the bathymetry changes abruptly. The behaviour of the phases along the two creeks is very different, due to the width of the section and the change of the depth. In the case of the Sancti-Petri creek, the phase increase quickly (from 220° to 350° in 4 km), although this value is reduced until 60%. Carraca creek increase, from its mouth, 300° in 6 km.

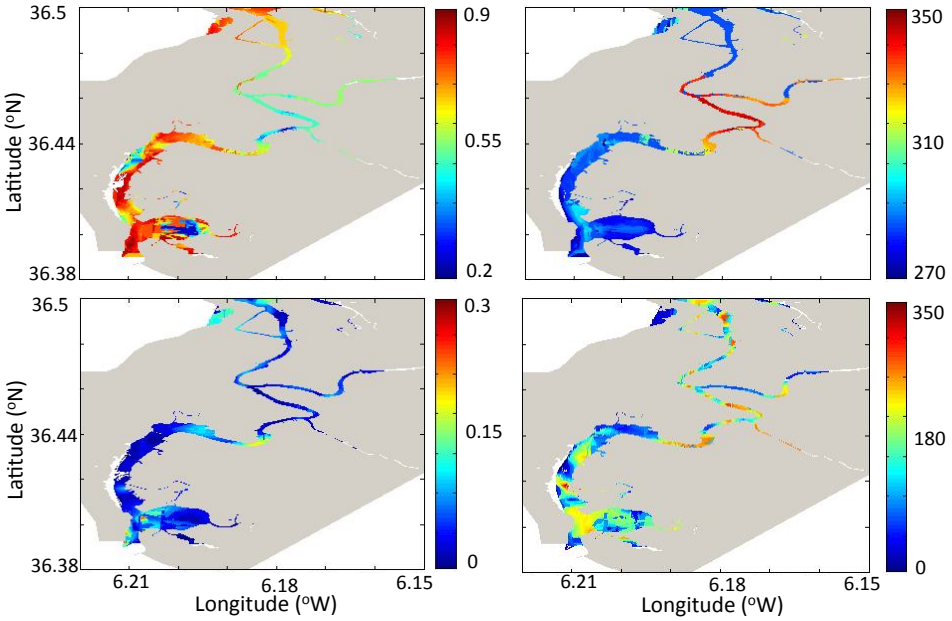

Figure 5.3: Spatial variation of the M2 constituents, amplitudes (a(m), u_a(m/s)) (upper-left, down-left) and phases (ϕ(°), u_ϕ(°)) (upper-right,down-right) of each indicated tidal component obtained from the harmonic analysis. The error bars in amplitudes and phases represent the 95% confidence interval.

5.2.2 Tidal Currents

At stations I1, I3 and I5 the depth-averaged tidal currents ($\underline{\mathbf{u}}$) are mainly aligned with the channel axis, which constricts the along-channel tide propagation. The principal orientation at I4 deviates from the channel axis 40° anticlockwise due to the abrupt change of depth where the channel connects with the inner bay, i.e., between areas B and C.

The maximum depth-averaged currents are measured at I3 on February 22 with values of 0.87 m/s, where the minimum is observed at I5 (0.009 m/s), as measured on February 29. This represents a reduction of almost a factor of $\sim$ 100. The same occurs if the whole

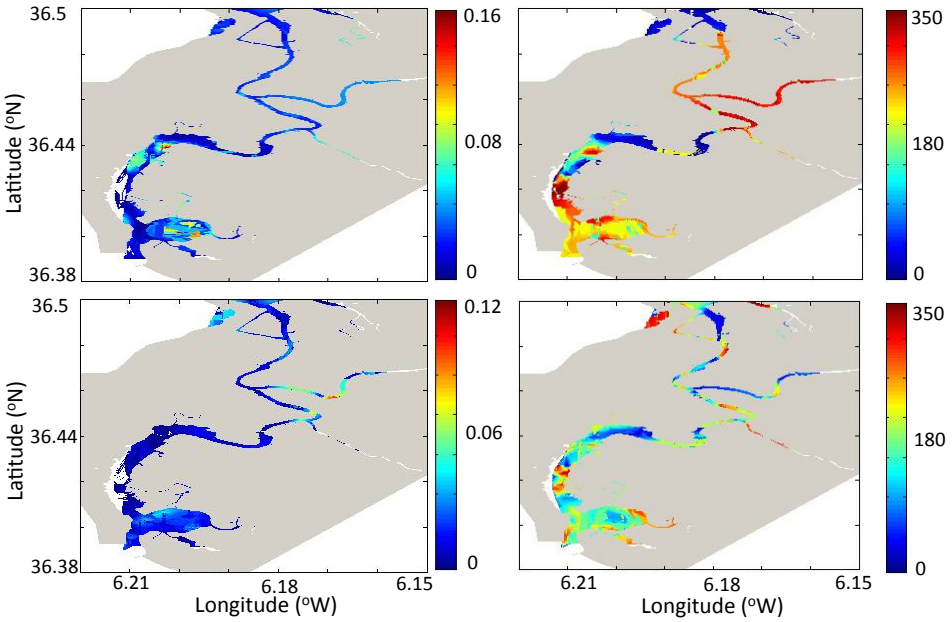

Figure 5.4: Spatial variation of the M2 constituents, amplitudes (a(m),u_a(m/s)) (upper-left, down-left) and phases (ϕ(°),u_ϕ(°)) (upper-right,down-right) of each indicated tidal component obtained from the harmonic analysis. The error bars in amplitudes and phases represent the 95% confidence interval.

interval is analyzed. The highest velocities are normally measured in the central sector: 0.36 m/s, at I3; 0.26 m/s at I1; and 0.24 m/s at I2. Thus, there is flow acceleration (deceleration) as the tide enters (leaves) the inlet.

The tidal excursion, defined as the lagrangian displacement of a fluid parcel by the tide (Bart Chadwick and Largier, 1999), ranges from 2 to 6 km. Because the tidal excursion is on the order of the length of the Puntales channel, and assuming that the main displacement is produced along the Puntales channel, (first-order) tidal movements are barely able to exchange water and solutes between the inner and outer bay at each tidal cycle.

The velocity field $\underline{\mathbf{u}}$ is better characterized in terms of the tidal ellipse parameters. These include the semi-major axis, M; the semi-minor axis, m, which indicates whether the current vector rotates cyclonically ($m > 0$) or anti-cyclonically ($m < 0$); inclination, ϵ; and phase, φ. Figure 5.12 shows the parameters for the constituents M2, K1 and M4. The semi-major axis is higher at station I3 and I4 due to the changes of the bathymetry. In particular, the semi-major axis for M2 reaches its highest values around ~ 0.6 m/s. Similarly to what is observed in the inner shelf (Quaresma and Pichon, 2013), the semidiurnal ellipses are cyclonic (anti-clockwise), except at I3. At station I3, approximately in the middle point in the Puntales channel, the rotation is anti-clockwise. This may be due to the negative relative vorticity production in the constriction, as dictated by the conservation of potential vorticity (Carbajal, 2004). The semidiurnal ellipses show eccentricities (calculated as $\sqrt{M^2 - m^2}/M$) larger than 0.9, revealing an almost linear polarization at all stations, as expected in narrow tidal channels. The semidiurnal ellipse inclinations, ϵ, coincide with the channel orientation ($\sim 60°$), except at I4 (see Figure 5.12). The amplitudes associated with diurnal components are sensibly lower, and the ellipses are less eccentric

(∼0.6). Diurnal ellipses are seemingly oriented along-channel, although relatively larger error bars were observed.

The overall picture of the tidal ellipse parameters of the depth-average current is verified with the results of the numerical model (insets in Figure 5.12). Between cross-sections at I3 and I5, the tide propagates along the Puntales channel direction while the current is primarily controlled by the width of the channel cross sections. The simulations show that the irregular boundaries, especially in the channel area, induce important variations in m and ϵ, which are visible in the patchy fields shown in the insets of the second and third row in Figure 5.12. This may explain the changes in m and ε at the different stations. The observed tidal ellipse parameters are, in general, well reproduced by the model.

Tidal elevation and tidal ellipse phases (Figures 5.2 and 5.12) and their relative difference allow for a simple characterization of the oscillatory motion. For the semidiurnal constituents at all stations, the tidal current is near to 90° , which is out of phase with the tidal elevation. This phase difference is typically found in systems in which the tidal propagation is partially standing due to a prominent reflection. However, high water occurs with small differences along the embayment (very low observed wave number) and the amplitudes, which co-oscillate with the inner shelf, do not show remarkable variations ($\eta_{M2}/\partial\eta_{M2}/\partial x = 218.56$ m and $L = 10000$ m, $218.56\,\mathrm{m} \ll 10000\,\mathrm{m}$). This suggests that the $\pi/2$ phase relation is associated with the reduced length of the embayment instead of a prominent tidal wave reflection ((Pethick, 1980; Friedrichs and Aubrey, 1988)). In fact, the inner Bay is characterized by tidal flats and salt marshes, which act as sponge layers for the tides, with mild slopes, and dry out at low water. This prevents a significant wave reflection.

The effect of friction can be clearly perceived in M and m at all stations because their values reduce with depth (not shown for brevity). Phases and inclinations, however, do not show notable variations in the water column; hence, the current structure is predominantly barotropic. The characteristic bottom boundary-layer thickness, estimated by $\delta_{\pm} = \left(2\,K_z/\left(\omega \pm f\right)\right)^{1/2}$, where $+(-)$ stands for the clockwise (anticlockwise) rotation of the ellipse, (Prandle, 1982; Souza and Simpson, 1996) affects the entire water column ($\delta_{\pm} > 18\,\mathrm{m}$ for all components). An interaction with the surface boundary layer is also expected. For instance, for the M2 constituent, the semi-major axis near the surface attains values of 0.4 m/s at I1, 0.56 m/s at I3, 0.42 m/s at I4 and 0.3 m/s at I5.

Figure 5.5 shows the flood and ebb currents during both spring and neap tides. The highest values are attained along the navigation channel, in particular, in the central portion of the constriction where it shoals and the currents converge during ebbs and floods. The Maximum Flood (MF) along-channel current attains values of $-1.7\,\mathrm{m/s}$ ($-1.5\,\mathrm{m/s}$) during spring (neap) tides, whereas the Maximum Ebb (ME) along-channel current exhibits lower values of $1.6\,\mathrm{m/s}$ ($1.3\,\mathrm{m/s}$) during spring (neap) tides, as expected for a flood-dominated estuary in terms of residual velocity.This behaviour is confirmed by the M2 and M4 tidal phases obtained from a harmonic analysis. The magnitude of the current amplitude is similar for the inner and outer portions of the bay ($0.5-0.3\,\mathrm{m/s}$) and slightly larger in the inner bay. As the tide propagates inside the bay ($\sim 3.2\,\mathrm{m}$ at the mouth during a spring tide), the channel convergence yields a small increase in the tidal range (a few

cm/km). The tidal range in the inner bay then decreases as a result of inverse shoaling. Regarding the water exchange between the outer and inner basins, the typical values of the tidal prism (following the equations of Jonge (1992)) are $\sim 5 \cdot 10^6 \mathrm{m}^3$ ($\sim 4 \cdot 10^6 \mathrm{m}^3$) during spring (neap) tides at the cross section where the current magnitudes are measured by the instrument I3. These values assure a poorly stratified water column, even during neap tides.

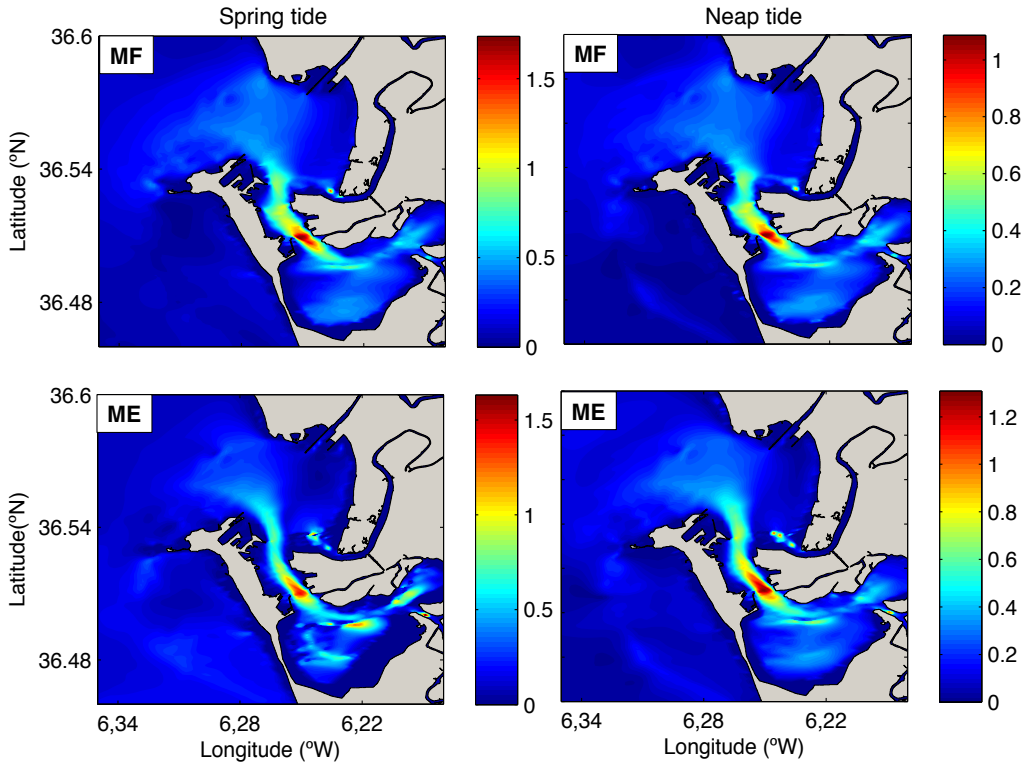

Figure 5.5: Current magnitude field (in m/s) before interventions at the maximum floods during spring tide (upper left panel) and neap tide (upper right panel) and at the maximum ebbs during spring tide (lower left panel) and neap tide (lower right panel).

A standard harmonic analysis was performed (Pawlowicz et al., 2002) on the elevations (first row of panels in Figure 5.6) and currents (second to fifth rows in Figure 5.6) obtained with the numerical model. This analysis is the basis for the analysis of the changes in tidal wave propagation in the Bay of Cádiz.

The amplitudes and phases for the M_2 and M_4 tidal constituents of the elevations (cotidal charts) are shown in panels (a) and (b) in Figure 5.6. As mentioned before, M_2 is the most energetic constituent inside the bay. S_2 was not shown because its spatial variations in amplitude and phase are very similar to those for M_2. Its amplitude attains a value of 1.05 m at the bay mouth. The tidal wave penetrates through the outer bay and along the constriction bay, increasing by 10% from the outer to the inner bay. The second most important components are the diurnals (0.09 m for the K_1 tides at the mouth). However, the variations along the bay are not significant, and the amplitudes are very homogeneous inside the bay (not shown) where only a minor reduction of 2% is observed. Although their amplitudes are lower ($\sim$ 0.06 m), another of the most influential components is quarter-

diurnals due to their implications for sediment transport and non-linear generation. A portion of the tidal wave energy associated with the semi-diurnal constituents is transferred to the quarter-diurnal overtides (M_4, MS_4, MN_4), which remarkably increases towards the inner bay (30%), because of the reduction in depth. Regarding the tidal phases, longer waves propagate faster as expected. The travel time through the bay (from the mouth to the marshes) for the M_2 is 1.5 hours (45°). The largest phase lags are experienced by the M_4 group, which increases above 50°. There is only a small variation in the phases of K_1 (4°) (not shown).

The harmonic constants for the M_2 and M_4 derived from the u and v tidal velocity time series are combined to define the tidal ellipse parameters, namely, the semi-major axis (second row of panels in Figure 5.6), the semi-minor axis (third row), the inclination of the semi-major axis (fourth row) of the ellipse, and the Greenwich phase (fifth row). Larger values of the semi-major axis, Ma, are observed (panels (c) and (d)) for all the constituents near the mouths of creeks and subestuaries and, in particular, along the constriction that connects the outer and the inner portions of the bay (1.2 m/s and 0.25 m/s for M_2 and M_4, respectively). The eccentricity of the M_2 is large (close to 1), because the semi-minor axis amplitudes, ma, are almost two orders of magnitude lower than the Ma values (panel (e)). Because ma exhibits values close to 0, the uncertainty in the sense of the rotation of the ellipse is significant (a positive value of ma indicates a cyclonic or anti-clockwise rotation). Nevertheless, the majority of the ma field is positive, which is consistent with the sense of rotation observed in the adjoining inner shelf (Quaresma and Pichon, 2013). The presence of circulation cells and the production of vorticity (both in panels (e) and (f)) can be identified by the patchy areas where the magnitude of ma increases. These areas are located near irregularities along the coastline and the leeward flow regions. The inclination field (panels (g) and (h)) reflects the complexities of the coastline. Overall, inclinations of approximately 120° (0° E-90° N), following the channel constriction and the Cádiz spit, respectively, dominate inside the bay and at along both sides of the spit. Regarding the tidal phases, it is remarkable that inside the bay, the M_2 current (panel (i)) is approximately 90° out of phase with the tidal elevation (panel (a)). This phase difference is typically found in systems in which the tidal propagation is partially standing. However, high water levels occur with only small differences along the embayment, and the amplitudes, which co-oscillate with the inner shelf, do not exhibit remarkable variation (panel (a)). These findings suggest that the π/s phase relationship is more strongly associated with the reduced length of the embayment instead of a prominent tidal wave reflection.

Down left and right panels in figure 5.3 shows the tidal currents of M2. Maximum tidal currents ($0.22\,m/s$), as should be expected, are found in the narrow channel connecting the Sancti-Petri and Carraca creek. This is likely due to the landward exponential decrease in channel width. There is a steady increase in strength of the M2 tidal current from the mouth of Sancti-Petri to the plain marsh (from $0.05\,m/s$ to $0.15\,m/s$). The values ($0.07\,m/s$) are so similar in the rest of the creeks. An increase in the lag between the slack waters and the maximum and minimum water levels, a result of a smaller reflected wave at the head due to the dissipation of tidal energy (Ippen and Harleman, 1966). Extensive salt marshes are present along the channel and one expects them to extract a large amount of energy from the tide (Blanton, 1969). The presence of overtides in the estuary

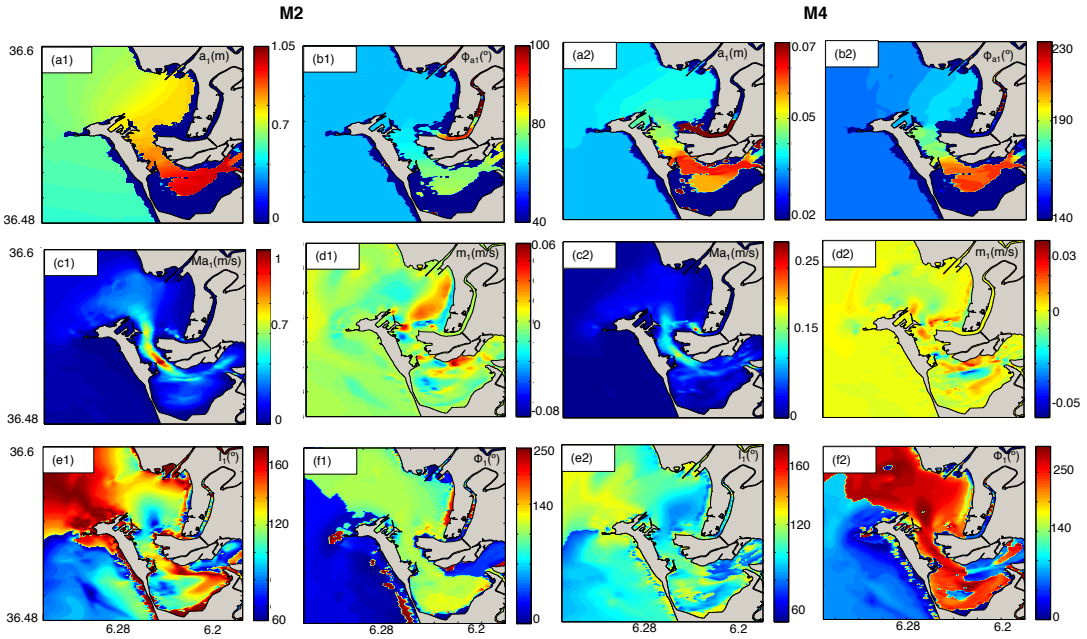

Figure 5.6: Tidal harmonic analysis results before the interventions. Panel 1 (first and second columns) shows the results for M_2 and panel 2 (third and fourth columns) for M_4. The amplitude (m) and phase (°) field of the tidal elevation are labeled in the panels as a and b, respectively. The semi-major axis (m/s), semi-minor axis (m/s), inclination ($0°E$-$90°N$) and phase (°) fields are labeled in the panels as c to f.

changes the duration of ebb and flood currents. The duration of ebb is 5:05 h (3:15 h) whereas the duration of flood current is 6:15 h (5:25 h) at Sancti-Petri (Carraca).

Down left and right panels in figure 5.4 shows the tidal currents of M4. The maximum M4 current are reached at secondary channels $0.1\,m/s$. The values in the rest of the creeks are very regular ($0.02\,m/s$). The results of 2M2–M4 are almost close to 200° at Sancti-Petri creek, which means that there is flood dominance (relatively brief strong flood). On the contrary, in Carraca creek the 2M2–M4 is approximately 91°, where there is ebb dominance (relatively brief strong ebb).

5.3 Tidal Energy Dissipation

Tidal dissipation is estimated by integrating the energy flux associated with the horizontal velocities (Gill, 1982), i.e. $E = \left(p + \rho_0 \frac{u^2+v^2}{2}\right) \cdot \mathbf{u}$, over a control volume $\mathscr{V}$ bounded by the surface $\mathscr{S}$ and averaging over the M2 tidal cycle (12.42 h). The tidal dissipation, R, reads as follows:

$$R = \iint_{\mathscr{S}} \langle E \rangle \, dS = -\rho_0 C_D \left\langle |\mathbf{u_b}|^3 \right\rangle S - \rho_0 K_z \left\langle \int_{-h}^{\eta} \left[\nabla_z^2 \underline{\mathbf{u}}\right] dz \right\rangle S - \rho_0 \iiint_{\mathscr{V}} K_{xy} \left\langle \left[\nabla_{xy}^2 \underline{\mathbf{u}}\right] \right\rangle dV \quad (5.1)$$

where the brackets denote the tidal average, ∇^2 denotes the laplacian operator and $\underline{\mathbf{u}}$ denotes the depth-averaged horizontal velocity. This equation demonstrates that there is a balance between the mean energy fluxes normal to the volume surface $\mathscr{S}$ (i.e., through the open boundaries of the Bay) and the mean energy dissipation (right-hand side terms).

The dissipation energy was calculated between stations I1 and I3. $\rho_0 = 1024\,\mathrm{kg/m^3}$ is the reference density measured at station I1. The dissipation of barotropic tidal energy contains three parts, of which the first term of the R.H.S of Eq. 5.1 represents the dissipation due to shear stresses at the bottom layer. A no-slip condition and the quadratic friction law were assumed. The bottom velocity $\mathbf{u_b}$ was computed at the deepest point with available data, typically between 1 m and 2 m above the bottom at each current profile. The drag coefficient C_D was estimated using the depth-averaged equation for the along-channel momentum and numerically integrated using field data (Díez-Minguito et al., 2012) (see Appendix A).

The second and third terms of the R.H.S. of Eq. 5.1 account for the dissipation of energy by vertical and horizontal dispersion, respectively. Horizontal shear stresses were estimated by finite differences at the stretch defined between I1 and I3. The coefficient K_{xy} is the horizontal eddy viscosity, and u and v are the velocity components across- and along-channel, respectively. Similarly, the vertical derivatives were estimated at those stations. The integrals in Eq. 5.1 were also discretized according to the spatial and temporal resolution of the data. In this work, the exchange coefficient is considered to be spatially uniform. The eddy viscosity coefficient, K_z, is simply estimated by fitting the theoretical vertical current profiles induced by wind Hansen and Rattray (1965) to the observed detided current profiles (see Appendix B). The fitted values of K_z range from $\sim 10^{-1}\,\mathrm{m^2/s}$ to $10^{-3}\,\mathrm{m^2/s}$. According to Dyer (1997), $K_{xy} = 10^{-2}\,\mathrm{m^2/s}$ is assumed.

We only consider the energy flux due to the work done by the pressure force associated with barotropic tidal motion. The advective contribution will be neglected because it is two orders of magnitude smaller than the barotropic flux (Zhong and Li, 2006). Thus, the depth-integrated energy flux per unit length can be provided by

$$\mathbf{F} = \left(F_x,\, F_y\right) = \rho\, g\, h \langle \underline{\mathbf{u}} \eta \rangle \tag{5.2}$$

where g is the gravity acceleration and h is the water depth. The bold fonts stand for vectors. Notice that the dimensional relationship in magnitude between the tidal dissipation and the depth-integrated energy flux is $\mathrm{F} = \dfrac{\mathrm{R} * \mathrm{S}}{\mathrm{L}}$, where S is the surface area and L is the distance between points. For the along-channel and cross-channel components (F_y and F_x, respectively), positive (negative) energy fluxes are outwards and eastward (inwards and westward), respectively.

Drag coefficient. The drag coefficient C_D is estimated using a semi-analytical model, in which the depth-averaged equation for the along-channel momentum is numerically integrated using the field data (Díez-Minguito et al., 2012). The model equation is derived assuming a balance between the local acceleration, the horizontal

pressure gradient and the vertical turbulent stress gradient, ignoring the convective terms. The equation reads as follows:

$$\frac{\partial(\eta+h)\underline{u}}{\partial t} - u(\eta)\frac{\partial \eta}{\partial t} + \frac{g(\eta+h)^2}{2\underline{\rho}}\frac{\partial \underline{\rho}}{\partial x} + g(\eta+h)\frac{\partial \eta}{\partial x} = \frac{1}{\underline{\rho}}\tau_b \tag{5.3}$$

where $u(\eta)$ is the along-channel current evaluated at the free surface. The bottom friction can be expressed in terms of the depth-averaged horizontal velocity and a constant drag coefficient, C_D, as $\tau_b = \underline{\rho} C_D \underline{u}|\underline{u}|$.

The temporal evolution of the tidally averaged drag coefficient, C_D, is shown in Figure 5.8. This result was obtained between stations I1 and I3, and therefore should be considered representative of the tidal propagation in that stretch. The range of the values obtained is $10^{-3} \leq C_D \leq 15 \cdot 10^{-3}$. The mean value is similar to those obtained in other studies in Cádiz Bay (Álvarez et al., 1999). The analysis of the Equation (5.3), from which C_D was estimated, showed that friction apparently balances the barotropic pressure gradient. This is consistent with a dynamically short estuary. The order of magnitude of the horizontal pressure gradient, $g(\eta+h)\partial\eta/\partial x$, is $\sim 1.4 \cdot 10^{-3}\mathrm{m}^2/\mathrm{s}^2$. The friction term is of the same order of magnitude, $\sim 10^{-3} m^2/s^2$, which dominates over the inertial terms, whose amplitudes do not exceed $\sim 5 \cdot 10^{-4}\mathrm{m}^2/\mathrm{s}^2$. The barotropic density gradient does not contribute significantly to the momentum equation, with a value of $\sim 3 \cdot 10^{-5}\mathrm{m}^2/\mathrm{s}^2$.

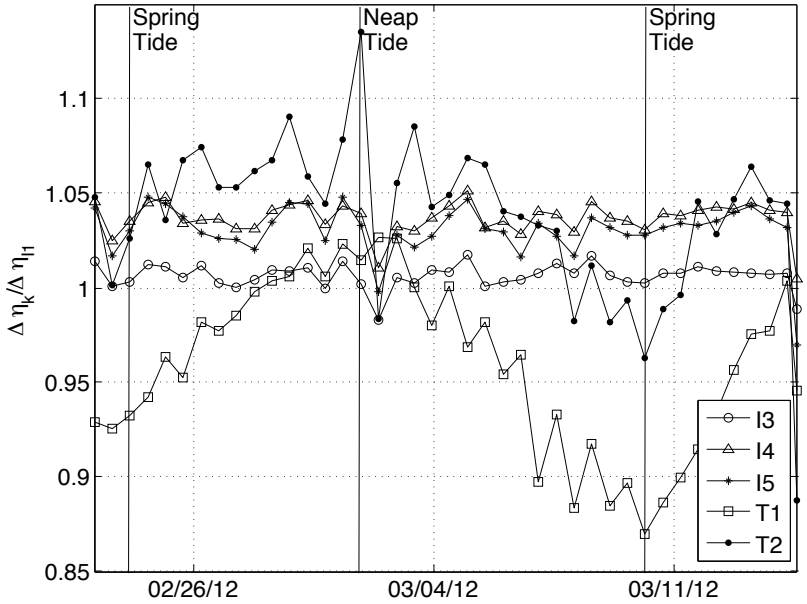

Figure 5.7: The ratio between the tidal range at stations I3 (circles), I4 (triangles), I5 (asterisks), T1 (squares) and T2 (dots), and the tidal range at I1, i.e. $\Delta\eta_k/\Delta\eta_{I1}$, where $k = \{I3, I4, I5, T1, T2\}$.

Vertical Eddy Viscosity Coefficient. The eddy viscosity coefficient, K_z, is simply estimated following the well-known stationary approach of Hansen and Rattray (1965)

$$\langle u \rangle(\xi) = \frac{\tau_w h}{\rho K_z}\left(\frac{3}{4}\xi^2 - \frac{1}{2}\xi\right), \tag{5.4}$$

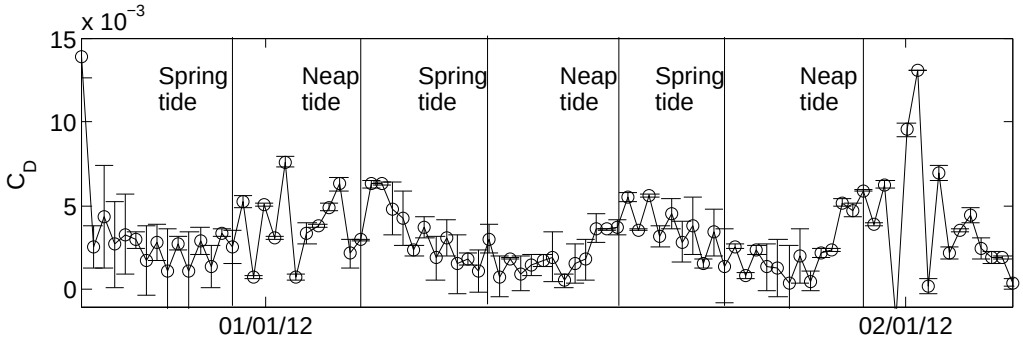

Figure 5.8: Temporal evolution (sub-tidal variations) of the drag coefficient C_D measured between station I1 and I3.

where $\xi = z/h$ is the normalized water depth, $z \in (-h, \langle\eta\rangle)$ and $\tau_w = \rho_a C_d |w| w$, being $\rho_a = 1.2\ kg/m^3$ and $C_d = 1.4 \cdot 10^{-3}$. The eddy viscosity coefficient K_z is estimated by fitting Eq. 5.4 to the observed tidally-averaged baroclinic current profiles at moorings I3.

5.3.1 Mean Tidal Energy Flux

The total amount of tidal energy that penetrates through the constriction from the adjacent shelf can be estimated by the energy flux at the monitoring stations using Equation 5.2. The energy flux is calculated using the time series of the currents and levels. Figure 5.9 shows the temporal evolution of the depth-integrated energy flux per unit channel length, $\mathbf{F} = (F_x, F_y)$, at I1, I3, I4 and I5. Their magnitudes are lower (higher) for neap (spring) tides at all of the stations, including the Puntales Channel. Diurnal oscillations can also be observed to be associated with the diurnal inequality. During neap tides, this variation is below $4.5 \cdot 10^3$ kW, whereas during spring tides, values lower than 6 kW/m are recorded. The along-channel components are the highest. At the outermost station, I1 (first panel), the fluxes are directed seaward most of the time. This behaviour, which is induced by the phase differences between elevations and (depth-averaged) currents, differs from that at the other stations. The energy flux, F_x, is normally directed inwards (negative) at stations I3-5, but can reverse during neap tides (stations I3 and I5). The net energy fluxes observed during the field survey were -5.11 kW/m and -5.5 kW/m at I3 and I4, respectively. These two stations exhibit the greatest values because of the energy concentration in the channel, which yields higher current ranges. The magnitude of the energy flux vectors are weaker both inside the outer (2.08 kW/m at I1) and the inner basins (-2.5 kW/m at I5). This is directly related to the magnitude of the horizontal currents at each station. Regarding the net across-channel tidal energy, the highest values are observed at I1 (-4.50 kW/m) and the lowest at I5 (-0.13 kW/m). The integrated (from cross-section I1 to I3) and time-average energy flux during the whole analysis interval is $-71 \cdot 10^3$ kW. This set of values is close to the observations and numerical estimations by previous studies (Álvarez et al., 1999; Kagan et al., 2001, 2005). The behaviour exhibited by the energy fluxes is closely related to the Stokes transport (see Eq. 5.2), which in turn influences transport of salt and other substances as in many other estuarine environments (Bowen and Geyer, 2003; Becker et al., 2009; Díez-Minguito et al., 2013).

Figure 5.10 (lower panel) shows that the highest dissipation per unit surface occurs during spring tides, which is related to the generation of the horizontal and vertical dispersion induced by higher energy fluxes. Energy dissipation for neap tides is typically $R \approx -1 \cdot 10^{-3}\,\mathrm{kW/m^2}$, with a much lower magnitude is than for spring tides ($-5 \cdot 10^{-3}\,\mathrm{kW/m^2}$). The negative sign indicates an energy loss. The obvious effect of the tidal energy dissipation is the reduction of tidal currents. The dissipated energy also increments the water temperature and destabilizes the water column, thus reducing stratification. The latter is often quantified by means of the Richardson number $Ri = -g/\rho_0 \left(\partial\rho/\partial z\right) \sqrt{(\partial u/\partial z)^2 + (\partial v/\partial z)^2}$, which expresses a ratio between the stabilizing effect of freshwater input and the vertical shear that favors mixing. The density data of the water column are not available (only near bottom), although the high dissipation rates and lower depths reinforce the hypothesis that the water column is poorly stratified under normal conditions. The Delft3D simulations show that energy dissipation is rather non-uniform in Cádiz Bay, as shown in Figure 5.10. The highest dissipation is attained near the thalweg an, in particular, where significant bathymetric changes occur.

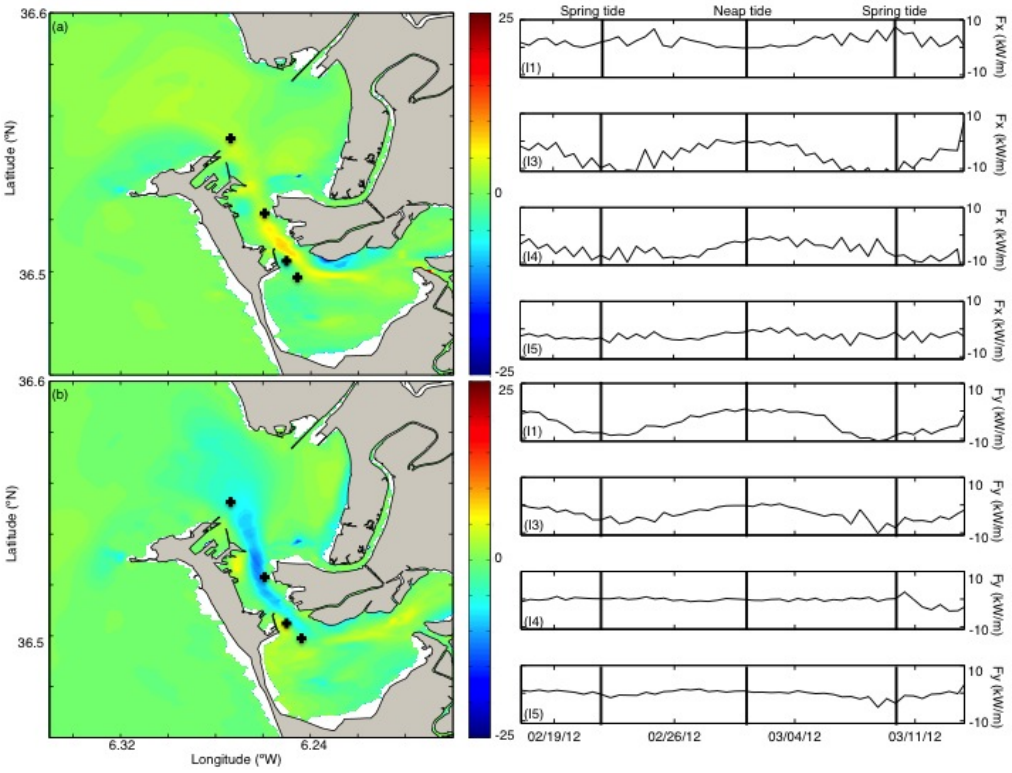

Figure 5.9: Right panels: Spatial evolution of the along- (up (a)) and across-channel (down (b)) depth-integrated period-averaged barotropic energy flux per unit length. Left panels: Temporal evolution of the along- (up (I1–$I5$)) and across-channel (down (I1–$I5$)) depth-integrated barotropic energy flux per unit length. Positive (negative) F_x values indicate an outwards(inward) direction. Positive (negative) F_y values iindicate and eastward (westward) direction.

The surface integral of the first and second terms of the R.H.S. of Eq. 5.1 over the Bay sea surface attains 96.7 % of the net tidal energy dissipation. The horizontal diffusion (third term of the R.H.S. of Eq. 5.1) contributes 3.3 %. Note that the net tidal energy dissi-

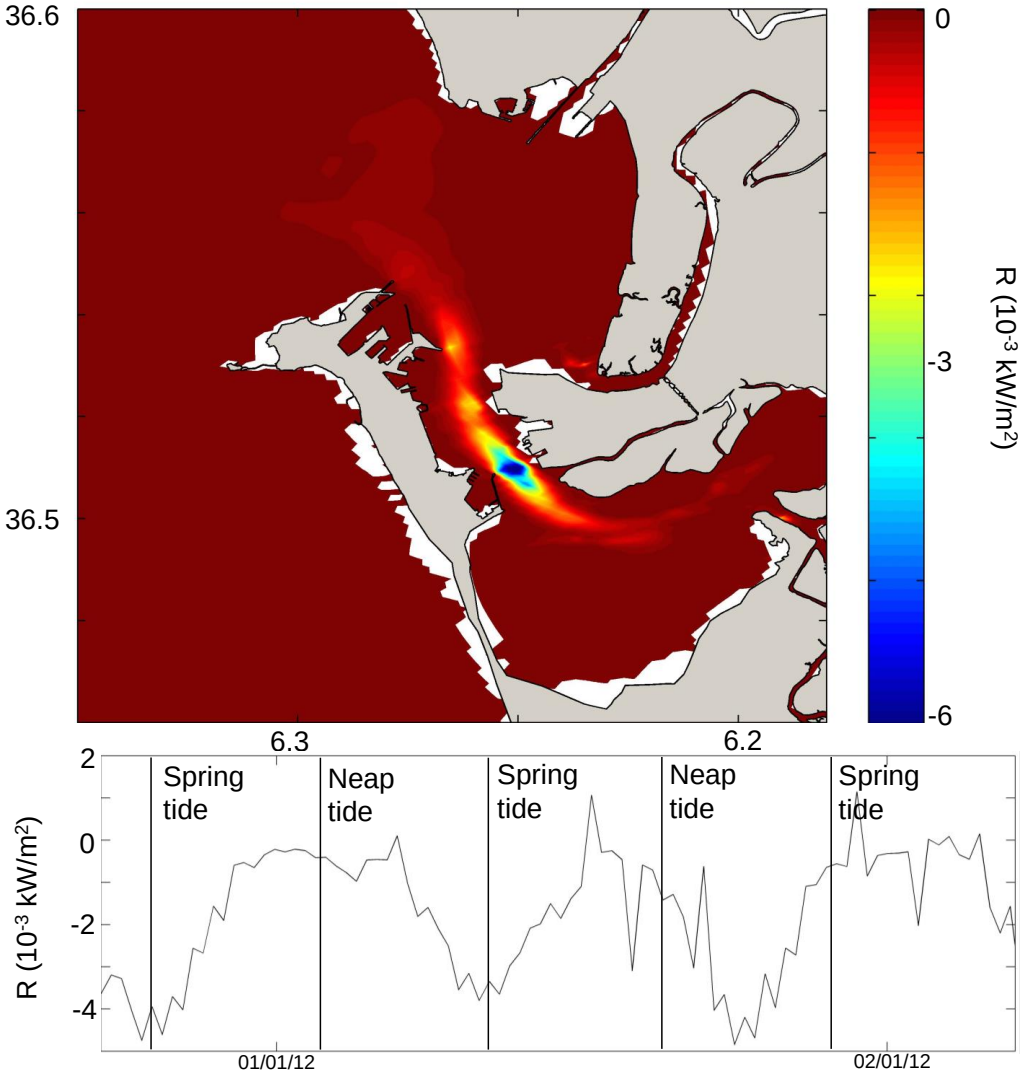

Figure 5.10: Tidal dissipation evolution, R, during the field survey. Upper panel: Spatial (mean) distribution of R. Lower panel: Temporal evolution of the mean dissipation energy, R, measured between stations I1 and I3. The negative sign indicates loss of energy.

pation at (e.g.) spring tides reaches $-60 \cdot 10^3$ kW (Figure 5.10, lower panel). As expected, this value is 15 % lower than the net energy transported by the tidal wave.

The previous sections show that the model can accurately simulate tidal elevations and tidal currents in Cádiz Bay. The model is employed to calculate the amount of the tidal energy flux entering the Bay mouth and assess the energy dissipated inside the Bay. The energy flux is calculated using the 30-day time-average series of currents. The cross- (along-) channel component is 2.2 kW/m (-4.5 kW/m), which is slightly larger than the measured data. The highest values are again reached in the central sector, where there are more abrupt changes in the bathymetry (see first column, Figure 5.9). In the central section, the energy flux is higher on the eastern shore, presumably because of the higher tidal range there. The energy flux of the I1 cross- (along-) channel component is calculated as 2.5 kW/m (-5 kW/m).

Figure 5.11 shows the temporal evolution of the depth-integrated energy flux per unit channel length, F = (Fx; Fy). In the left panel of the figure 5.11, it is represented the flux of energy along-channel. The positive (negative) values correspond when the water comes from (mouths in) the bay or Ocean. The highest values are reached in the maximum depths (4000 kW/m). In Sancti-Petri creek, two points are observed very close with different sign. It can be due to the difference between incident and reflected wave. The lost energy can be used to mix the water column or to move the sediment. For that reason it has been analyzed the flux energy associated to the M2 and M4 constituents (Figure 5.11). There is the same behaviour in both cases, where convergence points are observed. On the other hand, the maximum value reached to the mouth of the Carraca creek (-1000 kW/m).

In the left panel of the figure 5.11, it is represented the flux of energy cross-channel. The negative (positive) values correspond to the western (eastern). The highest values are reached in the highest section (2000 kW/m), in the mouth of the Sancti-Petri creek. In the rest of the creeks, the energy flux are so close to 0, de to the minimum width (L»W). The dissipation of tidal energy near the connection between both creeks due to the abrupt change in M2 and M4 current amplitude.

$$q_{res} = \int_0^{T_{M2}} q \, dt$$

5.4 Exchange between Outer and Inner Bay

The main driving force for the (barotropic) water exchange between the outer and inner basins at short time-scales is the sea level gradient induced by astronomical tides. The exchanged water transport through the cross-section, defined as $Q = \int_0^B \int_{-h}^{\eta} u \, dz dy$ (see panel 4 in Figure 5.1), mimics the tidal flow following the ebb-flood and spring-neap cycles. During spring (neap) tides, V_e ranges between $3.5 \cdot 10^8$ m^3 ($1.53 \cdot 10^8$ m^3) and $-3.5 \cdot 10^8$ m^3 ($-0.83 \cdot 10^8$ m^3/s). The comparison between these values and the overall freshwater inflow, which is normally on the order of ~ 20 m^3/s, again demonstrates the tidal dominance. The exchange processes are thus normally dominated on an intratidal scale by tidal action. In a wider context, the order of magnitude of the observed tidal transports

Date	$W(^\circ)$	$W(\mathrm{m/s})$	$\langle V_v, V_{res} \rangle$	τ (tidal cycles)
02/02 (1a)	SE	4.5	0.30	9
04/13 (1b)	SE	8.5	0.70	0
01/08 (2a)	NW	4.5	0.48	12
03/27 (2b)	NW	10	0.69	0

Table 5.1: Correlations between wind and the residual volume. The event identification is indicated after the date.

(or tidal prisms) in Cádiz Bay are similar to those in the Ems estuary (Jonge, 1992) and San Diego Bay (Bart Chadwick and Largier, 1999), for instance.

The residual water volume is evaluated from the difference between flood and ebb tidal prisms ($V_{\mathrm{res}} = V_{\mathrm{res,flood}} - V_{\mathrm{res,ebb}}$, Jonge (1992)). The exchanged volume between the inner and outer areas (panel 5 of Figure 5.1) are lower, and the residual contribution of wind, tides and, to a minor extent, density gradients can be determined. Within the field survey period, the values of V_{res} are observed between $1.86 \cdot 10^7\,\mathrm{m}^3$ and $-3.45 \cdot 10^8\,\mathrm{m}^3$, with an overall mean of $-3.95 \cdot 10^5\,\mathrm{m}^3$ (V_{res} positive is seaward). The main driver of the residual exchange is the wind forcing (panels 2 and 3 of Figure 5.1), which apparently exceeds the contribution of the tidally induced asymmetries. At the residual scale, the larger exchange inflows are attained approximately one week after strong NW winds (end January, end March 2012). Outflow is normally associated with SE winds (from February to mid-April 2012). This behaviour can be quantified with the non-zero lag cross correlation between wind and residual water transport time series. When the wind blows from the SE, the residual ebb volume is stronger than the flood volume, (Table 5.1 and Figure 5.1; hereinafter 1a and 1b). However, if the wind comes from the NW, the residual flood transport is dominated by the residual ebb volume (Table 5.1 and Figure 5.1; hereinafter 2a and 2b).

The non-zero lag cross correlations between these variables denoted by $\langle \cdot, \cdot \rangle, (\tau)$ are significant (Table 5.1). There is a high correlation (~ 0.7) between the residual volume and high wind velocity (1b, 2b) at the zero time lag. The correlation (~ 0.4) is lower in cases 1a and 2a, due to the lower wind velocity. The time lag in the volume residual occurs 9-12 tidal cycles after the changes in wind velocity.

5.4.1 Residual water volume exchanged through the cross-section at creeks

During the flood tide, flows entering the site are restricted to the confines of the main channel. The flood flows increase in relation to the rapid increase in tidal prism, and the mudflat become inundated. During the initial part of the ebb tide, water drains in sheet flow from the marsh to the main channel. On neap tides, the marsh plain lacks tidal inundation for several consecutive days. The residual water volume is evaluated from the difference between flood and ebb tidal prisms ($V_{\mathrm{res}} = V_{\mathrm{res,flood}} - V_{\mathrm{res,ebb}}$, Jonge (1992)). Figure 5.13 shows the residual water volume exchanged through the cross-section at creeks. In black color is represented the values of Sancti-Petri creek, where are observed the predominance of the flood flow. The values of V_{res} are observed between $8 \cdot 10^5\,\mathrm{m}^3$ and $-10 \cdot 10^5\,\mathrm{m}^3$, with an overall mean of $-8 \cdot 10^5\,\mathrm{m}^3$ (V_{res} positive is seaward). In red color is

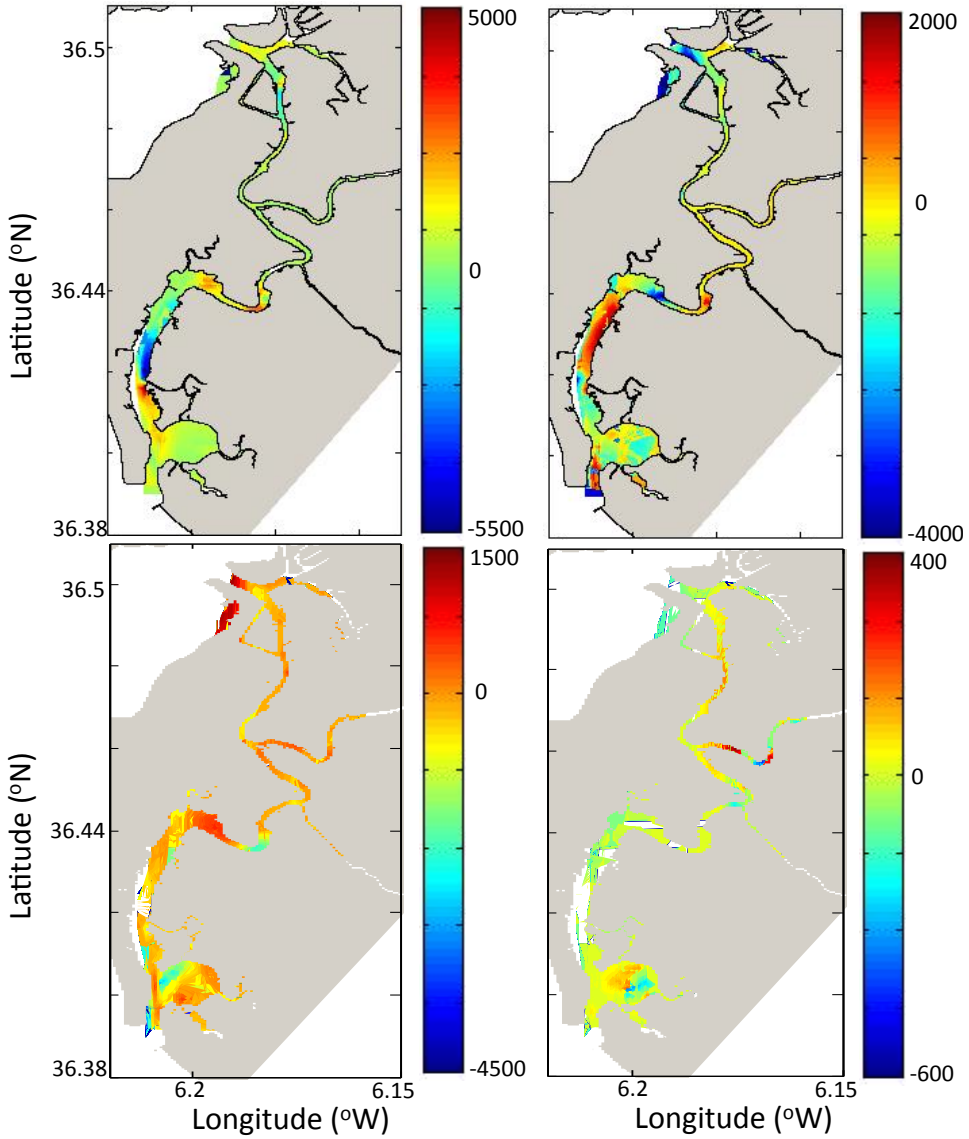

Figure 5.11: Spatial evolution of the depth-integrated period-averaged barotropic energy flux per unit length (kW/m). First row correspond to the the along- (left) and across- channel (right) energy flux; second row correspond to the the energy flux per unit length associated to M2 (left) and M4 (right) constituent.

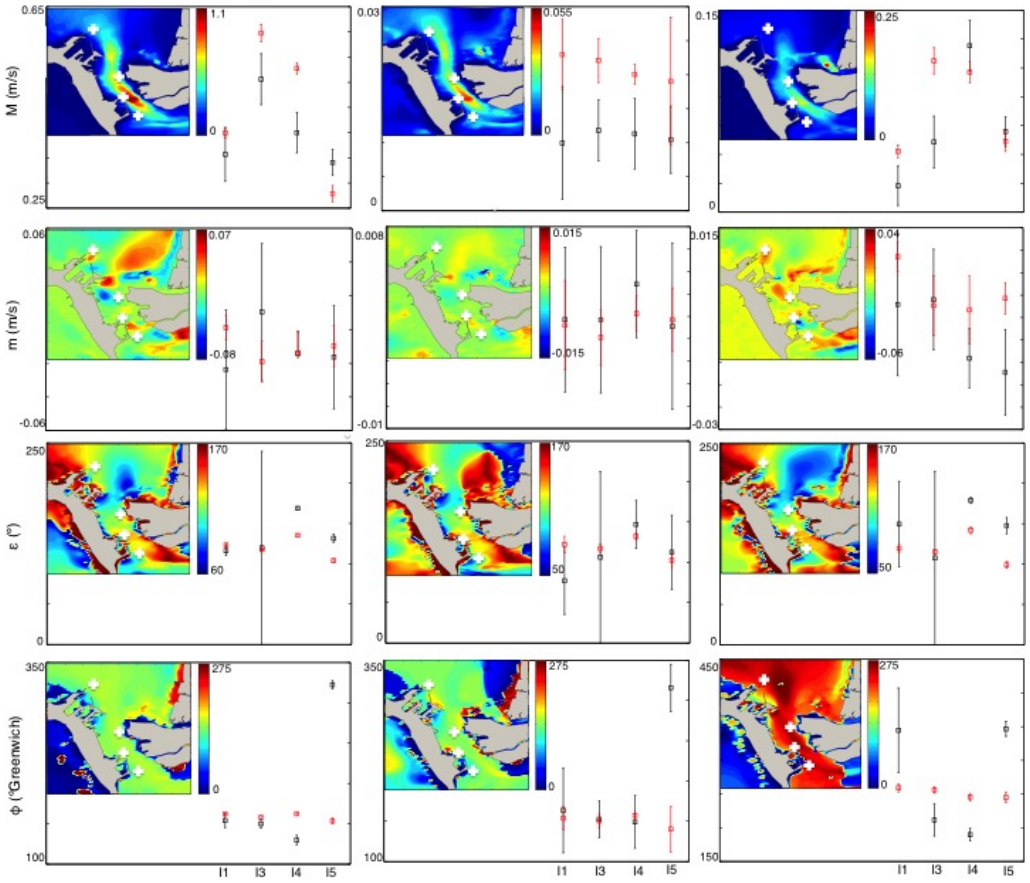

Figure 5.12: Tidal ellipse parameters of the depth-average current field. The first, second, third, and fourth rows show, respectively, the semi-major axis, semi-minor axis, inclination (respect to E-W direction), and phase for the M2 (first column), K1 (second column) and M4 (third column) constituents. The black (red) symbols correspond with observed (modeled) data. Tidal ellipse parameters from the DELFT3D simulations are shown in the insects. White crosses in the insects indicate the instrument locations.

represented the values of Carraca creek, where are observed the absolutely predominance of the ebb flow. The values of V_{res} are observed between $8 \cdot 10^5\,m^3$ and $5 \cdot 10^5\,m^3$, with an overall mean of $6 \cdot 10^5\,m^3$ (V_{res} positive is seaward).

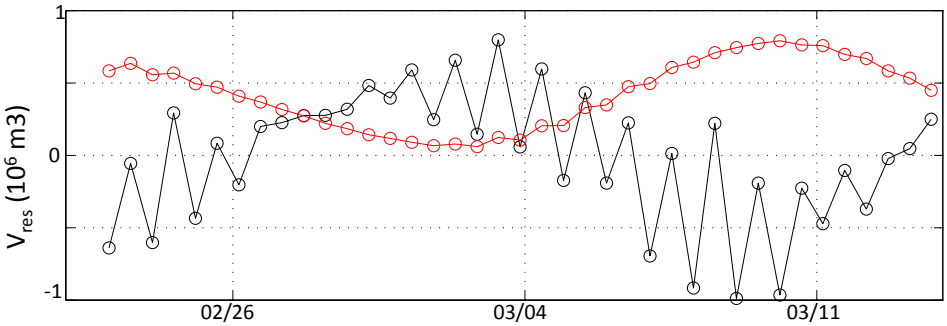

Figure 5.13: The residual water volume exchanged through the cross-section at Carraca (red) and Sancti-Petri creek (black).

Chapter 6
Morphodynamics of the tidally-dominated bay

This chapter analyzes the morphologic evolution of the Bay of Cádiz. Firstly, we focus on the tidal asymmetry and current magnitude to analyze the residual sediment transport pattern; for this analysis we use the model by Carniello et al. (2005) described in Chapters 3 and 4. In particular the relation between dynamical mechanisms and the bed form patterns predicted by this model will be investigated. These results were published in Zarzuelo et al. (2015a).

6.1 Introduction

The first part of this Chapter presents modeled tidal flow patterns in order to correlate the changes in the hydrodynamics with the sediment patterns. Next, the morphodynamics is analyzed in terms of the sediment transport patterns, month-averaged transport magnitudes and its governing mechanisms. Finally, the results on the influence of the wind effects on sediment dynamics are presented. In Figure 6.1, the three areas (A, B and C) of the Bay of Cádiz are defined.

6.2 Flow patterns and residual flow

Figure 6.2 (a) shows the residual transport magnitudes for the study site. Residual transports are estimated by time-averaging in each tidal cycle. The largest values ($\approx 1.3\,m^2/s$) are observed in the navigation channel. Other local maxima are located at the Carracas and Santi-Petri Creek and along the channel ($\approx 0.8\,m^2/s$) where the bathymetry deepens and has abrupt changes. The residual circulation pattern (Figure 6.2 (b)) indicates that the inner and outer basins operate rather independently. A remarkable feature of the residual transport vector field is the development of vortices in areas A, B and C. In all cases, the vortices (orange circle) extend to the maximum possible surface without significant changes in depth (submerged plains). Their diameters are on the order of $\sim 1.5\,km$, $\sim 0.8\,km$, and $\sim 3\,km$ for the A, B and C basins, respectively, and rotate clockwise. This behaviour concurs with the one observed in other estuaries (Robinson, 1981; Velasco Fuentes and Ochoa, 2003; Serrano et al., 2013; Nayak et al., 2014).

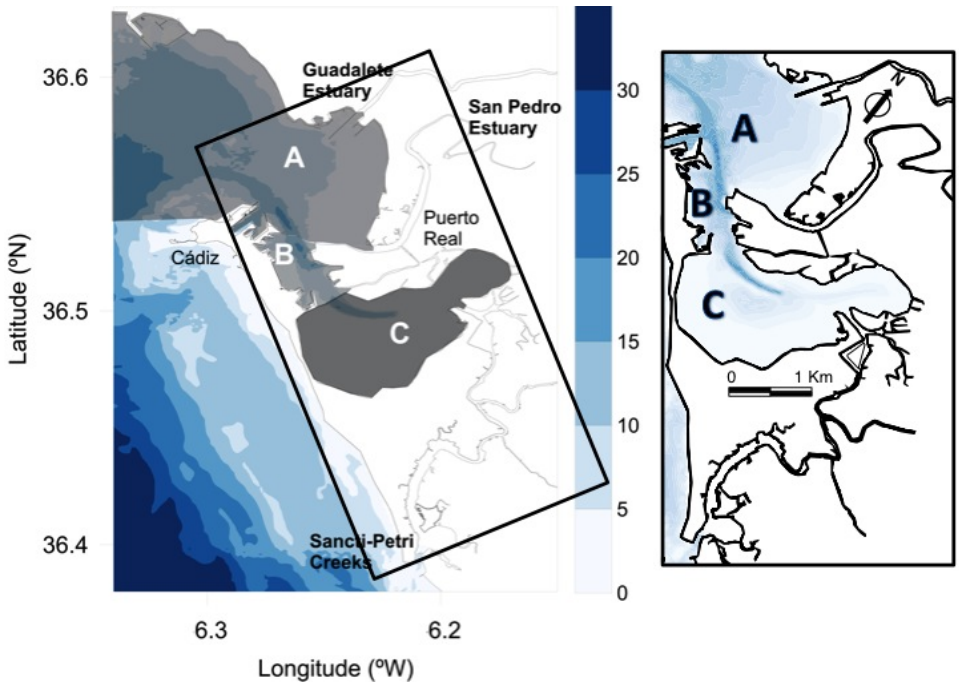

Figure 6.1: Location of the Bay of Cádiz. The outer, central, and inner areas of the Bay are denoted by A, B, and C, respectively.

An indication of the main drivers of these vortices can be obtained from the nondimensional Kelvin and Ekman numbers. On one hand, the Kelvin number, Ke, is a nondimensional width characterized by the ratio of the basin's width to the internal radius of deformation. A rough estimation of the Kelvin number for each basin ($Ke = 6.45$, 4.58, and 25.8, for A, B, and C, respectively), indicates that the residual flow is laterally sheared and deflected because of the Earth's rotation. Inertial effects appear to dominate in the constriction that connects the inner and outer portions of the Bay. On the other hand, the horizontal Ekman number provides information on the effects of viscous forces compared to Coriolis effects. As shown by the estimated Ek values ($Ek = 1.16$, 0.52, and 3.23 for the outer, central and inner portions, respectively), friction overwhelms the Coriolis effects. These vorticities are probably induced by lateral variations due to bathymetric and frictional effects (Valle-Levinson, 2008). The residual circulation is more complex along the length of B, most likely because of the irregular margins. At the central cross section of B, the residual transportt appears to orient outwards in the deeper portion, whereas the current is directed inwards near the margins. Nevertheless, this pattern vanishes near the connections with C and A. Smaller vortices are also visible along B, likely fed by the *cum sole* circulations in the basins.

6.3 Sediment transport patterns and magnitudes

Figure 6.3 illustrates the suspended sediment concentration (hereinafter SSC), mud sediment concentration (hereinafter MSC) and bottom elevation at the start and end of the simulation, using the parameter defined in section .

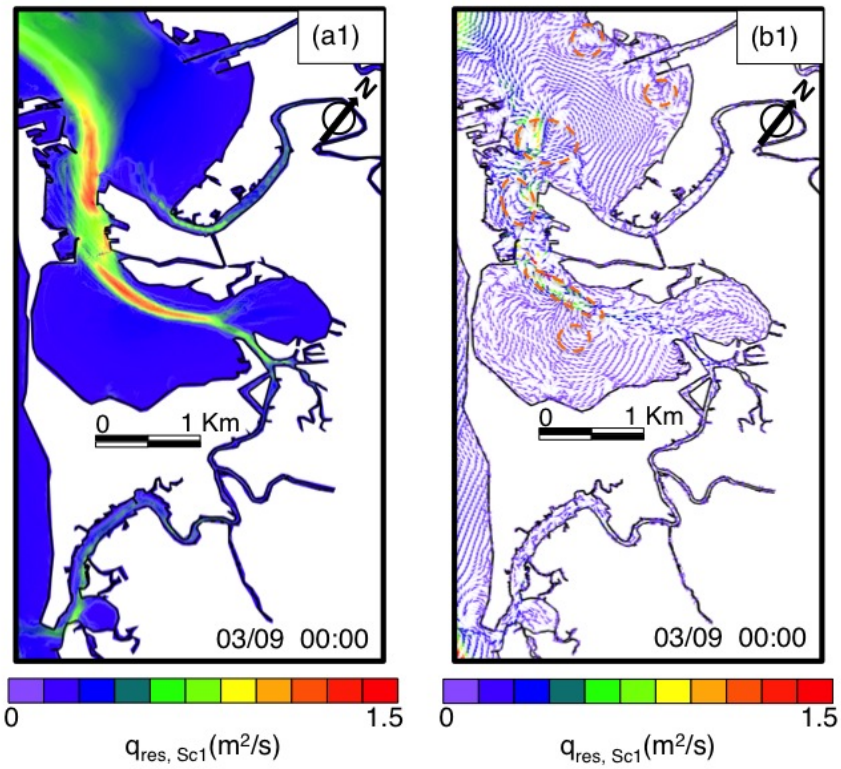

Figure 6.2: (a): Residual transport magnitudes (m^2/s). (b): Residual transport vector (m^2/s).

The magnitudes and variations of suspended sediment concentrations in major channels closely followed the strong tidal flow. The majority of the suspended sediments are eroded locally and transported through the channels. They can drop over the flanks or over shoal tops due to the combined effects of bottom friction and tidal asymmetry. These effects can cause sedimentation in the shallow parts through the convergence of advective transport, and erosion of deep parts through the divergence of advective transport. The SSC, MSC and bottom elevation at the 21 days can be observed in Figure 6.3. The sediment is eroded and then put into suspension due to high shear stresses caused by tidal currents and gets in suspension. It is then transported due to advective and diffusive processes and deposited due to the influence of gravity.

The nine time points are represented in figure 6.4. The sediment transport through the west channel in spring tides are higher than in moderate tides. The middle channel experiences increased SSC in the ebb tides. Sediment concentration increases at flood tide in the inner bay. Figure 6.5 shows the circulation of the SSC. Considering all the tidal cycles, SSC is lower during neap tide periods (4-6 - Figure 6.5) than in spring tide periods (1-3 and 7-9 - Figure 6.5). In spring tide periods, SSC values range from 0 to 5 mg/L in all the bay, except in the Valdelagrana beach and the mouth of the San Pedro River, where the maximum value is 10 mg/l. During flood periods (1,2,7 and 8 - Figure 6.5), the maximum concentration of the SSC is located in the west of the inner bay, while during ebb periods the SSC is located in Puntales Channel (3 and 9 - Figure 6.5). However, the highest values of SSC at neap tide periods are 3 mg/l. This behaviour is the same for to MSC, with lower values during neap tide periods (4-6 - Figure 6.6) than spring tide periods (1-3 and 7-9

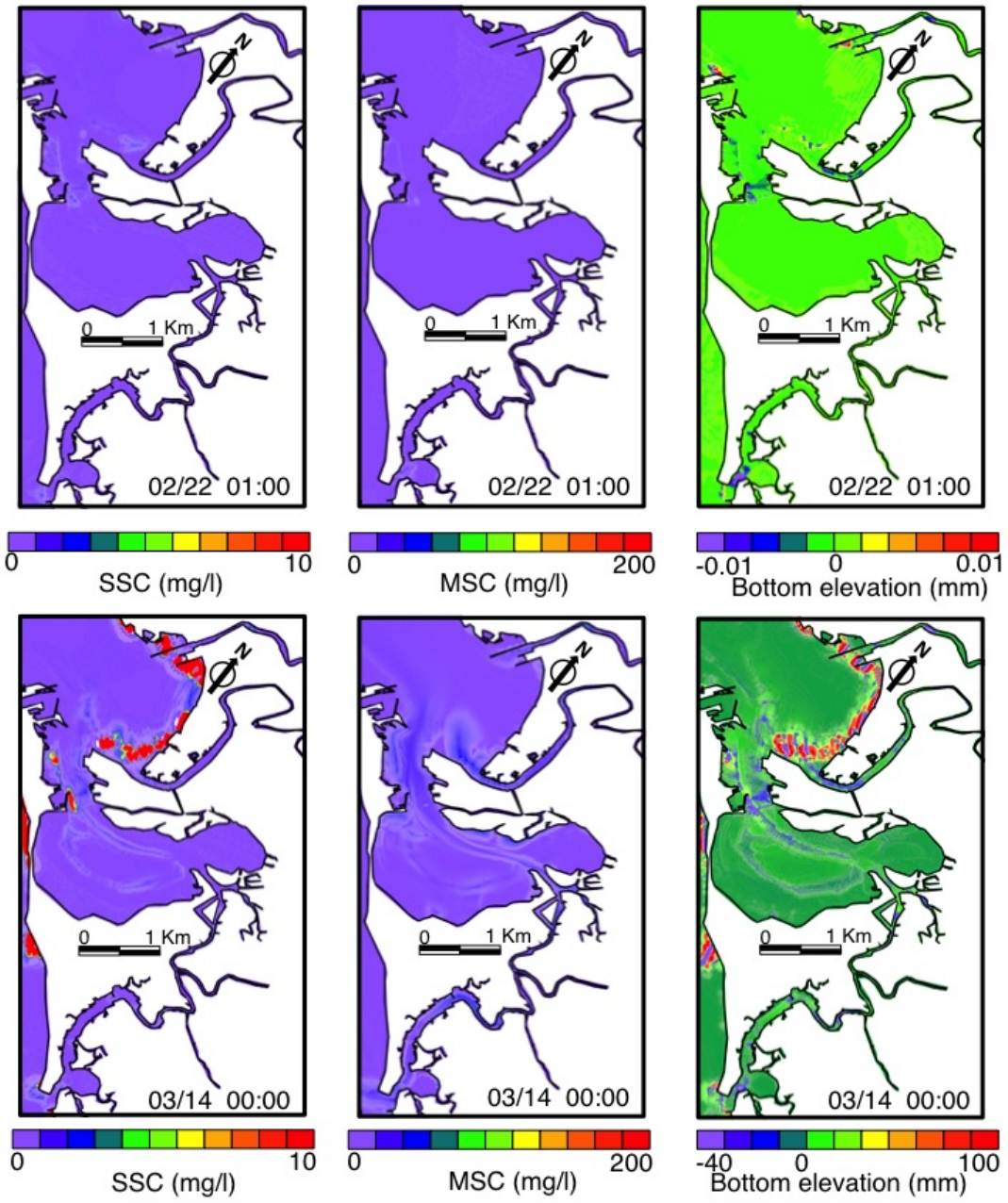

Figure 6.3: Start (top) and end of the simulation (bottom) of the sand concentration, mud concentration and bottom elevation, from left to right, in the Bay of Cádiz.

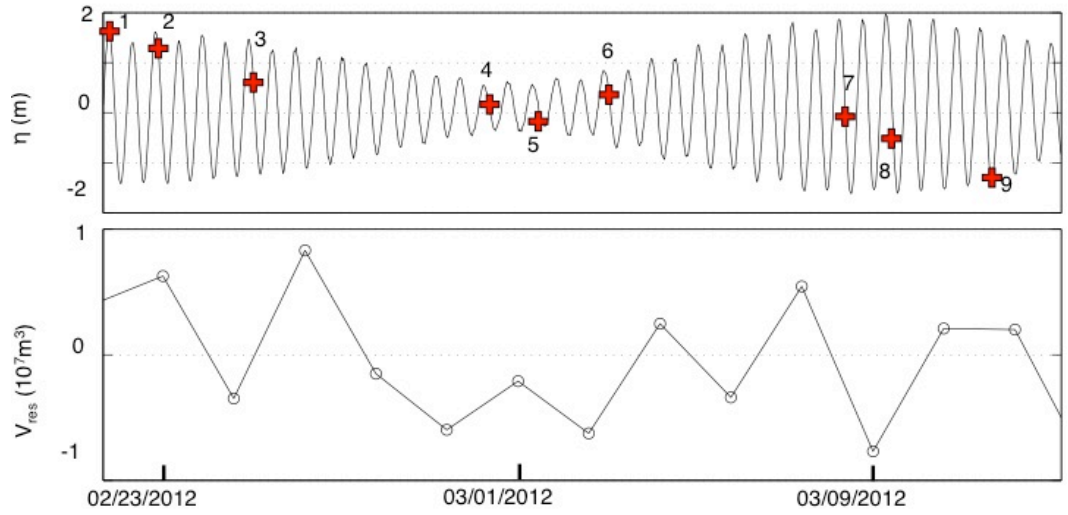

Figure 6.4: Representation of the water level (top) and water exchange (bottom). The nine points corresponds to study time.

- Figure 6.6). The maximum MSC at flood periods attains values of 150 mg/L (30 mg/L) during spring tide periods (8 - Figure 6.6) (neap; 6 - Figure 6.6), whereas the maximum MSC at ebb time exhibits lower values of 50 mg/L (10 mg/L) during spring tide periods (9 - Figure 6.6) (neap; 4 - Figure 6.6), as expected for a flood-dominated estuary in terms of residual velocity.

Figure 6.7 shows the bottom elevation evolution predicted by the simulations. The data indicate a strong sedimentation in the Inner bay (color blue in the figure 6.7). Furthermore, the navigation channel appears to be more pronounced at the end of the simulations (panel 9-Figure 6.7). This is an indication of the accelerated velocity pattern at the entrance of the bay. There is a weak deposition in the mouth of the Carracas and Sancti-Petri creek. In contrast, the results indicate erosion at the Valdelagrana beach (color red in the figure 6.7), which implies an accretion in the mouth of the San Pedro estuary. The changes at the rest of the bay are neglected. The spatial mean deposition rate is 1.8 mm/day (total sedimentation divided by 21 days, the same hereinafter) while the spatial mean erosion rate is 4.7 mm/day (total erosion divided by 21 days, the same hereinafter). Within the inner bay, the spatial mean sedimentation rate is about 0.8 mm/day. Within the west navigation channel in Puntales channel and close to the Valdelagrana beach, the spatial mean erosion is about 0.8 mm/day and 4 mm/day, respectively. Finally, at the south and the entrance of the Puntales channel have a spatial mean sedimentation rate of 1.2 mm/day.

The asymmetric behaviour of the creeks is noticed. Large quantities of suspended sediment are characteristic of tidal creeks. Strong tidal currents continuously resuspend resuspended and rework sediment in the channels, especially, during spring tide periods. Ebb and flood periods can follow mutually-evasive channels, and currents may be powerful enough to cause scouring at the channel base. Figure 6.8-a shows the suspended sediment concentration. The highest values are reached in the minimum depths (30 mg/l). In the mouth of the Sancti-Petri creek, there is a sediment concentration of 15 mg/l.

Figure 6.8-second panel shows the net evolution of the bottom elevation at the end of the simulation. The main impacts are located in the central part of the creek and at the mouth of the Sancti-Petri creek. There is a net deposition at the tidal flat, which is greater than 20 mm. This is indirectly confirmed by the necessity dredging of the navigable channel. There is a net slightly erosion within the Carraca creek. During the flood period large amounts of sediment are transported into the embayment, while during the ebb period a large amount of sediment leaves the embayment again. Due to erosion and deposition during the tidal cycle, the bottom evolves and usually organises itself in a pattern of shallow shoals separated by deep channels.

6.3.1 Wind effects

Wind-driven water exchanges between the basins are fundamental to the overall mixing of the bay. A constant or accelerating northerly wind drives water southward. A decelerating wind can be associated with net water transport in the opposite direction due to residual unbalanced hydrostatic forces. The circulation patterns continually change with the wind speed and direction (Figures 6.9, 6.10 and 6.11). The highest changes in MSC are reached when the wind blows persistently from the south (Figure 6.9). The MSC reaches the maximum values (200 mg/L) at the inner basin. This sediment could come from the creeks. On the other hand, the highest changes in SSC are found with wind from the north, specially north-eastern (Figure 6.10), where the sediments could come from the estuary. The maximum concentration of the SSC is located in the inner bay and close to Valdelagrana beach and the mouth of the San Pedro estuary. The concentration of the SSC and MSC is not significant when the wind blows from the north-west (Figure 6.11). The overall net erosion and deposition pattern indicates that the inner bay does not only receive sediments from creeks. Most of the sediments are deposited at the intertidal flats (west of the inner bay) and shallower areas (west of the navigation channel). The eroded sediments of the Valdelagrana beach and the mouth of the San Pedro estuary are transported and deposited in the inner bay at the ebb periods.

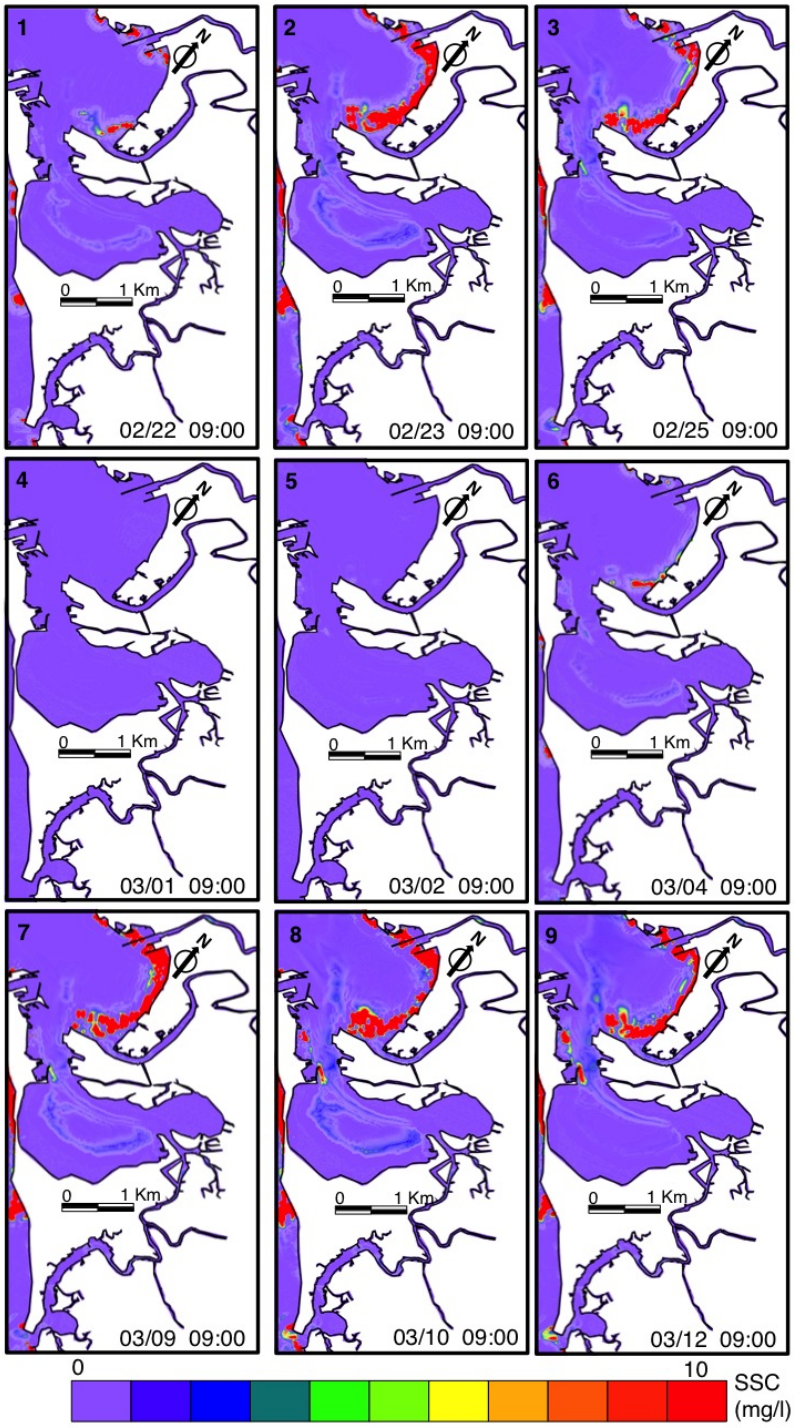

Figure 6.5: A time series of sand concentration in the Bay of Cádiz from February,22nd to March, 24th; according to the time points in Figure 6.4.

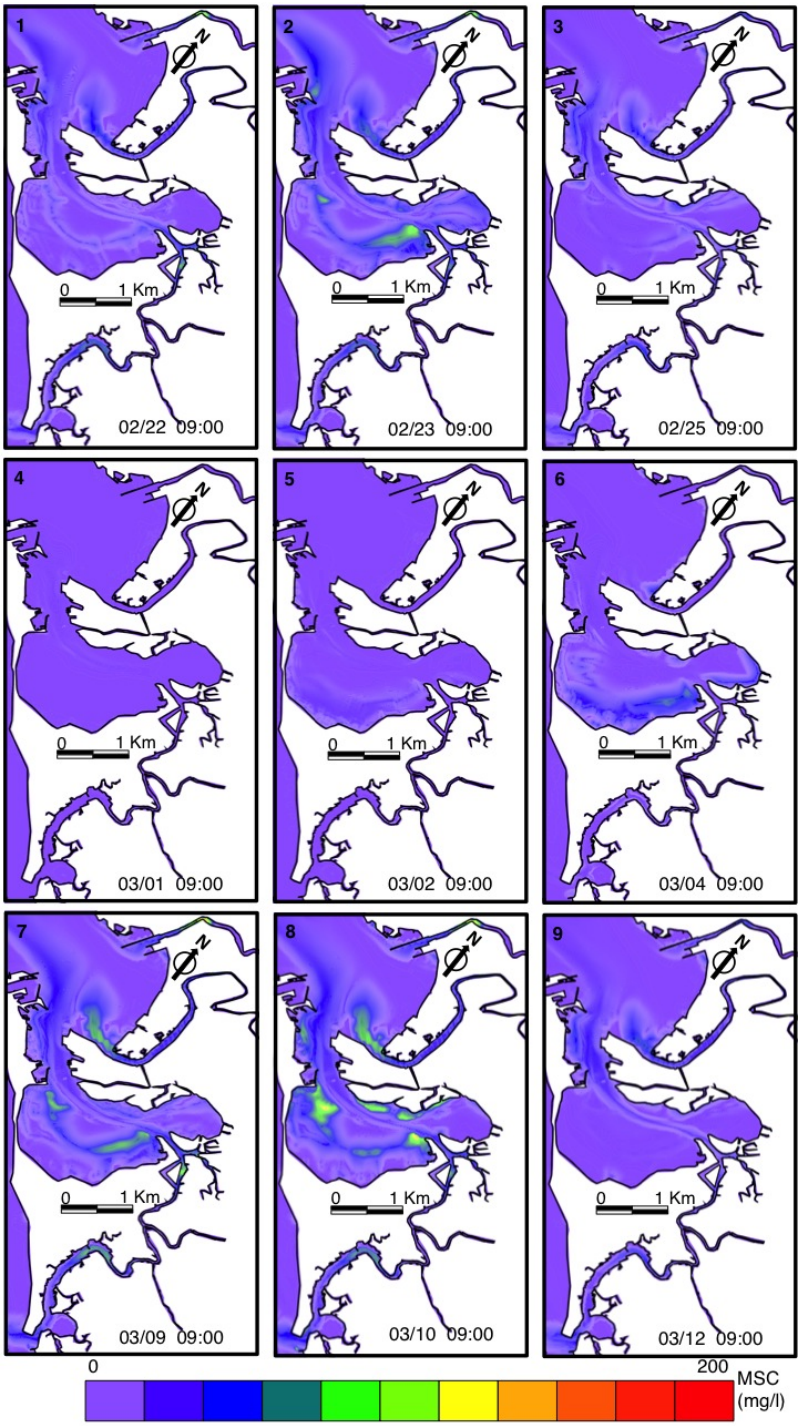

Figure 6.6: A time series of mud concentration in the Bay of Cádiz from February,22nd to March, 24th; according to the time points in Figure 6.4

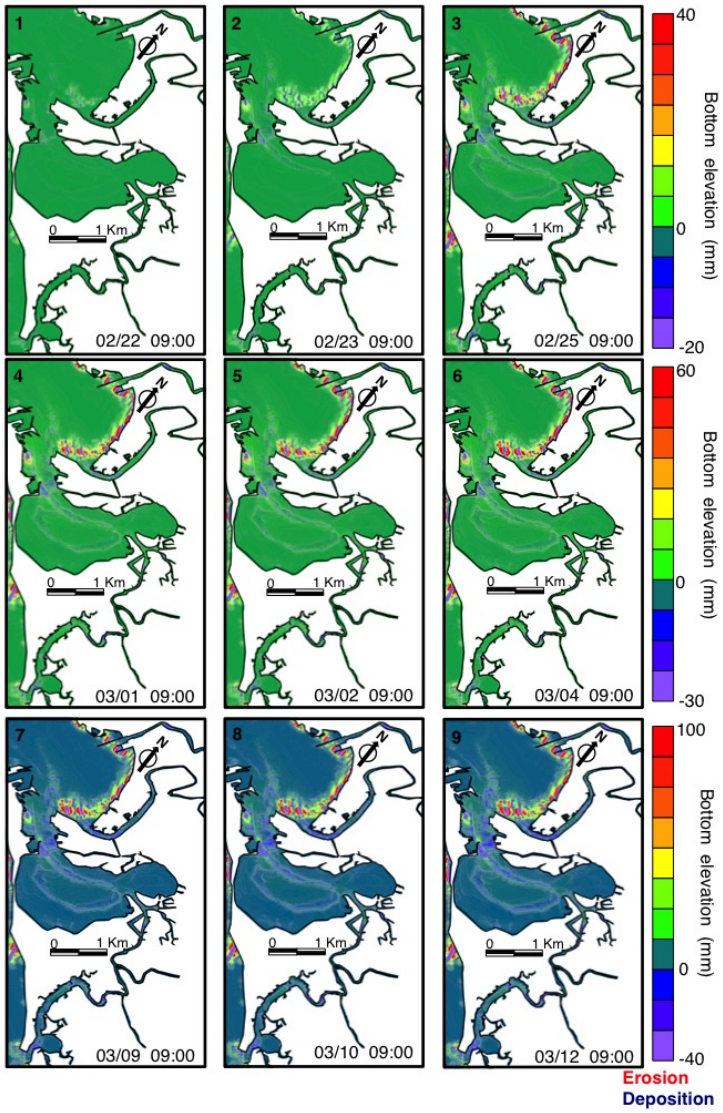

Figure 6.7: A time series of mud concentration in the Bay of Cádiz from February,22nd to March, 24th; according to the time points in Figure 6.4.

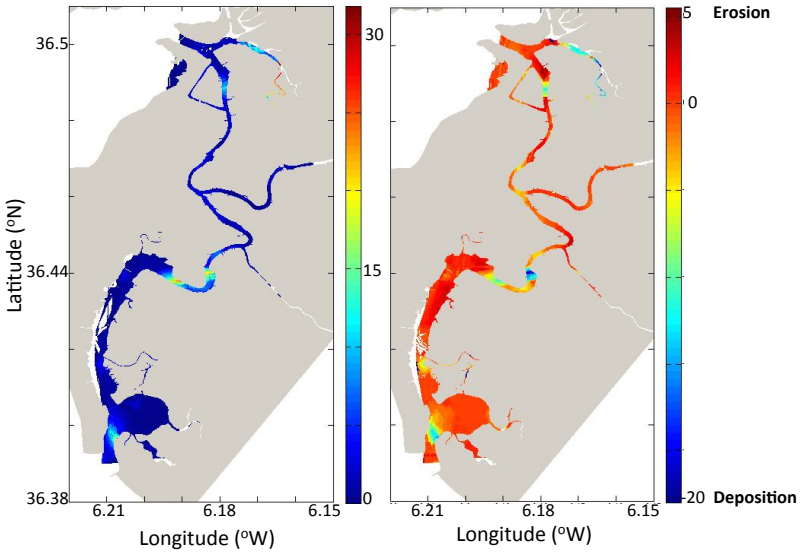

Figure 6.8: The suspended sediment concentration (mg/l) and the net evolution of the bottom elevation (mm) computed by the bed evolution model at the end of the simulation.

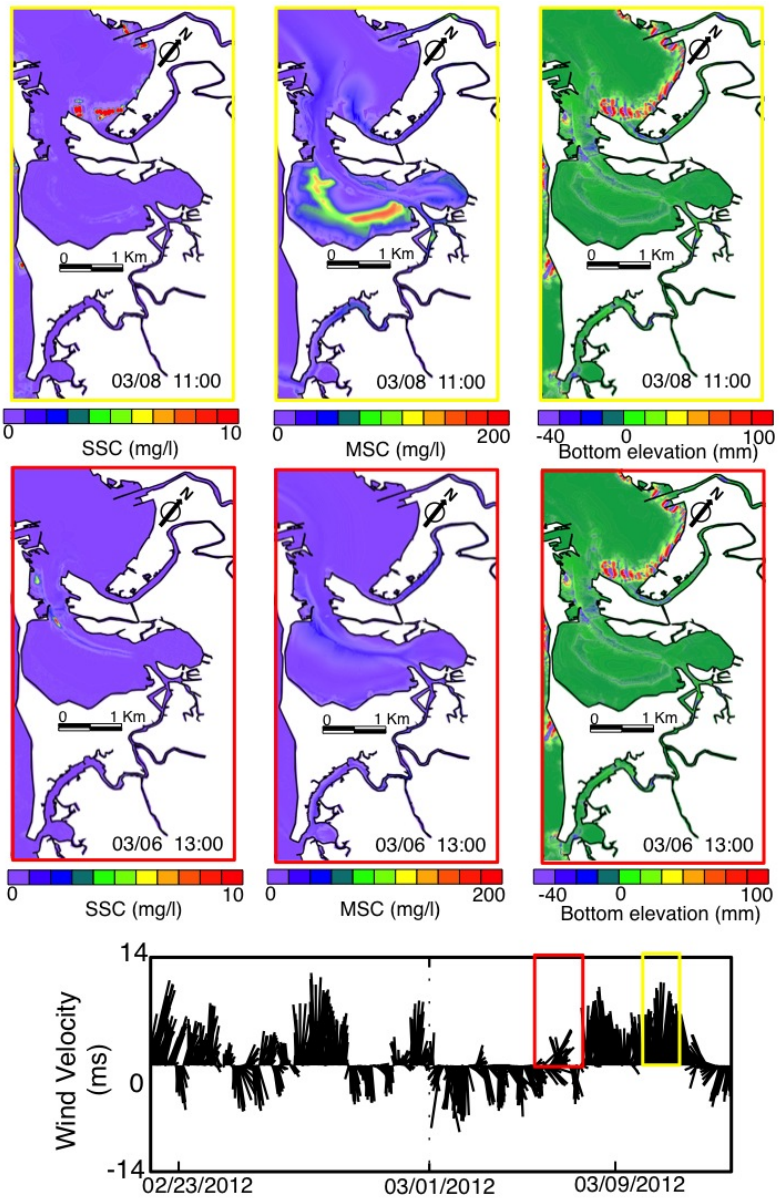

Figure 6.9: The sand concentration, mud concentration and bottom elevation, from left to right, evolution due to the wind from the Southwest.

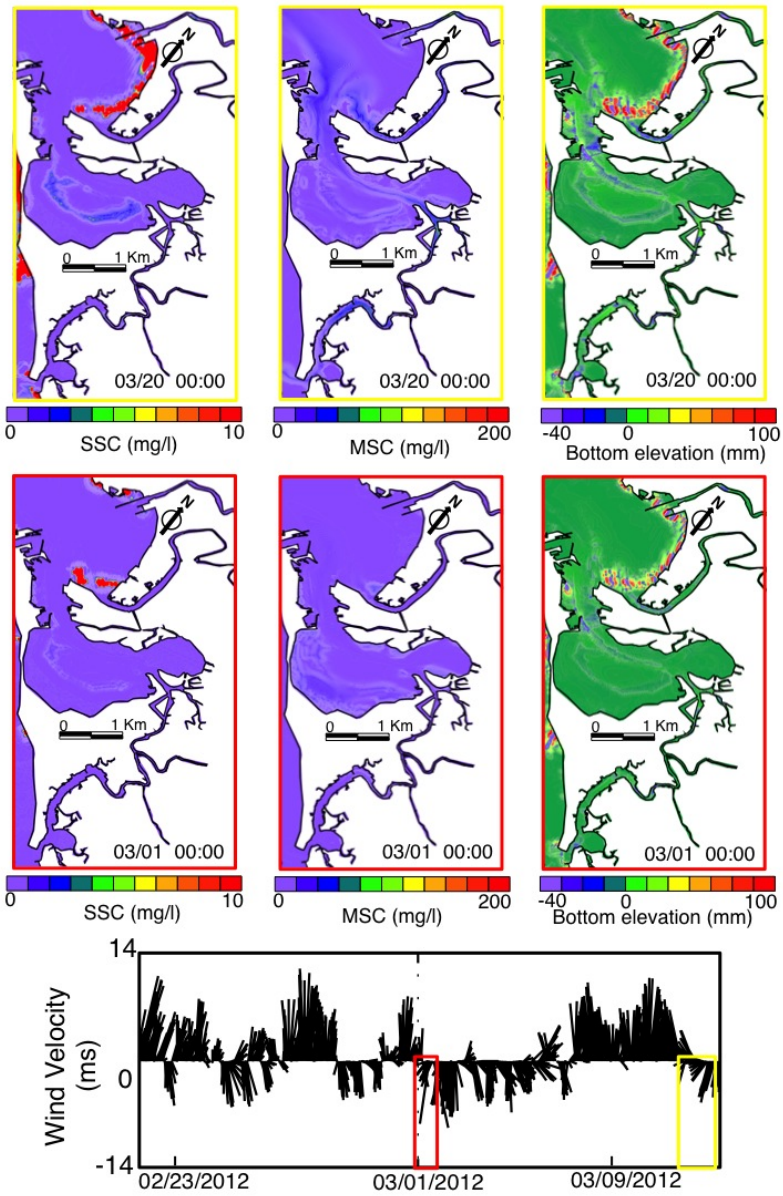

Figure 6.10: The sand concentration, mud concentration and bottom elevation, from left to right, evolution due to the wind from the Northeast.

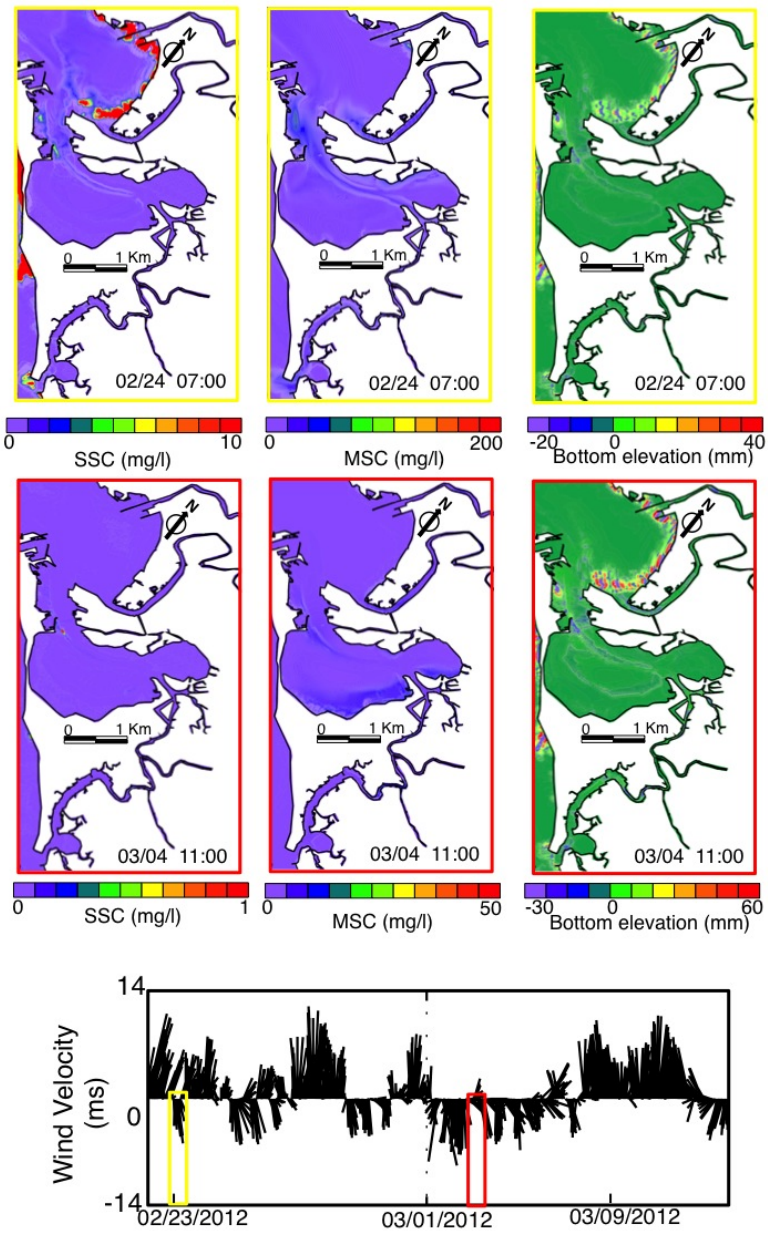

Figure 6.11: The sand concentration, mud concentration and bottom elevation, from left to right, evolution due to the wind from the Northwest.

Chapter 7
Response of the tidally-dominated bay to human interventions

This Chapter analyzes the hydro- and morphodynamical changes due to ongoing human interventions at the Bay of Cádiz: the new port terminal, the new navigation channel and the new bridge. The analysis is done first considering the isolated effect of each intervention, and then combining all of them into the future final configuration of the Bay. The procedure was to define four different scenarios and applied the numerical models; results are then compared and analyzed.

7.1 Description of the Scenarios

To accomplish the main objective of this Chapter –assessment of the impact of human interventions on the hydro- and morphodynamics of the Bay–, we firstly described the different configurations of the Bay that have been considered. Those configurations are considered as different *scenarios* ranging from the real and present situation (scenario 1) to the final configuration of the Bay when all the interventions are finished (scenario 4).

Scenario 1 (Sc_1): Configuration of the Bay in 2012, before interventions. This first scenario corresponds to the configuration of the Bay of Cádiz before any intervention carried out recently (upper left panel in Figure 7.1). This corresponds to the bathymetric data described in section 4.1 and the configuration during the field measurements. Both numerical models have been calibrated and tested for this scenario.

Scenario 2 (Sc_2): Configuration of Sc_1 including the new port terminal and navigation channel. Those interventions are expected to be finished by the end of 2016. The coastline of zone A will be expanded, whereas the bathymetry of this area will be increased 5 m in depth (P2.2 and P3.2, respectively, in Figure 7.1–upper right panel). The new container terminal is characterized by a length of 590 m, forming an area of 380,000 m^2 with a maximum depth of 16 m. Additionally, the operational scheme for the new terminal includes a significant dredging of $\sim 3.86 \cdot 10^6\,m^3$ to achieve a maximum depth of 20 m (new navigation channel). Accordingly, both the coastline and bathymetry of Sc_1 were adapted to include those changes. Delft3D model was used to simulate the hydrodynamics, whereas model by Carniello et al. (2012) simulate the morphodynamics.

Scenario 3 (Sc_3): Configuration of Sc_1 including the new bridge. "La Pepa" Bridge was completed on september, 2015. It is one of the longest (5 km) and highest (69 m over mean sea level) bridges of Europe, and crosses the Puntales Channel connecting the city of Cádiz with the Peninsula. Its affection on the Bay is mainly due to the nine piers set in the water that sustain the bridge (see Figure 7.1–lower left panel). Carniello et al. (2012) model is used to simulate this scenario; due to the small scale of the piers, it is important that the mesh of the model around the bridge can describe these elements accurately. Hence, the mesh is intensified around the piers adding 39509 triangle nodes and 78389 triangular elements (Figure 7.2). Alongside the bridge, the node distances arrange gradually from 5 to 20 m.

Scenario 4 (Sc_4): Expected configuration of the Bay after all interventions are finished –(Sc_1+Sc_2+Sc_3)–. This scenario represents the combination of all the interventions into a unified scenario, which will correspond to the future and final configuration of the Bay of Cádiz (Figure 7.1, lower right panel) by the end of 2016. Carniello et al. (2012) model is used to simulate this scenario considering all the particularities previously specified.

The hydro- and morphodynamics of the Bay of Cádiz for Sc_1 was described in detail in previous chapters. Hence no section is devoted within this Chapter to this scenario. The following sections deal with Scenarios 2, 3 and 4.

7.2 Scenario 2

7.2.1 Hydrodynamics

The tidal range is weakly affected by the morphological and coastline changes. Differences of 1% (0.4%) are modeled for spring (neap) tides with respect to the pre-intervention values. Differences in the flow are also detected between Sc_1 and Sc_2, not only near where the interventions are planned. The current magnitude increases to (~ 0.05 m/s) close to the new terminal. This value weakly decreases by approximately (0.01 m/s) in the deepened areas, although these variations are below the accuracy of the model's results and may not represent a real decrease in the current magnitude.

Figure 7.3 presents the current magnitude difference between Sc_2 and Sc_1. The decrease in current magnitude is greater along the *thalweg* of the deepened navigation channel. In contrast, the current magnitudes increase at the channel edges. The maximum positive difference ($|\mathbf{U}_2| - |\mathbf{U}_1| \approx 0.5$ m/s) is observed close to the new terminal and occurs during a spring tide MF (upper left panel in Figure 7.3). The maximum negative difference (-0.1 m/s) occurs at the maximum flood near the new channel. The magnitude decreases (increases) by 50% (40%) during the spring and neap tides close to P2.2 (P3.2). During the neap tides, the changes are significant in Area C, with a landward increase and an inward decrease. After the interventions, the velocity in the northern portion of B decreases, whereas the velocity in the rest of Area B increases markedly.

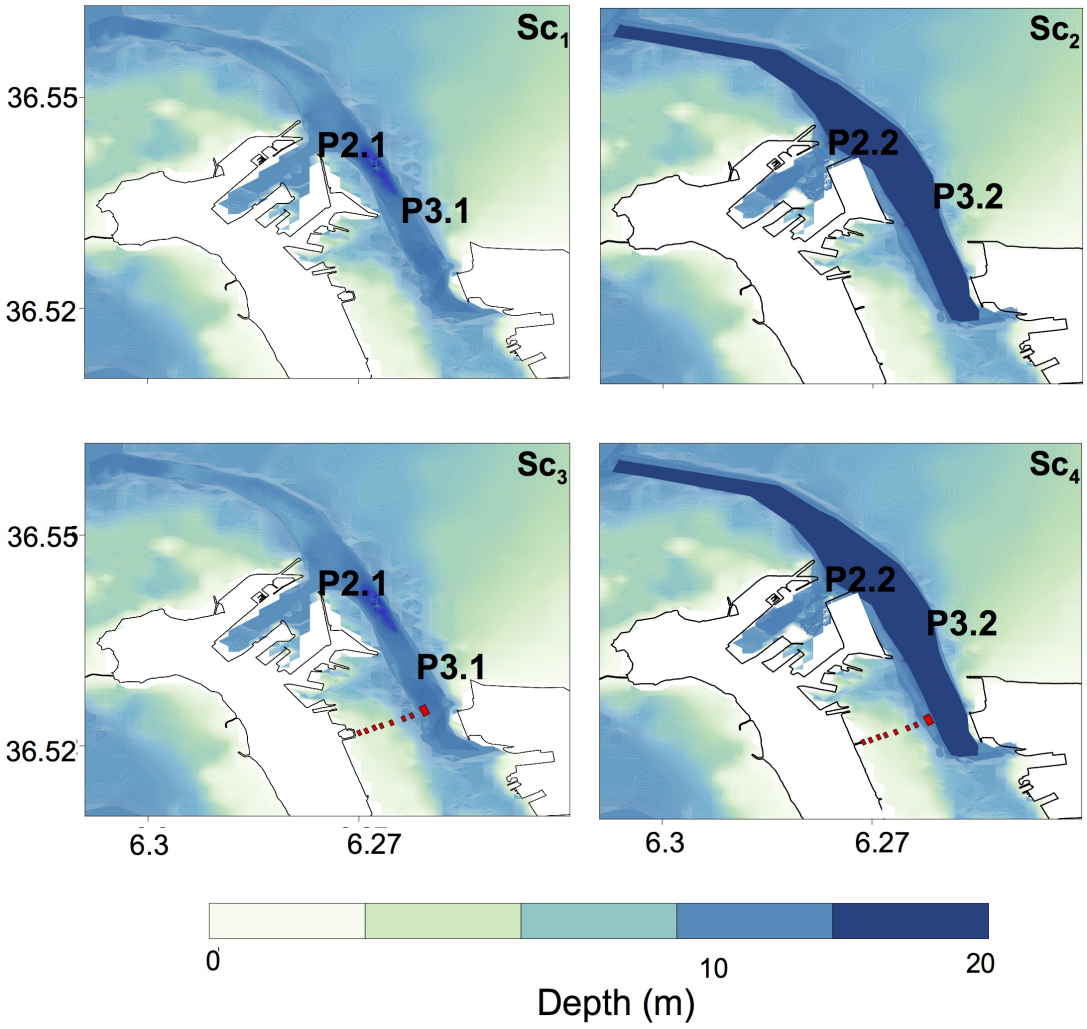

Figure 7.1: Initial configuration before intervention (SC_1). Final configuration after new terminal and new navigation channel (Sc_2). Final configuration after new bridge (Sc_3), the piers are respresented in color red in the right panel. Final configuration after all interventions (Sc_4). Labels P2.1 (P2.2) and P3.1 (P3.2) correspond to the terminal (new terminal) and the navigation channel (new navigation channel), respectively.

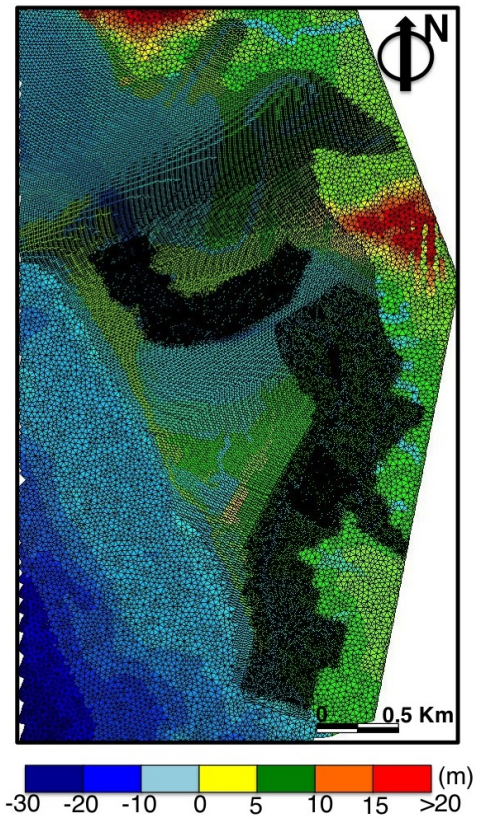

Figure 7.2: Representation of the second mesh corresponding with the numerical model II.

Regarding the current direction, greater differences in the velocity directions occur during ebb periods (bottom panels in Figure 7.3). Close to the new terminal and in the navigation channel, the directions of the velocities are significantly affected. In the inner bay, the maximum ebb velocity changes significatly. In the central section, the direction of the velocity of Sc_2 is close to that of Sc_1, the reference configuration.

The simulations indicate that the planned changes in the coastline and bathymetry will have an impact on tide propagation and hence, on tidal constituents. Figure 7.4 shows the differences between the tidal parameters before and after the interventions. The deepening of the channel increases the tidal range in the central and inner areas of the bay (panels (a) and (b)), whereas the deepening mainly produces a decrease in tidal range inside the harbor. Nevertheless, the relative variation in the M_2 amplitude barely exceeds 1%, and the phase lag does not increase above 1°. The differences in the $M4$ values are as large as 10%, which impact the residual behaviour. The relative differences in the tidal ellipse parameters are greater in relative terms.

After the interventions, the current amplitudes decrease significantly near the new port terminal and where the channel has deepened. The semi-major axis, Ma, decreases more than 15% for M_2 in that area. Ma increases by more than 10% for M_2 along the rest of the constriction, whereas the changes in M_4 are negligible. The most significant differences occur in the semi-minor axis. Relative differences of 40% and 30% for the M_2 and M_4, respectively, are observed in ma. In addition, the sign of ma changes, inverting the rotation sense of the ellipse. Nevertheless, the differences are concentrated locally,

where the interventions are performed. The inclination of the semi-major axis (panels (g) and (h)) and the ellipse phases (panels (i) and (j)) are barely affected, and thus, the $\pi/2$ phase relationship between the elevation and currents is maintained.

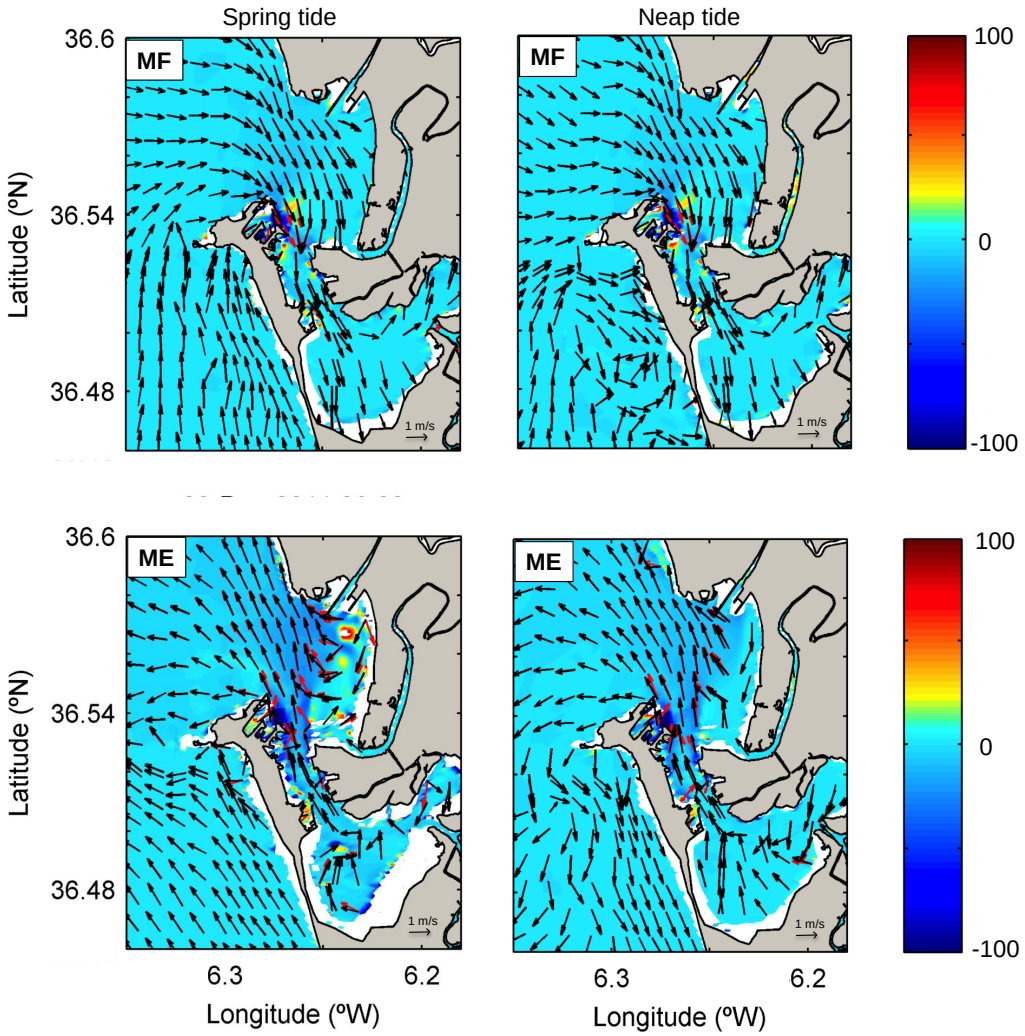

Figure 7.3: Current vector field before ($\mathbf{U}_1$, red arrows) and after ($\mathbf{U}_2$, black arrows) modifications for the MF and the ME during spring and neap tides (see labels). The colormap in the background indicates the magnitudes of the differences between both scenarios, $|\mathbf{U}_2| - |\mathbf{U}_1|$, expressed in %.

7.2.2 Morphodynamics

Figure 7.5 (a) shows the residual current magnitudes for Sc_1. Residual currents are estimated by time-averaging over each tidal cycle. The residual currents are, in general, one order of magnitude lower than the tidal currents. Larger values ($\approx 0.3\,m/s$) are observed in the mouth of the San Pedro estuary. Other local maxima occur at the Carracas Creek and along the channel where the bathymetry deepens and there are abrupt changes in the bathymetry. The residual circulation pattern (black arrows in Figure 7.5, panel (b)) indicates that the inner and outer basins operate rather independently. A remarkable feature

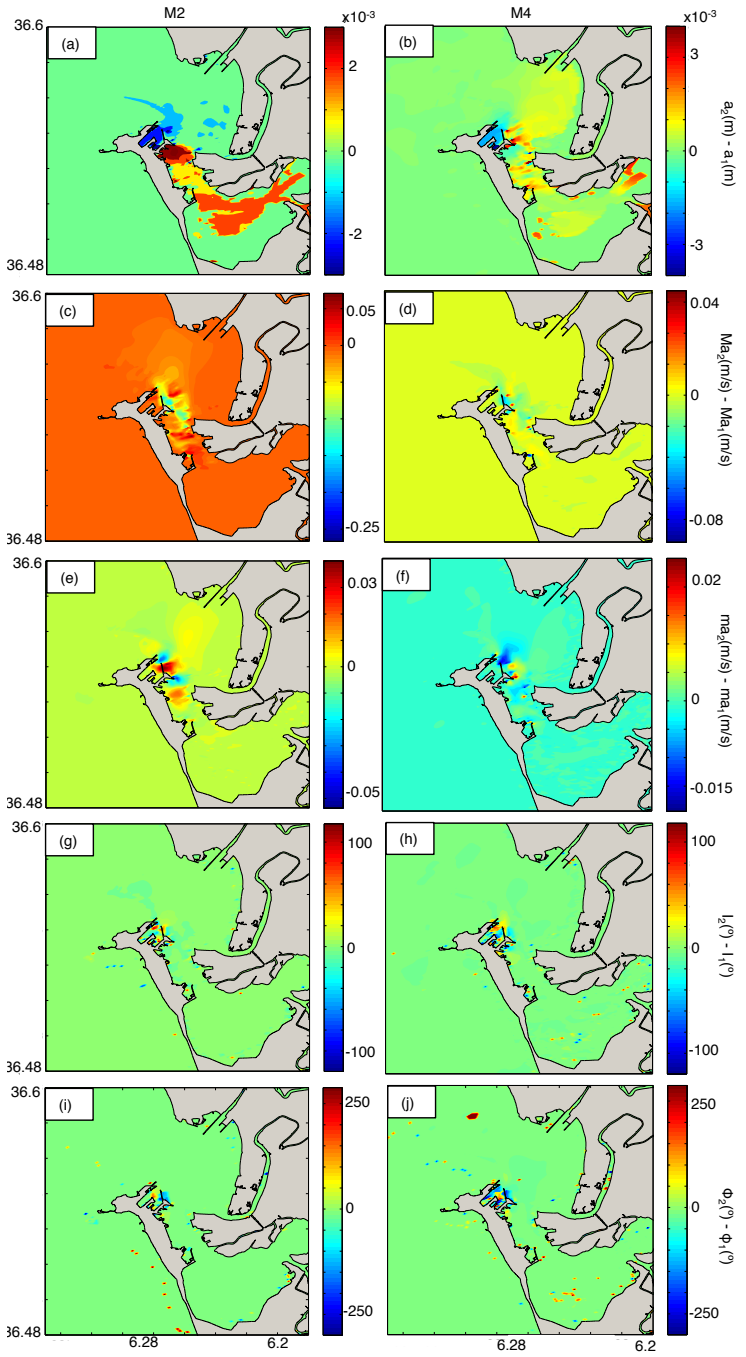

Figure 7.4: Absolute differences in tidal parameters between Sc_2 and Sc_1. As in Figure 5.6, the first (second) column shows the results for the M_2 (M_4) constituent. Here the subindices 1 and 2 refer to the Sc_1 and Sc_2 scenarios, respectively.

of the residual current vector field is the development of vortices in areas A, B and C. In all cases, the vortices extend to the maximum possible surface without significant changes in depth (submerged plains). Their diameters are on the order of ~ 1.5 km, ~ 0.8 km, and ~ 3 km for the A, B and C basins, respectively, which rotate clockwise. This behaviour was observed in other estuaries, as noted by Robinson (1981), Velasco Fuentes and Ochoa (2003), Serrano et al. (2013) and Nayak et al. (2014).

$$\nabla(\overline{q_x}, \overline{q_y}) = \partial(q_x)/\partial x + \partial(q_y)/\partial y$$

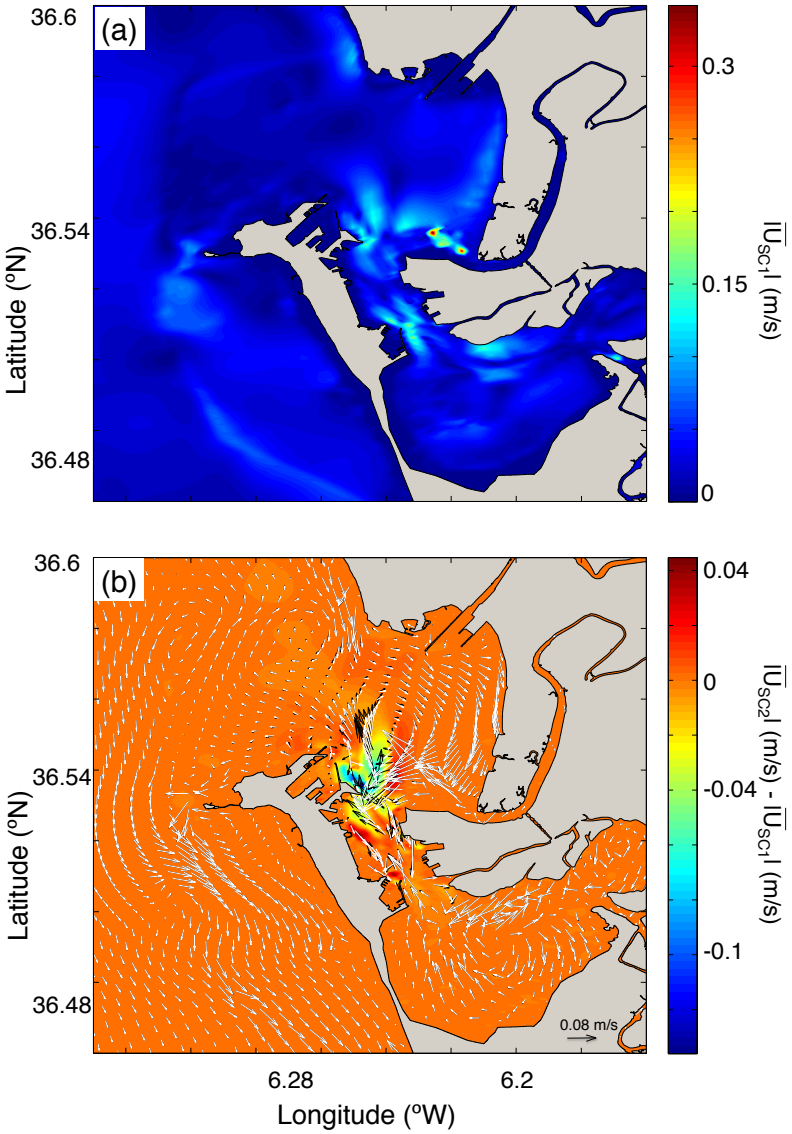

Figure 7.5: Panel (a): Residual current magnitudes (m/s) before interventions (Sc_1). Panel (b): Residual current before (black arrows) and after (white arrows) planned interventions. The colormap in the background represents the variation in the magnitudes ($|\overline{\mathbf{U}}_2| - |\overline{\mathbf{U}}_1|$).

When comparing the two scenarios, the effects of the interventions on the residual circulation pattern are apparent (Figure 7.5 and 7.6). As shown by the differences of the magnitudes in Figure 7.5 (colormap in panel (b)), the magnitudes of the residual currents after the interventions $||\mathbf{U}_2||$, tend to decrease respect to the values of Sc_1 in the inner and

central portion of the bay (3 cm/s and 4 cm/s, respectively). The greatest decreases occur near the new terminal (14 cm/s). The increase is strongest between the channel and the inner portion of the bay (1 cm/s). Close to the Zona Franca port (P1), the residual current magnitude increases when the dredging is included in the model (3.5 cm/s). Figure 7.5b) shows the vectors of the residual currents for Sc_2 (white arrows) and Sc_1 (red arrows). The vectors rotate clockwise around P2.2 with the dredging, but this orientation changes as the current moves eastward. In B, two sections are differentiated. In the left side the vectors rotate clockwise, with the opposite on the right side. An increase (decrease) in the velocity of the water may cause erosion (sedimentation) processes. The changes from erosion to sedimentation, or vice versa, will be determined by the direction of residual currents, as has been discussed previously. Nevertheless, the real storage of sedimentation will depend on sediment availability.

The residual currents allow for the evaluation of their vector divergences, which provide a first estimate of the morphological trend of the embayment after the interventions. Figure 7.6(a) shows the divergence of the residual current, $\nabla(\overline{u},\overline{v}) = \partial(u_2 - u1)/\partial x + \partial(v_2 - v1)/\partial y$, corresponding to the current status of the Bay (Sc_1). The positive, divergent (negative, convergent) values correspond to areas of erosion (sedimentation). The present areas of sedimentation are mainly located in the navigation channel, favoring the accumulation of sediment and the decrease in the channel depth. If there are sediments to be mobilized in the bottom of the bay, they may be transported towards locations where sedimentation is more likely to occur. However, these areas could also be fed by sediments that come from the outer parts of the bay.

The changes in the morphological trend are evaluated by again comparing both scenarios. Figure 7.6(b) shows the difference between the divergences for scenario Sc_2 and Sc_1, i.e., $\nabla(\overline{u}_2-\overline{u}_1, \overline{v}_2-\overline{v}_1) = \partial\overline{u}/\partial x + \partial\overline{v}/\partial y$. Red (blue) values correspond to increased (decreased) rates of erosion or sedimentation. The majority of the morphological activity is located near the interventions and in central section (B). Overall, after the interventions, the erosion rates decrease, whereas the deposition rates increase. Several areas switch in character from deposition-dominated to erosion-dominated areas (blue shades in Figure 7.6(b)) or viceversa (red shades in Figure 7.6(b)). The west and south margins of the inner bay, the north of area B, and the navigation channel (P3.2) are expected to gain sediment volume. In the contrast, the areas in the middle of B and close to P3.2 lose sediment via increased erosion.

The sediment transport changes depending the tide, causing erosion and deposition. Figures 7.7 and 7.9 show the sand and mud concentration at flood and ebb tide period, respectively. Before the interventions (a1-Figures 7.7 and 7.9), the values of SSC are close to 10 mg/l in the west of the Puntales Channel, but up to 4 mg/l within the bay. At ebb period, there is a concentration of the SSC at the mouth of the San Pedro estuary. After the sediment extraction has led to a pronounced increase/decrease of the SSC. The highest changes are observed at flood period (c1-Figure 7.7). The maximum decrease of the SSC (-70%) is found at the west of the new channel navigation (c1-Figure 7.7). On the other hand, at ebb period(c1-Figure 7.9), the values of the SSC grow up to 5 mg/l close to the mouth of the San Pedro estuary and decrease 4 mg/l close to P1.

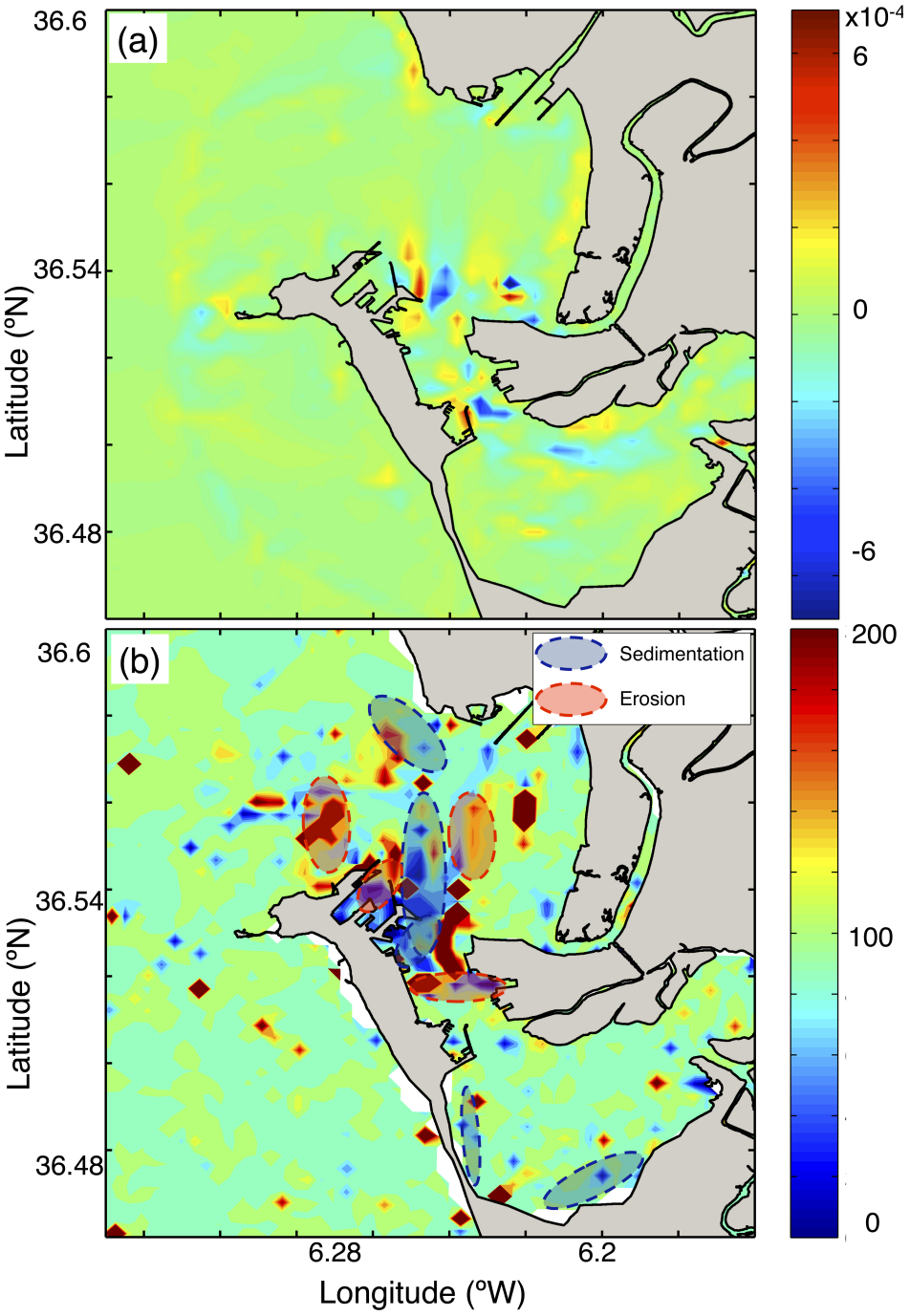

Figure 7.6: Panel (a): Divergence of the residual current (in m/s) for Sc_1. Panel (b): Differences in the divergence (in %) between Sc_2 and Sc_1 (blue = decrease, orange = no changes and red = increase).

Before the interventions, the values of MSC are higher at ebb (up to 140 mg/l; b1-Figure 7.9) than flood period (up to 40 mg/l; b1-Figure 7.7). The maximum values of MSC are found at inner bay, San Pedro estuary and inside the creeks. At flood period, the MSC is reduced up to −20 mg/l at the inner bay, this sediment could be move to the Puntales Channel, where the MSC is increased up to 25 mg/l (c2-Figure 7.7). However at ebb period, the MSC is decreased at the north of the Puntales Channel close to the new navigation channel up to 30 mg/l (c2-Figure 7.9).

There are not differences between flood and ebb period, the bottom elevation (c3-Figures 7.8 and 7.10) is increase up to 10% at the mouth of the San Pedro estuary, which causes a erosion. In the contrary the bottom elevation is decreased up to 50% at the Puntales channel close to the new navigation channel, which causes a strong deposition. Finally, the inner bay is weakly affected by the dredging, decreasing up to 10%.

7.3 Scenario 3

The affection of the Bridge piers is evaluated. Simulations with and without piers are carried out from February, 22 to March, 14, 2012 (Figure 7.11). The differences of tidal level, flow rate per unit width and residual transports are analyzed, in particular, changes on tidal prism, sand sediment concentration, mud sediment concentration and bottom elevation.

7.3.1 Hydrodynamics

7.3.1.1 Tidal Level

M2, K1 and M4 are the three of the major tidal components in the Bay of Cádiz (Zarzuelo et al., 2015a,b). The amplitude of M2 tidal components is increased by 5% in the inner bay (c1-Figure 7.12). Tidal phase lag between M2 and M4 is delayed in the inner bay, while the tidal phase is overtaken the mouth of Carracas Creeks (c1and c3-Figure 7.13). The amplitude of M4 tidal components is decreased by 5% around the navigation channel in the inner bay and increased in the rest of the inner bay (c3-Figure 7.12). K1 tidal component remains largely unchanged, except tiny differences in the south of the Puntales Channel (c2-Figure 7.12 and c2-Figure 7.13).

Differences in water elevation occur mainly during high and low tide. At high water (c1-Figure 7.14), tidal level is higher outside than inside the bay, 50 cm higher in Sc_1 (a1-Figure 7.14), and 52 cm higher in Sc_3(b1-Figure 7.14). The bridge affects tidal level in an obvious way at high tide (c1-Figure 7.14). Tidal level does not change obviously in the north of the bridge, and rises at south of the bridge, with a maximum increase of 2 cm at the inner bay. The tidal level at low tide is contrary to that at high tide, which is higher inside than outside the bay, 80 cm lower in Sc_1 (a2-Figure 7.14), and 82 cm lower in Sc_3 (b2-Figure 7.14). It slightly decreases at north of the bridge, and increases at south, with a maximum increase of 2 cm at the entrance of the inner bay. Due to the blocking effect of the bridge, in-out differences on tidal elevation increase.

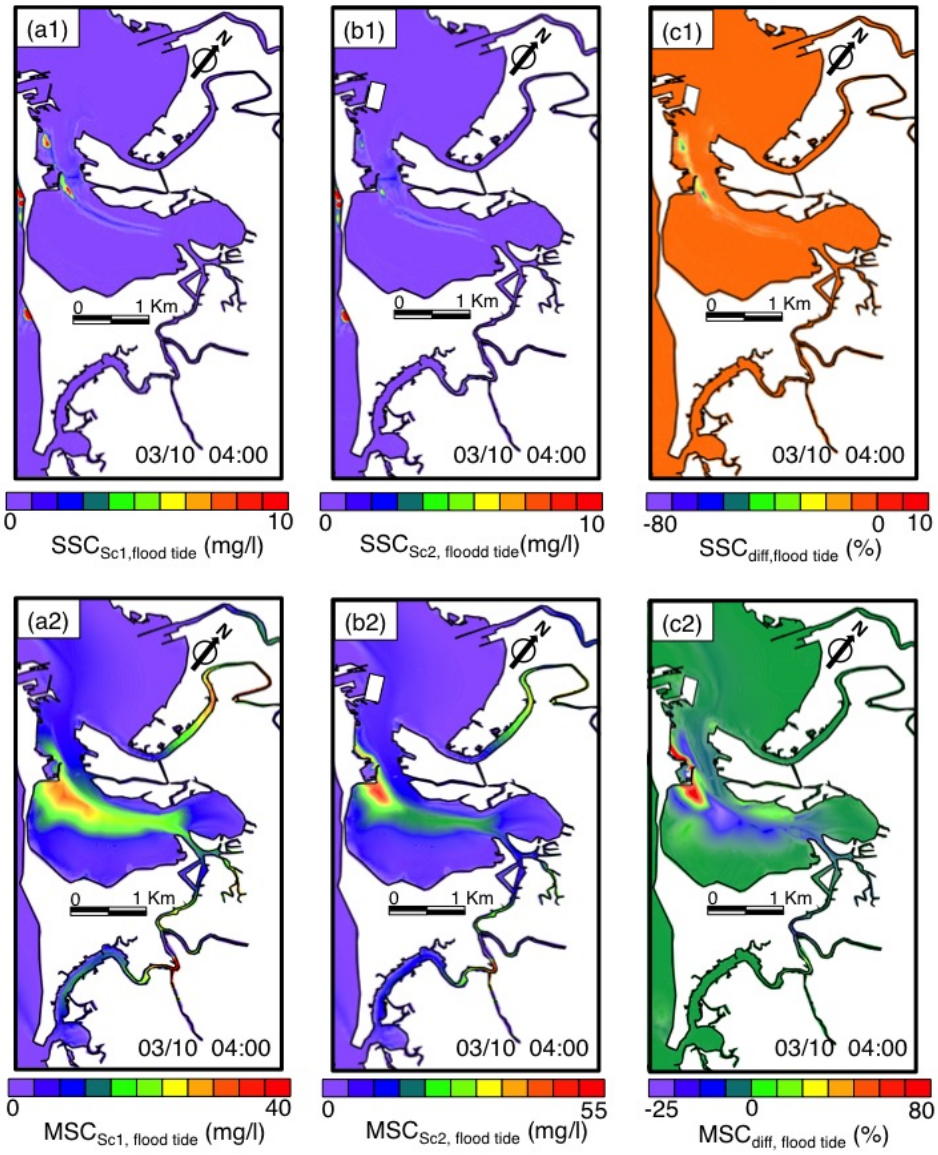

Figure 7.7: A time series of sand concentration (mg/l) and mud concentration (mg/l) in the Bay of Cádiz at flood tide period 03/10 04:00 (panels 1 and respectively). Panels a, b and c correspond to Sc_1, Sc_2 and $Sc_2 * 100/Sc_1$, respectively (blue = decrease and red = increase).

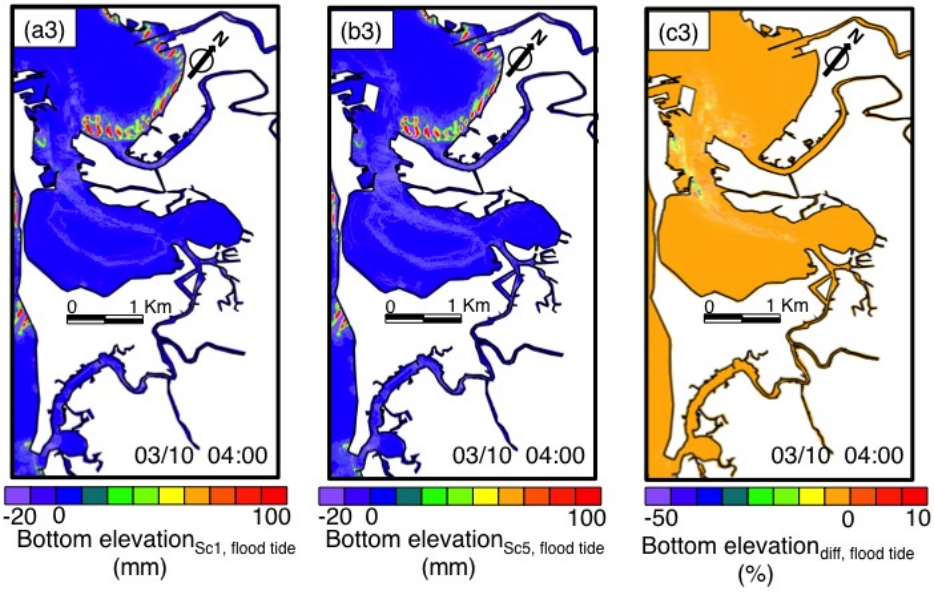

Figure 7.8: A time series of bottom elevation (mm) in the Bay of Cádiz at flood tide period 03/10 04:00. Panels a, b and c correspond to Sc_1, Sc_2 and $Sc_2 * 100/Sc_1$, respectively (blue = decrease and red = increase).

7.3.1.2 Flow rate per unit width

The flow rate per unit width pattern changes after the bridge construction, especially at flood and ebb tide (Figures 7.15 and 7.16), when water flow is relatively stronger. It is evident that the bridge affects flow rate per unit width (c1 and c2-Figures 7.15, 7.17, 7.16 and 7.18), especially at the south of the bridge. At flood period (Figure 7.15), the flow rate per unit width along the y direction decreases (35%) notably between fourth and fifth piers, near the main channel at the constriction. It also decreases in the inner basin. There is an increase close to the Zona Franca Port (80%). The highest changes of the flow rate per unit width along the x direction are located in the inner bay, with a maximum decrease of 25%.

At ebb tide (Figure 7.16), the flow rate per unit width along the y direction decreases at the south-west of the waterway at the Puntales Channel, with maximum decrease of $3\,m^2/s$. It increases around of the fourth and fifth piers, due to minor migration of major flow axis after bridge construction. The flow rate per unit width along -x direction is contrary to along -y direction, which is reduced close to the bridge ($4\,m^2/s$). The decrease of the flow is found in the entrance of the inner bay, with $2\,m^2/s$ larger than the current situation.

During high (Figure 7.17) and low tide (Figure 7.18), flow rate per unit width inside the bay decreases, especially in the bay entrance with a decrease of $-2.5\,m^2/s$.

The flow rate pattern shows that the piers have a important influence on the exchange flow (b2 and c2-Figure 7.19). At flood tide (c1 and c2-Figure 7.15), the flow rate per unit width between two adjacent piers (fourth and fifth) decreases $-4.5\,m^2/s$ and in the highest pier increase $2.5\,m^2/s$; flow rate per unit width on the north and south sides of bridge is not notably affected by the piers, except close to the fourth and fifth piers above mentioned. At high tide, tidal flow of the bay is relatively weak (c1 and c2-Figure 7.17), but

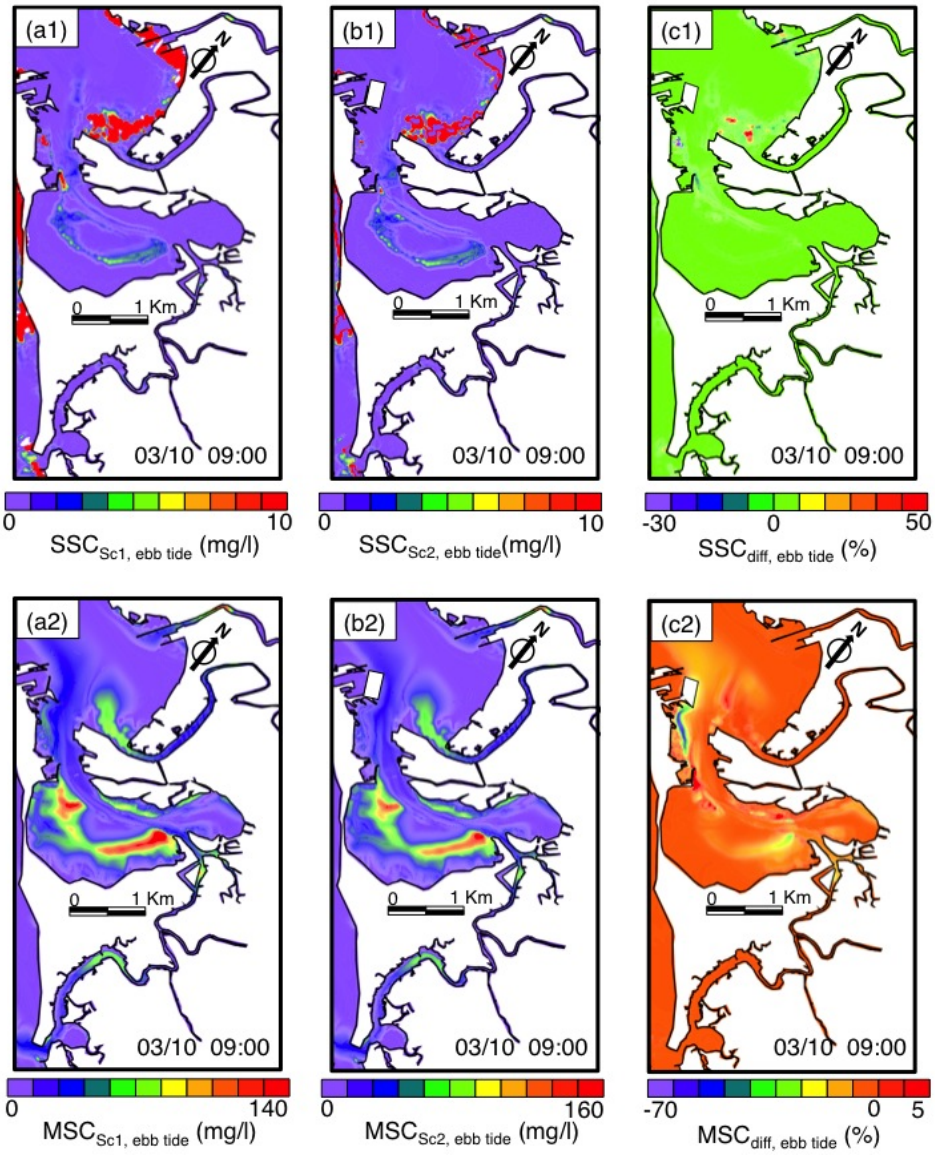

Figure 7.9: A time series of sand concentration (mg/l) and mud concentration (mg/l) in the Bay of Cádiz at ebb tide period 03/10 09:00 (panels 1 and 2, respectively). Panels a, b and c correspond to Sc_1, Sc_2 and $Sc_2 * 100/Sc_1$, respectively.

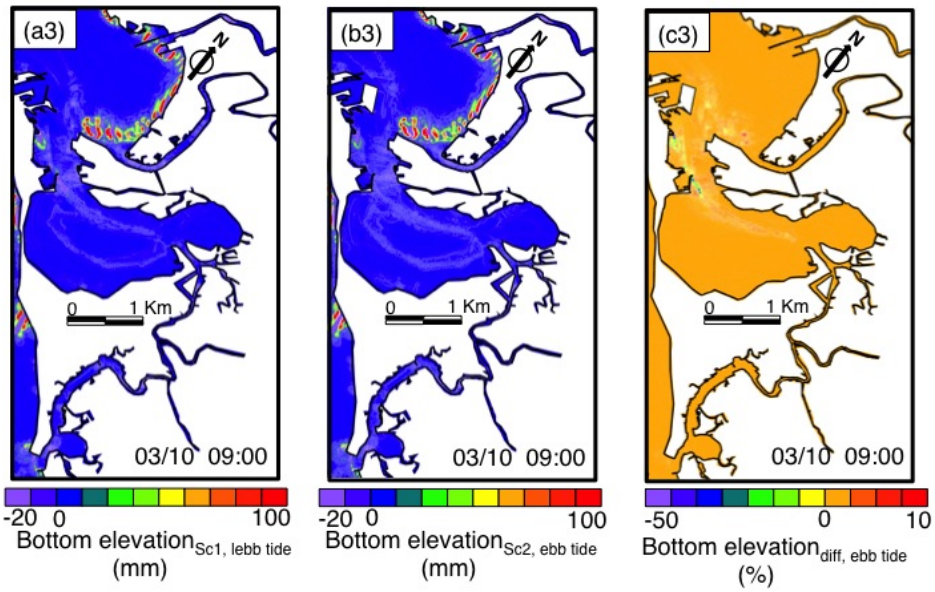

Figure 7.10: A time series of bottom elevation (mm) in the Bay of Cádiz at ebb tide period 03/10 09:00. Panels a, b and c correspond to Sc_1, Sc_2 and $Sc_2 * 100/Sc_1$, respectively.

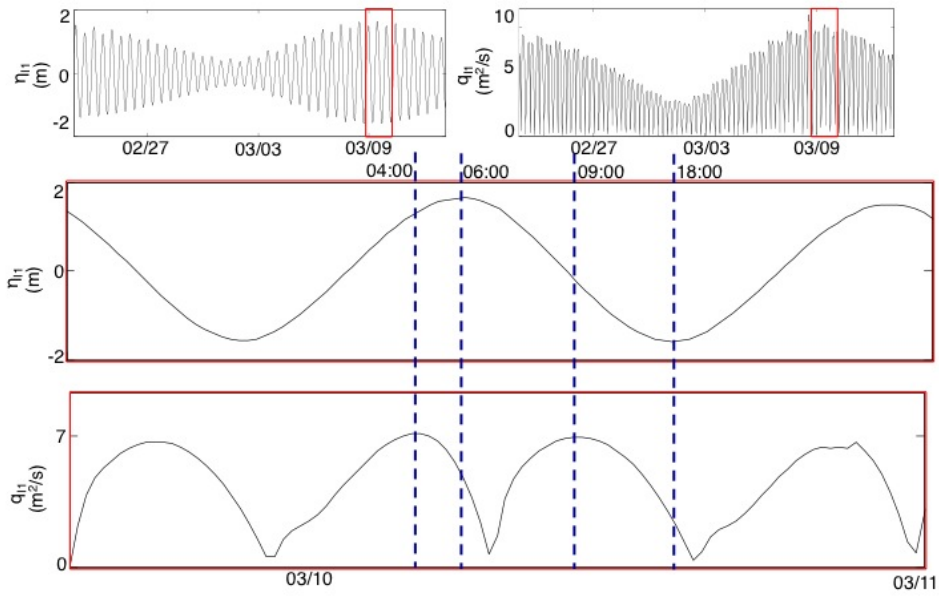

Figure 7.11: Tidal level (upper panel) and Tidal current velocity (lower panel) in the reference point I_1. Vertical dashed lines indicate middle flood (04:00), high water (06:00), middle ebb (09:00) and low water (18:00) times during spring tide. Comparisons at these times are discussed in the main text.

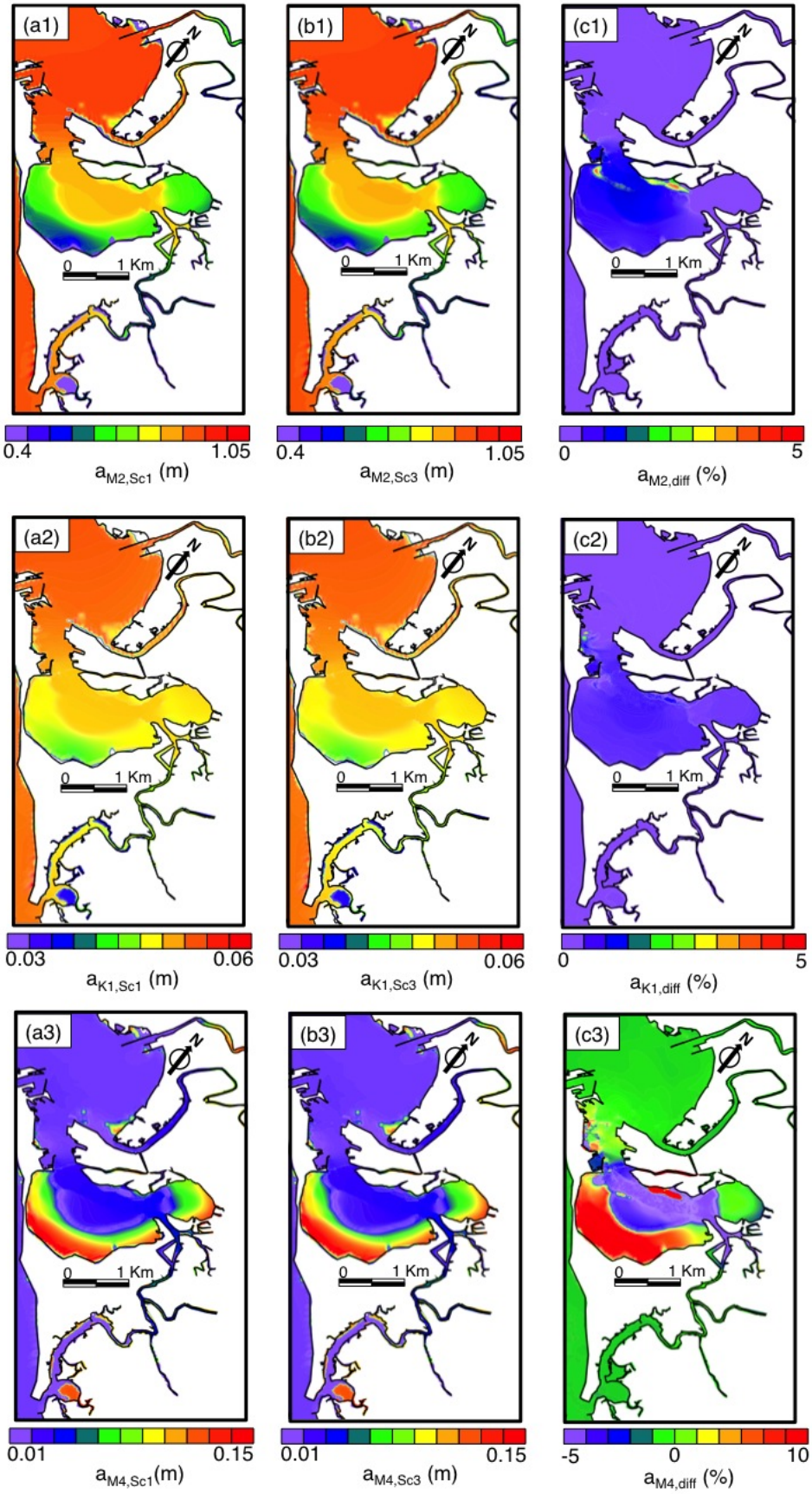

Figure 7.12: Influence of the cross-bay bridge on tide amplitude in bay (From Febreuar 22 to March 14, 2012). (a1), (a2) and (a3) M2, K1 and M4 amplitude, respectively (Sc_1). (b1), (b2) and (b3) M2, K1 and M4 amplitude, respectively (Sc_3). (c1) and (c2) Difference at M2, K1 and M4 amplitude, respectively ($Sc_3 * 100/Sc_1$) (blue = decrease and red = increase).

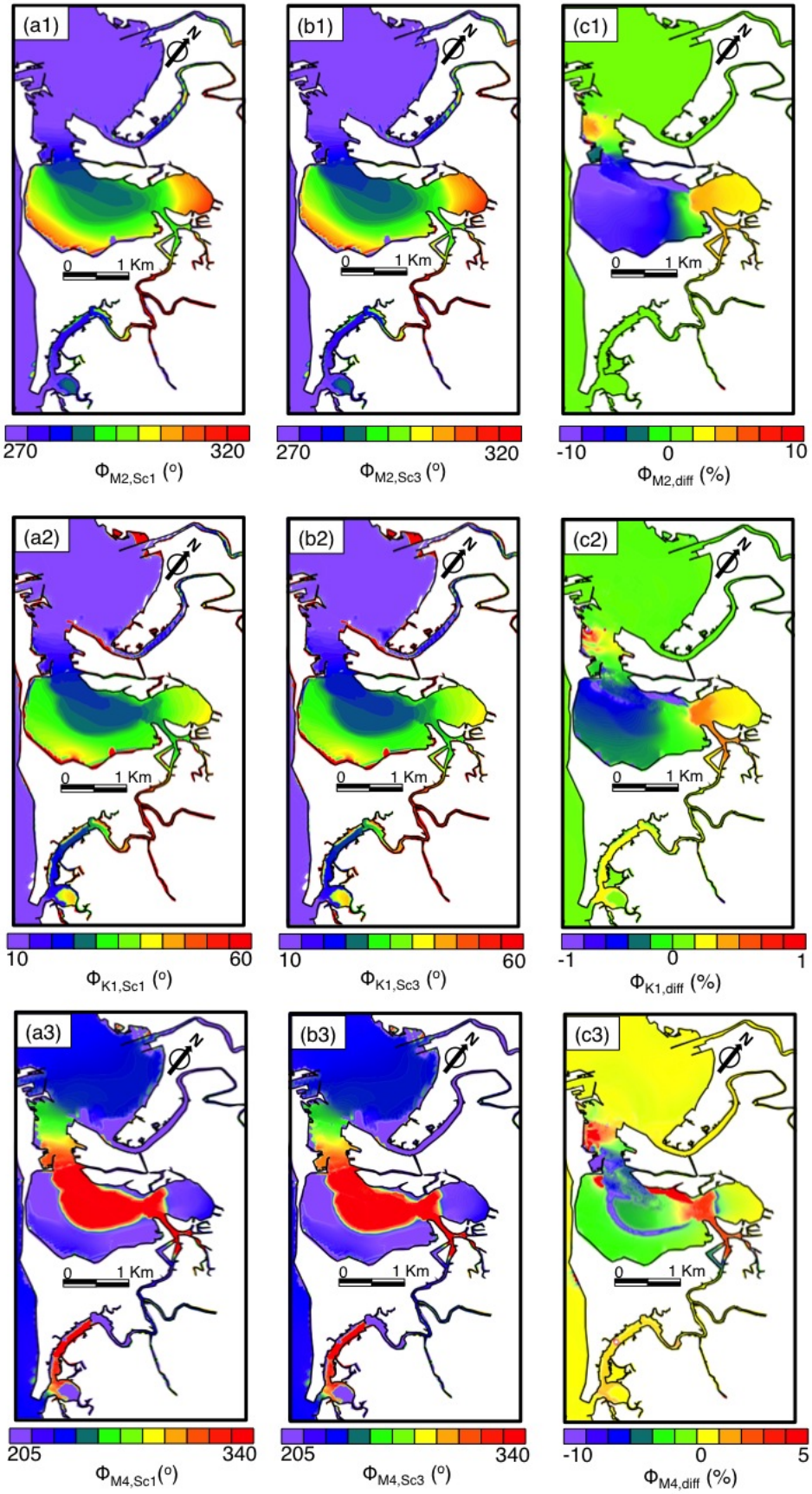

Figure 7.13: Influence of the cross-bay bridge on tide amplitude in bay (From Febreuar 22 to March 14, 2012). (a1), (a2) and (a3) M2, K1 and M4 amplitude, respectively (Sc_1). (b1) and (b2) M2, K1 and M4 amplitude, respectively (Sc_3). (c1) and (c2) Difference at M2, K1 and M4 amplitude, respectively ($Sc_3 * 100/Sc_1$).

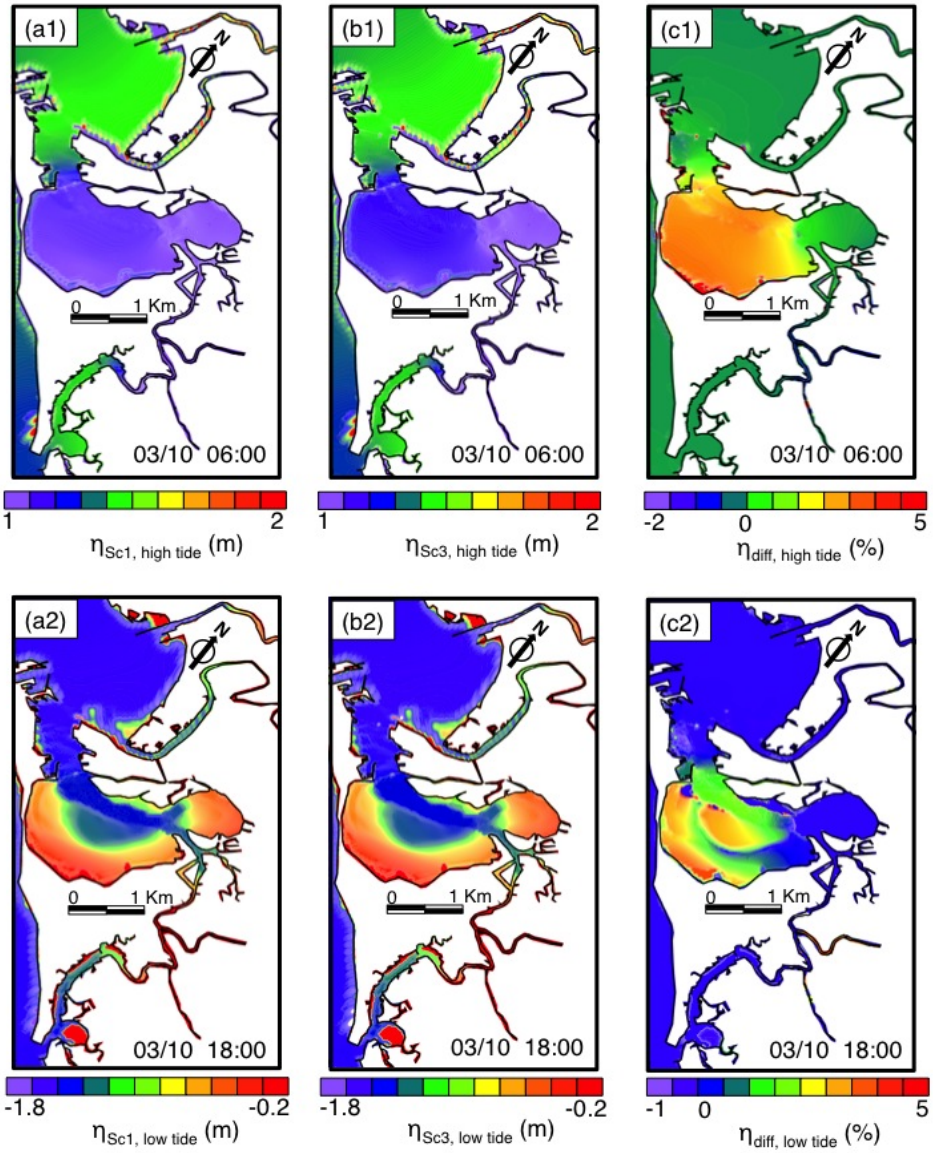

Figure 7.14: Influence of the cross-bay bridge on tidal level in bay (March 10, 2012). (a1) and (a2) High tide/low tide (Sc_1) according to the time slices in Figure 7.11. (b1) and (b2) High tide/low tide (Sc_3). (c1) and (c2) Difference at high tide/low tide ($Sc_3 * 100/Sc_1$).

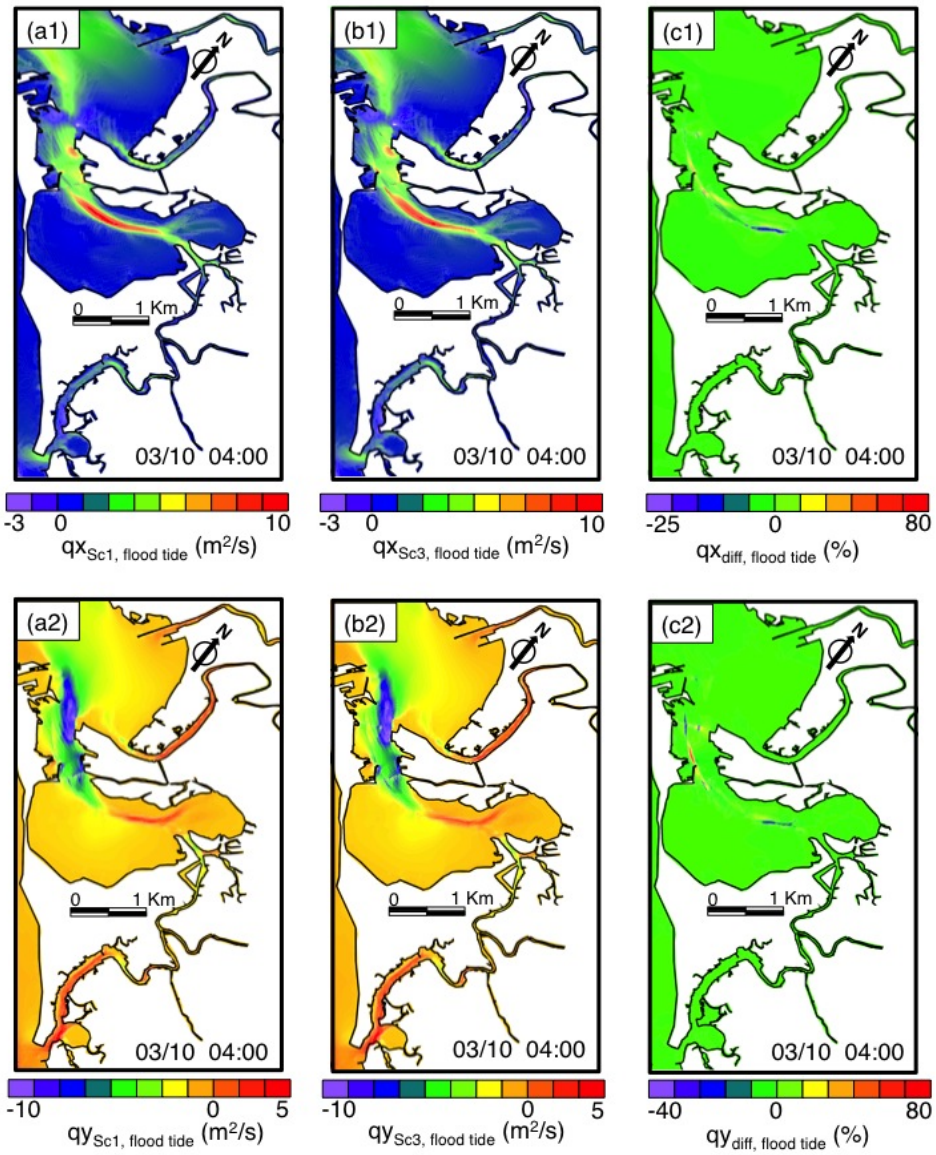

Figure 7.15: Influence of the cross-bay bridge on tidal level in bay (March 10, 2012). (a1) and (a2) Flow rate per unit width (q_x and q_y, respectively) at flood tide (Sc_1) according to the time slices in Figure 7.11. (b1) and (b2) Flow rate per unit width (q_x and q_y, respectively) at flood tide (Sc_3). (c1) and (c2) Difference at flow rate per unit width (q_x and q_y, respectively) at flood tide ($Sc_3 * 100/Sc_1$).

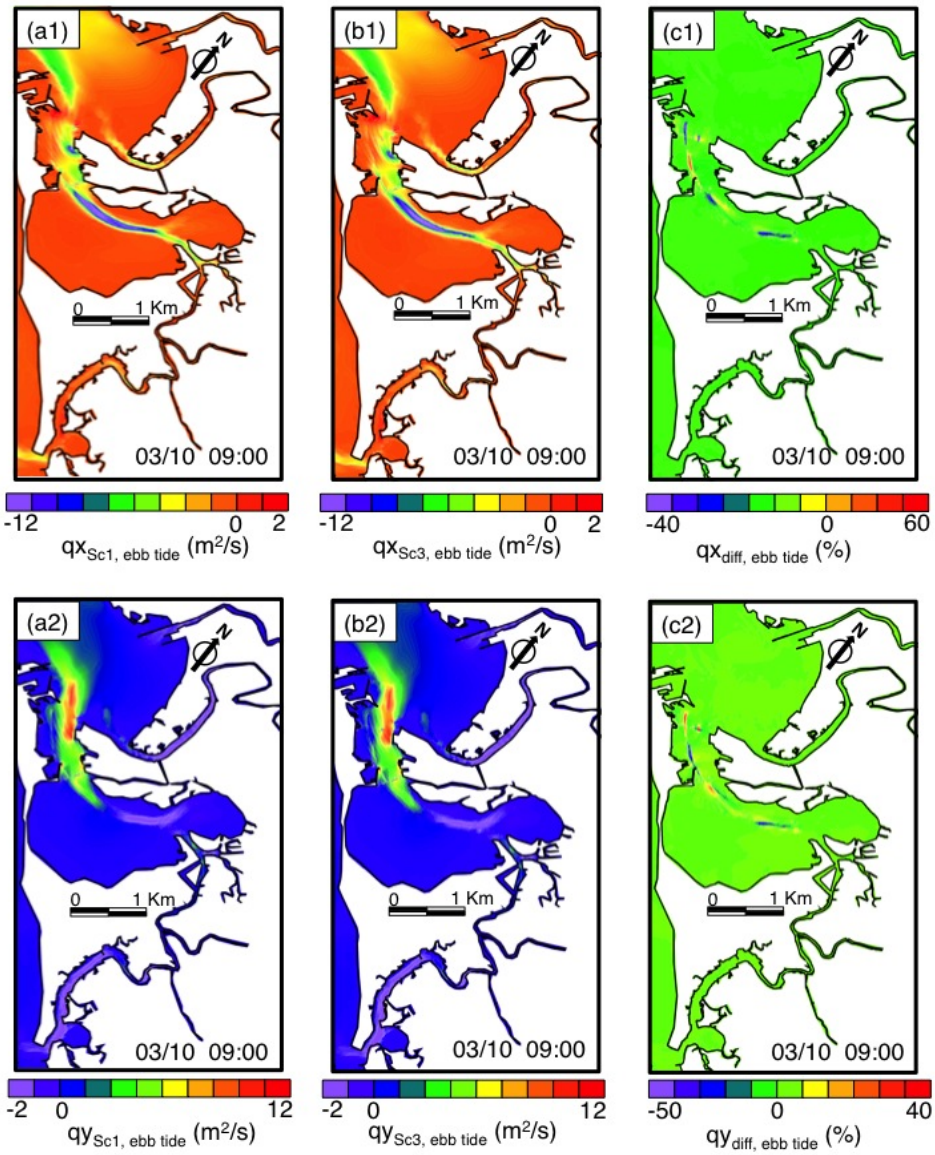

Figure 7.16: Influence of the cross-bay bridge on tidal level in bay (March 10, 2012). (a1) and (a2) Flow rate per unit width (q_x and q_y, respectively) at ebb tide (Sc_1) according to the time slices in Figure 7.11. (b1) and (b2) Flow rate per unit width (q_x and q_y, respectively) at ebb tide (Sc_3). (c1) and (c2) Difference at flow rate per unit width (q_x and q_y, respectively) at ebb tide ($Sc_3 * 100/Sc_1$).

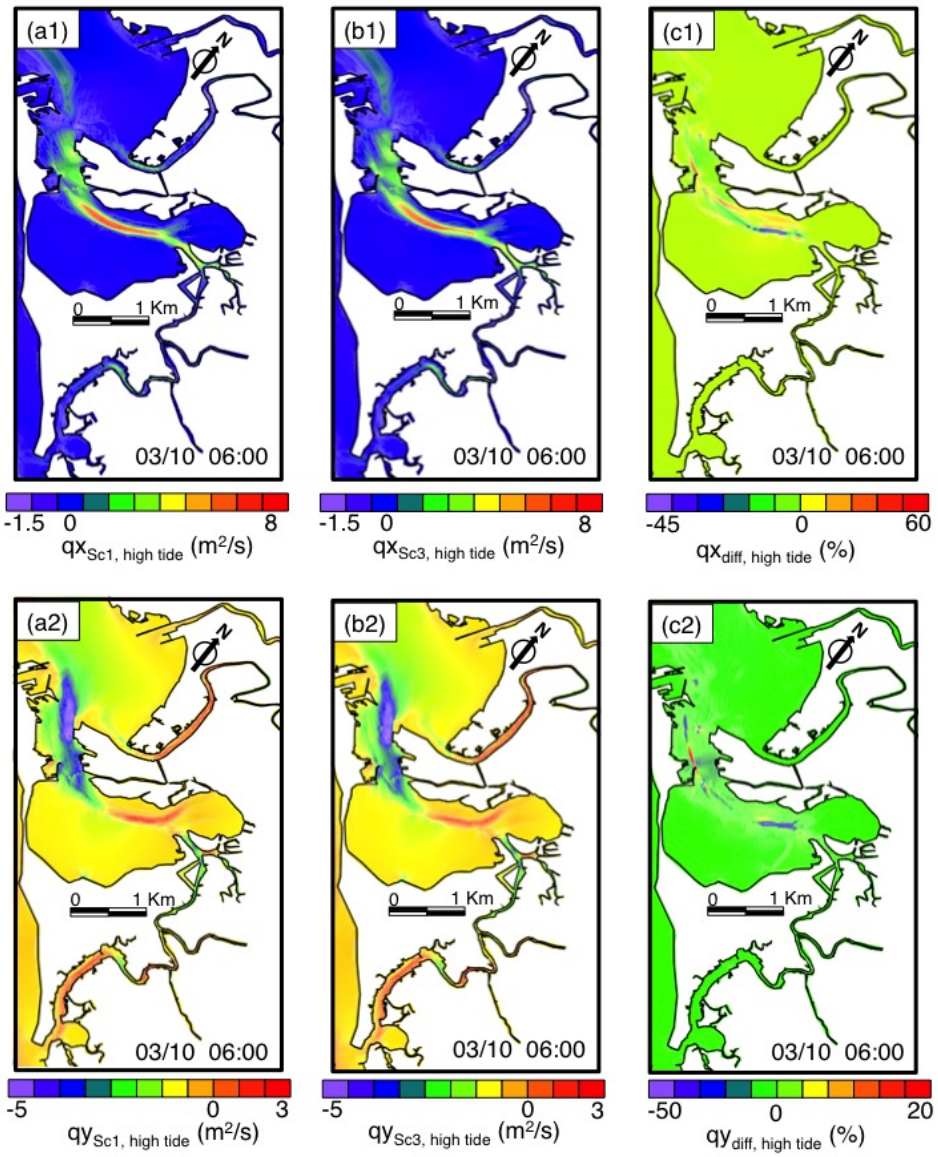

Figure 7.17: Influence of the cross-bay bridge on tidal level in bay (March 10, 2012). (a1) and (a2) Flow rate per unit width (q_x and q_y, respectively) at high tide (Sc_1) according to the time slices in Figure 7.11. (b1) and (b2) Flow rate per unit width(q_x and q_y, respectively) at high tide (Sc_3). (c1) and (c2) Difference at flow rate per unit width (q_x and q_y, respectively) at high tide ($Sc_3 * 100/Sc_1$).

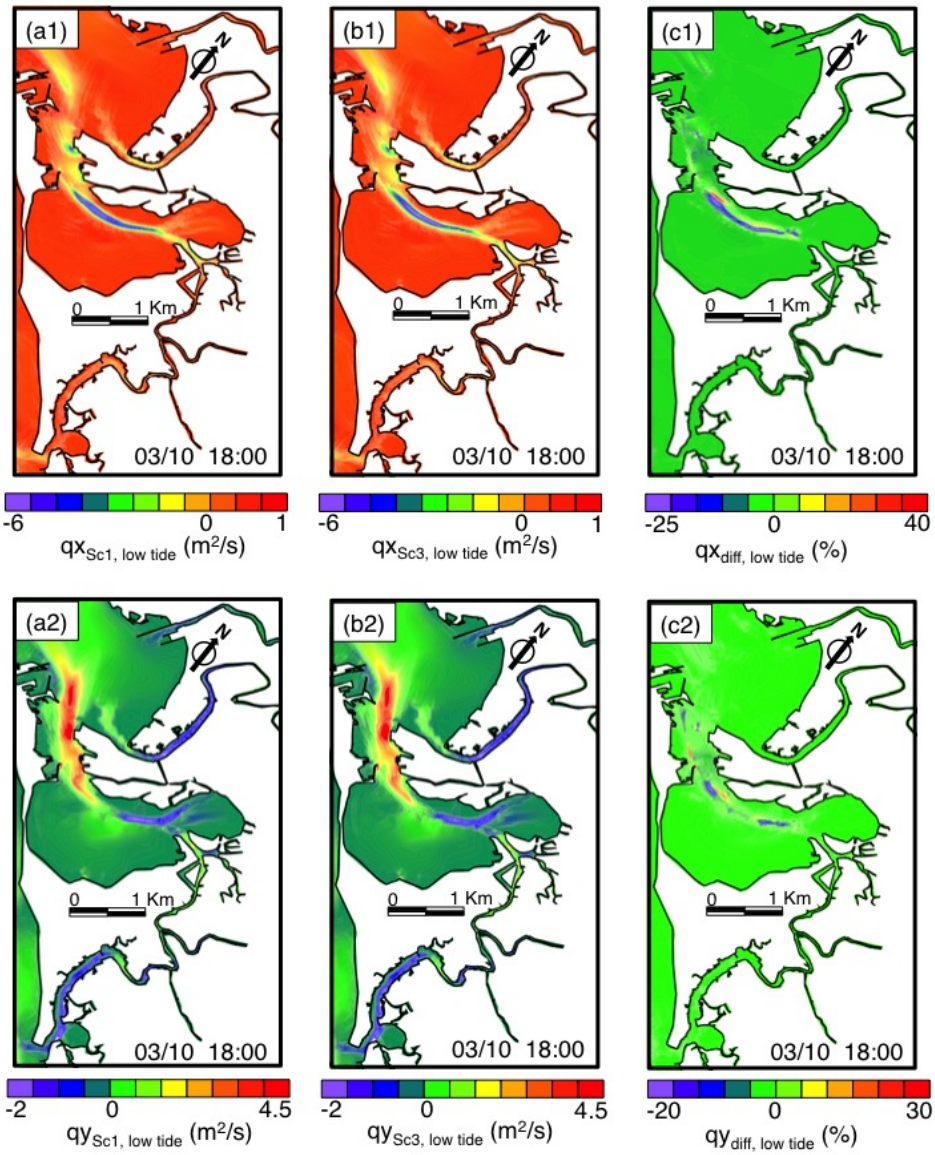

Figure 7.18: Influence of the cross-bay bridge on residual flow in bay (March 10, 2012). (a1) and (a2) Flow rate per unit width (q_x and q_y, respectively) at low tide (Sc_1) according to the time slices in Figure 7.11. (b1) and (b2) Flow rate per unit width (q_x and q_y, respectively) at low tide (Sc_3). (c1) and (c2) Difference at flow rate per unit width (q_x and q_y, respectively) at low tide ($Sc_3 * 100/Sc_1$).

the influence on the circulation is still obvious, decreases the flow rate per unit width on the north side of bridge. At ebb tide (c1 and c2-Figure 7.16), the flow rate per unit width between two adjacent sets of piers (fourth and fifth) increases $3\,m^2/s$; however, the bridge has a stronger influence on the south side of bridge. At low tide (c1 and c2-Figure 7.18),flow rate per unit width is also relatively weak. At flood tide and ebb tide, flow rate per unit width between the piers has and increases of 60%.

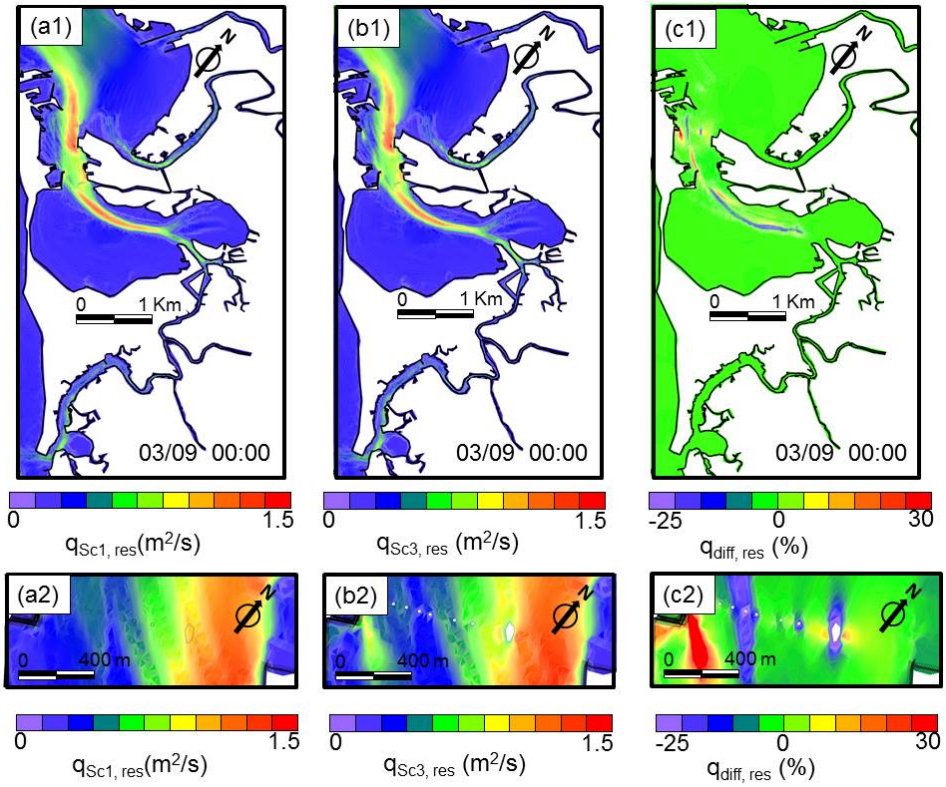

Figure 7.19: Influence of the cross-bay bridge on tidal level in bay (March 10, 2012). (a) Without bridge (Sc_1); (b) with bridge (Sc_3); (c) difference of residual transport ($Sc_3 * 100/Sc_1$).

Residual transports are caused by multiple factors, ranging from nonlinearities in the bed stress, continuity equation, and advection term in momentum equation, to irregular topography. Comparing with the tidal currents, residuals are much smaller in magnitude. Its significance in on the long-term mass transport. Residual transport in Figure 7.19 are arranged along the SW waterway at the Puntales Channel, which are all formed under the influence of topography. The maximum decrease inside the bay is caused by low current (c1-Figure 7.19). The maximum changes occur near to the bridge. Residual transport s decrease slightly after the bridge construction (c1-Figure 7.19). Figure 7.20 shows the vectors of the residual transports for Sc_3 (red arrows) and Sc_1 (black arrows). In the left side of the navigation channel streamlines associated to the residual transports rotate clockwise, with the opposite on the right side of the navigation channel. In the inner basin, the vector rotates anticlokwise in left side of the navigation channel and clockwise in right side of the navigation channel. The changes from erosion to sedimentation will

be determined by the direction of residual transports. Nevertheless, the real storage of sedimentation will depend on sediment availability.

Ten cross-sections are chosen to evaluate the tidal prism (Figures 7.21 and 7.22). The tidal prism is increased by 2-3% after construction. Tidal prism rises at all cross-sections except at San Pedro estuary and Carracas creek, in which slightly decreases approx. 0.5%. The tidal prism of the Guadalete estuary and the Sancti-Petri creek are apparently not affected by the interventions.

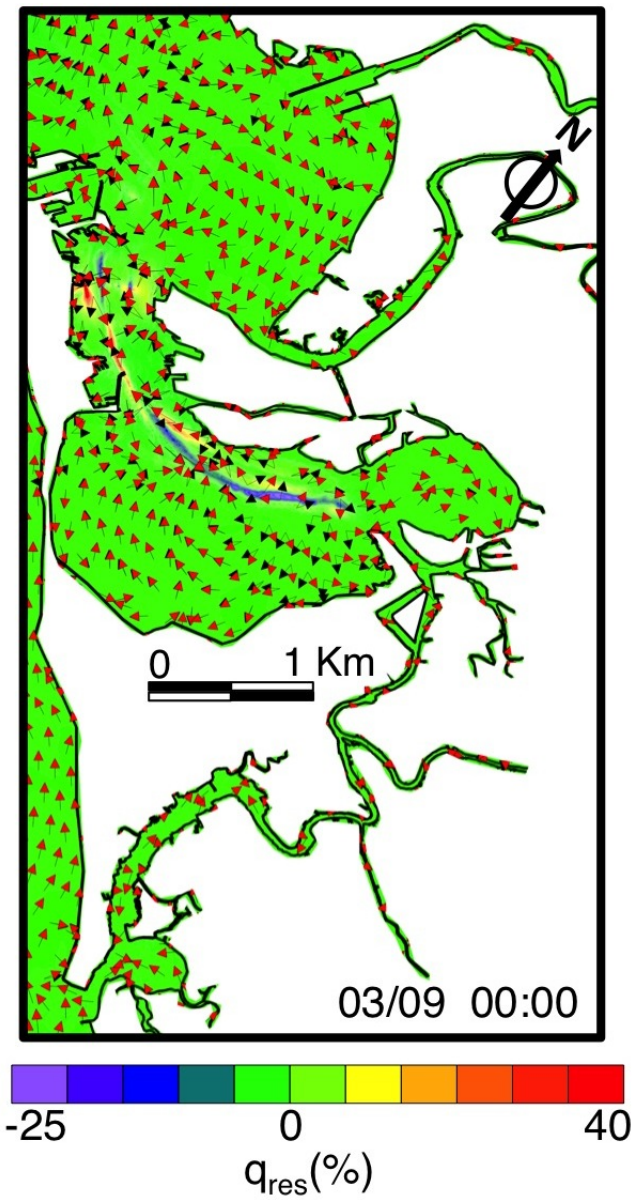

Figure 7.20: Residual transport at Sc_3 (red arrows) and Sc_1 (black arrows). The colormap in the background represents the variation in the magnitudes ($Sc_3 * 100/Sc_1$).

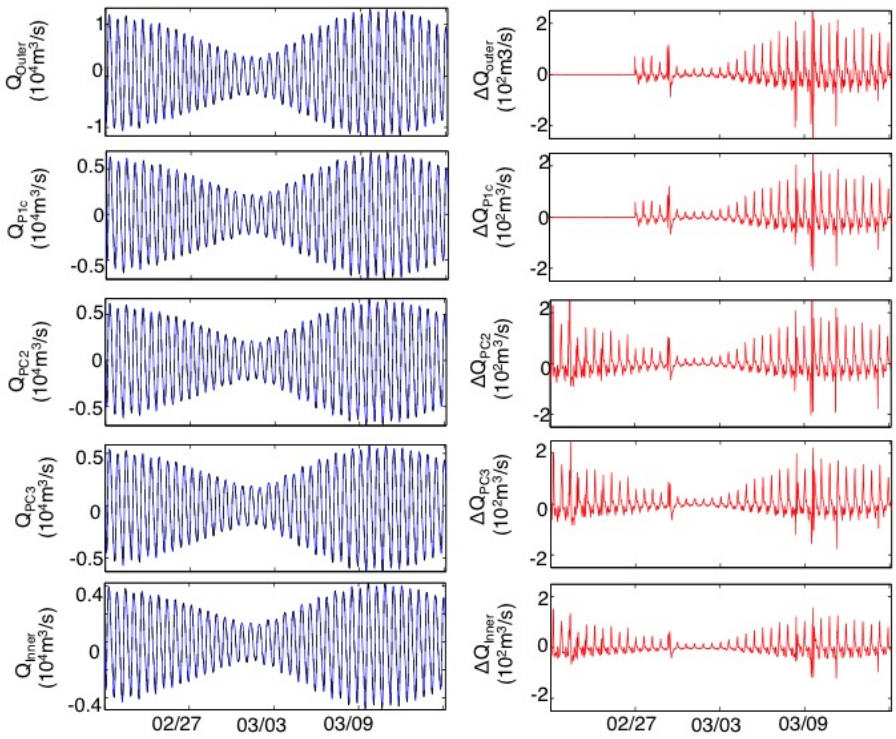

Figure 7.21: Influence of the cross-bay bridge on flow rate in different section along the bay. Blue line corresponds to scenario without bridge; black line corresponds to scenario with bridge; red line corresponds to the difference between with and without bridge.

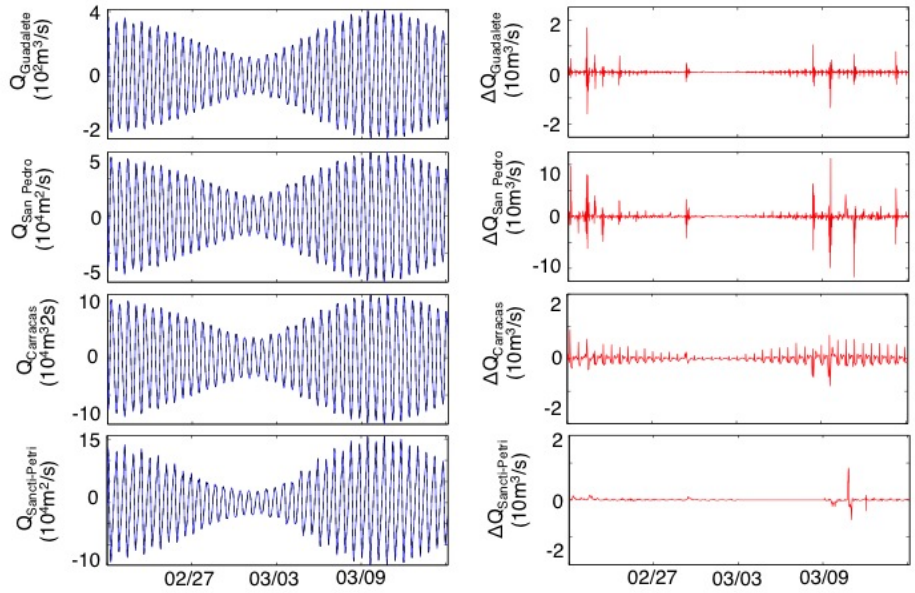

Figure 7.22: Influence of the cross-bay bridge on flow rate in the mouth of the Guadalete estuary, San Pedro estuary, Carracas Creek and Sancti-Petri Creek, from upper to lower respectively. Blue line corresponds to scenario without bridge; black line corresponds to scenario with bridge; red line corresponds to the difference between with and without bridge.

7.3.2 Morphodynamics

The highest changes are reached during flood tide (Figure 7.23). The MSC (middle panel-Figure 7.23) is more affected than the SSC (upper panel-Figure 7.23). The decrease of the SSC (60%) is located at the south of the bridge, which is displaced to the south of the Puntales channel, where the concentration of the SSC increase until 70%. The concentration of the MSC increase over 60% in the inner bay. This mud mainly seems to come from the mouth of the Carracas creek and the middle of the navigation channel, where there is a decrease of MSC (40%). Before the construction of the bridge, the southern area of the Puntales channel and the entrance of the inner bay are eroded (red color; lower panel-Figure 7.23). At south-west of the bridge the bottom elevation is reduced around 10%. In the case of the sediment evolution after interventions before the construction of the bridge at ebb period (Figure 7.25), the changes are lower than the flood period.

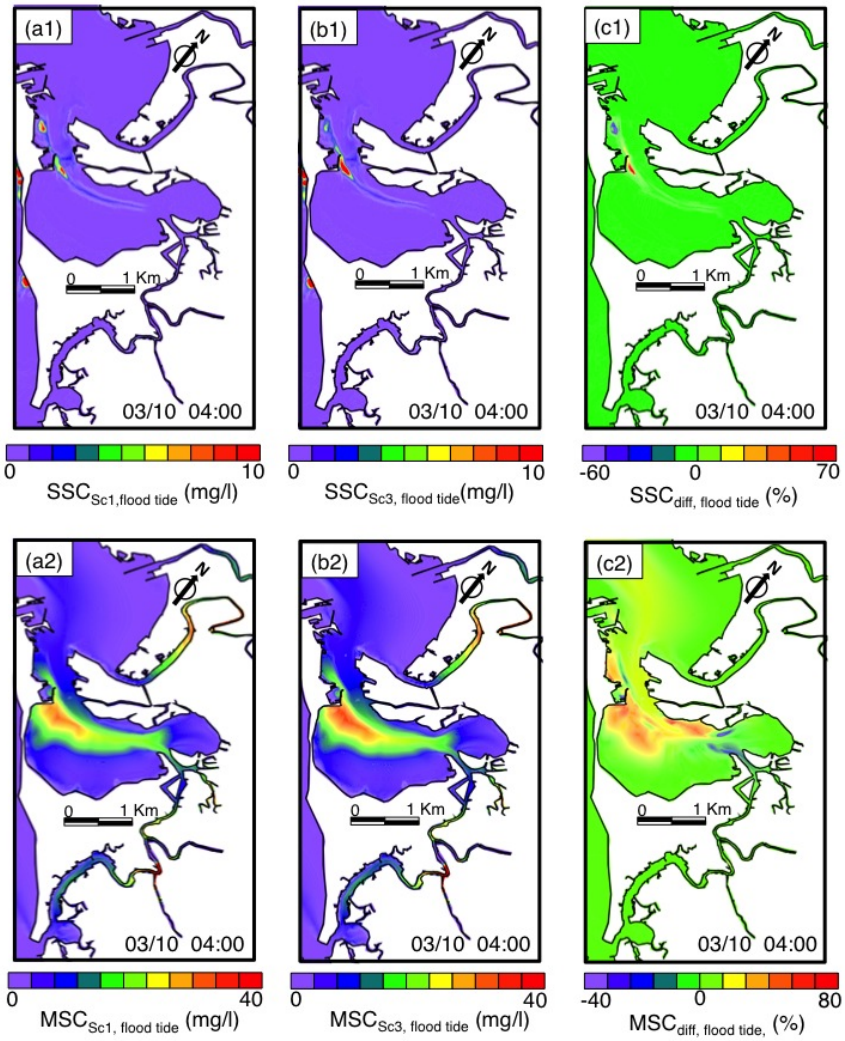

Figure 7.23: A time series of sand concentration (mg/l) and mud concentration (mg/l) in the Bay of Cádiz at flood tide period 03/10 04:00 (panels 1 and respectively). Panels a, b and c correspond to Sc_1, Sc_3 and $Sc_3 * 100/Sc_1$, respectively (blue = decrease and red = increase).

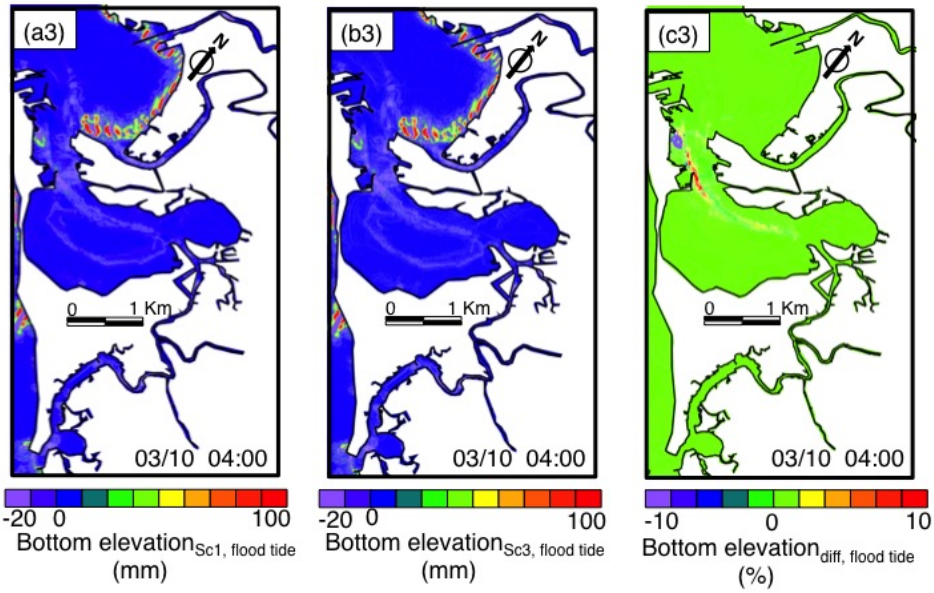

Figure 7.24: A time series of bottom elevation (mm) in the Bay of Cádiz at flood tide period 03/10 04:00. Panels a, b and c correspond to Sc_1, Sc_3 and $Sc_3 * 100/Sc_1$, respectively (blue = decrease and red = increase).

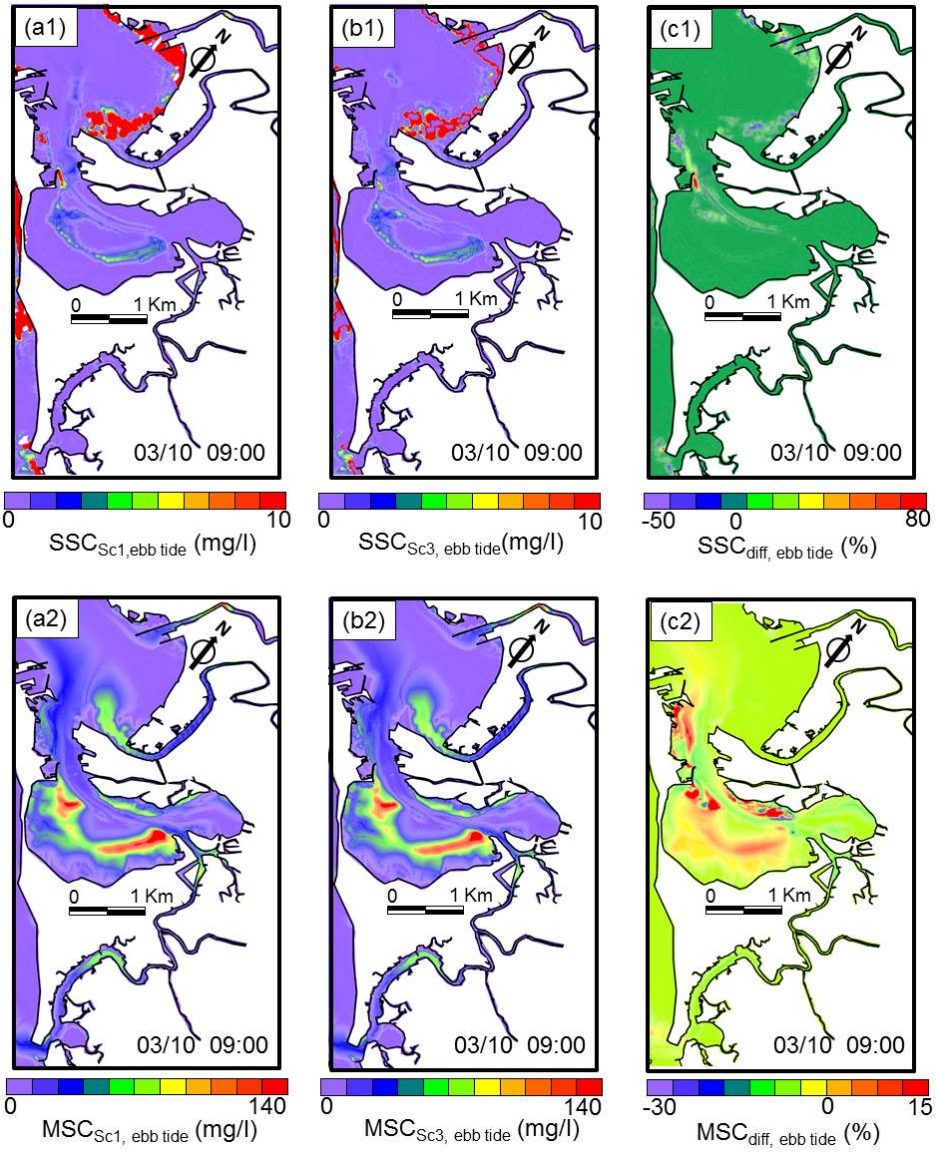

Figure 7.25: A time series of sand concentration (mg/l) and mud concentration (mg/l) in the Bay of Cádiz at ebb tide period 03/10 09:00 (panels 1 and 2, respectively). Panels a, b and c correspond to Sc_1, Sc_3 and $Sc_3 * 100/Sc_1$, respectively.

7.4 Scenario 4

7.4.1 Hydrodynamics

7.4.1.1 Tidal Level

The amplitude of M2 tidal components is increased at Puntales Channel (5%) and is decreased by 5% in the inner bay (c1-Figure 7.27). Tidal phase of the three constituents is delayed in the inner bay (5%) while the tidal phase is overtaken the mouth of Puntales Channel (10%) (c -Figure 7.28). The changes of the amplitude of M4 tidal components are

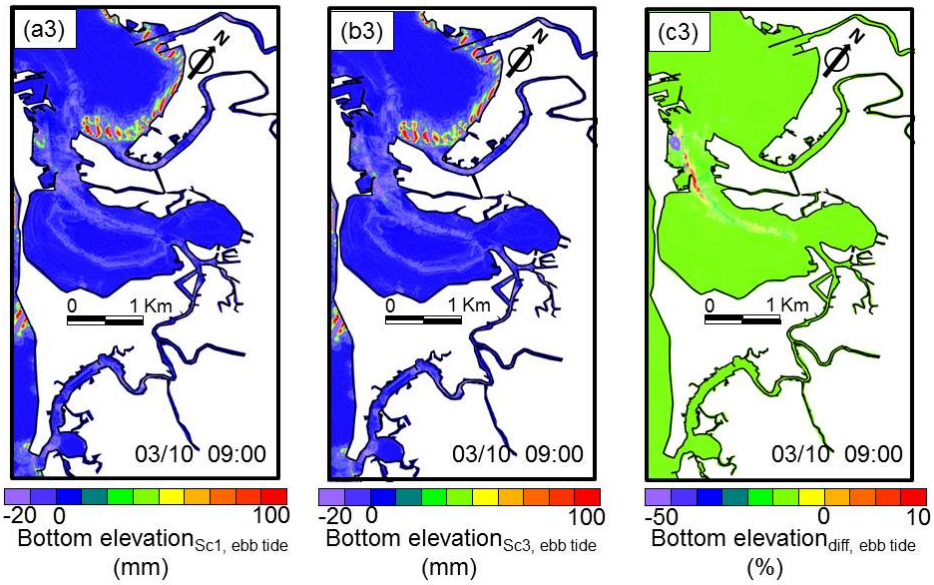

Figure 7.26: A time series of bottom elevation (mm) in the Bay of Cádiz at ebb tide period 03/10 09:00. Panels a, b and c correspond to Sc_1, Sc_3 and $Sc_3 * 100/Sc_1$, respectively.

different at the north of Puntales Channel than at the south. There is an increase of 10% at the north and a decrease of 20% at the south of the Puntales Channel (c3-Figure 7.27). The inner bay is also affected, and it experienced a decrease (10%). The amplitude of K1 tidal components does not shows differences (c2-Figure 7.27).

Figure 7.29 shows the changes in water level before the future constructions at high and low tide. The highest changes are found in the inner bay. At high tide, tidal level is higher outside than inside the bay, 50 cm higher in the model without bridge (a1-Figure 7.29), and 51 cm higher with bridge (b1-Figure 7.29). Tidal level does not change in the outer bay, however near the Puntales Channel, inner bay and Carracas creeks do. The tidal level (c1-Figure 7.29) rises at Puntales Channel, with a maximum increase of 2 cm at the middle. However, the tidal level decrease through the inner bay, with the maximum reduction of 3 cm at Carracas creek. The tidal level at low tide is contrary to that at high tide, which are higher inside than outside the bay, 80 cm lower in the model without bridge piers (a2-Figure 7.29), and 83 cm lower in the model with bridge (b2-Figure 7.29). The effects of the constructions are proportionally higher at low tide than at high tide. The free surface elevations in the outer basin does not notice the constructions. The maximum increases are found at San Pedro estuary (2 cm) and Puntales Channel (2 cm), however the maximum decrease are observed at the mouth of Carracas creek (5 cm).

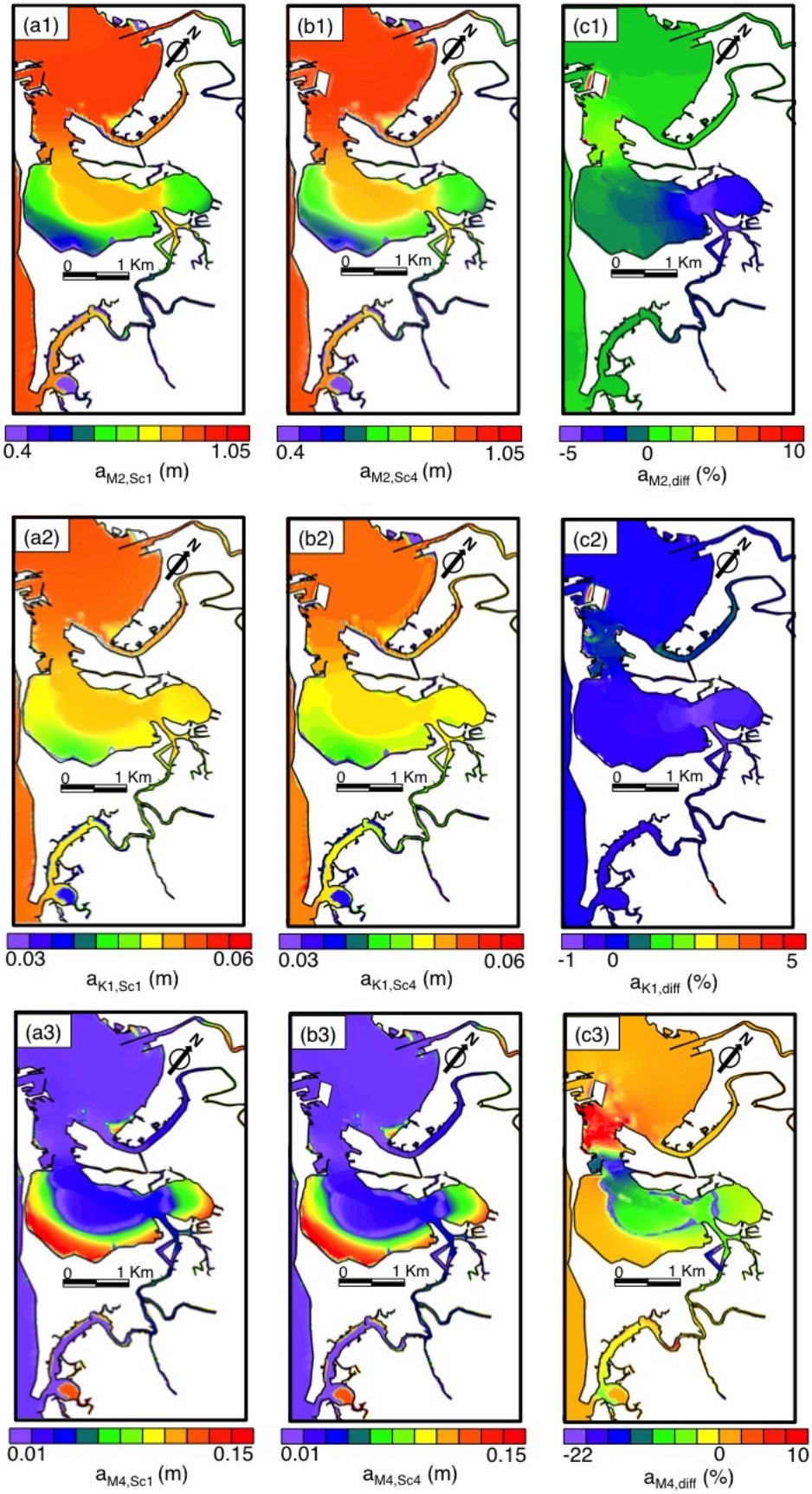

Figure 7.27: Influence of the cross-bay bridge on tide amplitude in bay (From Febreuar 22 to March 14, 2012). (a1), (a2) and (a3) M2, K1 and M4 amplitude, respectively (Sc_1). (b1) and (b2) M2, K1 and M4 amplitude, respectively (Sc_4). (c1) and (c2) Difference at M2, K1 and M4 amplitude, respectively ($Sc_4 * 100/Sc_1$).

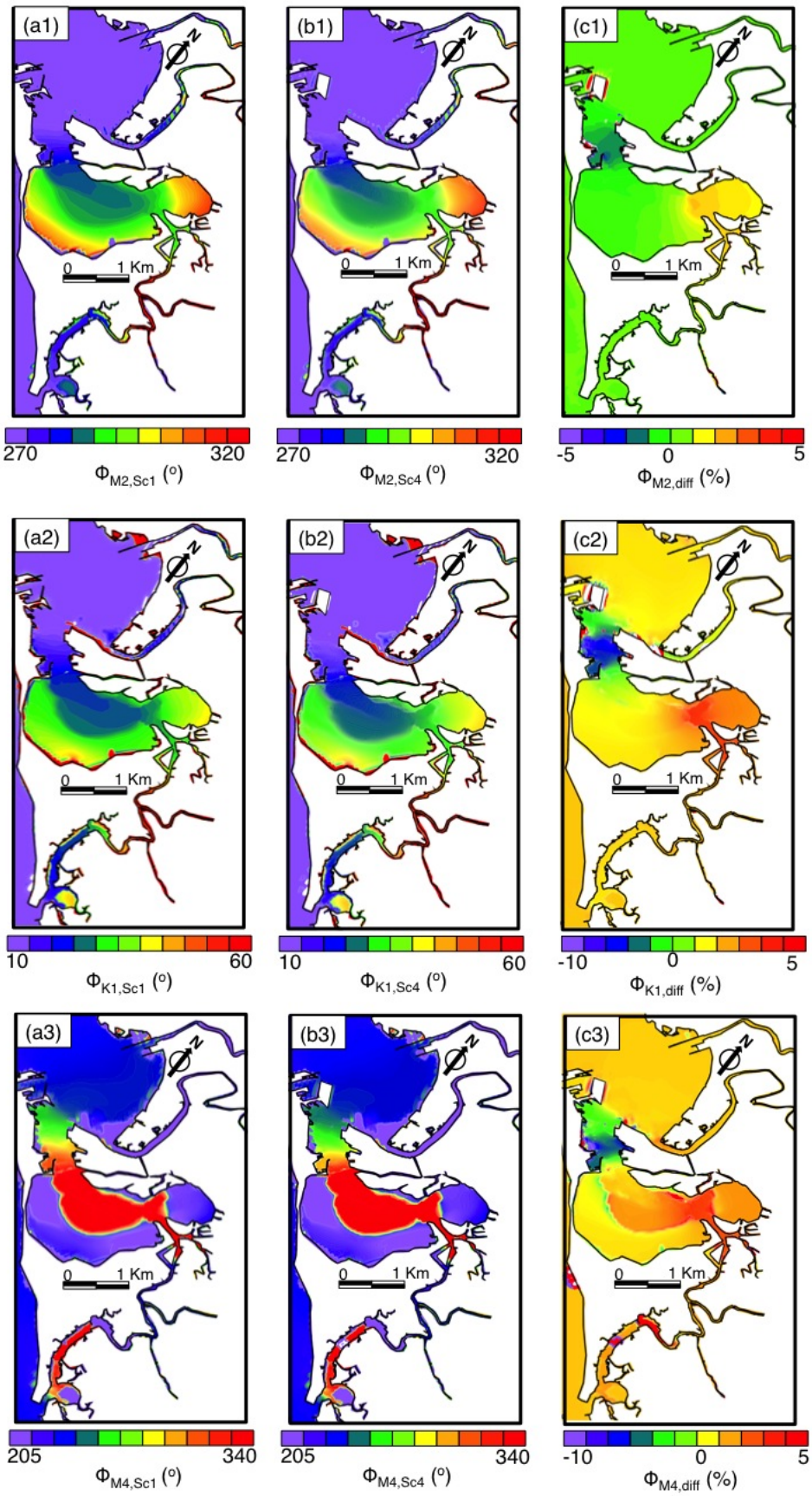

Figure 7.28: Influence of the cross-bay bridge on tide amplitude in bay (From Febreuar 22 to March 14, 2012). (a1), (a2) and (a3) M2, K1 and M4 amplitude, respectively (Sc_1). (b1) and (b2) M2, K1 and M4 amplitude, respectively (Sc_1). (c1) and (c2) Difference at M2, K1 and M4 amplitude, respectively ($Sc_4 * 100/Sc_1$).

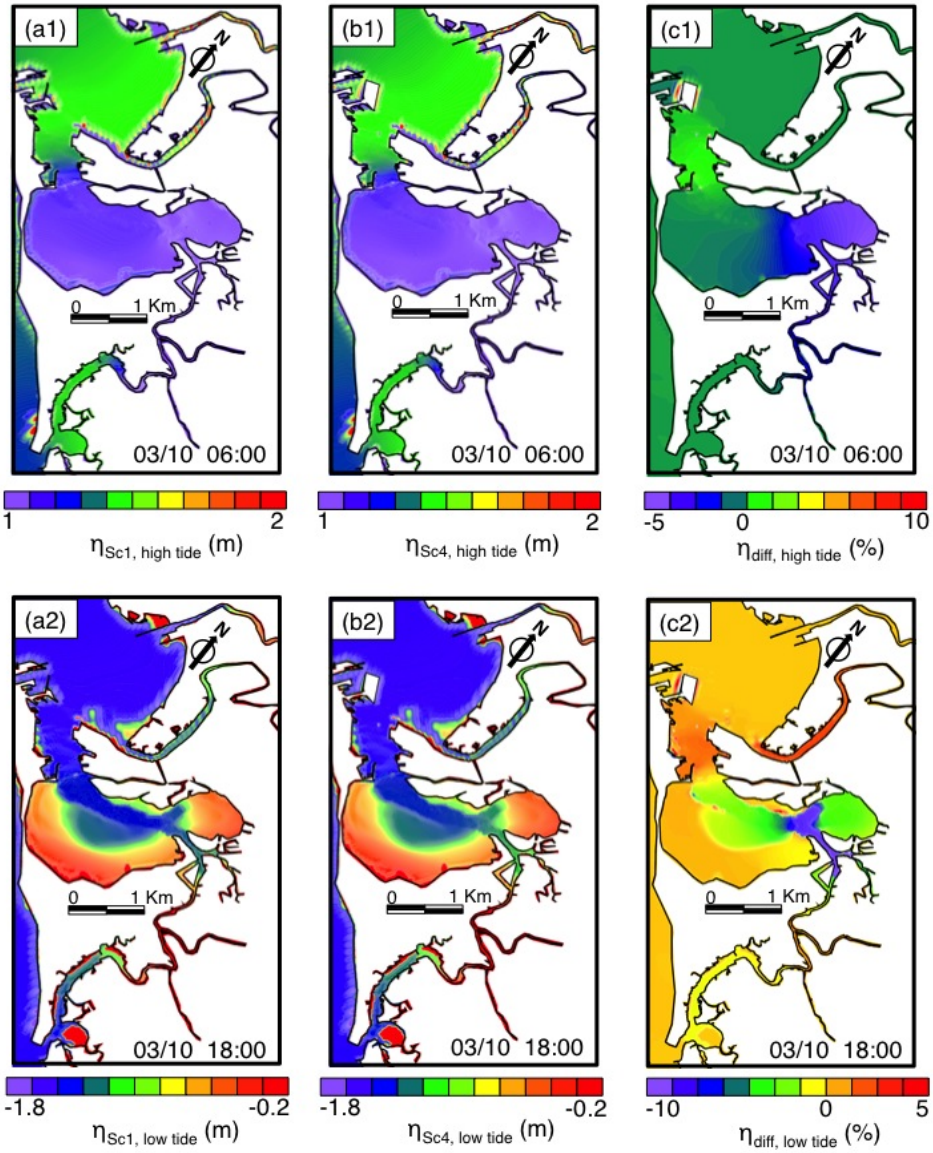

Figure 7.29: Influence of the cross-bay bridge on tidal level in bay (March 10, 2012). (a1) and (a2) High tide/low tide (Sc_1) according to the time slices in Figure 7.11. (b1) and (b2) High tide/low tide (Sc_4). (c1) and (c2) Difference at high tide/low tide ($Sc_4 * 100/Sc_1$).

7.4.1.2 Flow rate per unit width

The flow rate per unit width is analysed before and after constructions (Figures 7.30, 7.32, 7.31 and 7.33). Along the navigation channel the tidal flow increases after alterations. At flood tide (Figure 7.30), the flow rate per unit width along the y and the x direction decreases ($-5\,m^2/s$) at the navigation channel. However there is an increase close to the new terminal ($2\,m^2/s$).

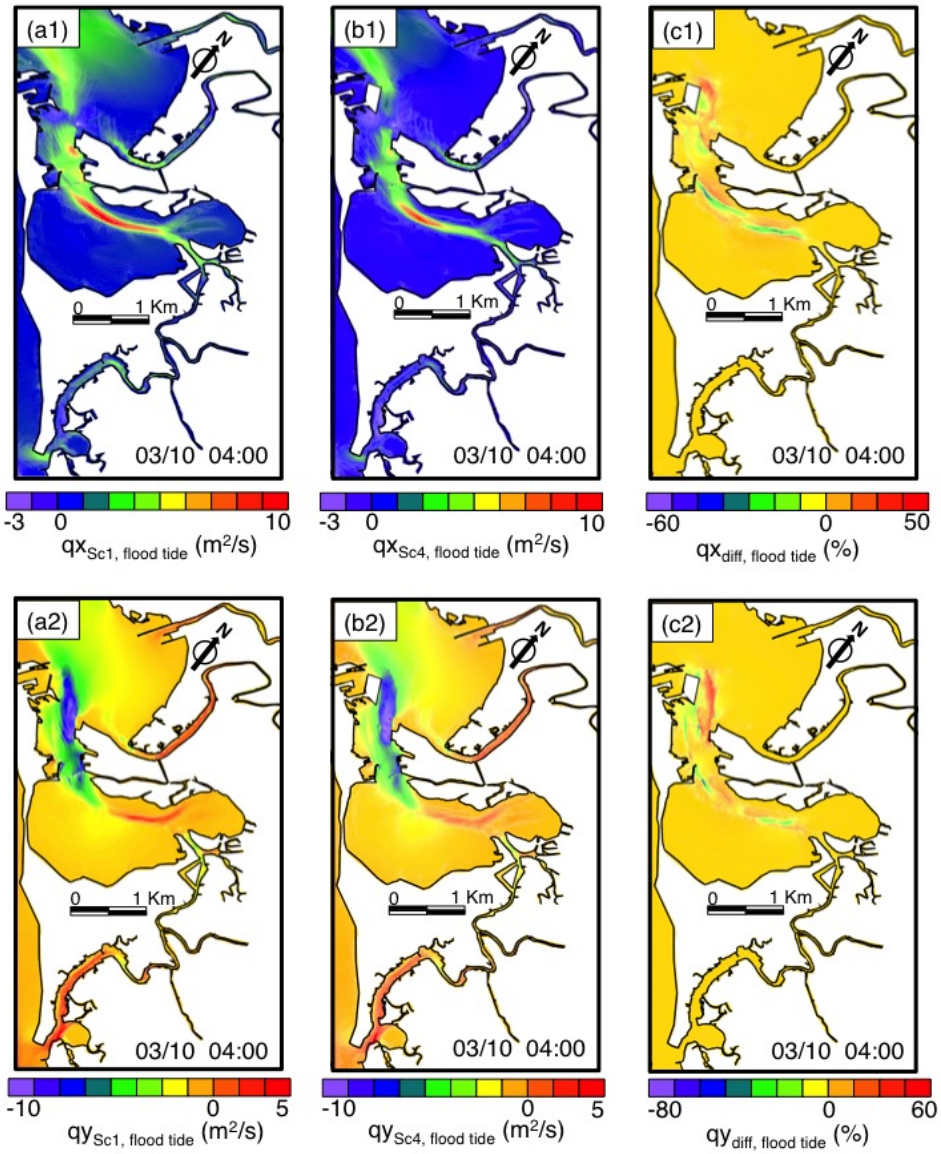

Figure 7.30: Influence of the cross-bay bridge on tidal level in bay (March 10, 2012). (a1) and (a2) Flow rate per unit width (q_x and q_y, respectively) at flood tide (Sc_1) according to the time slices in Figure 7.11. (b1) and (b2) Flow rate per unit width (q_x and q_y, respectively) at flood tide (Sc_4). (c1) and (c2) Difference at flow rate per unit width (q_x and q_y, respectively) at flood tide ($Sc_4 * 100/Sc_1$).

During ebb tides (Figure 7.31), the flow rate per unit width along the y direction decreases at the west of the navigation channel, with maximum decrease of $-2\,m^2/s$. It in-

creases at the east margin of the navigation channel ($5\,m^2/s$). The flow rate per unit width along -x direction is reduced inside the inner bay ($-1\,m^2/s$) and is increased close to the new terminal ($2\,m^2/s$).

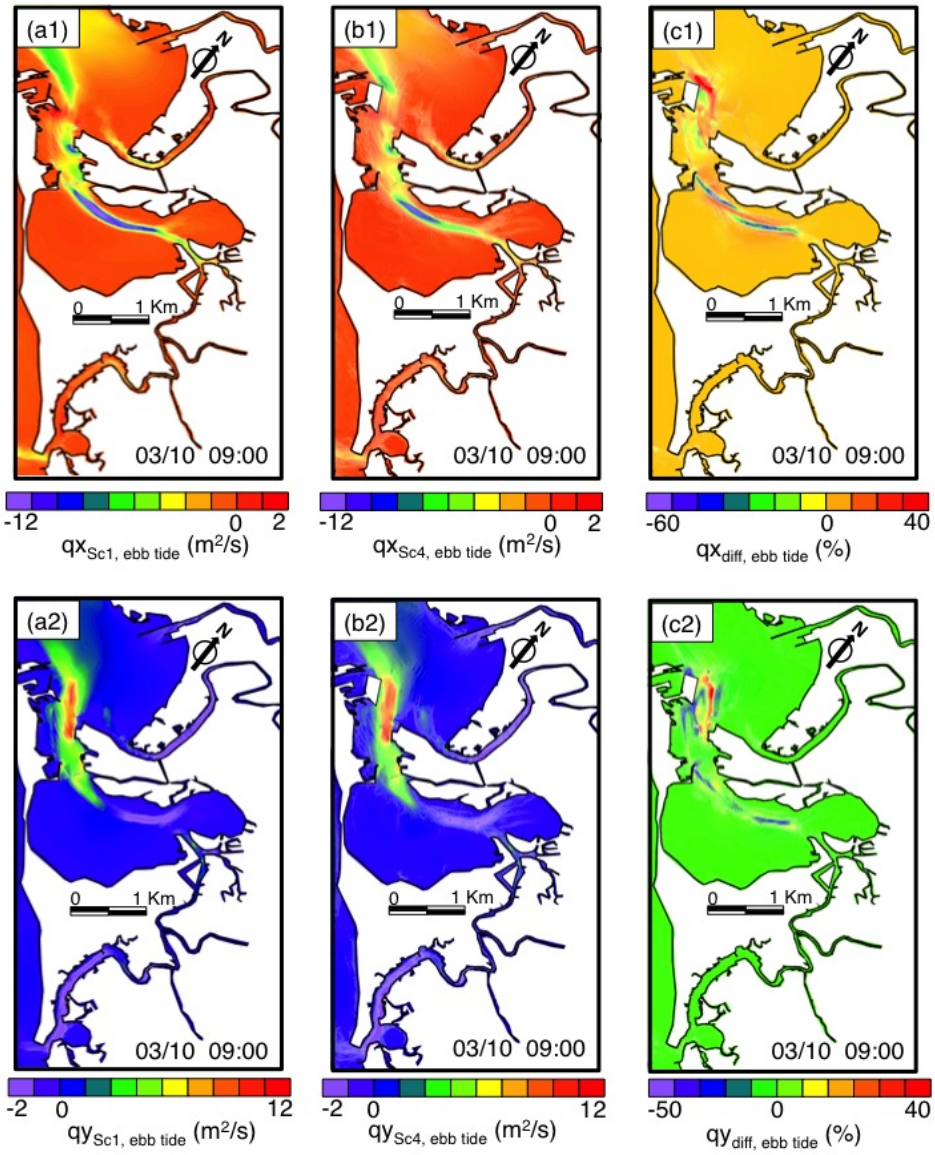

Figure 7.31: Influence of the cross-bay bridge on tidal level in bay (March 10, 2012). (a1) and (a2) Flow rate per unit width (q_x and q_y, respectively) at ebb tide (Sc_1) according to the time slices in Figure 7.11. (b1) and (b2) Flow rate per unit width (q_x and q_y, respectively) at ebb tide (Sc_4). (c1) and (c2) Difference at flow rate per unit width (q_x and q_y, respectively) at ebb tide ($Sc_4 * 100/Sc_1$).

The changes during high water (Figure 7.32) are higher than low water (Figure 7.33). During high tide, the flow rate per unit width along the y direction (c2-Figure 7.32) increases (decreases) at the east (west) margin of the new channel ($1\,m^2/s$ ($-1.5\,m^2/s$)) and the flow rate per unit width along -x direction (c1-Figure 7.32) increases (decreases) close to the new terminal, i.e. inner bay and the new channel navigation ($1\,m^2/s$ ($-4\,m^2/s$ and

$-1\,m^2/s$, respectively)). During low tide, the flow rate per unit width along the y direction (c2-Figure 7.33) only increase near the new terminal ($2\,m^2/s$). In the case of the -x direction (c1-Figure 7.33), the flow increases also around the new terminal ($2\,m^2/s$); however at the entrance of the inner bay the flow increases (decreases) around $1\,m^2/s$ ($-1\,m^2/s$).

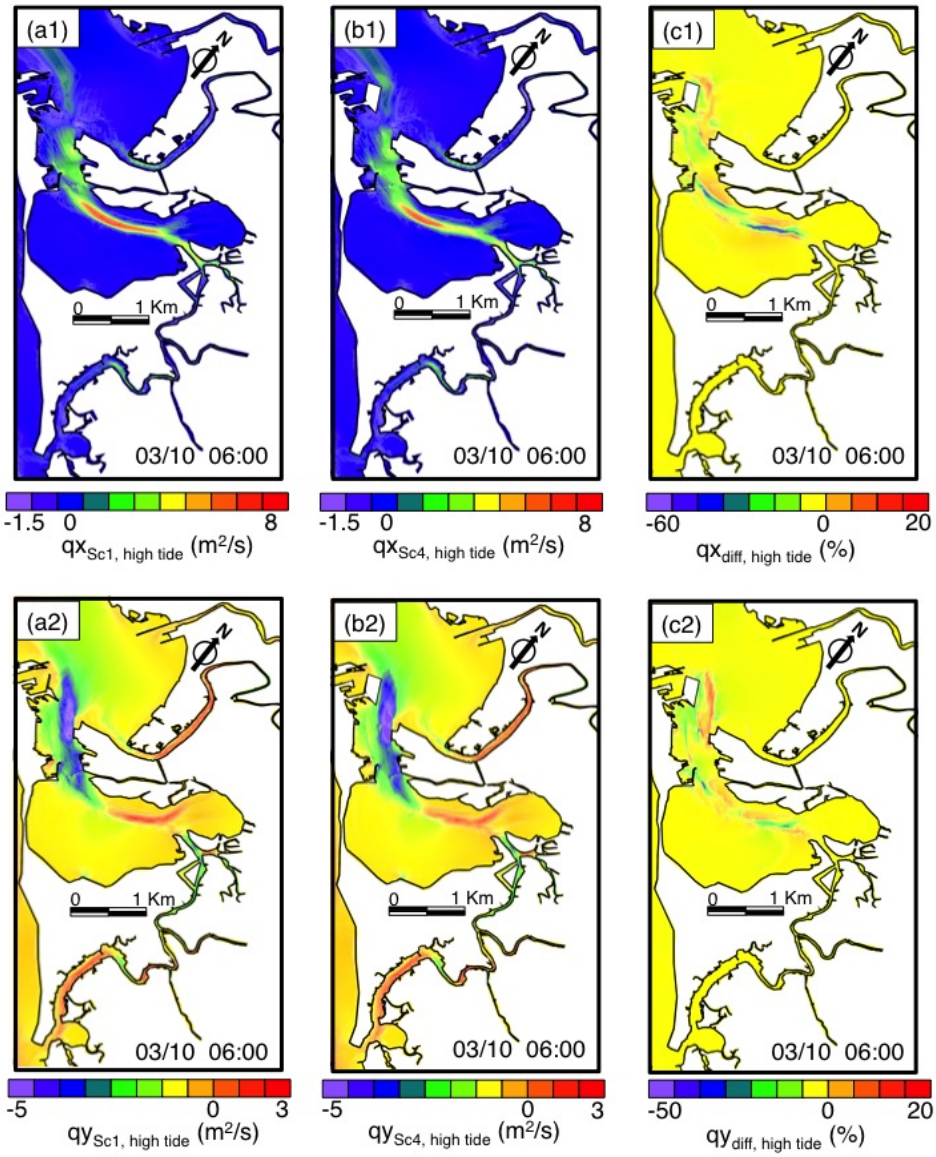

Figure 7.32: Influence of the cross-bay bridge on tidal level in bay (March 09, 2012). (a1) and (a2) Flow rate per unit width (q_x and q_y, respectively) at high tide (Sc_1) according to the time slices in Figure 7.11. (b1) and (b2) Flow rate per unit width (q_x and q_y, respectively) at high tide (Sc_4). (c1) and (c2) Difference at flow rate per unit width (q_x and q_y, respectively) at high tide ($Sc_4 * 100/Sc_1$).

Residual transport Figure 7.34 changes along the navigation channel at the inner bay, with a maximum decrease of $-2\,m^2/s$. The maximum increase is found around the new terminal ($3\,m^2/s$). Figure 7.35 shows the vectors of the residual transports for Sc_4 (red arrows) and Sc_1 (black arrows). The vectors rotate clockwise around P2.2 with the inter-

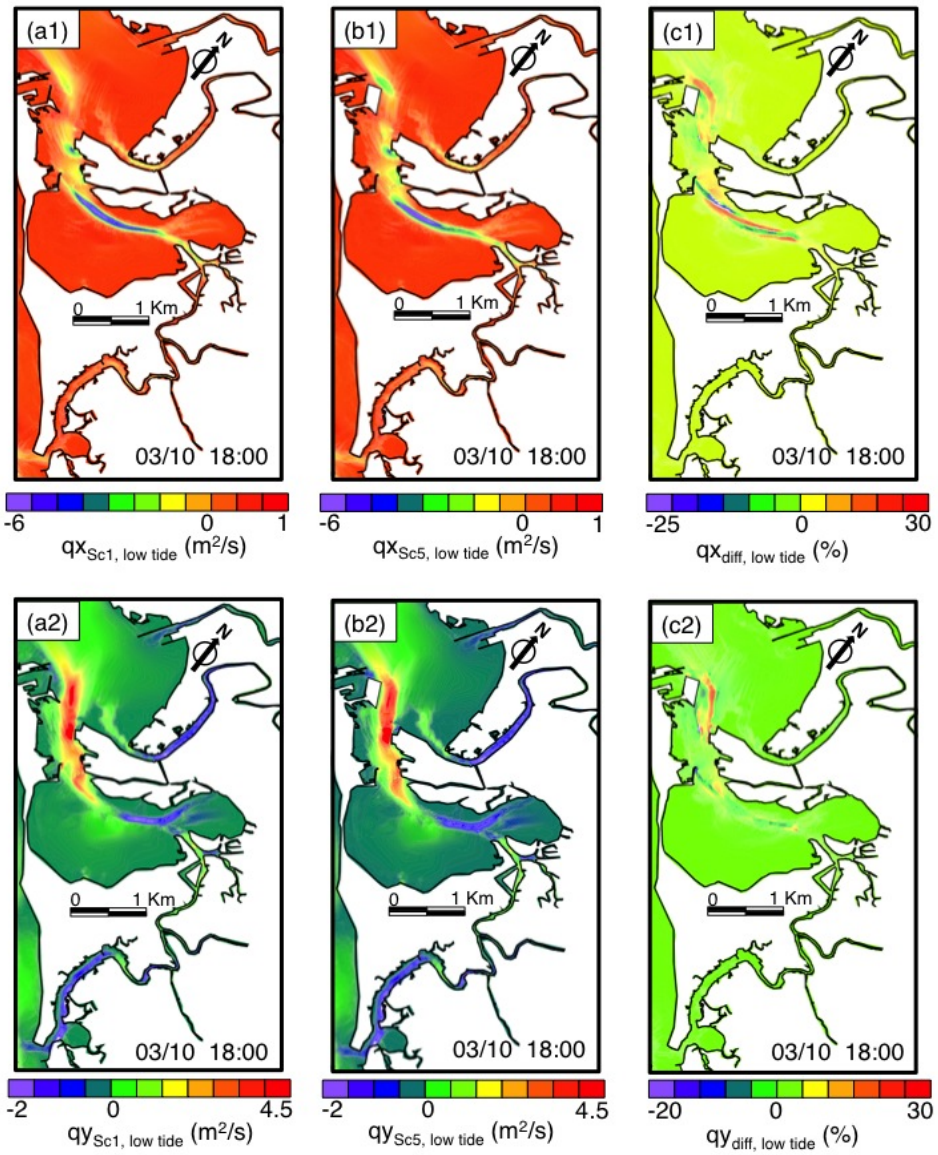

Figure 7.33: Influence of the cross-bay bridge on tidal level in bay (March 10, 2012). (a1) and (a2) Flow rate per unit width (q_x and q_y, respectively) at low tide (Sc_1) according to the time slices in Figure 7.11. (b1) and (b2) Flow rate per unit width (q_x and q_y, respectively) at low tide (Sc_4). (c1) and (c2) Difference at flow rate per unit width (q_x and q_y, respectively) at low tide ($Sc_4 * 100/Sc_1$).

ventions, but this orientation changes as the current moves eastward. In B and C, two sections are differentiated. In the left side the vectors rotate clockwise, with the opposite on the right side. Influence of the cross-bay bridge on flow rate is analyzed in Figures 7.36 and 7.37. The tidal prism is increased by 3-4% after construction. In this scenario, tidal prism also increases at San Pedro estuary and Carracas creek which slightly decreases by 2%. The tidal prism of the Sancti-Petri creek (Guadalete estuary) slightly increases by 1%(0.3%).

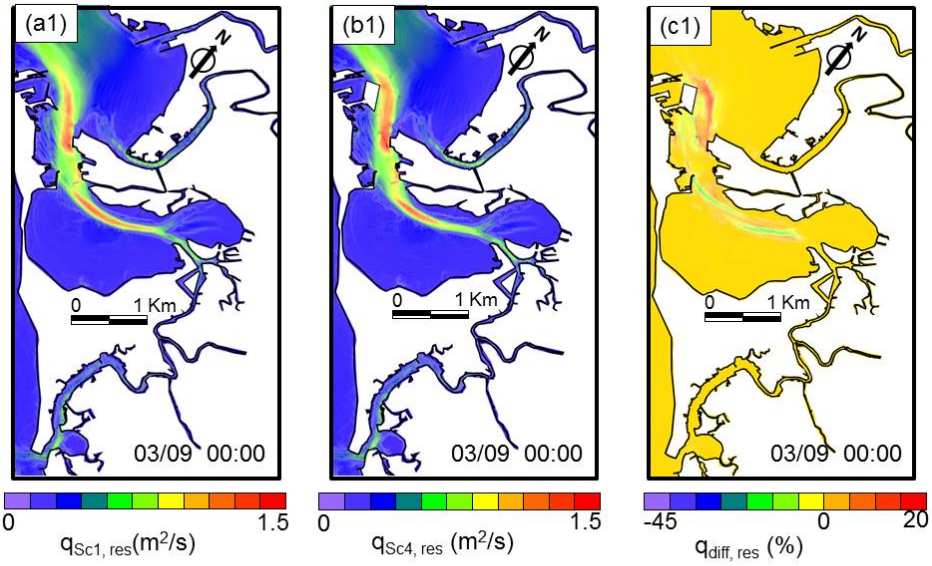

Figure 7.34: Influence of the cross-bay bridge on tidal level in bay (March 10, 2012). (a) Without bridge (Sc_1); (b) with bridge (Sc_4); (c) difference of residual transport ($Sc_4 * 100/Sc_1$).

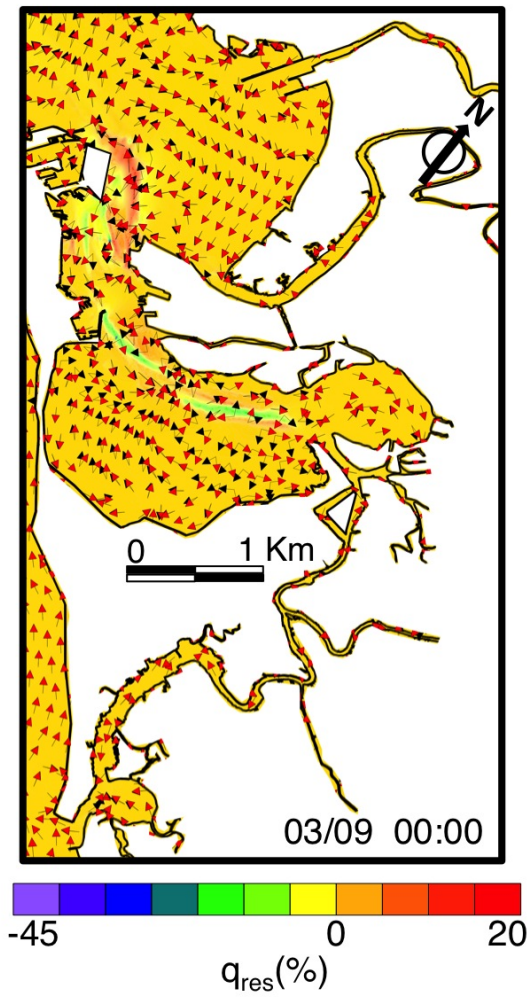

Figure 7.35: Residual transport at Sc_4 (red arrows) and Sc_1 (black arrows). The colormap in the background represents the variation in the magnitudes ($Sc_4 * 100/Sc_1$).

7.4.2 Morphodynamics

This reference scenario assesses the future conditions of the Bay. The new bridge and the sediment extraction by dredging the port has led to a pronounced increase in SSC. The highest changes are reached during flood tide. At flood tide, the planned constructions (left-upper panel-Figure 7.38) leads to an slightly decrease of 2 mg/l in SSC in the inner bay, but up to 5 mg/l in the west of Puntales Channel. The typical concentrations in these sections (right upper panel-Figure 7.38) are 5 mg/l and 10 mg/l, respectively; implying the impact of the future interventions will be substantial. The MSC (middle panel-Figure 7.38) is most affected than the SSC. The inner bay is the most affected, the MSC is reduced by 25% and only is increased close to Trocadero creek and the west of the Puntales Channel(30%); this MSC could come from the inner bay. At flood and ebb tide period before the all constructions, the west of Puntales channel and at the entrance of the inner bay the sediment is deposited (green color; lower panel-Figures 7.38 and 7.38). At ebb

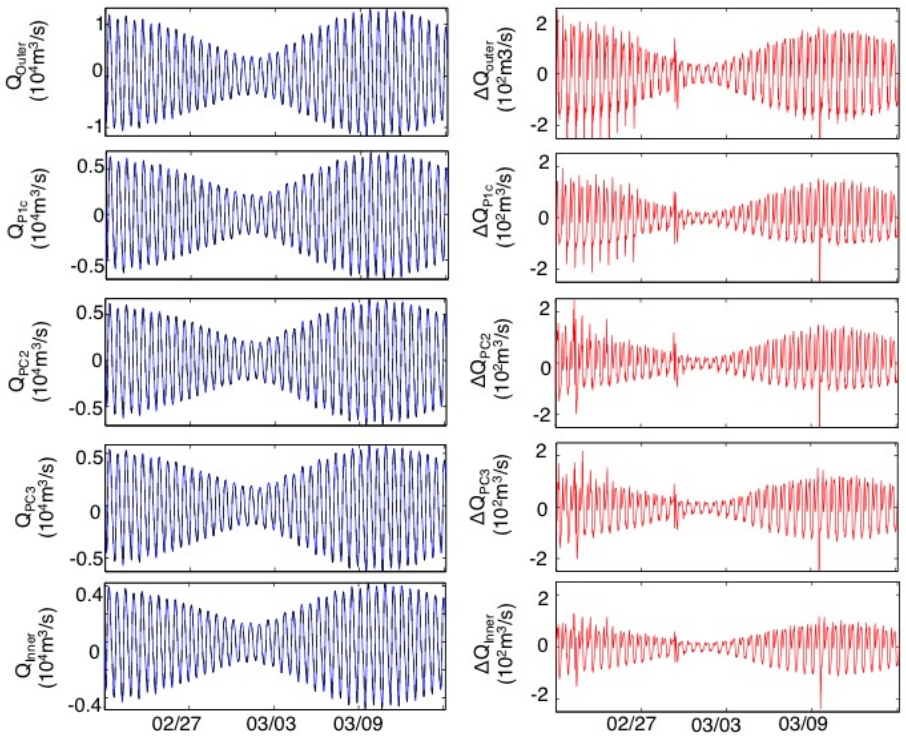

Figure 7.36: Influence of the cross-bay bridge on flow rate in different section along the bay. Blue line corresponds to scenario without bridge; black line corresponds to scenario with bridge; red line corresponds to the difference between with and without bridge.

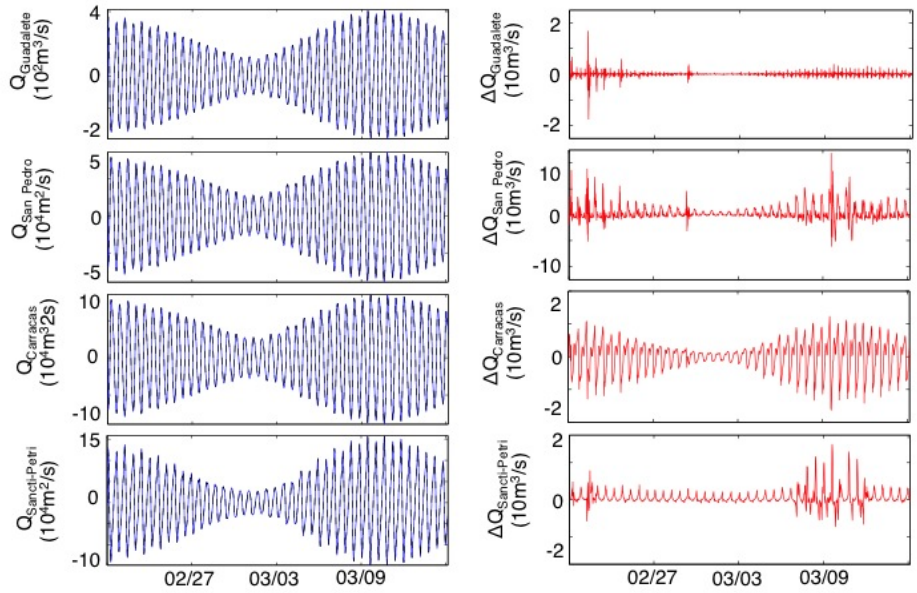

Figure 7.37: Influence of the cross-bay bridge on flow rate in the mouth of the Guadalete estuary, San Pedro estuary, Carracas Creek and Sancti-Petri Creek, from upper to lower respectively. Blue line corresponds to scenario without bridge; black line corresponds to scenario with bridge; red line corresponds to the difference between with and without bridge.

tide period, the increase of SSC in the mouth of the San Pedro estuary is significant (50%). In the case of the MSC, all bay suffer an increase of 10-15%.

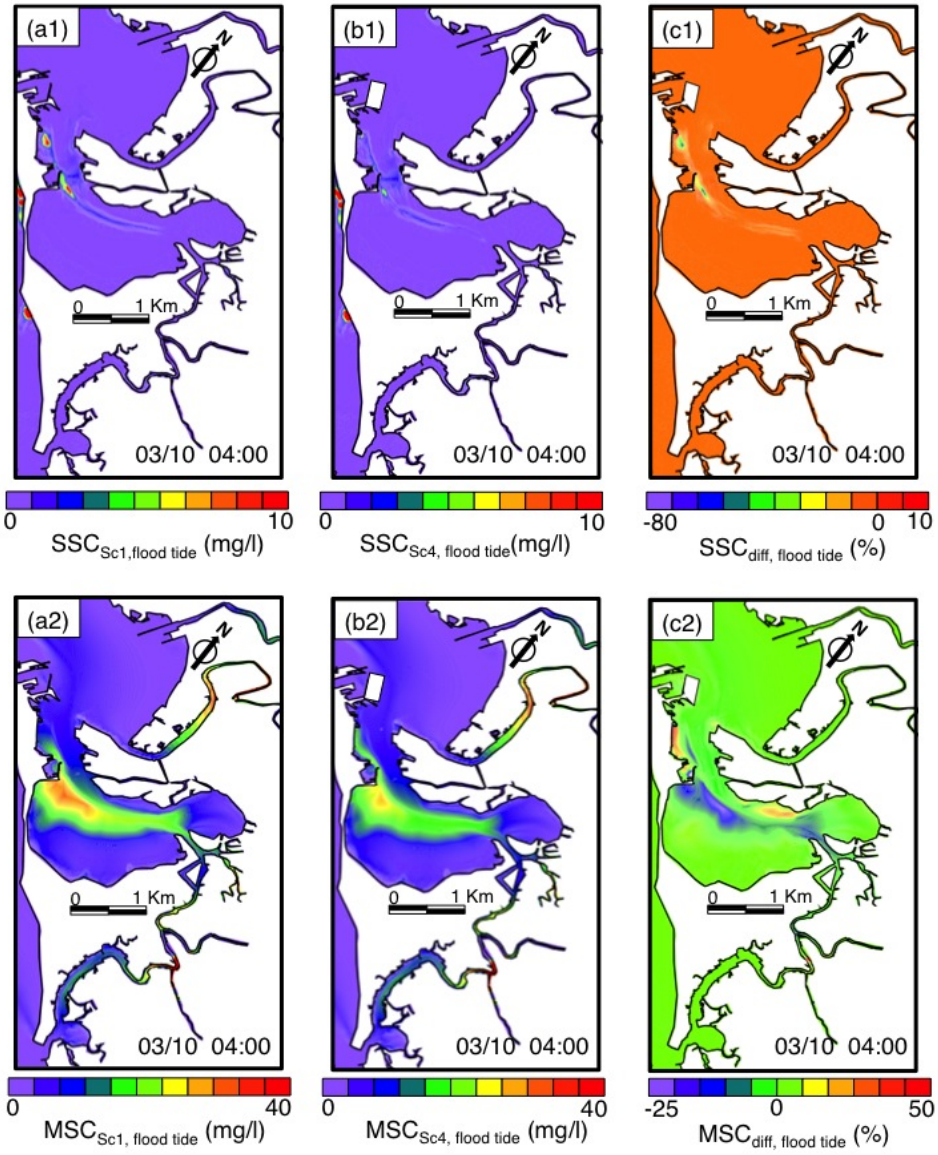

Figure 7.38: A time series of sand concentration (mg/l) and mud concentration (mg/l) in the Bay of Cádiz at flood tide period 03/10 04:00 (panels 1 and respectively). Panels a, b and c correspond to Sc_1, Sc_4 and $Sc_4 * 100/Sc_1$, respectively (blue = decrease and red = increase).

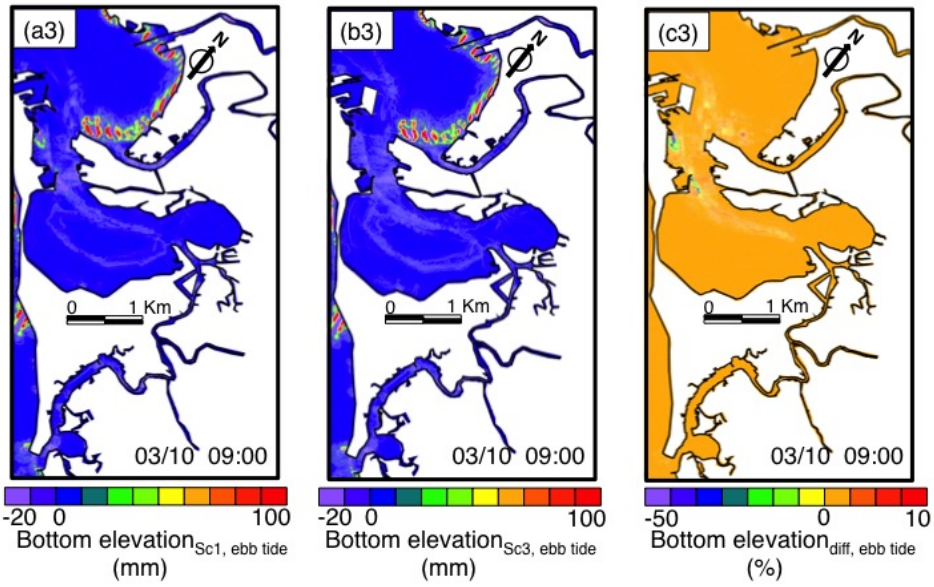

Figure 7.39: A time series of bottom elevation (mm) in the Bay of Cádiz at flood tide period 03/10 04:00. Panels a, b and c correspond to Sc_1, Sc_4 and $Sc_4 * 100/Sc_1$, respectively (blue = decrease and red = increase).

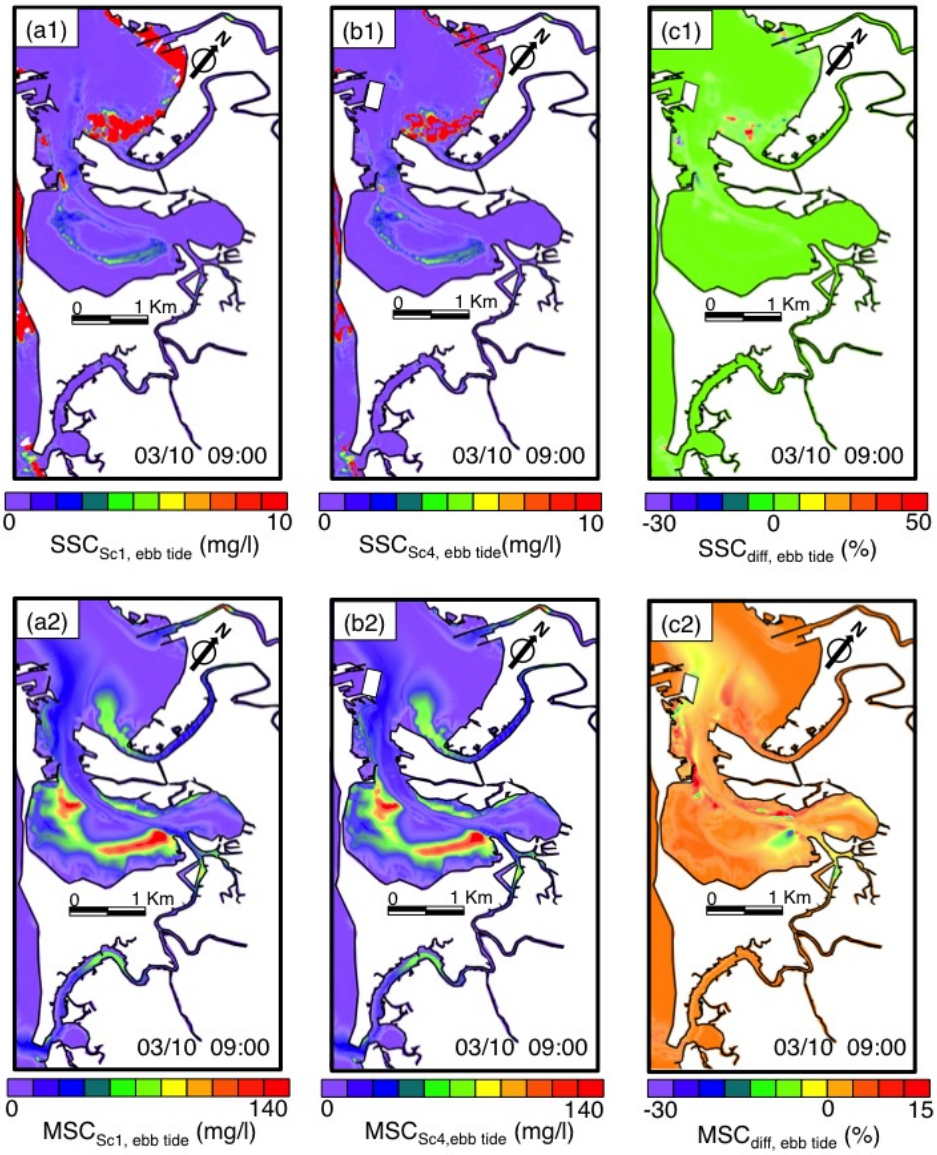

Figure 7.40: A time series of sand concentration (mg/l) and mud concentration (mg/l) in the Bay of Cádiz at ebb tide period 03/10 09:00 (panels 1 and 2, respectively). Panels a, b and c correspond to Sc_1, Sc_4 and $Sc_4 * 100/Sc_1$, respectively.

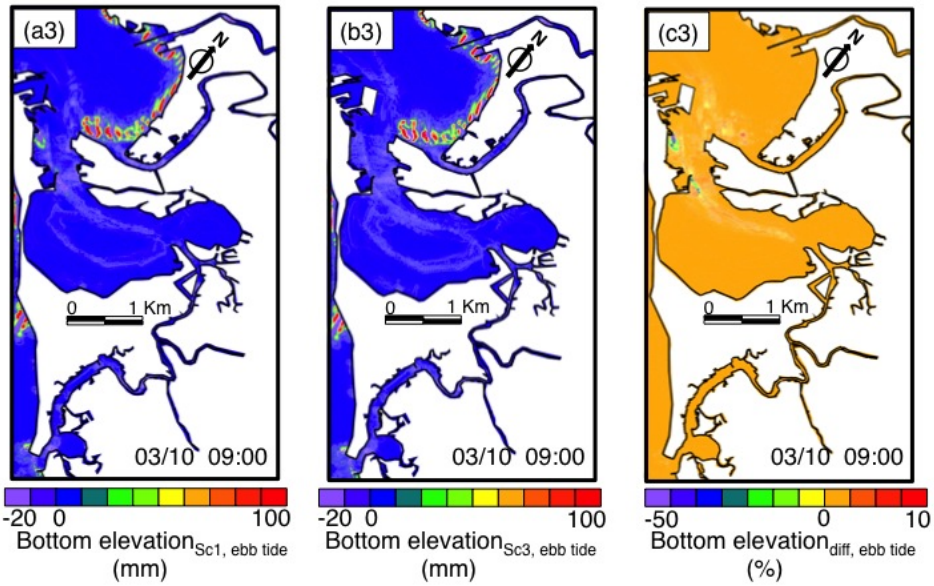

Figure 7.41: A time series of bottom elevation (mm) in the Bay of Cádiz at ebb tide period 03/10 09:00. Panels a, b and c correspond to Sc_1, Sc_4 and $Sc_4 * 100/Sc_1$, respectively.

Chapter 8
Conclusions

8.1 Main conclusions

Tidally dominated coastal embayments are generally affected by man-made alterations that modify the tidal exchange, disrupting the pathway of the tidal flows and altering the tidal range and the flushing characteristics of these systems. It is still under research how constricted bays behave and how they respond to planned human interventions that significantly altered the morphology of these embayments.

To gain insight into the previos questions, this Thesis has mainly focused on (1) the understanding of the current behaviour, evolution and physical processes underlying the dynamics of the Bay of Cádiz, and (2) the assessment of the consequences of the ongoing and planned human interventions on the hydrodynamics and morphodynamic of this short, altered and irregular embayment. The hydro- and morphodynamic evolution was analyzed by means of field data and numerical modeling.

The most important conclusions of the Thesis are summarized by presenting the conclusions obtained for the specific objectives that were formulated in Section 1.2.2:

1. *To characterize the Bay of Cádiz for a better understanding of the impact that the tidal flats and the complex geometry has on this type of sites.*

   The Bay of Cádiz is a low–inflow, short, and tidally driven estuary located in the SW portion of the Iberian Peninsula, facing towards the Gulf of Cádiz (Atlantic Ocean). Historical records indicate that the first human settlements at this bay were formed more than 3,000 y.a. because the geostrategic location of the area. Tides are semidiurnal, with M2 (12.42 h) tides as the main tidal constituent. The tidal range is mesotidal, with typical values during the neap and spring tides of $\sim$1 m and $\sim$4 m, respectively. The Bay can be divided into two basins (inner and outer basins) that are connected through a constriction know as the Puntales channel, with area of 140 km^2. Three different areas can thus be identified: A deeper outer (up to 15 m) area connected with the open sea a shallower inner area (up to 8 m), and the Puntales channel (up to 18 m). A dense tidal channel network flows into the bay, as Sancti–Petri and Carracas creeks act as the main tidal channels.

2. *To record in situ measurements of the main hydrodynamic variables: water levels, currents, waves, temperature, salinity and turbidity.*

The sea level, currents and wind data were collected at seven moorings during a three month field survey. This has been the first long-term field survey carried out in the area measuring hydrodynamics simultaneously at different stations. The locations of stations I1-I4 were selected considering the future location of the new bridge, which crosses the constriction, and the new port terminal, to evaluate their possible impacts on the water exchange between the inner and outer basins. Station T1 was located at the San Pedro river mouth, whereas stations T2 and T3 were placed on Carracas and Sancti–Petri creeks, respectively. These data were used to analyze and characterize the behaviour of the Bay and to calibrate and validate the numerical models.

3. *To implement the numerical models at both the intratidal and subtidal time scales. The models should solve the Navier-Stokes equations under the shallow water and Boussinesq assumptions, including all the relevant forcing factors: the tide, wind, river discharges and wave conditions*.

   Two numerical models were implemented at the Bay. The models were calibrated and tested with water levels and currents (both at tidal and residual scales) measured during the field survey. The comparison between measured and modeled variables indicates that they are correctly reproduced by the models. In general, the coupled model correctly reproduced the main processes involved in the estuarine system.

   A reasonable agreement between the observed and computed tidal wave characteristics was obtained for both instruments (I1 and I2).The Delft3D was calibrated and tested with water level ($R \sim 0.99$), tidal current ($R \sim 0.88$), residual current ($R \sim 0.8$) and wave height($R \sim 0.8$) data obtained through a field survey from December 2011 to January 2012. The largest discrepancies were observed for the eastern velocity component.

   Carniello et al. (2005) combines wind-waves with tidal fluxes, and excellent agreements (I1-I4; T1-T3) were obtained during a period of 40 days with water level ($R \sim 0.99$), tidal current ($R \sim 0.88$), residual current ($R \sim 0.8$) and tidal prism ($R \sim 0.73$) data obtained through a field survey from February 2012 to March 2012. Secondly, the sediment transport and bed evolution module was coupled with the wind-wave tidal module (I2), with a good agreement for suspended sediment concentration ($R \sim 0.66$).

4. *To analyze the current hydrodynamic behaviour along the bay and assess the governing processes and dominant physical mechanisms*.

   The asses of (barotropic) tidal and subtidal flows was focused on the analysis of semidiurnal, diurnal and quarter-diurnal tidal constituents; the characterization of the tidal wave transformation and energy variability; and at a subtidal time scale, the water volume exchange between the inner and outer bay. The measurements were additionally constrained with the results obtained from the Delft3D numerical model.

The semi-diurnal species are the most energetic within the estuary. Their amplitudes increase slightly as the tidal wave propagates into the bay through the Puntales Channel due to channel convergence. During normal conditions, with low inflows, the flood and ebb tidal prisms (both on the order of $\approx 10^8 \mathrm{m}^3$) indicate that Cádiz Bay is tidally dominated and flood-dominated. The latter is also confirmed by the relative phase difference between the M2 and M4 elevations. The amount of dissipated tidal energy, which is more significant at the constriction site, destabilizes the water column, resulting in a weakly stratified system.

The velocity field is characterized in terms of the tidal ellipse parameters. Ellipses are mainly oriented along the Puntales Channel, although the artificial construction along the margins seem to shift the inclinations at some moorings. As in the adjoining inner shelf, the semidiurnal ellipses show positive semi-minor axes (anticyclonic rotation), except at the confluence of the channel and the inner bay, where the change in the bottom slope induces negative relative vorticity. This location coincides with the maximum dissipation of tidal energy. The M2 tidal current is near $\pi/2$, and is out of phase with M2 tidal elevation, which is indicative of a dynamically short estuary in terms of tides. This behaviour is rather associated with the reduced length of the embayment instead of a prominent tidal wave reflection.

At a larger time scale, the residual water volume exchange between the inner and outer bay ($|V_{\mathrm{res}}| < 4 \cdot 10^7\,\mathrm{m}^3$) is controlled by the wind action, the contribution of which exceeds that of the tidally induced asymmetries. The larger exchange inflows are attained after strong NW winds, whereas the largest outflows are normally associated with SE winds. The cross-correlation between wind and residual volumes attains values as high as 0.70 for winds over 8 m/s. A lower cross-correlation is found for weaker winds. The response lags are close to zero for strong winds, although values as high as ≈ 6 days are typically observed for wind velocities lower than 5 m/s.

5. *To assess the current morphodynamic evolution along the bay and to analyze the sediment transport patterns.*

   During the flooding periods large amounts of sediment are transported into the embayment, while during the ebbs a large amount of sediment leaves the embayment back offshore. Due to erosion and deposition during the tidal cycle, the bottom evolves and usually organizes itself in a pattern of shallow shoals separated by deep channels. The velocity of the flow, the water elevation and the sediment concentration show periodic behaviour on the tidal time scale. This behaviour will be stable on the tidal time scale due to friction at the sea–bed. Wind-driven water exchanges between the basins are fundamental to the overall mixing of the bay. A constant or accelerating north wind drives water southward and vice versa. The MSC is affected by south wind, in contrast the SSC is affected by the north wind.

6. *To apply the model to different scenarios to evaluate the potential changes in the dynamics due to the ongoing and planned human interventions.*

   Using the models we can simulate different scenarios corresponding to the future interventions and performed long-term hydro- and morphodynamic simulations.

Four scenarios are represented: Scenario 1 (hereinafter Sc_1) correspond to the current situation, Scenario 2 (hereinafter Sc_2) features the construction of the new port terminal and the deepening of the navigation channel, Scenario 3 (hereinafter Sc_3) corresponds to the new bridge, and finally, on top of these interventions, Scenario 4 (hereinafter Sc_4) includes all interventions, which corresponds to the future scenario. Our results indicate that these variables play an important role in the dynamics of these environments.

The response to these human interventions show that the dredging activity has exerted profound impacts on the morphological evolution of the embayment system: the deeper channels have experienced further erosion while the shallower shoals (ridges) have accreted further higher, and the overall stability of the embayment system has been maintained.

Major channel deepening works will alter the sediment transport regime. The influence of the construction is greater in the outer and central sectors of the bay. The influence of the dredging and the new terminal are concentrated at the entrance to the central section of the bay and close to the channel. The dredge increased siltation in the shallower areas close to the new channel, which subsequently reduced the amount of sediment input into the basins and will increase the requirement for maintenance dredging. The magnitudes and variations of suspended sediment concentrations in major channels closely follow the strengths of tidal flow. The hydrodynamic changes and their effect on sediment erosion, deposition and transport may cause secondary geomorphological changes away from the dredge location, including the potential erosion of intertidal areas.

The comparison of the previous studies with our results shows that there are notable increases (reductions) close to the dredged area (surroundings of the dredged area). This Thesis has evaluated tidal elevations and residual tidal currents and correlated the changes in the hydrodynamics with the sediment patterns after interventions, concluding that the maximum changes are found close to the interventions. Furthermore, compared to our results, there are several similarities for areas where erosion and sedimentation dominate. Previous studies showed that baroclinic processes influence an estuary's suspended sediment dynamics, and the magnitude of estuarine circulation increases as a result of deepening. Over the long term, the sediment dredged from the channels may reduce the sediment concentration in the estuary. The quantity of sediment could depend on the seasonal variation or availability of sediment. Most authors agree that intertidal areas provide a natural sink for sediment to accumulate.

The influence of the bridge has been analyzed too. The bridge's influences at the Puntales Channel and the inner bay are the largest. Especially at the west of the Puntales Channel, the influence of the fourth pier (from the west) is accumulated here. The results indicated that the tidal current changed obviously around the piers and in the inner bay while unobvious in the outer bay. Although tiny impact due to a single pier, accumulated blockage effect of the whole bridge could induce the tidal change in the bay entrance. Due to the bridge construction, the difference of tidal

elevation between the inside water and outside water increased. The net variation of the bottom elevation provided by the model clearly shows the crucial role of wind waves in driving the lagoon bathymetry evolution and the net erosion of tidal flats, in particular in the central southern part of the basin. Furthermore we can observe the deposition within the main channels, which periodically need dredging.

The future development of the bay depends heavily on the future constructions. In conclusion, the interventions have a relatively large impact on the bay dynamics, which is most obvious for the tidal flow and the residual current. The results indicate that the ability of the bay to exchange water and transport sediment between the inner and outer bay will deteriorate, thus impacting the ecological environment of the bay. For example, the changes could promote sedimentation in the inner bay because of the lower current velocities. It is suggested that (i) the main channels will become even shallower, which will concentrate the tidal currents running through them, or (ii) the shallow areas will become so deep that the tidal currents are not very effective at transporting sediment.

The hydro- and morphodynamic changes show that the effects of future interventions are far from damped out, and it will take many decades before a new equilibrium will be reached. Given that the proposed methodology can be applied to simulate altered bays, our results highlight the importance of analyzing the effects that these interventions can produce in similar environments.

8.2 Futures Lines

In this Thesis, the complex hydrodynamics and morphodynamics of the Bay of Cádiz were investigated. The application of the numerical models enabled to determine the response of the bay to the ongoing and planned human interventions. Given their large variability, the Thesis focused on the recent constructions. Notwithstanding additional scenarios could be considered as a continuation of this work.

Some of these additional scenarios could represent extreme weather conditions, like a strong wind situation or a strong high sea level. On the other hand, the primitive situation (5500 a.C.-Figure 2.2) of the Bay of Cádiz could be represented and assessed. Finally, the extension of the mesh including all the Gulf of Cádiz should be designed to consider the whole system.

In the last 10 to 15 years, the rate of global sea level rise has increased by about 50 percent, and is now averaging 3 millimeters per year. The scientific consensus is that human-induced global warming is a major contributor to this accelerated rise. The analysis of the water exchange and sediment transport between basins using temporal scaling and the ratios of erosion rate as a function of sea level rise rate should be included to further explore the behaviour of the Bay.

Climate change is also likely to have an effect over time on the functioning of tidal creeks and the fate of terrestrial sediments in the coastal marine area. The long-term fate of the tidal creek and sediment that is eroded from the land will depend on the balance

that is established between export of sediment during spates and return of sediment between spates. Over time, it is likely that the balance of processes will change as the tidal creek infills with sediment. Those aspects should also be analyzed in detailed.

Appendix A
Correlation Coefficients

The coherence between the model and measurements was analyzed by the root-mean-square error (RMSE), the correlation coefficient (R), and the model performance (skill, S). Considering that M_n and C_n are the measured data and the computed data, respectively, at N discrete points, the RMSE is given by

$$RMSE = \sqrt{\frac{1}{N}\sum_{n=1}^{N}(M_n - C_n)^2}. \tag{A.1}$$

The correlation coefficient (R) between M_n and C_n is defined by

$$R = \left(\frac{1}{N}\sum_{n=1}^{N}(M_n - \bar{M}_n)(C_n - \bar{C}_n)\right) / (\sigma_C \sigma_M), \tag{A.2}$$

where σ_M and σ_C are the standard deviations of the measured and computed data, respectively. The overbar represents the mean value. The correlation ranges from 0 (no correlation) to 1 (strong correlation). The model performance (skill parameter S) formulation proposed by Wilmott (1981) is given by

$$S = 1 - \frac{\sum_{n=1}^{N}|C_n - M_n|^2}{\sum_{n=1}^{N}\left(\left|C_n - \bar{M}_n\right|^2 + \left|M_n - \bar{M}_n\right|^2\right)}. \tag{A.3}$$

This skill formulation ranges from 0 (poor skill) to 1 (high skill).

Bibliography

Aldridge, J. (1997). Hydrodynamic model predictions of tidal asymmetry and observed sediment transport paths in Morecambe Bay. *Estuarine, Coastal and Shelf Science*, 44:39–56.

Álvarez, O., Izquierdo, A., Tejedor, B., and Mañares, R. (1999). The Influence of Sediment Load on Tidal Dynamics, a Case Study: Cádiz Bay. *Estuarine, Coastal and Shelf Science*, 48:439–450.

Álvarez, O., Tejedor, B., Tejedor, L., and Kagan, B. A. (2003). A note on sea-breeze-induced seasonal variability in the K1 tidal constants in Cádiz Bay , Spain. *Estuarine, Coastal and Shelf Science*, 58:805–812.

Andrews, D. and McIntyre, M. (1978). An exact theory of non–linear waves on a Lagrangian-mean flow. *Journal of Fluid Mechanics*, 89 (4):609–646.

Armanini, A. (1995). Non-uniform sediment transport: dynamics of the active layer. *Journal of Hydraulic Research*, 33 (5):611–622.

Armanini, A. and Di Silvio, G. (1988). Bedload and suspended transport of particles of non uniform grain-size in non-stationary condition. *Excerpta of the Italian Contributions to the Field of Hydraulic Engineering*, 3:11–34.

Arteaga, O., D.Schulz, H., and Ross, A. (2008). Dialectical Georchaeology in the Bay of Cádiz. *Geoarqueología Dialética en la Bahí de Cádiz. RAMPAS.*, 10:21–116.

Aubrey, D. G. and Speer, P. E. (1985). A study of non linear shallow inlet estuarine system Part I: Observations. *Estuarine, Coastal and Shelf Science*, 21(5674):185–205.

Barnard, P., Schoellhamer, D., Jaffe, B., and Lester, J. (2013). Sediment transport in the San Francisco Bay Coastal System: An overview. *Marine Geology*, 35:3–17.

Bart Chadwick, D. and Largier, J. (1999). Tidal exchange at the bay-ocean boundary. *Journal of Geophysical Research*, 104(C12):29901–29924.

Becker, M. L., Luettich, R. A., and Seim, H. (2009). Effects of intratidal and tidal range variability on circulation and salinity structure in the Cape Fear River Estuary, North Carolina. *Journal of Geophysical Research*, 114(C4):C04006.

Blanton, J. (1969). Energy dissipation in a tidal estuary. *Journal of Geophysical Research*, 74(23):5460–5466.

Blanton, J. O., Lin, G., and Elston, S. (2002). Tidal current asymmetry in shallow estuaries and tidal creeks. *Continental Shelf Research*, 22(11-13):1731–1743.

Booij, N., Ris, R. C., and Holthuijsen, L. H. (1999). A third-generation wave model for coastal regions: 1. Model description and validation. *Journal of Geophysical Research*, 104(C4):7649.

Bowen, M. M. and Geyer, W. R. (2003). Salt transport and the time-dependent salt balance of a partially stratified estuary. *Journal of Geophysical Research*, 108(C5):3158.

Burchard, H. and Hofmeister, R. (2008). A dynamic equation for the potential energy anomaly for analysing mixing and stratification in estuaries and coastal seas. *Estuarine, Coastal and Shelf Science*, 77(4):679–687.

Carbajal, N. (2004). A note on tidal current rotation. *Ocean Dynamics*, 54(5):531–536.

Carballo, R. (2009). *Numerical Modelling of the Currents in the Ría de Muros y Noya and thair Energy Potential. Ph. D. Thesis, USC, Santiago de Compostela (Spain)*. PhD thesis.

Carniello, L., D'Alpaos, A., and Defina, A. (2011). Modeling wind waves and tidal flows in shallow micro-tidal basins. *Estuarine, Coastal and Shelf Science*, 92(2):263–276.

Carniello, L., Defina, A., and D'Alpaos, L. (2012). Modeling sand-mud transport induced by tidal currents and wind waves in shallow microtidal basins: Application to the Venice Lagoon (Italy). *Estuarine, Coastal and Shelf Science*, 102–103:105–115.

Carniello, L., Defina, A., Faherazzi, S., and D'Alpaos, L. (2005). A combined wind wave-tidal model for the Venice lagoon, Italy. *Journal Geophysical Research*, 110:F04007.

D'Alpaos, A., Lanzoni, S., Marani, M., and Rinaldo, A. (2010). On the tidal prism channel area relations. *Journal of Geophysical Research*, 115(F1):F01003.

De la Paz, M., Gómez-Parra, A., and Forja, J. (2008). Tidal-to-seasonal variability in the parameters of the carbonate system in a shallow tidal creek influenced by anthropogenic inputs , Rio San Pedro (SW Iberian Peninsula). *Continental Shelf Research*, 28:1394–1404.

Defina, A. (2000). Two-dimensional shallow water equations for partially dry areas. *Water Resources Research*, 36:3251–3264.

Del Río, L., Benavente, J., Gracia, F., Alonso, C., and Rodríguez-Polo, S. (2015). Anthropogenic influence on spit dynamics at various timescales: Case study in the bay of cadiz (spain). 12:123–138.

Díez-Minguito, M., Baquerizo, a., Ortega-Sánchez, M., Navarro, G., and Losada, M. a. (2012). Tide transformation in the Guadalquivir estuary (SW Spain) and process-based zonation. *Journal of Geophysical Research*, 117(C3):C03019.

Díez-Minguito, M., Contreras, E., Polo, M., and Losada, M. (2013). Spatio-temporal distribution, along-channel fluxes, and post-riverflood recovery of salinity in the guadalquivir estuary (sw spain). *J. Geophys. Res. Oceans*, 118:2267–2278.

Dingemands, M., Radder, A., and Vriend, H. (1987). Computation of the D r i v i n g Forces of Wave- Induced Currents. *Coastal Engineering*, 11:539–563.

Dingemans, M., Radder, A., and De Vriend, H. (1987). Computation of the driving forces of wave-induced currents. *Coastal Engineering*, 11:539–563.

Dyer, K. R. (1997). *Estuaries: A Physical Introduction, 2nd ed., John Wiley, Chichester, U. K.*

D'Alpaos, L. and Defina, A. (1995). Modellazione matematica del comportamento idrodinamico di zone a barena solcate da una rete di canali minori. *Estratto da Rapp. e Studi, Ist. Veneto di Sci., Lett. ed Arti, Venice, Italy.*

Egbert, G. and Erofeeca, S. (2002). Efficient inverse modeling og barotroptic ocean tides. *Journal of Atmosphere Ocean Tech.*, 19:183–204.

Eldeberky, Y. and Battjes, J. A. (1996). Spectral modeling of wave breaking: application to Boussinesq equations. *Geophysical Research*, 101:1253–1264.

Elias, E. and Hansen, J. (2012). Understanding processes controlling sediment transports at the mouth of a highly energetic inlet system (San Francisco Bay, CA). *Marine Geology*, 345:207–221.

Ferrón, S., Ortega, T., Gómez-Parra, A., and Forja, J. (2007). Seasonal study of dissolved CH4, CO2 and N2O in a shallow tidal system of the bay of Cádiz (SW Spain). *Journal of Marine Systems*, 66(1-4):244–257.

Fredsoe, J. (1985). Turbulent boundary layer in wave-current motion. *Journal of Hydraulic Engineering*, 110(8):1103–1120.

Friedrichs, C. and Aubrey, G. (1988). Non-linear Tidal Distortion in Shallow Estuaries : a Synthesis. *Estuarine, Coastal and Shelf Science*, 27(6784):521–545.

Garcia, M. (2008). Sedimentation Engineering: Processes, Measurements, Modeling, and Practice. *ASCE Manuals and Reports on Engineering Practice*, 10. ASCE, Reston, Virginia:1132.

Gartner, W. (1986). *Tidal and residual currents in South San Francisco Bay.* PhD thesis.

Gill, A. (1982). *Atmosphere-Ocean Dynamics. Academic Press, New York 662 pp.*

Groeneweg, J.and Klopman, G. (1998). Changes of the mean velocity profiles in the combined wave–current motion in a GLM formulation. *Journal of Fluid Mechanics*, 370:271–296.

Groeneweg, J. (1999). Wave–current interactions in a generalised Lagrangian Mean formulation. *PhD thesis, Delft University of Technology, Delft, The Netherlands.*

Gutiérrez-Mas, J. (2011). Glycymeris shell accumulations as indicators of recent sea-level changes and high-energy events in Cádiz Bay (SW Spain). *Estuarine, Coastal and Shelf Science*, 92(4):546–554.

Gutiérrez-Mas, J., Achab, M., and Gracia, F. (2004). Structural and physiographic control on the Holocene marine sedimentation in the Bay of Cádiz (SW Spain). *Estuarine, Coastal and Shelf Science*, 17/2:153–161.

Gutiérrez-Mas, J. and Gracia, F. (1994). Morphostructural controls on the coastal sedimentary dynamics in the Southatlantic Spanish margin (province of Cádiz, Spain). *Gaia*, 9:87–90.

Gutiérrez-Mas, J., Moral, J., Sánchez, A., Dominguez, S., and Muñoz Perez, J. (2003). Multicycle sediments on the continental shelf of Cádiz (SW Spain). *Estuarine, Coastal and Shelf Science*, 57(4):667–677.

Hansen, D. and Rattray, M. (1965). Gravitational circulation in straits and estuaries. *Journal of Marine Research*, 23:104–122.

Hansen, J., Elias, E., List, J., Erikson, L., and Barnard, P. (2013). Tidally influenced alongshore circulation at an inlet-adjacent shoreline. *Continental Shelf Research*, 56:26–38.

Hasselmann, K. (1973). Measurements of wind-wave growth and swell decay during the Joint North SeaWave Project (JONSWAP). *Dtsch. Hydrogr. Zeit. Suppl.,*, 12 (A8):1–95.

Hernández-Molina, F., Somoza, L., and Lobo, F. (2000). Seismic stratigraphy of the Gulf of Cádiz continental shelf: a model for Late Quaternary very high–resolution sequence stratigraphy and response to sea–level fall, in Hunt D., Gawthorpe R.L. (Eds.), Sedimentary Responses to Forced Regressions. *Geological Society of London, Special Publications*, 172:329–362.

Hirano, M. (1971). River bed degradation with armouring. *Transactions Japan Society of Civil Engineers*, 3:619–632.

Hirano, M. (1972). Studies on variation and equilibrium state of a river bed composed of non-uniform material. *Transactions Japan Society of Civil Engineers 4*, 4:128–129.

Hole, W. (2004). An Idealized Study of the Structure of Long, Partially Mixed Estuaries. *Journal of physical oceonagraphy*, pages 2677–2691.

Holthuijsen, L., Booij, N., and Herbers, T. (1989). A prediction model for stationary, short-crested waves in shallow water with ambient currents. *Coastal Engineering*, 13:23–54.

Holthuijsen, L., Booij, N., and Ris, R. (1993). A spectral wave model for the coastal zone. *Proceedings of the 2nd International Symposium on Ocean Wave Measurement and Analysis, New Orleans*, pages 630–641.

Hong, B. and Shen, J. (2012). Response of estuarine salinity and transport processes to potential future sea-level rise in the Chesapeake Bay. *Estuarine, Coastal and Shelf Science*, 104–105:33–45.

Iglesias, G. and Carballo, R. (2009). Seasonality of the circulation in the Ría de Muros (NW Spain). *Journal of Marine Systems*, 78(1):94–108.

Iglesias, G., Sánchez, M., Carballo, R., and Fernández, H. (2012). The TSE index e A new tool for selecting tidal stream sites in depth-limited regions. *Renewable Energy*, 48:350–357.

Ippen, A. and Harleman, D. (1966). Tidal dynamics in estuaries. *Estuary and coastline hydrodynamics, McGraw-Hill*, pages 493–545.

Jonge, V. N. D. (1992). Tidal flow and residual flow in the Ems Estuary. *Estuarine, Coastal and Shelf Science*, 34:1–22.

Kagan, B., Álvarez, O., and Izquierdo, A. (2005). Weak wind-wave / tide interaction over fixed and moveable bottoms : a formulation and some preliminary results. *Continental Shelf Research*, 25:753–773.

Kagan, B. A., Tejedor, L., Álvarez, O., Izquierdo, A., Tejedor, B., and Mañanes, R. (2001). Weak wave–tide interaction formulation and its application to Cádiz Bay. *Continental Shelf Research*, 21:697–725.

Knowles, N. and Cayan, D. (2004). Elevational dependence of projected hydrologic changes in the San Francisco estuary and watershed. *Climate Change*, 62:313–336.

Kolmogorov, A. (1942). Equations of turbulent motion of an incompressible fluid. IZV Akad. Nauk. *USSR, Ser. Phys.*, 6:56–58.

Largier, J., C.J.Hearn, and Chadwick, D. (1996). *Density structures in low-inflow "estuaries". In D.G. Aubrey and C.T. derichs (eds), Buoyancy Effects on Coastal and Estuarine Dynamics. Coastal and Estuarine Studies. Vol. 53, pp 227241*.

Lesser, G., Roelvink, J., Van Kester, J., and Stelling, G. (2004). Development and validation of a three-dimensional morphological model. *Coastal Engineering*, 51(8-9):883–915.

Li, P., Li, G., Qiao, L., Chen, X., Shi, J., Gao, F., Wang, N., and Yue, S. (2014). Modelin the tidal dynamic changes induced by the bridge in Jiaozhou Bay, Qingdao, China . *Continental Shelf Research*, 84:43–53.

Ligero, R., Barrera, M., Casas-Ruiz, M., Sales, D., and López-Aguayo, F. (2002). Dating of marine sediments and time evolution of heavy metal concentrations in the Bay of Cádiz, Spain. *Environmental Pollution*, 118(1):97–108.

Lin, W., Sanford, L. P., Alleva, B. J., and Schwab, D. J. (1998). Surface wind wave modeling in Chesapeake Bay. *paper presented at the Third International Conference on Ocean Wave Measurements and Analysis, Am. Soc. of Civ. Eng.*, Virginia Beach:Va.

Lin, W., Sanford, L. P., Alleva, B. J., and Suttles, S. E. (2002). Wave measurements and modeling in Chesapeake Bay. *Continental Shelf Research*, 22:2673–2686.

Liu, Z., Wie, H., Guangshan, L., and Zhang, J. (2004). Bottom Stratification and Water Exchange in Enclosed Bay with Narrow Entrance. *Estuarine, Coastal and Sheld Science*, 61:25–35.

Lu, Y., Ji, R., and Zuo, L. (2009). Morphodynamic responses to the deep water harbor development in the Caofeidian sea area, China's Bohai Bay. *Coastal Engineering*, 56:831–843.

Lv, X., Yuan, D., Ma, X., and Tao, J. (2014). Wave characteristics analysis in Bohai Sea based on ECMWF wind field. *Ocean Engineering*, 91:159–171.

Maldonado, A. and Nelson, C. (1999). Interaction of tectonic and depositional processes that control the evolution of the Iberian Gulf of Cádiz margin. *Marine Geology*, 155:217–242.

Mehta, A. (1989). Cohesive sediment transport. I: process description. *Journal of Hydraulic Engineering*, 115:1076–1093.

Murray, W. (1977). Erosion of coarse sand-clayey silt mixtures. *Journal of Hydraulic Division*, 103 (HY10):1222–1227.

Nayak, R. K., Salim, M., Mitra, D., Sridhar, P. N., Mohanty, P. C., and Dadhwal, V. K. (2014). Tidal and Residual Circulation in the Gulf of Khambhat and its Surrounding on the West Coast of India. *Journal of the Indian Society of Remote Sensing*.

Nielsen, P. (1986). *Analysis of Natural Waves by Local Approximations*.

Olabarrieta, M., Warner, J., and Kumar, N. (2011). Wave-current interaction in Willapa Bay. *Journal of Geophysical Research*, 116:C12014.

Pawlowicz, R., Breardsley, B., and Lentz, S. (2002). Classical tidal harmonic analysis including error estimates in MATLAB using T_TIDE. *Computers and Geosciences*, 28:929–937.

Periáñez, R., Casas-ruíz, M., and Bolívar, J. (2013). Tidal circulation , sediment and pollutant transport in Cádiz Bay (SW Spain): A modelling study. *Ocean Engineering*, 69:60–69.

Pethick, J. (1980). Velocity Surges and Asymmetry in Tidal Channels J. s. Pethick. *Estuarine and Coastal Marine Science*, II:331–345.

Prandle, D. (1982). The vertical structure of tidal currents and other oscillatory flows. *Continental Shelf Research*, 1(2):191–207.

Prandtl, L. (1945). Uber ein neues formelsystem fur die ausgebildete turbulenz (On a new formation for fully developed turbulence). *Nachrichten der Akademie der Wissenschaften (Report of Academy of Sciences, Gottingen, Germany)*, pages 6–19.

Pritchard, D. and Hogg, A. (2003). Cross-shore sediment transport and the equilibrium morphology mudflats under tidal currents. *Journal of Geophysical Research*, 108 (C10):3313.

Quaresma, L. S. and Pichon, A. (2013). Modelling the barotropic tide along the west-iberian margin. *Journal of Marine Systems*, 109-110:S3–S25.

Ris, R. C., Holthuijsen, L. H., and Booij, N. (1999). A third-generation wave model for coastal regions: 2. Verification. *Journal of Geophysical Research*, 104(C4):7667.

Robinson, I. (1981). Tidal vorticity and residual circulation. *Deep Sea Research*, 28A (3):195–212.

Rodi, W. (1984). Turbulence model and their application in hydraulics.

Rueda, J. L. and Salas, C. (2003). Seasonal variation of a molluscan assemblage living in a Caulerpa prolifera meadow within the inner Bay of Cádiz (SW Spain). *Estuarine, Coastal and Shelf Science*, 57(5-6):909–918.

Safak, I., Wiberg, P., Richardson, D., and Kurum, M. (2015). Control son residence time and Exchange in a systems of shallow coastal bays. *Continental Shelf Research*, 97:1–20.

Sánchez-Lamadrid, A., Jiménez, T., Ruiz, J., Gutiérrez, G., Muñoz, J., Saavedra, M., Juárez, A., Romero, M., and Pérez, A. (2002). Bahía de Cádiz Proteccion de los recursos naturales pesquero y aplicaciones para instalaciones Acuicolas (Consejería de Agricultura y Pesca de la Junta de Andalucía).

Schoen, J., Stretch, D., and Tirok, K. (2014). Wind-driven circulation patterns in a shallow estuarine lake: St Lucia, South Africa. *Estuarine, Coastal and Shelf Science*, 146:49–59.

Schuttelaars, H. and de Swart, H. (2000). Multiple morphodynamic equilibria in tidal embayments. *journal of Geophysical Research*, 105:24105–24118.

Scully, M. (2010). Wind modulation of dissolved oxygen in Chesapeake Bay. *Estuaries and Coasts*, 33:1164–1175.

Serrano, D., Ramírez-Félix, E., and Valle-Levinson, A. (2013). Tidal hydrodynamics in a two-inlet coastal lagoon in the Gulf of California. *Continental Shelf Research*, 63:1–12.

Shi J., L. C. and X., D. (2010). Three-dimensional modeling of tidal circulation within the north and south passages of the partially-mixed Changjiang River Estuary, China. *Journal of Hydrodynamics, Ser. B*, 22(5):656–661.

Simonin, O., Uittenbogaard, R., and Baron, F. nd Viollet, P. (1989). Possibilities and limitations to simulate turbulence fluxes of mass and momentum, measured in a steady stratified mixing layer. *Proceedings XXIII IAHR Congress, Ottawa, August 21– 25. National Research Council Canada*, pages A55–A62.

Soulsby, R., Hamm, L., Klopman, G., Myrhaug, D., Simons, R., and Thomas, G. (1993). Wave–current interaction within and outside the bottom boundary layer. *Coastal Engineering*, 21:41–69.

Souza, A. and Simpson, J. (1996). The modification of tidal ellipses by stratification in the Rhine ROFI. *Continental Shelf Research*, 16(8):997–1007.

Stive, M. and Wind, H. (1986). Cross-shore mean flow in the surf zone. *Coastal Engineering*, 10:235–340.

Svendsen, I. (1985). On the formulation of the cross-shore wavecurrent problem. *Proc. Workshop European Coastal ZonesQ. National Technical University of Athens, Athens*, 1:1–9.

Torfs, H. (1995). Erosion of mud/sand mixtures. *PhD thesis, Katholieke Universiteit Leuven, Leuven*.

Umgiesser, G. and Bergamasco, A. (1993). A staggered grid finite element model of the Venice lagoon. *JFinite Elements in Fluid: New Trends and Applications*, pages 659–668.

Valle-Levinson, A. (2008). Density-driven exchange flow in terms of the Kelvin and Ekman numbers. *Journal of Geophysical Research*, 113(C4):C04001.

Valle-Levinson, A. (2010). *Contemporary issues in estuarine physics*. Cambridge University Press.

Valle-Levinson, A. and Blanco, J. L. (2004a). Observations of wind influence on exchange flows in a strait of the chilean inland sea. *Journal of Marine Research*, 62(5):720–740.

Valle-Levinson, A. and Blanco, L. (2004b). Observations of wind influence on exchange flows in a strait of the Chilean Inland Sea. (1990):721–741.

Van der Spek, A. (1997). Tidal asymmetry and long–term evolution of holocene tidal basins in the netherlands, simulation of paleo–tides in the schelde estuary. *Marine Geology*, 141:71–90.

Van der Westhuysen, A. J. (2010). Modeling of depth-induced wave breaking under finite depth wave growth conditions. *Journal of Geophysical Research*, 115(C1):C01008.

Van der Westhuysen, A. J., Zijlema, M., and Battjes, J. a. (2007). Nonlinear saturation-based whitecapping dissipation in SWAN for deep and shallow water. *Coastal Engineering*, 54(2):151–170.

Van Kesteren, W., Cornelisse, J., and Kuijper, C. (1997). Dynaster Bed Model, Bed Strength, Liquefaction and Erosion. *In Cohesive Sediment (Rep. 55). Hydraulics and Rijkswaterstaat, Delft*.

Van Ledden, M. (2003). Sand-mud segregation in estuaries and tidal basins. *Ph.D. Thesis, T.U. Delft, Dep. of Civil Engineering and Geosciences*, report 03-2.

Van Ledden, M., Wang, Z., Winterwerp, H., and De Vriend, H. (2004). Sand-mud morphodynamics in a short tidal basin. *Ocean Dynamics*, 54:385–391.

Van Maren, D., van Kessel, T., Cronin, K., and Sittoni, L. (2015a). The impact of channel deepening and dredging on estuarine sediment concentration. *Continental Shelf Research*, 95:1–14.

Van Maren, D., Van Kessel, T., Cronin, K., and Sittoni, L. (2015b). The impact of channel deeping and dredging on estuarine sediment concentration. *Continental Shelf Research*, 95:1–14.

Van Rijn, L. (1984). Sediment transport, part II: suspended load transport. *Journal of Hydraulic Engineering*, 110 (11):1613–1641.

Van Rijn, L. (1993). Principles of Sediment Transport in Rivers. *Estuaries and Coastal Seas,Aqua Publications, Amsterdam, Netherlands.*

Van Rijn, L., Walstra, D., Grasmeijer, B., Sutherland, J., Pan, S., and Sierra, J. (2003). The predictability of cross-shore bed evolution of sandy beaches at the time scale of storms and seasons using process-based profile models. *Journal Coastal Engineering*, 47:295–327.

Van Vledder, G., Zijlema, M., and Holthuijsen, L. (2010). Revesiting the JONSWAP bottom friction formulation. *Proceedings of the 32th Conference of Coastal Engineering. ASCE, Shanghai, China.*

Vaz, N., Dias, J., and Chambel, L. (2009). Three-dimensional modelling of a tidal channel: The Espinheiro Channel (Portugal). *Continental Shelf Research*, 29:29–41.

Velasco Fuentes, O.U., S. J. and Ochoa, J. (2003). *Nonlinear Processes in Geophysical Fluid Dynamics.* Springer-Science+Business Media, B.V.

Venier, C., D'Alpaos, A., and Marani, M. (2014). Evaluation of sediment properties using wind and turbidity observations in the shallow tidal areas of the Venice Lagoon. *Journal of Geophysical Research.*

Verboom, G. and Slob, A. (1984). Weakly reflective boundary conditions for two-dimensional water flow problems. *5th International Conference on Finite Elements in Water Resour- ces, June 1984, Vermont, Adv. Water Resources*, 7. Delft Hydraulics, Delft, The Netherlands. Delft Hydraulics Publication:322.

Vidal, J. (2002). Caracteriazión dinámica de la marea y dl sedimento en el sistema intermareal del Caño de Sancti-Petri. *Tesis Doctoral*, Universidad de Cádiz.

Waiters, R., Cheng, R., and Conomos, T. (1985). Time scales of circulation and mixing processes of San Francisco Bay waters. *Hydrobiologia*, 129:37–58.

Walstra, D., Roelvink, J., and Groeneweg, J. (2000). Calculation of wave-driven currents in a 3D mean flow model. Edge, B. *Coastal Engineering*, 2. ASCE, New York,:1050–1063.

Wang, Y., Tang, L., Wang, C., Liu, C., and Z.D., D. (2014). Combined effects of channel dredging, land reclamation and long-range jetties upon the long-term evolution of channel-shoal system in Qinzhou bay, SW China. *Ocean Engineering*, 91:340–349.

Williamson, H. and Ockenden, M. (1993). Laboratory and field investigations of mud and sand mixtures. *In: Proceedings of the First International Conference on Hydro-Science and Engineering*, Washington, DC.:622–629.

Wilmott, C. (1981). On validation of models. *Physical Geographic*, 2:184–194.

Wong, K. C. and Moses-Hall, J. E. (1998). On the relative importance of the remote and local wind effects to the subtidal variability in a coastal plain estuary. *Journal of Geophysical Research: Oceans (1978–2012)*, 103(C9):18393–18404.

Zarzuelo, C., Díez-Minguito, M., Ortega-Sánchez, M., López-Ruiz, A., and Losada, M. (2015a). Hydrodynamics and response to planned human interventions in a highly altered embayment: The example of the Bay of Cádiz (Spain). *Estuarine, Coastal and Shelf Science*, 167:75–85.

Zarzuelo, C., Ortega-Sánchez, M., Díez-Minguito, M., , and Losada, M. (2015b). Observations of tidal and subtidal exchange flows in a constricted Bay. *Ocean Engineering (Under Review)*.

Zazo, C. (1999). El Cuaternario Marino–Continental y el límite Plio-Pleistoceno en el litoral de Cádiz. *Ph.D. Thesis, Universidad Complutense*, pages 67—74.

Zhong, L. and Li, M. (2006). Tidal energy fluxes and dissipation in the Chesapeake Bay. *Continental Shelf Research*, 26(6):752–770.